

POLISH
ACADEMY
OF SCIENCES

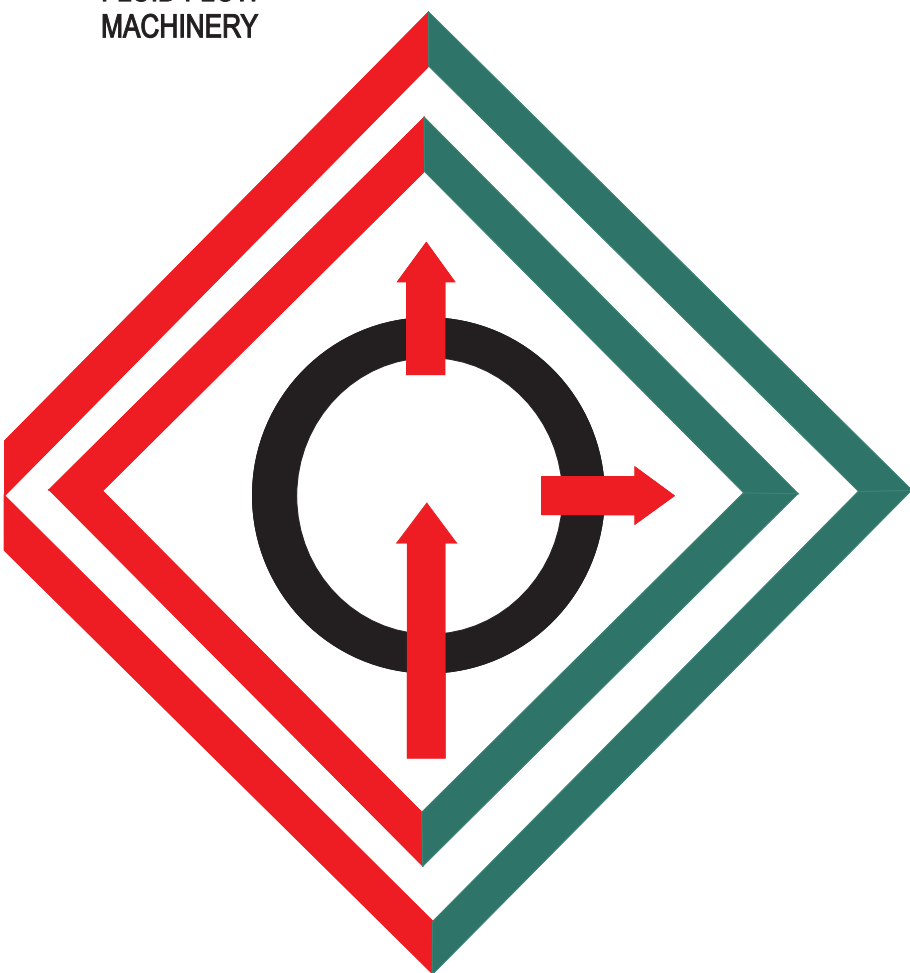
COMMITTEE OF
THERMODYNAMICS
AND COMBUSTION

INSTITUTE OF
FLUID FLOW
MACHINERY

archives of thermodynamics

QUARTERLY

ISSN 1231-0956



Vol. 44
2023
No. 3

Aims and Scope

The aim of the quarterly journal Archives of Thermodynamics (AoT) is to disseminate knowledge between scientists and engineers worldwide and to provide a forum for original research conducted in the field of thermodynamics, heat transfer, fluid flow, combustion and energy conversion in various aspects of thermal sciences, mechanical and power engineering. Besides original research papers, review articles are also welcome.

The journal scope of interest encompasses in particular, but is not limited to:

Classical and extended non-equilibrium thermodynamics,	Energy transition,
Thermodynamic analysis including exergy,	Advanced energy carriers,
Thermodynamics of heating and cooling,	Energy storage and efficiency,
Thermodynamics of nuclear power generation,	Energy in buildings,
Thermodynamics in defense engineering,	Hydrogen energy,
Advances in thermodynamics,	Combustion and emissions,
Experimental, theoretical and numerical heat transfer,	Turbomachinery,
Thermal and energy system analysis,	Thermal energy conversion,
Renewable energy sources including solar energy,	Integrated energy systems,
Secondary fuels and fuel conversion,	Distributed energy generation,
Heat and momentum transfer in multiphase flows and nanofluids,	Thermal incineration of wastes and waste heat recovery.

Supervisory Editors

T. Bohdal, *Koszalin University of Technology, Koszalin, Poland*

M. Lackowski, *The Szwedzki Institute of Fluid Flow Machinery, Gdańsk, Poland*

Honorary Editor

J. Mikieliewicz, *The Szwedzki Institute of Fluid Flow Machinery, Gdańsk, Poland*

Editor-in-Chief

P. Ocioń, *Cracow University of Technology, Cracow, Poland*

Section Editors

P. Lampart, *The Szwedzki Institute of Fluid Flow Machinery, Gdańsk, Poland*

S. Polesek-Karczewska, *The Szwedzki Institute of Fluid Flow Machinery, Gdańsk, Poland*

I. Szczygiel, *Silesian University of Technology, Gliwice, Poland*

A. Szłęk, *Silesian University of Technology, Gliwice, Poland*

Managing Editor

J. Frączak, *The Szwedzki Institute of Fluid Flow Machinery, Gdańsk, Poland*

Members of Programme Committee

P. Furmański, *Warsaw Univ. Tech., Poland*

S. Pietrowicz, *Wrocław Univ. Sci. Tech., Poland*

J. Badur, *Inst. Fluid Flow Mach., Gdańsk, Poland*

R. Kobylecki, *Częstochowa Univ. Tech., Poland*

T. Chmielniak, *Silesian Univ. Tech., Gliwice, Poland*

J. Wajs, *Gdańsk Univ. Tech., Poland*

D. Kardaś, *Inst. Fluid Flow Mach., Gdańsk, Poland*

International Advisory Board

J. Bataille, *Ecole Centr. Lyon, France*

S. Michaelides, *Texas Christian Univ., USA*

A. Bejan, *Duke Univ., Durham, USA*

M. Moran, *Ohio State Univ., USA*

W. Blasiak, *Royal Inst. Tech., Stockholm, Sweden*

W. Muschik, *Tech. Univ., Berlin, Germany*

G.P. Celata, *ENEA, Rome, Italy*

I. Müller, *Tech. Univ., Berlin, Germany*

L.M. Cheng, *Zhejiang Univ., Hangzhou, China*

H. Nakayama, *JAEA, Japan*

M. Colaco, *Federal Univ. Rio de Janeiro, Brazil*

S. Nizetic, *Univ. Split, Croatia*

J.M. Delhay, *CEA, Grenoble, France*

H. Orlande, *Federal Univ. Rio de Janeiro, Brazil*

M. Giot, *Univ. Catholique Louvain, Belgium*

M. Podowski, *Rensselaer Polyt. Inst., USA*

K. Hooman, *Univ. Queensland, Australia*

R.V. Rao, *Sardar Vallabhbhai Nat. Inst. Techn., India*

D. Jackson, *Univ. Manchester, UK*

A. Rusanov, *Inst. Mech. Eng. Prob., Kharkiv, Ukraine*

D.F. Li, *Kunming Univ. Sci. Tech., China*

A. Vallati, *Sapienza Univ. Rome, Italy*

K. Kuwagi, *Okayama Univ. Science, Japan*

M.R. von Spakovsky, *Virginia Polyt. Inst., USA*

J.P. Meyer, *Univ. Pretoria, South Africa*

H.R. Yang, *Tsinghua Univ., Beijing, China*

**POLISH ACADEMY OF SCIENCES
COMMITTEE OF THERMODYNAMICS AND COMBUSTION
INSTITUTE OF FLUID FLOW MACHINERY**

archives of thermodynamics

QUARTERLY

Vol. 44

2023

No. 3

Editorial Office

IMP PAN Publishers

The Szewalski Institute of Fluid Flow Machinery, Fiszerza 14, 80-231 Gdańsk, Poland,
Phone: (+48) 58-341-12-71 int. 141, E-mail: redakcja@imp.gda.pl
<https://www.imp.gda.pl/archives-of-thermodynamics/>

Copyright © by the Polish Academy of Sciences, 2023

Copyright © by the Szewalski Institute of Fluid Flow Machinery, 2023

Publication funding of this journal is provided by resources of the Polish Academy of Sciences and the Szewalski Institute of Fluid Flow Machinery

Terms of subscription outside Poland

Annual subscription rate outside Poland (2023) is 152 EUR. Price of single issue is 38 EUR. Previously published volumes are available on request. Subscription orders should be sent directly to **IMP PAN Publishers, The Szewalski Institute of Fluid Flow Machinery PASci, ul. Fiszerza 14, 80-231 Gdansk, Poland**; dr Jarosław Frączak, phone: (+48) 58-52-25-230; e-mail: jfrk@imp.gda.pl. Payments should be transferred to the bank account of IMP PAN: IBAN 28 1130 1121 0006 5498 9520 0011 at Bank Gospodarstwa Krajowego; Code SWIFT: GOSKPLPW

Warunki prenumeraty w Polsce

Roczna prenumerata (2023 r.) wynosi 260.00 PLN. Cena pojedynczego numeru wynosi 65.00 PLN. Osiągalne są również wydania archiwalne. Zamówienia z określeniem okresu prenumeraty, nazwiskiem i adresem odbiorcy należy kierować bezpośrednio do Wydawcy (Instytut Maszyn Przepływowych im. R. Szewalskiego PAN, ul. Fiszerza 14, 80-231 Gdańsk, dr Jarosław Frączak, e-mail: jfrk@imp.gda.pl). Wpłaty prosimy kierować na konto Instytutu Maszyn Przepływowych PAN nr 28 1130 1121 0006 5498 9520 0011 w Banku Gospodarstwa Krajowego

Articles in *Archives of Thermodynamics* are abstracted and indexed within:

Applied Mechanics Reviews • Arianta • Baidu Scholar • BazTech • Cabell's Directory • Celdes • Chemical Abstracts Service (CAS) – CAPlus • CNKI Scholar (China National Knowledge Infrastructure) • CNPIEC • EBSCO (relevant databases) • EBSCO Discovery Service • Elsevier – SCOPUS • ESCI (Emerging Sources Citation Index) • Genamics JournalSeek • Google Scholar • Inspec • Index Copernicus • J-Gate • Journal TOCs • Naviga (Softweco) • Paperbase • Pirabase • POL-index • Polymer Library • Primo Central (ExLibris) • ProQuest (relevant databases) • ReadCube • Referativnyi Zhurnal (VINITI) • SCImago (SJR) • Summon (Serials Solutions/ProQuest) • TDOne (TDNet) • TEMA Technik und Management • Ulrich's Periodicals Directory/ulrichsweb • WorldCat (OCLC)

ISSN 1231-0956

ISSN 2083-6023 (Online)

Journals PAS – Electronic Library Polish Academy of Sciences

<https://journals.pan.pl/ather>

Typeset in L^AT_EX by

Drukarnia Braci Grodzickich Sp.j. 05-500 Piaseczno, ul. Geodetów 47a

Printed and bound by

Gimpo, 02-858 Warszawa, ul. Transportowców 11

Contents

M. KUMAR SAHU, S. MISHRA, AND A. KUMAR: Optimization of geometric and flow parameters of solar air heater roughened with artificial roughness by Taguchi method	3
R. KUMAR SINGH AND P. CHANDRA: Geometrical and optical analysis of small-sized parabolic trough collector using ray tracing tool SolTrace.....	35
M. KASZUBA, P. ZIÓŁKOWSKI, AND D. MIKIELEWICZ: Performance of cryogenic oxygen production unit with exhaust gas bleed for sewage sludge gasification and different oxygen purities.....	63
J. SUN, G. ZHANG, J. TIAN, AND Y. ZHU: Thermodynamic analysis of hybrid ceramic bearings with metal inner rings.....	83
A.A. HUSSEIN: Mixed convection heat transfer in trapezoidal lid-driven cavity with uniformly heated inner circular cylinder	99
A. ROMANIAK, M.J. KOWALCZYK, M. ŁĘCKI, A. GUTKOWSKI, AND G. GÓRECKI: Investigation of thermal-flow characteristics of the minichannel heat exchanger of variable louvers height.....	119
S. DHAWAN, A. SABHARWAL, R. PRASAD, S. SHREYA, A. GUPTA, AND Y. PARVEZ: Performance analysis of a lithium-ion battery of an electric vehicle under various driving conditions.....	143
E. PELIŃSKA-OLKO: Emissivity measurement of black paint using the calorimetric method.....	161
P. KWAŚNICKI, A. GRONBA-CHYŁA, A. GENEROWICZ, J. CIUŁA, I. WIEWIÓRSKA, AND K. GASKA: Alternative method of making electrical connections in the 1st and 3rd generation modules as an effective way to improve module efficiency and reduce production costs	179
R. WIŚNIEWSKI, A. KANIA, W. ZIMA, AND J. TALER: Off-grid power supply – the future of district heating.....	201

R.K. CHIDAMBARAM, R. KANNA, P. GOPAL, AND S.K. ARUMUGAM: Experimental and numerical analysis of vortex generators designed for utility vehicles	217
M. CHAUDHARI, S.L. SHARMA, AND A. DEBBARMA: Exergetic performance anal- ysis of solar air heater with inverted L-shape ribs as roughness element....	241
J. BOSNJAK, N. BODROZIC COKO, M. JURCEVIC, B. KLARIN, AND S. NIZETIC: Use of reinforced ice as alternative building material in cold regions: an overview.....	269
P. GÓRSZCZAK, M. RYWOTYCKI, M. HOJNY, AND G. FILO: Modular heat stor- age in waste heat recovery installations	301
M.K. DUBEY AND O. PRAKASH: Effect of artificial coarseness on the performance of rectangular solar air heater duct: a comparative study.....	325

Optimization of geometric and flow parameters of solar air heater roughened with artificial roughness by Taguchi method

MUKESH KUMAR SAHU^{a,*}
SHIVAM MISHRA^b
AVINASH KUMAR^a

^a Cambridge Institute of Technology, Department of Mechanical Engineering, Tatisilwai, Ranchi, Jharkhand, Pin-835103, India

^b G L Bajaj Institute of Technology and Management, Department of Mechanical Engineering, Greater Noida, Uttar Pradesh, Pin-201308, India

Abstract The paper presents the investigation of the optimum design parameters of a solar air heater (SAH) having wire ribs as artificial roughness by using the Taguchi method. The solar air heater has arc shape roughness geometry with apex upstream flow on the absorber plate. The objective of this paper is to obtain a set of parameters that deliver maximum thermo-hydraulic performance. For this objective, a new parameter the thermo-hydraulic improvement parameter (η_{THIP}), has been introduced. For the present analysis, the effects of Reynolds number (Re), relative roughness pitch (P/e), angle of attack (α), and relative roughness height (e/D_h), denoted by A, B, C, and D, respectively, have been considered. An ($L_{18} = 6^1 \cdot 3^2$) orthogonal array (OA) was chosen as an experimental plan for applying the Taguchi method. The set of control factors for the solar air heater SAH which delivers the maximum Nusselt number (Nu), and minimum friction factor (fr) – are $A_6B_2C_2$, and $A_1B_1C_3$ respectively. To obtain the maximum THIP the experimental set-up requires only one single run using the parameter $A_6B_2C_2$, hence there is no need to run it all 54 times.

Keywords: Roughness; Nusselt number; Friction factor; Taguchi method; Optimization

*Corresponding Author. Email: mks.nitjsr@gmail.com

Nomenclature

A_c	–	surface area of the absorber plate, m^2
A_o	–	area of orifice plate, m^2
C_{pa}	–	specific heat of air, J/kgK
C_d	–	coefficient of discharge for orifice meter
D	–	hydraulic diameter of duct, m
e	–	roughness height, m
e/D_h	–	relative roughness height
f	–	friction factor
G	–	velocity of air, m/s
h	–	heat transfer coefficient, $\text{W/m}^2\text{K}$
H	–	depth or height of solar air heater duct, m
Δh	–	height of U-tube manometer fluid column, m
Δh_1	–	height of micromanometer fluid column, m
I	–	intensity of solar radiation, W/m^2
K_a	–	thermal conductivity of air, W/mK
L	–	length of solar air heater duct, m
\dot{m}	–	mass flow rate of air, kg/s
N	–	number of glass cover
Nu	–	Nusselt number
P	–	roughness pitch, m
P_m	–	pumping power, W
ΔP_D	–	pressure drop across the test section, N/m^2
ΔP_o	–	pressure drop across orifice meter, N/m^2
P/e	–	relative roughness pitch
Re	–	Reynolds number
Q_u	–	useful heat gain, W
SN-R	–	signal-to-noise ratio
T_a	–	ambient temperature, K
T_{bm}	–	mean temperature of the bottom plate, K
T_{fi}	–	air inlet temperature, K
T_{fm}	–	mean air temperature in the duct, K
T_{fo}	–	outlet air temperature, K
T_{pm}	–	mean absorber plate temperature, K
ΔT	–	rise in air temperature, K
W	–	width of solar air heater duct, m
W/H	–	aspect ratio of collector duct

Greek symbols

α	–	angle of attack, deg
β_R	–	ratio of orifice diameter (D_2) to pipe internal diameter (D_1)
ε	–	emissivity
η_{th}	–	thermal efficiency
η_{eff}	–	thermohydraulic (effective) efficiency
μ	–	absolute viscosity of air, Ns/m^2
ρ	–	air density, kg/m^3
ρ_m	–	density of fluid used in micromanometer, kg/m^3
ρ_u	–	density of fluid used in U-tube manometer, kg/m^3

Subscripts

c	–	glass cover
p	–	plate
r	–	roughened
s	–	smooth

Acronyms

DOE	–	design of experiment
GI	–	galvanized iron
OA	–	orthogonal array
SAH	–	solar air heater
THIP	–	thermo-hydraulic improvement parameter
THPP	–	thermo-hydraulic performance parameter

1 Introduction

Since energy demand is increasing globally and it will increase more rapidly in the coming years, we have to harness and obtain more energy from the various available non-conventional energy sources that are free, more reliable and environment-friendly.

Various studies on different types of solar air heaters (SAHs) and other solar thermal systems which are focused to convert solar energy into useful heat energy for various applications have been reported. Solar air heaters are the most used device in thermal energy conversion systems worldwide. Due to simplicity in construction and ease of operation SAHs are effectively used in various domestic, industrial, and agricultural applications such as drying crops, fruits and vegetables, room and space heating, preheating, dehydration of various products, and coal drying [1]. However, it has been found by investigators *via* their research that SAHs have low thermal efficiency (η_{th}) due to the poor thermal conductivity property of air and low heat exchange between the air and smooth absorber plate. In addition to these, irregular solar intensity and availability of solar energy throughout the day are also the other major reasons for the low thermal efficiency of the SAHs [2]. Hence, the different heat transfer augmentation techniques and modifications on SAH absorber plates are employed by the investigators to obtain enhanced heat transfer rates and thermal performances.

To improve the thermal performance of SAHs various enhancement techniques like the use of fins, baffles and obstacles have been adopted [3–5]. It further includes different types of absorber plates such as V-groove, corrugated type, application of packing bed and porous materials in the air-flow

path in the duct of SAH. Numerous research has also been carried out with the use of thin wire ribs as artificial roughness and its geometries on the absorber plate of the SAH to obtain higher efficiency and outlet air temperature (T_{fo}) compared to the smooth plate SAH. The presence of artificial roughness in the form of ribs breaks the laminar sublayer and it is responsible for creating turbulence in the path of core-fluid flow which increases the heat transfer rate [5].

It is reported by the researchers that the use of any type of heat transfer augmentation technique in SAHs enhances the heat transfer coefficient (h) but it also increases the friction factor (f) in terms of more pumping power (P_m) as compared to simple SAH. Therefore, in order to analyze the overall performance of a SAH, by using any type of heat transfer augmentation techniques, Webb and Eckert [6] and Lewis [7] proposed a thermo-hydraulic performance parameter (THPP) that evaluated the heat transfer and friction factor (pumping power) characteristics simultaneously of the enhanced SAH to the reference (smooth) SAH, which is discussed in details in the further section of the present paper. For optimizing different system and operating parameters like the number of glass covers (N), the emissivity of the absorber plate (ε_p), mean absorber plate temperature (T_{pm}), rise in the air temperature (ΔT), tilt angle (β), and solar radiation intensity (I) for smooth flat plate SAH, Varun *et al.* [8] have used stochastic iterative perturbation technique (SIPT).

Further, Rao and Waghmare [9] applied teaching learning based optimization (TLBO) to optimize the thermal efficiency of a flat plate SAH. Optimization of smooth absorber plate SAH has been done by Siddhartha *et al.* [10] by using the particle swarm optimization (PSO) algorithm. Chamoli [11] has used the preference selection index (PSI) approach for the optimization of a V-down perforated baffled roughened rectangular channel. Similarly, Chauhan *et al.* [12] have used the preference selection index (PSI) algorithm to optimize the thermal efficiency of impinging air jet SAH. Bilen *et al.* [13] employed the Taguchi method to optimize the heat transfer from the surface of a rectangular block. Varun *et al.* [14] performed their experimental work and used the Taguchi method to optimize the thermo-hydraulic (effective) efficiency of SAH duct roughened with combined inclined and transverse rib geometry. Aghaie *et al.* [15] performed CFD (computational fluid dynamics) simulation-based study to optimize the geometry of angled ribs SAH and its thermo-hydraulic efficiency by using the Taguchi method. An experimental study was performed by Chauhan *et al.* [16] who employed Taguchi design of experiments (DOE) method for optimizing the thermo-hydraulic performance parameter (THPP) of im-

pinging air jet SAH. Chamoli [17] applied the Taguchi method to optimize the flow and geometrical parameters of the roughened channel with V-down perforated baffles. Hu *et al.* [18] optimized the thermal efficiency of solar air collectors with holes on the baffle by the Taguchi method. The Taguchi method has also been used by investigators for the optimization of different types of heat exchangers [19, 20]. Kotcioglu *et al.* [21] used this method to optimize the plate-fins type heat exchanger. Similarly, Chamoli *et al.* [22] optimized the shape of the heat exchanger with compound inserts, whereas Zeng *et al.* [23] employed the Taguchi method for optimizing the heat exchanger with a vortex-generator fin.

The above literature review revealed that Taguchi optimization techniques have been used for the optimization of the thermo-hydraulic (effective) efficiency (η_{eff}), thermal efficiency and thermo-hydraulic performance parameter of the smooth plate, baffle, impinging air jets, and for roughened SAHs.

For calculation and analyzing the performance *via* experimental works, multiple runs or trials need to be carried out to analyze the effects of various roughness and flow parameters on the performance of the roughened SAHs. Also, investigating the effects of all roughness parameters on heat transfer, friction factor and thermo-hydraulic performance of SAHs is a very time-consuming process. The various types of equipment, different devices (to read the input and output data/parameters), and their cost are also involved in the fabrication of the experimental setup. By applying any of the optimization methods, we are able to predict and find the combination sets of design and flow parameters by which we will obtain the optimum (maximum) performance from the SAH, and this also allows to save time and cost.

In the last few years, the Taguchi method has been used widely as an optimization technique to optimize the performances of various devices which are used in heat transfer applications such as heat exchangers and various types of SAHs. It is the technique developed by Taguchi [24, 25] based on orthogonal arrays (OA) of experiments with optimum values of process parameters providing reduced variance. Taguchi method is one of the optimization techniques which has been extensively used to obtain the set/combination of system parameters to optimize the performance of the systems [26, 27]. It also helps to minimize the costs which are involved in running multiple experimental runs [28, 29].

Based on the above review, it can be seen that not many papers have been presented by the researchers, especially for the artificial roughened type SAHs to optimize its thermo-hydraulic performance parameter by using the Taguchi method (see Table 1).

Table 1: Summary of investigations carried out by researchers for different types of SAHs by using the Taguchi method.

Type of solar air heater	Orthogonal array	Parameters		Optimization factor	Authors and reference
		Definition	Range		
Transverse and inclined roughened solar air heater	$L_{27} (3^3)$	Relative roughness pitch (P/e)	3–8	Thermo-hydraulic (effective) efficiency (η_{eff})	Varun <i>et al.</i> , 2009 [14]
		Mean plate temperature (T_{pm})	68–112		
		Irradiation (I)	800–1000		
		Reynolds number (Re)	1200–11600		
Impinging jet solar air heater	$L_{16} (3^4)$	Jet diameter ratio (D_j/D_j)	0.043–0.109	Thermo-hydraulic performance parameter (THPP)	Chauhan <i>et al.</i> , 2017 [16]
		Streamwise pitch ratio (X/D_h)	0.435–1.739		
		Spanwise pitch ratio (X/D_h)	0.435–1.304		
Machined rib solar air heater	$L_{16} (4^4)$	Rib relative pitch (P/H)	1–2	Thermo-hydraulic performance parameter (THPP)	Aghaie <i>et al.</i> , 2015 [15]
		Rib relative height (e/H)	0.05–0.75		
		Rib relative tip width (a/H)	0–1		
		Rib relative front projection ($s/(H - a)$)	0–1		
V-down perforated baffle rectangular channel	$L_{16} (4^4)$	Relative roughness pitch (P/e)	1–4	Nusselt number (Nu) and friction factor (f)	Chamoli, 2015 [17]
		Relative roughness height (e/D_h)	0.287–0.6		
		Open area ratio (β)	12–44		
		Reynolds number (Re)	4100–18600		
Holes on baffle solar air heater	$L_{27} (4^3)$	Hole size	1/2–1/6	Thermal efficiency (η_{th})	Hu <i>et al.</i> , 2018 [18]
		Hole location	0–1/3		
		Hole number	3–9		
		Inlet flow rate (Re)	0.0044–0.0132		

A novel parameter, the thermo-hydraulic improvement parameter (η_{THIP}), which evaluates in equal proportions of the increment in Nusselt number and friction factor for the present enhanced roughened surface SAH compared to the conventional smooth plate surface SAH is introduced and applied as an optimization parameter.

In this paper, the extended work compared to what has been previously investigated by Sahu *et al.* [30,31] is presented. The objective is to determine the set and combination of flow and roughness parameters for experimental studies (for the present arc shape apex-upstream roughened SAH), that will provide and which delivers the maximum Nusselt number, thermo-hydraulic improvement parameter, and the minimum friction factor using the Taguchi-based design of experiment (DOE) method.

2 Details of the experimental set-up

The experimental set-up rig was designed and fabricated as per the guidelines of the American Society of Heating, Refrigerating and Air-Conditioning Engineers (ASHRAE) standards [32] and was installed at the terrace to conduct experiments in actual outdoor conditions. Figure 1 is the schematic representation of the detailed experimental setup. It consists of a centrifugal blower, two wooden rectangular ducts, galvanized iron (GI) pipes and GI sheets (for SAHs absorber and bottom plates), one main air control valve, orifice plates and flanges (for two ducts), U-tube manometers (for two ducts), micromanometers (for two ducts). Each rectangular duct is suitably divided into three subsections, i.e. entry, test, and exit sections with the length (L) of 650 mm, 1200 mm and 300 mm, respectively.

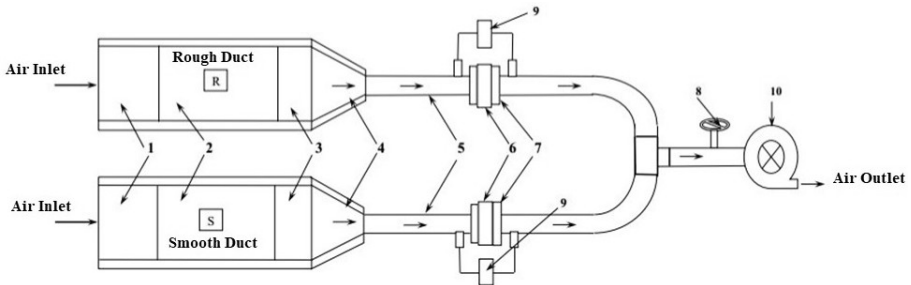


Figure 1: Schematic diagram of experimental set-up: 1 – entry section, 2 – test section, 3 – exit section, 4 – header, 5 – flow pipe, 6 – orifice meter, 7 – flange pipe, 8 – control valve, 9 – U-tube manometer, 10 – centrifugal suction blower.

The duct has a width of 330 mm (W) and 30 mm height (H) with an aspect ratio of $W/H = 11$.

One main air control valve (denoted by δ) is used to regulate the mass flow rate of air in both SAH ducts. Two sides and the bottom of the duct were insulated with 50 mm thick glass wool insulation adequately. A glass of 4 mm thickness was used for glazing with a distance of 30 mm between the glass cover and the absorber plate. The absorptivity of the glass cover was determined using a spectrophotometer, which measured the amount of radiation absorbed by the glass at different wavelengths [1, 4]. The glass cover has an absorption of 0.06, transmission of 0.86 and reflection of 0.08. Absorber and bottom plates are made of a 1 mm thick galvanized iron (GI) sheet which is painted black to enhance absorptivity. It has an absorptivity of 0.88, a transmittance of 0.08 and a reflectivity of 0.04. Wire ribs are tack welded at three points on the absorber plate as shown in Fig. 2. As the area occupied is very less it will not alter the thermal resistance and does not affect the results. Also, a commercially available high-temperature adhesive was used which is designed specifically for the use of solar thermal collectors. The adhesive has a thermal conductivity of $0.2 \text{ W}/(\text{m}^2\text{K})$ and a thermal resistance of $0.001 \text{ K}/\text{W}$.

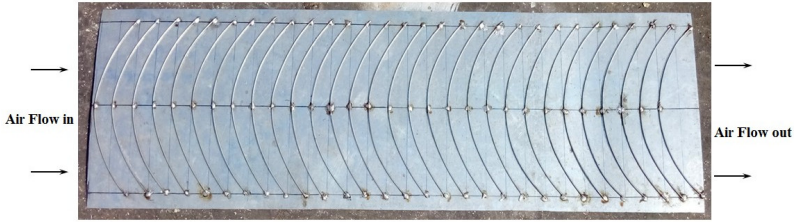


Figure 2: Photographic view of an arc-shape wire roughened absorber plate with apex upstream flow.

The photographic and schematic view of arc shape wire roughened absorber plate with apex upstream flow is shown in Figs. 2 and 3, respectively. Digital thermal temperature indicators which give temperature in $^{\circ}\text{C}$ were used to measure the air temperatures. They were installed at the inlet and outlet of the test section in both SAH ducts. Thermocouples (fifteen) were used to measure the absorber plate temperatures at different locations. Two micromanometers (one for smooth SAH and one for roughened SAH) (Flowtech) with an accuracy of $\pm 0.01 \text{ mm}$ of water column were used to measure pressure drop along the SAH test (ΔP_D) sections. A digital pyra-

nometer (Virtual Hydromet) with accuracy of $\pm 0.5\%$ was used for measuring the intensity of solar radiation on a horizontal surface.

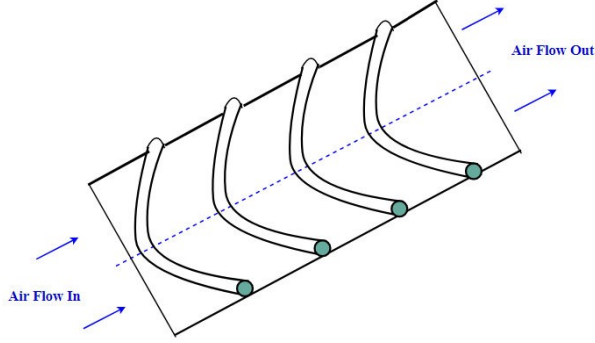


Figure 3: Absorber plate with roughness elements geometry.

2.1 Experimental procedure and data collection

Experimental runs were carried out outdoors under bright sunlight conditions between the months of March to May 2017 between 10.00 am and 4.00 pm on clear sky days. The readings were noted down when the system attained a steady state for at least 30 min. Figure 4 shows the variations of solar intensity versus local time (hrs) for some selected days on which

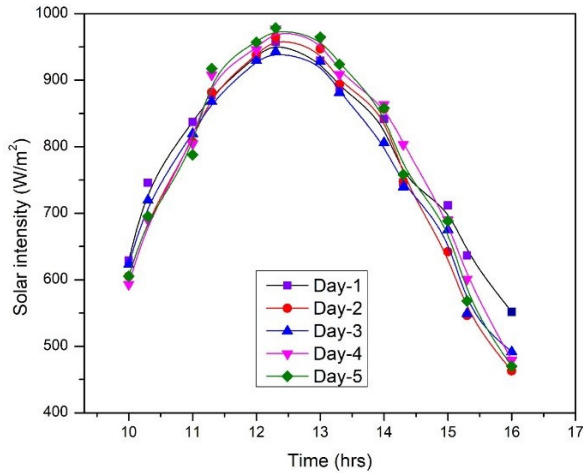


Figure 4: Variation of solar intensity versus local time for five different days.

the study was conducted. It can be seen, from Fig. 4 that solar intensity increases up to 1.00 pm and after that it starts decreasing.

2.2 Data reduction

The mass flow rate of air is calculated using equation [30,31]:

$$\dot{m} = C_d A_o \sqrt{\frac{2\rho \Delta P_o}{1 - \beta_R^4}}, \quad (1)$$

where C_d is the coefficient of discharge evaluated by calibration which amounts to 0.61, whereas β_R is the ratio of orifice diameter (D_2) to air (fluid) flow pipe internal diameter (D_1) and equals 0.60. Parameter ρ stands for the air density and A_o represents the area of an orifice plate.

The pressure drop across the orifice meter (ΔP_o) was been calculated using the U-tube manometer fluid difference head (column) reading (Δh), having a 300 mm scale, with water as manometric fluid [29–31]:

$$\Delta P_o = \rho_u g \Delta h, \quad (2)$$

where ρ_u is the density of water (manometer fluid) and g is gravitational acceleration.

Useful heat energy gain by air was computed from [33,34]

$$Q_u = \dot{m} C_{pa} (T_{fo} - T_{fi}), \quad (3)$$

Heat transfer coefficient for the test section ducts was computed using the expression [30,31]

$$h = \frac{Q_u}{A_c (T_{pm} - T_{fm})}, \quad (4)$$

where A_c is the surface area of the absorber plate, and T_{pm} is the mean absorber plate temperature, which is the average of all temperatures measured by thermocouples located over the absorber plate (at 15 measurement points), and is calculated from

$$T_{pm} = \frac{1}{15} \sum_{i=1}^{15} T_i. \quad (5)$$

Temperature T_{fm} is an arithmetic mean of the entry (inlet) and exit temperature of the air flowing through the SAH duct and is expressed as [30,31]

$$T_{fm} = \frac{T_{fi} + T_{fo}}{2}. \quad (6)$$

Figure 5 shows the locations of thermocouples in the inlet (entry) and outlet (exit) sections, and on the absorber plate.

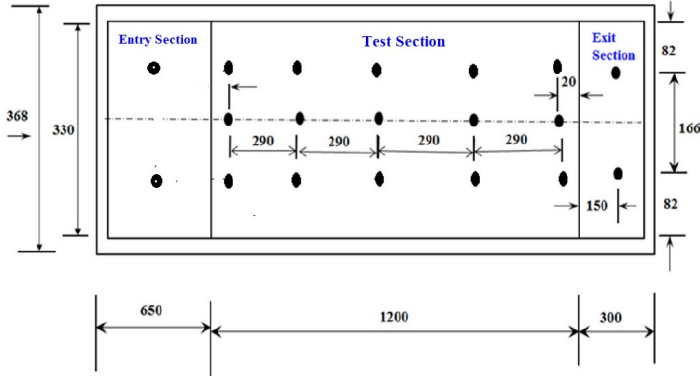


Figure 5: Locations of digital thermocouples in the entry and exit sections and on the absorber plate (all dimensions in mm).

The Nusselt number is given by [30, 31]

$$\text{Nu} = \frac{hD_h}{K_a}, \quad (7)$$

where K_a is the thermal conductivity of air, and D_h is the hydraulic diameter of the duct which can be calculated from

$$D_h = \frac{2WH}{W + H}. \quad (8)$$

The Reynolds number is evaluated by [30, 31]

$$\text{Re} = \frac{GD_h}{\mu}, \quad (9)$$

where μ is the absolute air viscosity and G is the mass velocity of air, which can be evaluated as

$$G = \frac{\dot{m}}{WH}. \quad (10)$$

To calculate the friction factor for SAHs, the following equation is used [30, 31, 33, 34]:

$$f = \frac{2\rho\Delta P_D D_h}{4L_f G^2}, \quad (11a)$$

where L_f is the distance between two pressure taps in the test section of the SAH duct. The pressure drop across the SAH test section (ΔP_D)

is calculated by using the micromanometer fluid difference head reading (Δh_1) which have the least count of 0.01 mm of water column:

$$\Delta P_D = \rho_m g \Delta h_1. \quad (11b)$$

2.3 Thermal and thermo-hydraulic performance criterion

The thermal efficiency of a SAH can be determined using the equation [4]

$$\eta_{th} = \frac{Q_u}{I A_c}. \quad (12a)$$

The evaluation of the thermo-hydraulic performance criterion included both, the thermal and hydraulic performance of a SAH, as introduced by Webb and Eckert [7] and Lewis [6], and follows the equation:

$$\eta_{THPP} = \frac{\frac{Nu_r}{Nu_s}}{\left(\frac{f_r}{f_s}\right)^{1/3}}, \quad (12b)$$

where Nu_r , Nu_s and f_r , f_s are the Nusselt number and the friction factor for a roughened and smooth duct solar heater, respectively.

2.4 Thermo-hydraulic (effective) efficiency of solar air heater

The effective efficiency of the solar air heater was determined by considering pressure drop and the power needed to force the airflow across the SAH duct, in addition to thermal energy gain (Q_u). Hence, the thermo-hydraulic efficiency or effective efficiency takes both, i.e. pumping power and thermal energy gain, and is given by equation [35]

$$\eta_{eff} = \frac{Q_u - \frac{\dot{W}_p}{C_f}}{I A_c}, \quad (13)$$

where C_f is conversion factor and \dot{W}_p is a pump work, which is defined as

$$\dot{W}_p = \frac{\dot{m} \Delta P_D}{\rho}. \quad (14)$$

2.5 Thermo-hydraulic improvement parameter

Thermo-hydraulic improvement parameter (THIP) which is applied as an optimization parameter in the present paper, can be evaluated as

$$\eta_{\text{THIP}} = \frac{\text{NNIF}}{\text{FFIF}}, \quad (15)$$

where NNIF is the Nusselt number improvement factor which is calculated (in percentage) by

$$\text{NNIF} = \frac{\text{Nu}_r - \text{Nu}_s}{\text{Nu}_s} \times 100 \quad (16)$$

and FFIF is the friction factor improvement factor which is expressed (in percentage) by

$$\text{FFIF} = \frac{f_r - f_s}{f_s} \times 100. \quad (17)$$

It can be seen from Eq. (15) that when NNIF is higher than FFIF the THIP becomes greater than 1 ($\eta_{\text{THIP}} > 1$), which is desirable for the use of any type of enhancement technique in the SAHs and also in other thermal systems.

2.6 Uncertainty analysis

An error analysis was done as per the methodology suggested by Kline and McClintock [26]. For the investigated roughened absorber solar air heaters, the maximum uncertainty values for dimensionless numbers are obtained as:

- thermal efficiency: $\pm 5.61\%$,
- Reynolds number: $\pm 4.87\%$,
- friction factor: $\pm 5.14\%$,
- thermo-hydraulic efficiency: $\pm 8.47\%$.

3 Experimental design and plan for optimization

3.1 Taguchi method

The Taguchi method is well-known method that has been used for the design of experiments (DOE) and as an optimization tool in different industries and numerous areas of engineering *via* experiments. It analyzes and evaluates all different design factors/parameters which are used in the

experiments and determines the best choices of factors/parameters that deliver us target optimum performance values by selecting desired control factors with the minimal number of experiment trails/runs.

The Taguchi method uses standard tables of experiments called orthogonal arrays (OA) which are represented by [24, 25]

$$OA = L_N A^n, \quad (18)$$

where L_N is the number of experimental/test runs, A denotes levels of the factors/variables and n is the number of factors.

For studying a large number of parameters with a lesser number of experimental trials (runs), the OA was adopted, and after that, the effect of main and interacting experimental parameters was converted into the signal-to-noise ratio (SN-R).

In the Taguchi method, firstly one has to choose and select the desired objective performance as the target function to which we have to optimized. After selecting the objective function, the control factors which are to be varied, are chosen. Then, the affecting factors are assigned with their levels according to experimentation, and these assigned control factors and their levels are numerically tested by the signal-to-noise ratio (SN-R) analysis.

3.2 Plan for optimization

In the present analysis, the number of test runs (N) was considered as 18. Furthermore, Reynolds number, relative roughness pitch and angle of attack were considered as factors (n) with their levels (A), 6, 3, and 3, respectively. Hence, we obtained an orthogonal array of $L_{18} = 6^1 \times 3^2$.

The present study accommodates the mixed L_{18} design array including three control factors: Reynolds number (Re), relative roughness pitch (P/e) and angle of attack (α) varying with levels 6, 3, and 3, respectively. The same is tabulated in Table 2.

Tables 3 and 4 tabulates 18 experimental runs based on the orthogonal array (OA) and a signal-to-noise ratio (SN-R) respectively, which was used to determine the sensitivity of the parameters on the physical behavior. It also presents the results obtained from the experimental runs which were converted into signal-to-noise ratio (SN-R).

The Taguchi technique defines an optimum condition as a case where least variation of a system performance is observed by noise factor or best SN-R represents optimum system configuration. Quality characteristics using SN-R are classified in two cases: higher-is-better (HB) and the lower-

Table 2: Control factors ($L_{18} = 6^1 \times 3^2$) used in the experiments with their values and levels.

Control factors		Level					
		I	II	III	IV	V	VI
A	Reynolds number (Re)	2983	4717	7459	9435	11556	13955
B	Relative roughness pitch (P/e)	8	10	15	–	–	–
C	Angle of attack (α), deg	45	60	75	–	–	–

Table 3: Experimental plan and results of OA ($L_{18} = 6^1 \times 3^2$) for control factors and output responses.

Exp. run number	Control factors			Results		
	<i>A</i>	<i>B</i>	<i>C</i>	Nusselt number	Friction factor	Thermo- hydraulic improvement parameter
	Reynolds number (Re)	Relative roughness pitch (P/e)	Angle of attack (α)	Nu	f_r	(η_{THIP})
1	2983	8	45	17.7	0.0202	54.98851
2	2983	10	60	19	0.0200	70.35294
3	2983	15	75	14.15	0.0176	24.88525
4	4717	8	45	29.95	0.0188	87.40027
5	4717	10	60	31.5	0.0184	103.04380
6	4717	15	75	22.94	0.01635	54.20538
7	7459	8	45	50.96	0.0174	118.40960
8	7459	10	60	53.2	0.0172	131.60490
9	7459	15	75	40.94	0.0152	100.10300
10	9435	8	45	67.04	0.0168	127.93730
11	9435	10	60	72.12	0.0166	149.21850
12	9435	15	75	54.45	0.01465	114.14260
13	11556	8	45	84.93	0.0163	147.97850
14	11556	10	60	91.59	0.0161	171.76220
15	11556	15	75	69.14	0.014	141.95300
16	13955	8	45	105.9	0.0158	153.11290
17	13955	10	60	112.5	0.0156	173.05830
18	13955	15	75	85.4	0.0136	144.2752

is-better (LB). The characteristic equations for these two cases are, respectively:

for higher-is-better:

$$SN - R = -10 \log \left(\frac{1}{N} \sum \frac{1}{y^2} \right) \quad (19)$$

and for lower-is-better:

$$SN - R = -10 \log \left(\frac{1}{N} \sum y^2 \right), \quad (20)$$

where N is the number of experimental runs, and y^2 is the observed experimental data.

Table 4 represents the experimental plan and its signal-to-noise ratio. In the present analysis, the Nusselt number and thermo-hydraulic improvement parameters are considered as higher-is-better criterion, whereas the friction factor for the roughened surface (f_r) is considered as a lower-is-better criterion.

Table 4: Experimental design (L_{18}) with its SN-R values.

Exp. run number	Results					
	Nusselt number	Signal-to-noise ratio	Friction factor	Signal-to-noise ratio	Thermo- hydraulic improvement parameter	Signal-to-noise ratio
1	17.70	24.95947	0.0202	33.89297	54.98851	34.80544
2	19.00	25.57507	0.0200	33.97940	70.35294	36.94565
3	14.15	23.01513	0.0176	35.08975	24.88525	27.91884
4	29.95	29.52794	0.0188	34.51684	87.40027	38.83026
5	31.50	29.96621	0.0184	34.70364	103.04380	40.26044
6	22.94	27.21187	0.01635	35.72964	54.20538	34.68085
7	50.96	34.14459	0.0174	35.18902	118.40960	41.46774
8	53.20	34.51823	0.0172	35.28943	131.60490	42.38544
9	40.94	32.24296	0.0152	36.36313	100.10300	40.00895
10	67.04	36.52668	0.0168	35.49381	127.93730	42.13995
11	72.12	37.16111	0.0166	35.59784	149.21850	43.47646
12	54.45	34.71996	0.01465	36.68325	114.14260	41.14896

Continued on next page

Table 1. *Continued from previous page.*

Exp. run number	Results					
	Nusselt number	Signal-to-noise ratio	Friction factor	Signal-to-noise ratio	Thermo- hydraulic improvement parameter	Signal-to-noise ratio
13	84.93	38.58122	0.0163	35.75625	147.9785	43.40397
14	91.59	39.23696	0.0161	35.86348	171.76220	44.69855
15	69.14	36.79459	0.014	37.07744	141.9530	43.04289
16	105.90	40.49792	0.0158	36.02686	153.1129	43.70023
17	112.50	41.02305	0.0156	36.13751	173.0583	44.76385
18	85.40	38.62916	0.0136	37.32922	144.2752	43.18383

The application of the Taguchi method and its procedure which is used for the present investigation is given by the flow chart shown in Fig. 6.

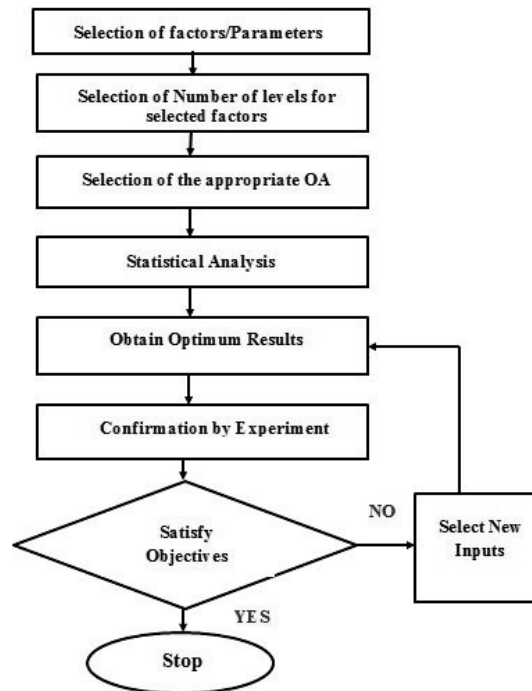


Figure 6: Flow chart of the Taguchi method for optimal design.

4 Result and discussion

4.1 Thermal efficiency

By using the present apex-upstream roughened SAH the maximum thermal efficiency of 65.2% has been observed, corresponding to $e/D_h = 0.0454$, $P/e = 10$, $\alpha = 60$ deg and for the highest Reynolds number considered in the present analysis, i.e. $Re = 13955$, while for the smooth plate SAH the maximum thermal efficiency obtained for the highest Reynolds number was 41.4%.

4.2 Comparison of Nusselt numbers in SAH duct

Figure 7 shows the comparison of experimental values of the Nusselt number for roughened duct and smooth plate SAH as a function of Reynolds number for different values of relative roughness pitch. The other fixed parameters, $\alpha = 60$ deg and $e/D_h = 0.0454$, are shown in the figure. It is observed that Nu for both SAHs increases with increasing Re values, however, the Nu values for roughened SAH are larger compared to the smooth plate SAH. Furthermore, the maximum value of Nu was attained at the relative roughness pitch (P/e) of 10.

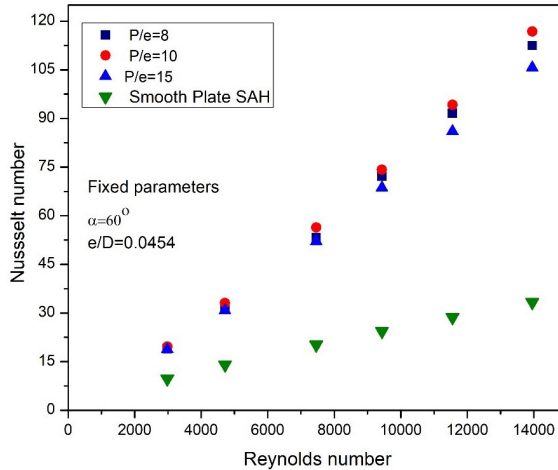


Figure 7: Effect of relative roughness pitch (P/e) on Nusselt number as a function of Reynolds number for apex-upstream roughened SAH and smooth plate SAH.

Figure 8 shows the comparison of the Nusselt number change with the Reynolds number between the smooth plate SAH and the apex-upstream

roughened SAH at various angles of attack. It can be observed that Nu attains maximum value for roughened SAH of $\alpha = 60^\circ$.

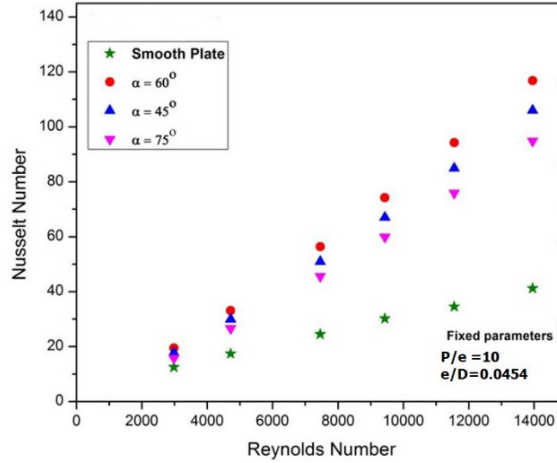


Figure 8: Effect of angle of attack (α) on Nusselt number as a function Reynolds number for apex-upstream roughened SAH and smooth plate SAH.

4.3 Comparison of SAH duct pressure drop

Figures 9 and 10 show the comparison of experimental values of pressure drop in the roughened duct and the smooth plate SAH for different Reynolds number values. Figure 9 shows the comparison of the pressure drop variation (ΔP_D) for the roughened duct with different values of the relative roughness pitch (P/e) and fixed values of $\alpha = 60^\circ$ and $e/D_h = 0.0454$ with that for the smooth plane SAH as a function of Reynolds number. It can be observed from the figure that ΔP_D increases for both SAH ducts with an increase in the values of Re, and ΔP_D values for smooth duct are lower compared to those for roughened SAH for all values of Re.

Figure 10 shows the comparison of pressure drop (ΔP_D) between the apex-upstream roughened SAH with different values of α , and for the smooth plate SAH as function of Re. It can be seen from the figure that pressure drop for both SAHs increases with increasing Re, however, the values of ΔP_D for roughened SAH are larger as compared to the smooth plate SAH. Furthermore, it is observed that the maximum value of ΔP_D corresponds to $\alpha = 60^\circ$ for roughened SAH.

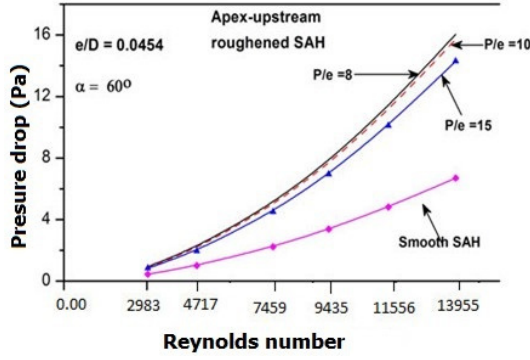


Figure 9: Effect of relative roughness pitch (P/e) on pressure drop as a function of Reynolds number for apex-upstream roughened SAH and smooth SAH.

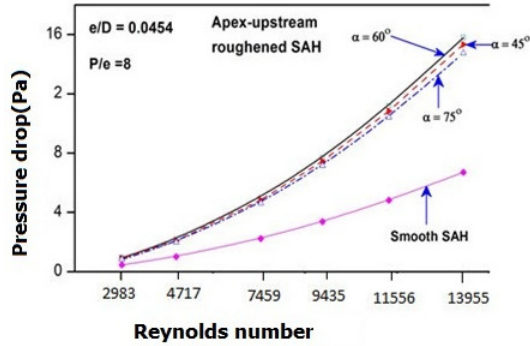


Figure 10: Effect of angle of attack (α) on the pressure drop as a function of Reynolds number for apex-upstream roughened and smooth SAHs.

4.4 Analysis

Figures 11–13 represent the mean effect plots for Nusselt number, friction factor, and thermo-hydraulic improvement parameter, respectively. Their performance values and results obtained are presented in Tables 5–7.

Figure 11 shows the effect of three control factors: A, B, and C on Nu and it can be observed from the figure that there is a continuous increase in Nusselt number as factor A (Re) increases from level 1 to 6. This is because by increasing the Re, turbulent intensity increases in the fluid flow inside the duct. Thus, higher values of mass flow rate result in higher rates of heat transfer coefficient h , and hence in higher values of Nu. Furthermore, it can be seen from Table 5) and Fig. 11, that Nu increases with an increase in

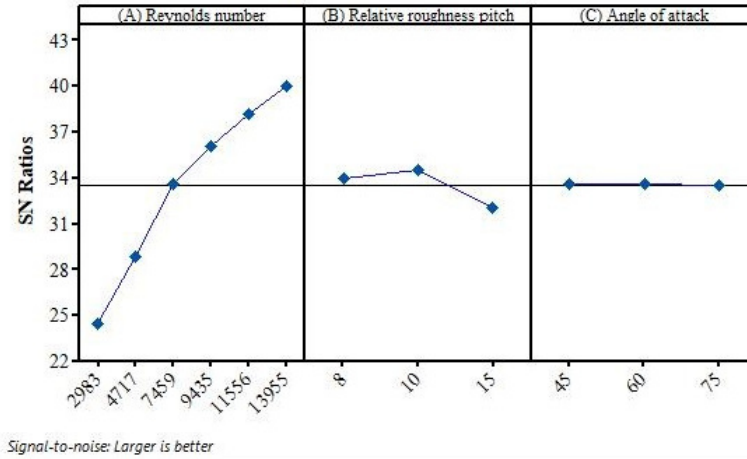


Figure 11: Variation of Nusselt number with change in the design parameters of A, B, and C.

the factor B (P/e) from 1st level to 2nd level and after that, it decreases down to 3rd level with further P/e increase. In the present analysis, the maximum value of Nu is observed at $P/e = 10$. This is due to the reason that number of reattachment points decreases (which in turn reduces the heat transfer rate) with an increase in the value of P/e . It is reported by the researchers that maximum heat transfer occurs at the attachment points between two roughness ribs (also called inter-rib space) and the reattachment of the flow between two roughness ribs does not occur for the higher values of pitch. Reattachment of flow occurs for $P/e > 8$ while the optimum value for maximum heat transfer varies in the P/e range of 8–12, which again depends on the type of rib roughness and its geometries used on the absorber plate. For factor C (α), the Nusselt number slightly increases from 1st level to 2nd level with an increase in α from 45 to 60 deg and after that, it decreases. The Nu has its lowest value for $\alpha = 75$ deg in the present analysis while the maximum value of Nu was obtained for $\alpha = 60$ deg. Angling roughness ribs creates span-wise counter-rotating secondary flow along the length of the absorber plate in the test section, which enhances the heat transfer coefficient significantly. Furthermore, due to alignment of ribs at an angle with respect to flow on the absorber plate the vortices creates on the upstream and downstream sides of the ribs. These vortices move along the flow at the absorber plate surfaces and merge with the (main) core flow and thus helps in increasing the heat transfer rate. The generation

of secondary flows and vortices occurs maximum for the alignment of ribs at an angle of $\alpha = 60$ deg for the present roughness geometry.

In Table 5, Delta is the difference between the highest and lowest average response values for each factor. After calculation of Delta values, the factor which have highest Delta value has been assign as Rank 1, the factor which have second highest Delta value has been assign as Rank 2 and so on.

Table 5: Response table for signal-to-noise ratios (SN-R) for Nusselt number (Nu).

Level	A (Re)	B (P/e)	C (α)
1	24.52	34.04	33.60
2	28.90	34.58	33.62
3	33.64	32.10	33.50
4	36.14	—	—
5	38.20	—	—
6	40.05	—	—
Delta	15.53	2.48	0.12
Rank	1	2.00	3.00

Figure 12 shows the effect of three control factors on the friction factor f_r . Furthermore, from Fig. 12 and Table 6 it can be seen that f_r attains its

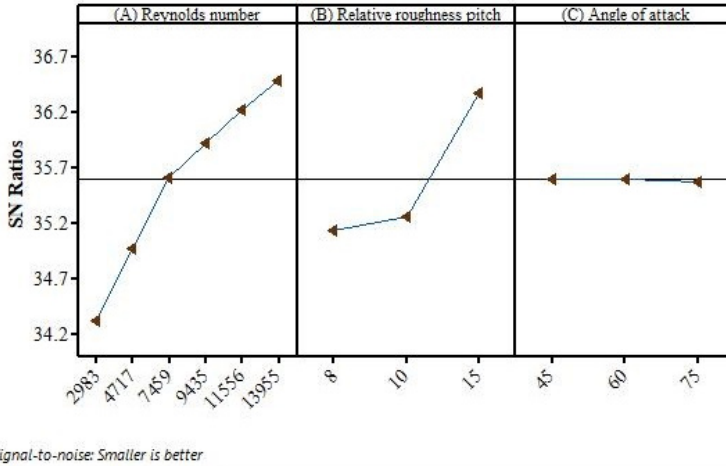


Figure 12: The effects of design parameters of A, B, and C on the friction factor.

minimum value corresponding to control factors A (Re) = 2983, B (P/e) = 8 and C (α) = 45 deg. In the present analysis, the friction factor has its minimum for $P/e = 8$ and $\alpha = 45$ deg because at these values of roughness parameters least turbulence is developed in the fluid flow and due to this less pressure drop in the SAH duct takes place, which results in the lowest values of friction factor.

Table 6: Response table for signal-to-noise ratios (SN-R) for friction factor (f_r).

Level	A (Re)	B (P/e)	C (α)
1	34.32	35.15	35.60
2	34.98	35.26	35.62
3	35.61	36.38	35.58
4	35.92	—	—
5	36.23	—	—
6	36.50	—	—
Delta	2.18	1.23	0.02
Rank	1	2	3

Figure 13 represents the mean effects of control factors on THIP. As demonstrated in the figure, an increasing trend can be observed for THIP for all values of control factor A (Re). It can also be seen that growth in THIP

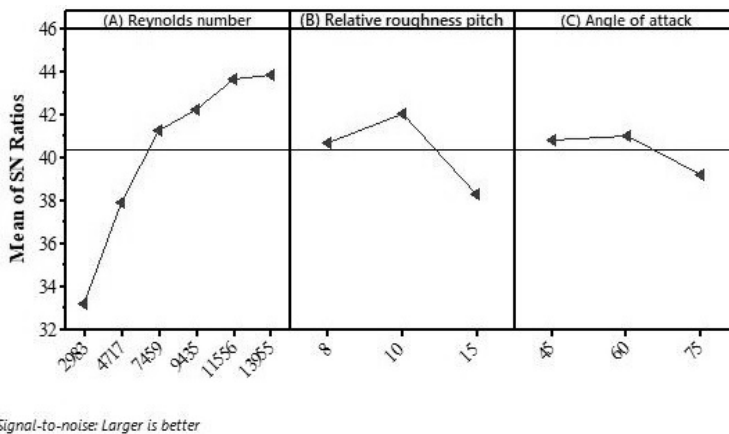


Figure 13: The effects of design parameters of A, B and C on the thermo-hydraulic improvement parameter (THIP).

is steeper up to the 3rd level of $Re = 7459$ and afterward, with further increase in Re the THIP curve increment rate is relatively lower. This is due to the reason that when the value of Re increases, there is an increment in the pressure drop and pumping power in the SAH duct, as THPP is the ratio of the Nusselt number improvement factor to the friction factor improvement factor (Eq. (15)) and at a higher range of Re the enhancement in friction factor and pressure drop is more dominant (or relatively more) over the enhancement in the heat transfer coefficient and Nu . Furthermore, from Fig. 13 and Table 7, it can be concluded that the highest THIP is observed for $Re = 13955$, $P/e = 10$ and $\alpha = 60$ deg.

Table 7: Response table for signal-to-noise ratios (SN-R) for thermo-hydraulic improvement parameter (THIP).

Level	A (Re)	B (P/e)	C (α)
1	33.22	40.72	40.82
2	37.92	42.09	41.07
3	41.29	38.33	39.25
4	42.26	—	—
5	43.72	—	—
6	43.88	—	—
Delta	10.66	3.76	1.81
Rank	1	2	3

4.5 Contribution ratio

Figure 14 represents the detailed representation of the contribution ratio percentage of each control factor to the Nusselt number, friction factor, and thermo-hydraulic improvement parameters. It can be seen from the figure that the parameter A (Re) contributes to 94.09% for Nu , 66.17% for (f_r) and 85.85% for THIP, respectively, of the total effect. This reveals that Nu , f_r , and THIP are majorly affected by parameter A. As it can be seen, the parameter B (P/e) contribution ratio is 4.74% for Nu , and parameter C (α) contribution ratio for Nu is 1.18%. The contribution ratios of factors B and C for friction factor are 33.65%, and 0.18%, respectively. Hence, it can be concluded, that Reynolds number (A) is the most effective parameter that affects the performance of roughened SAH, i.e. the Nusselt number, friction

factor and thermo-hydraulic improvement parameter, more than P/e and α . The contribution ratios of each control factor on every performance parameter are tabulated in Table 8. Thus, the optimum level of control factors for Nu is $A_6B_2C_2$, for f_r is $A_1B_1C_3$ and for THIP is $A_6B_2C_2$, which are also shown in Fig. 15.

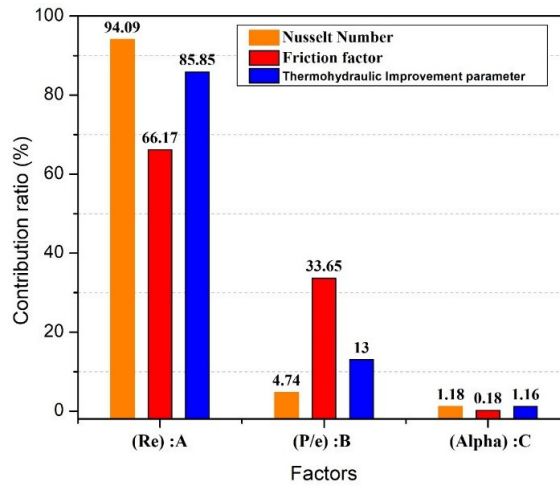


Figure 14: The contribution ratio of each parameter to Nusselt number, friction factor and thermo-hydraulic improvement parameter.

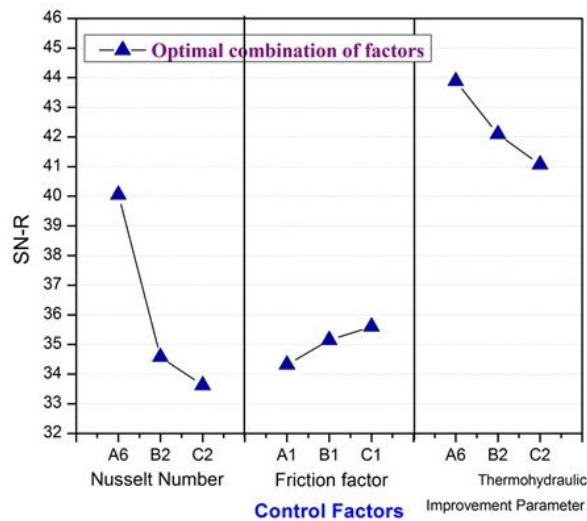


Figure 15: Optimal combination of control factors for Nu, f_r and THIP.

Table 8: Optimum performance conditions and the contribution ratios of each control factors on the different performances.

	Parameter		
	A	B	C
	Reynolds number (Re)	Relative roughness pitch (P/e)	Angle of attack (α)
Nusselt number (Nu)			
Optimum level	Level – VI	Level – II	Level – II
Optimum value	13955	10	60 deg
Contribution ratio	94.09%	4.74%	1.18%
Friction factor (f)			
Optimum level	Level – I	Level – I	Level – I
Optimum value	2983	8	45 deg
Contribution ratio	66.17%	33.65%	0.18%
Thermo-hydraulic improvement parameter (THIP)			
Optimum level	Level – VI	Level – II	Level – II
Optimum value	13955	10	60 deg
Contribution ratio	85.85%	13%	1.16%

5 Experiments for confirmation

In the Taguchi design of the experimental method, a confirmation experiment is done to validate the results. This is performed by consideration of a new set of control factors which is further done by setting $A_6B_2C_2$, $A_1B_1C_3$, and $A_6B_2C_2$ to predict the Nusselt number, friction factor, and thermo-hydraulic improvement parameter, while Table 9 takes into account the results of confirmation tests carried out with optimum design parameters.

The estimated value of signal-to-noise for Nu, f_r , and THIP were calculated by taking a summation of an average performance by considering the contribution of each parameter at an optimum level using the following equations [16, 17]:

$$\eta_{Nu} = \overline{T_{Nu}} + \left(A_6 - \overline{T_{Nu}} \right) + \left(B_2 - \overline{T_{Nu}} \right) + \left(C_2 - \overline{T_{Nu}} \right), \quad (21)$$

$$\eta_{f_r} = \overline{T_f} + \left(A_1 - \overline{T_{f_r}} \right) + \left(B_1 - \overline{T_{f_r}} \right) + \left(C_3 - \overline{T_{f_r}} \right) \quad (22)$$

and

$$\eta_{THIP} = \overline{T_{Nu}} + \left(A_6 - \overline{T_{THIP}} \right) + \left(B_2 - \overline{T_{THIP}} \right) + \left(C_2 - \overline{T_{THIP}} \right), \quad (23)$$

where \overline{T} represents the average experimental temperature and A_6 , B_2 , C_2 is the mean response for factors at designated levels for Nu.

A comparison of values of Nu, f_r , and THIP obtained from both experiments and the prediction are presented in Table 9. As can be seen from the comparison of initial parameters and optimum parameters obtained from the Taguchi method, shown in the table, an improvement in the SN ratio for Nu is 16.16 dB with an error of 15.90%. The obtained improvement in the SN ratio for f_r is 4.2 dB with an error of 6.56% while the achieved improvement in the SN ratio for THIP is 11.48 dB with an error of 12.74%. This indicates that the experimental results are very close to the predicted results. The results obtained from confirmation experiments proved the validity of the Taguchi approach used in the optimization of the design parameters.

Table 9: Results of the confirmation experiment

Parameters		Initial parameters	Optimum control parameters		
			Prediction	Experimental	Improvement of signal-to-noise ratio, dB
Nusselt number (Nu)	Level	$A_1B_1C_1$	$A_6B_2C_2$	$A_6B_2C_2$	–
	SN-R, dB	24.95	34.57	41.11	16.16
Friction factor (f)	Level	$A_1B_1C_1$	$A_1B_1C_3$	$A_1B_1C_3$	–
	SN-R, dB	33.89	35.59	38.09	4.2
Thermo-hydraulic improvement parameter (THIP)	Level	$A_1B_1C_1$	$A_6B_2C_2$	$A_6B_2C_2$	–
	SN-R, dB	34.80	40.38	46.28	11.48

6 Conclusions

The present study applies the Taguchi design of experimental methods, to find the configuration of a set of roughness and flow parameters to maximize the Nusselt number and the thermo-hydraulic improvement parameter, and minimize the losses due to friction for a roughened solar air heater (SAH). Further, the Reynolds number, relative roughness pitch, and angle of attack

were taken as control factors for the present study. Based on the results of the investigation, the following conclusions are drawn.

1. The Nusselt number, friction factor and thermo-hydraulic improvement parameter are very much influenced by the control factors *viz.* the Reynolds number, relative roughness pitch, and angle of attack.
2. The contribution ratio of the control factors: Reynolds number (A), relative roughness pitch (B), and angle of attack (C), on the Nusselt number (Nu) is 94.09%, 4.74%, and 1.18%, respectively. For the friction factor (f_r) it is 66.17%, 33.65%, and 0.18%, and for the thermo-hydraulic improvement parameter (THIP) it is 85.85%, 13.00%, and 1.16%, respectively.
3. An optimal value of the parameters for maximum Nu is $A_6B_2C_2$, i.e. Reynolds number of 13955, relative roughness pitch of 10, and angle of attack of 60 deg. The optimal condition for minimum friction factor is $A_1B_1C_3$, i.e. Reynolds number of 2983, relative roughness pitch of 8, and an angle of attack of 45 deg. For maximum thermo-hydraulic improvement parameter the combination of optimal design parameters is $A_6B_2C_2$, i.e. Reynolds number of 13955, relative roughness pitch of 10, and angle of attack of 60 deg.
4. The experimental confirmation shows a 16.16 dB improvement in the signal-to-noise ratio (SN-R) for the Nusselt number. For the friction factor and thermo-hydraulic improvement parameter, it shows 4.2 dB and 11.48 dB improvements in SN-R values, respectively.
5. The Taguchi method is most effective when dealing with a small number of factors and parameters that can be controlled. In the present analysis, there are only 3 control factors considered. There are also many factors that affect the performance of the solar air heater such as type of absorber plate material, flow rate of air, wind velocity, angle, and orientation of the SAH, etc.

It may be challenging to design an experiment that includes all relevant factors and interactions. In the future, researchers can consider other control factors for their analysis.

The results of this study show that that using for the present roughened solar air heater an optimized configuration of roughness and flow parameters, which are obtained by applying the Taguchi method there is no need to run the experimental set-up all 54 times.

Received 2 December 2022

References

- [1] Khan B.H.: *Non-Conventional Energy Resources* (2nd Edn.). Tata McGraw Hill, New Delhi 2012.
- [2] Sahu M.K., Prasad R.K.: *A review of the thermal and hydrodynamic performance of solar air heater with roughened absorber plates*. J. Enhanc. Heat Transf. **23**(2016), 47–89.
- [3] Sahu M.K., Sharma M., Matheswaran M.M., Maitra K.: *On the use of various configurations of fins to enhance the performance in rectangular duct of solar air heaters – A review*. J. Sol. Energy Eng. **141**(2019), 3, 030802.
- [4] Duffie J.A., Beckman W.A.: *Solar Engineering of Thermal Processes* (2nd Edn.). Wiley, New York 1991.
- [5] Sahu M.K., Priyam A., Mishra S., Bishnoi P.: *A detailed review on research, technology, configurations and application of wire ribs as artificial roughness in rectangular solar air heater duct*. Proc. Inst. Mech. Eng. E J. Process Mech. Eng. **235**(2021), 4, 1211–1234.
- [6] Lewis M.J.: *Optimizing the thermohydraulic performance of rough surfaces*. Int. J. Heat Mass Tran. **18**(1975), 1243–1248.
- [7] Webb R.L., Eckert E.R.G.: *Application of rough surface to heat exchanger design*. Int. J. Heat Mass Tran. **15**(1972), 1647–1658.
- [8] Varun, Sharma N., Bhat I.K., Grover D.: *Optimization of a smooth flat plate solar air heater using stochastic iterative perturbation technique*. Sol. Energy **85**(2011), 2331–2337.
- [9] Rao R.V., Waghmare G.: *Optimization of thermal performance of a smooth flat-plate solar air heater using teaching-learning-based optimization algorithm*. Cogent. Eng. **2**(2015), 3–28.
- [10] Siddhartha, Sharma N., Varun: *A particle swarm optimization algorithm for optimization of thermal performance of a smooth flat plate solar air heater*. Energy **38**(2012), 406–413.
- [11] Chamoli S.: *Preference selection index approach for optimization of V down perforated baffled roughened rectangular channel*. Energy **93**(2015), 1418–1425.
- [12] Chauhan R., Singh T., Thakur N.S., Patnaik A.: *Optimization of parameters in solar thermal collector provided with impinging air jets based upon preference selection index method*. Renew. Energ. **99**(2016), 118–126.
- [13] Bilen K., Yapici S., Celik C.: *A Taguchi approach for investigation of heat transfer from a surface equipped with rectangular blocks*. Energ. Convers. Manage. **42**(2001), 951–961.
- [14] Varun, Patnaik A., Saini R.P., Singal S.K., Siddhartha: *Performance prediction of solar air heater having roughened duct provided with transverse and inclined ribs as artificial roughness*. Renew. Energ. **34**(2009), 2914–2922.

- [15] Aghaie A.Z., Rahimi A.B., Akbarzadeh A.: *A general optimized geometry of angled ribs for enhancing the thermo-hydraulic behavior of a solar air heater channel – A Taguchi approach*. Renew. Energ. **83**(2015), 47–54.
- [16] Chauhan R., Singh T., Kumar N., Patnaik A., Thakur N.S.: *Experimental investigation and optimization of impinging jet solar thermal collector by Taguchi method*. Appl. Therm. Eng. **116**(2017), 100–109.
- [17] Chamoli S.: *A Taguchi approach for optimization of flow and geometrical parameters in a rectangular channel roughened with V down perforated baffles*. Case Stud. Therm. Eng. **5**(2015), 59–69.
- [18] Hu J., Liu K., Ma L., Su X.: *Parameter optimization of solar air collectors with holes on baffle and analysis of flow and heat transfer characteristics*. Sol. Energy **174**(2018), 878–887.
- [19] Turgut E., Cakmak G., Yildiz C.: *Optimization of the concentric heat exchanger with injector turbulators by Taguchi method*. Energ. Convers. Manage. **53**(2012), 268–275.
- [20] Chamoli S., Yu P., Kumar A.: *Multi-response optimization of geometric and flow parameters in a heat exchanger tube with perforated disc inserts by Taguchi Grey relational analysis*. Appl. Therm. Eng. **103**(2016), 1339–1350.
- [21] Kotcioglu I., Cansiz A., Khalaji M.N.: *Experimental investigation for optimization of design parameters in a rectangular duct with plate-fins heat exchanger by Taguchi method*. Appl. Therm. Eng. **50**(2013), 604–613.
- [22] Chamoli S., Yu P., Yu S.: *Multi-objective shape optimization of a heat exchanger tube fitted with compound inserts*. Appl. Therm. Eng. **117**(2017), 708–724.
- [23] Zeng M., Tang L.H., M. Lin M., Wang Q.W.: *Optimization of heat exchangers with vortex-generator fin by Taguchi method*. Appl. Therm. Eng. **30**(2010), 1775–1783.
- [24] Taguchi G.: *Taguchi Techniques for Quality Engineering*. Quality Resources. McGraw-Hill, New York 1987.
- [25] Ross P.J.: *Taguchi Techniques for Quality Engineering*. McGraw-Hill, New York, 1988.
- [26] Kline S.J., McClintock F.P.: *Describing uncertainties in single sample experiments*. Mech. Eng. **75**(1953), 3–8.
- [27] Taguchi G., Konishi S.: *Orthogonal Arrays and Linear Graphs: Tools for Quality Engineering*. American Supplier Institute, Dearborn 1987.
- [28] Taguchi G., Jugulum R.: *The Mahalanobis Taguchi Strategy. A Pattern Technology System*. Wiley, New York 2002.
- [29] Roy R.K.: *Design of Experiments Using the Taguchi Approach*. Wiley, Hoboken 2001.
- [30] Sahu M.K., Matheswaran M.M., Bishnoi P.: *Experimental study of thermal performance and pressure drop on a solar air heater with different orientations of arc-shape rib roughness*. J. Therm. Anal. Calorim. **144**(2021), 1417–1434.
- [31] Sahu M.K., Matheswaran M.M., Bishnoi P.: *Experimental investigation of augmented thermal and performance characteristics of solar air heater ducts due to varied orientations of roughness geometry on the absorber plate*. Arch. Thermodyn. **41**(2020), 3, 147–182.

- [32] ASHRAE Standard 93-97. Method of testing to determine the thermal performance of solar collector. 1977.
- [33] Sahu M.K., Prasad R.K.: *Second law optimization and parametric study of a solar air heater having artificially roughened absorber plate*. Arch. Thermodyn. **40**(2019), 2, 107–135.
- [34] Sahu M.K., Prasad R.K.: *Thermohydraulic performance analysis of an arc shape wire roughened solar air heater*. Renew. Energ. **108**(2017), 598–614.
- [35] Cortes A., Piacentini R.: *Improvement of efficiency of a bare solar collector by means of turbulence promoters*. Appl. Energ. **36**(1990), 253–261.

Geometrical and optical analysis of small-sized parabolic trough collector using ray tracing tool SolTrace

RAMAN KUMAR SINGH*
PRAKASH CHANDRA

National Institute of Technology Patna, Department of Mechanical Engineering, Bihar 800005, India

Abstract The present work is aimed at geometrical optimization and optical analysis of a small-sized parabolic trough collector (PTC). Improving the performance of parabolic trough collectors can greatly justify the use of solar energy. An optimized curvature geometry, the location of the absorber tube, and the heat flux distribution along the circumference of the absorber tube are major features in the geometric optimization and optical modelling of parabolic trough collectors. Rim angle, aperture width, the diameter of the absorber tube, receiver position, and the optimum value of heat flux are the major parameters considered in this work for geometrical and optical analysis. The Monte Carlo ray tracing method has been adopted for analysis. The non-uniform heat flux distribution profile obtained from optical analysis of the proposed parabolic trough collector has been compared with the profile available in the literature, and good agreement has been obtained, which proves the feasibility and reliability of the model and method used for this study. An experimental new small-sized parabolic trough collector has been fabricated for the optimized rim angle of 90 deg after a successful laser light feasibility test. The effect of the absorber tube position along the optical axis on the heat flux profile was analysed and found to be substantial. Furthermore, the sensitivity analysis of the parabolic trough collector using the software applied has been discussed separately.

Keywords: Parabolic trough collector; SolTrace; Monte Carlo ray tracing method; Non-uniform heat flux distribution; Optical analysis; Geometrical analysis

*Corresponding Author. Email: ramanks.phd19.me@nitp.ac.in

Nomenclature

A_s	–	surface area, m^2
A_p	–	aperture area, m^2
CR	–	concentration ratio
DNI	–	direct normal irradiation, W/m^2
f	–	focal length, m
H	–	height of the trough, m
L	–	length of the trough, m
LCR	–	local concentration ratio
l	–	length of the absorber tube, m
d_o	–	outer diameter of the absorber tube, m
r_r	–	rim radius, m
W_a	–	aperture width, m
x, y	–	Cartesian coordinates, m
q	–	local heat flux, W/m^2

Greek symbols

α_D	–	acceptance angle, deg
ϕ_r	–	rim angle, deg

Acronyms

CFD	–	computational fluid dynamics
CSHFD	–	circumferential solar heat flux distribution
CSP	–	concentrated solar power
CTG	–	circumferential temperature gradient
MCRT	–	Monte Carlo ray tracing
PTC	–	parabolic trough collector
SEGS	–	solar energy generating system

1 Introduction

The parabolic trough collector (PTC) is a line-focused type of concentrated solar power (CSP) technology that is prominently used due to its wide temperature range (up to 400°C). The reflector and absorber tubes are two major components of PTC. A reflector concentrates incoming beam radiation at the focus of the aperture at which the absorber tube is kept so that the heat transfer fluid (HTF) passing through it gets heated [1, 2]. Optical performance significantly influences PTC's overall efficiency. By using the method of ray tracing, the optimal configuration of the collector with maximum performance can be obtained. The thermal performance of PTC systems depends upon optical efficiency, which is significantly influenced by the geometry of the collector, heat flux intensity distribution along the

absorber tube circumference, the location of the absorber tube, etc. Various numerical and experimental analyses have been carried out by numerous researchers to investigate the heat flux distribution around the absorber surface of PTC and other CSP technologies.

Wang [3] conducted a review study related to slope error in reflector surface and sun shape using six different optical modelling tools: SolTrace, Tonatiuh, Solar PILOT, Tracer, Solstice, and Heliosim. Mwesigye *et al.* [4] estimated the heat flux profile on the receiver tube surface of PTC using Monte Carlo ray tracing (MCRT) and coupled it to computational fluid dynamics (CFD) for heat transfer analysis. Particularly, they analysed rates of entropy generation at a range of rim angles, concentration ratios, and temperatures of flowing fluid.

Many times, the optical efficiency of the PTC system does not reach expectations due to geometrical and optical faults such as receiver position inaccuracy, misalignment, slope, and profile error, among others. It is important to design by figuring out what these errors are and what they mean for how well PTC works. Donga *et al.* [5] studied the influence of receiver location on the optical and thermal performance of a PTC. The simulation was carried out by coupling MCRT heat flux distribution data with CFD. They found that the error in receiver position had a significant impact on thermal performance and the heat flux profile. Zhao *et al.* [6] simulated heat flux distribution along the circumference of absorber tubes by combining coordinate transformation with the MCRT method. They reported the substantial effects of inaccuracies in receiver position, tracking errors, geometrical concentration ratios, and incident angle on the solar heat flux distribution profile. The error becomes larger with an increase in incident angle and a decrease in geometrical concentration ratios. Treadwell examined the effects of receiver location errors in the lateral direction from the focus [7]. When the receiver position was shifted along the lateral y -direction by $\pm 10\%$ of its diameter from the focus, no major change in the performance of the PTC was detected. He also recommended that the receiver tube's diameter be expanded to compensate for misalignment without compromising the PTC's performance significantly. Treadwell and Grandjean said that the receiver positioning error affected the PTC's annual performance, depending on how much the receiver was moved [8]. The above-mentioned literature shows that the receiver position error has a considerable effect on the optical efficiency of the PTC and the heat flux distribution throughout the circumference of the absorber tube, and hence on the thermal performance of the PTC system.

The generation of circumferential solar heat flux distribution (CSHFD) is essential in concentrating solar collectors since it is one of the boundary conditions for the PTC receivers' thermal analysis. Various works from the past are available; a few of them have been discussed here. Ghomrassi analysed numerically the thermal performance of the PTC receiver tube for different diameters by coupling CSHFD obtained in SolTrace software to CFD [9]. Jeter proposed a semi-finite analytical approach for evaluating the CSHFD of the PTC receiver [10]. Wang *et al.* [11] investigated the thermal performance of the PTC system numerically by the finite element method (FEM). Solar flux densities are evaluated by using the solar ray tracing method. Cheng *et al.* [12] investigated the thermal performance of the PTC receiver by combining MCRT with the finite volume method (FVM) and compared their findings with the experimental results of Dudley *et al.* [13]. It was found that the numerical results were quite close to the experimental results. Among other techniques, the MCRT method is extensively used for obtaining focused solar heat flux distribution [5, 6, 9, 11, 12, 14].

From the above discussion, it is clear that for the efficient functioning of PTC systems, the optimised collector geometry, the optical model for concentrated heat flux distribution, and the correct location of the absorber tube are crucial, among other factors. Aperture width, focal length, and rim angle are the parameters that define the size and curvature of a parabolic trough. The rim angle is a single parameter having the capability to define the cross-section of the parabolic trough [15, 16]. Since some smaller and larger rim angles are not good for a reliable PTC, this study gives an optimal rim angle for a new small-sized PTC based on the average and peak values of CSHFD over the absorber tube. More heterogeneous heat flux densities around the circumference of the absorber tube may result in a higher circumferential temperature gradient (CTG), increased thermal stress and strain, damaging the receiver tube and reducing system stability and safety. The impacts of the receiver dislocation from the focus point as well as the sensitivity analysis of the PTC have also been discussed.

2 Numerical simulation for design optimization and fabrication of parabolic trough collector

In this section, the numerical modelling of a new small-sized parabolic trough collector and fabrication of a laboratory-scale experimental setup for an indoor experiment have been discussed. In this work, the two major

components of PTC, namely the reflector and absorber, were analysed. Other components, such as the sun tracking mechanism, the glass cover, the heat transfer fluid (HTF), and so on, are irrelevant in this study.

2.1 Consideration of design parameters

To define the physical structure of a parabolic trough, there are mainly four geometric parameters: trough length, aperture width, rim angle, and focal length. The size of the absorber tube can be determined by its diameter and length. The two dimensional (2D) cross-sectional view in Fig. 1 depicts critical elements for designing a new small-size PTC. The length of the trough or collector has been determined (1 m) based on prior work related to small-sized PTC, which reported the length of the collector in the range of 1–3 m [17–20]. The lower the aperture width of the trough, the shorter the geometric factor, resulting in greater optical efficiency. For a particular absorber diameter, however, the concentration ratio reduces as the aperture width lowers, resulting in large thermal losses. Kalogirou *et al.* [21] proposed that the aperture width be reduced to a length ratio of 0.64 after aperture width optimization to achieve the goal of having a small geometric factor and a high concentration ratio. Based on the above literature, we can figure out that the aperture width is 0.64 m for the analysis of the present work.

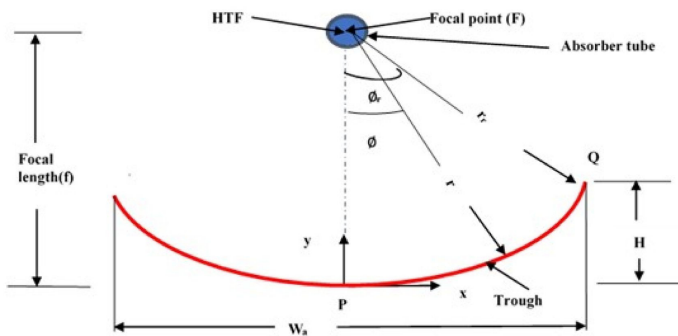


Figure 1: 2D sectional view of present PTC.

One of the critical criteria for the proper operation of any PTC system is the selection of the optimum rim angle [16]. A ray tracing software based on the MCRT algorithm has been adopted for analysing the effect of different rim angles on the concentrated heat flux and selecting the optimum one. The parameters of PTC that have been used in the analysis of CSHFD are listed in Table 1.

Table 1: Parameters of the parabolic trough collector used in the circumferential solar heat flux distribution analysis.

Parameters	Units	Numerical value
Collector length	mm	1000
Aperture width	mm	640
Absorber tube outer diameter	mm	21
Absorber tube inner diameter	mm	19
Absorber tube length	mm	1000
Direct normal irradiance	W/m ²	1000
Concentration ratio	–	9.38
Reflectivity of concentrator	–	0.88
Absorptivity of the absorber tube	–	0.95
Slope error concentrator	mrاد	2
Specularity error of concentrator	mrاد	0.5
Sun shape (pillbox)	mrاد	4.65
Desired number of ray interaction	–	10 ⁶
Maximum number of generated sun rays	–	10 ⁸

The analysis has been carried out for a rim angle ranging within 30–130 deg, with a gap of 10 deg to obtain the maximum collection of solar heat flux for a non-ideal concentrator, having the slope and specularity errors mentioned in Table 1.

As the rim angle decreases, the focal length increases, and concentrated heat flux falls on a very small region of the bottom outer surface of the absorber tube while the rest of the tube receives direct normal irradiation (DNI). In this case, the peak value of heat flux (51.3 kW/m²) is very high, 51.3 times the DNI (1 kW/m²), which can cause thermal stress and damage to the absorber tube due to the high CTG. In Fig. 2, the effect of one of the smaller rim angles (30 deg) on concentrated heat flux density is shown through a ray-intersection plot, contour plot and surface plot.

As the rim angle increases, the focal length reduces, and the reflected radiations from the outer portion of the concentrator travel a relatively greater distance. In this case, the outer part of the reflector also contributes less to reflection. Also, it is clear from Fig. 3 that as the rim angle increases, the intensity of heat flux decreases (16.8 kW/m²). Large rim angles are also restricted due to economic constraints and are practically uncomfortable and difficult to handle. Figure 3 depicts the effect of one of the larger rim angles (130 deg) on heat flux distribution.

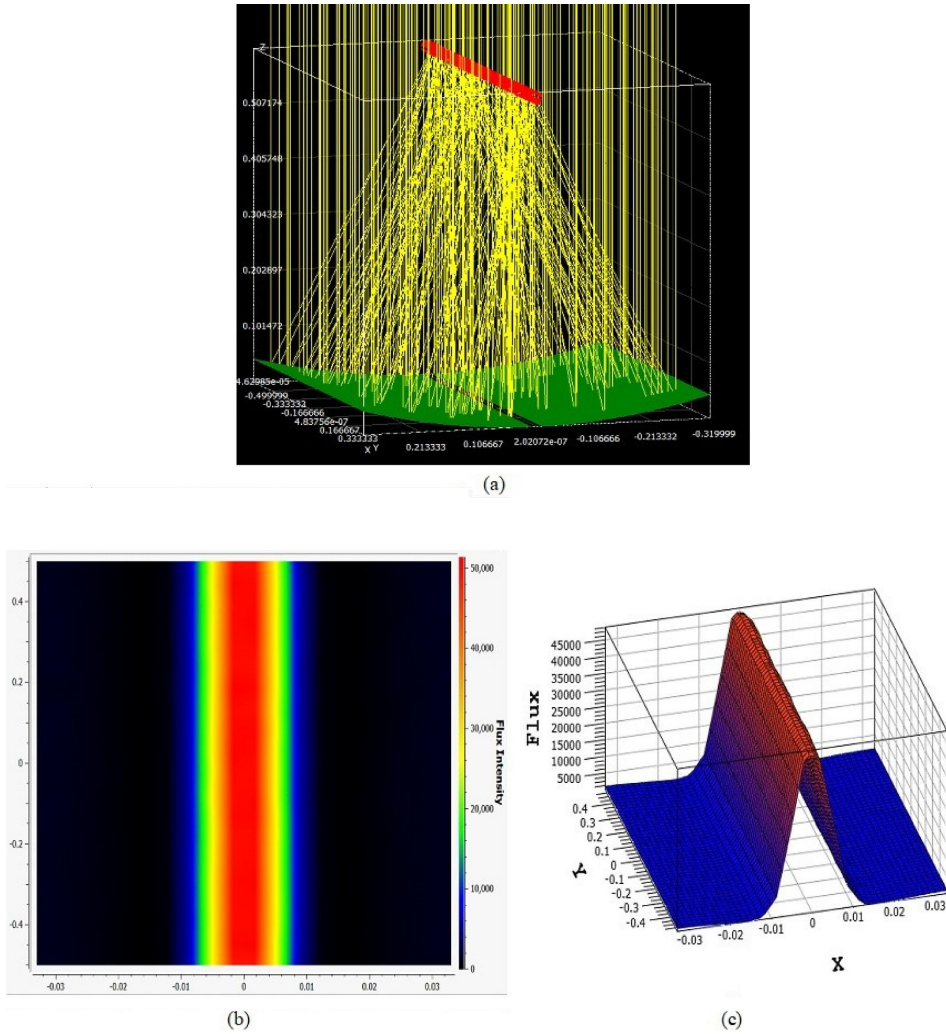
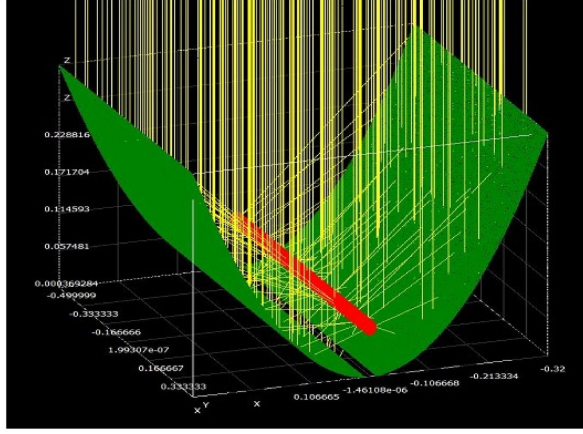


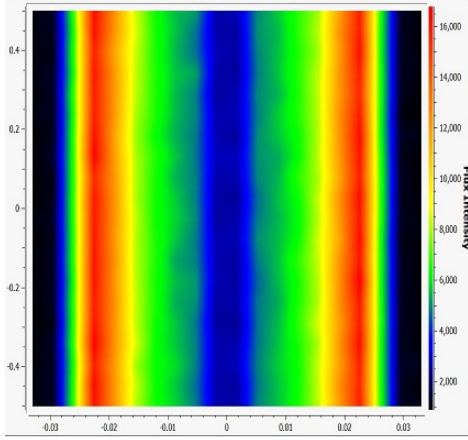
Figure 2: Effect of small rim angle (30 deg) on heat flux: (a) ray intersection plot, (b) contour plot, (c) surface plot.

As it follows from the above discussion, due to some reasons, a range of smaller and larger rim angles are not suitable for a reliable PTC. In the third case, a medium range of rim angles (90 deg) has been taken for analysing its effect on heat flux intensity, which is shown in Fig. 4.

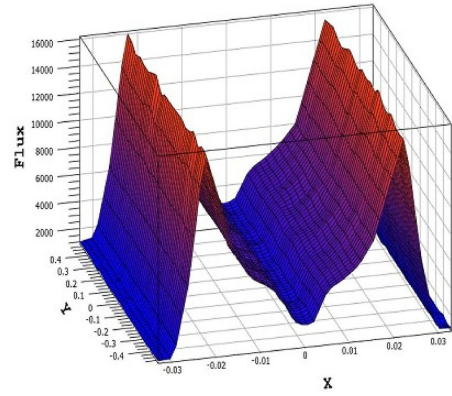
In the case of a 90-degree rim angle, the peak value of heat flux is 19.4 kW/m^2 , which can be seen in the contour and surface plot in Fig. 4.



(a)



(b)



(c)

Figure 3: Effect of larger rim angle (130 deg) on heat flux intensity: (a) ray-intersection plot, (b) contour plot, (c) surface plot.

For ease of analysis, the rest of the rim angle range (30–130 deg) and its effect on heat flux intensity have been tabulated in Table 2.

Table 2 shows that the optimum value of average heat flux for a 90-degree rim angle is 8.58 kW/m^2 , while smaller rim angles of 30 deg and larger rim angles of 130 deg have relatively very high (51.3 kW/m^2) and poor values (16.85 kW/m^2) of peak heat flux, respectively, in comparison to 19.44 kW/m^2 of peak heat flux for a 90-degree rim angle.

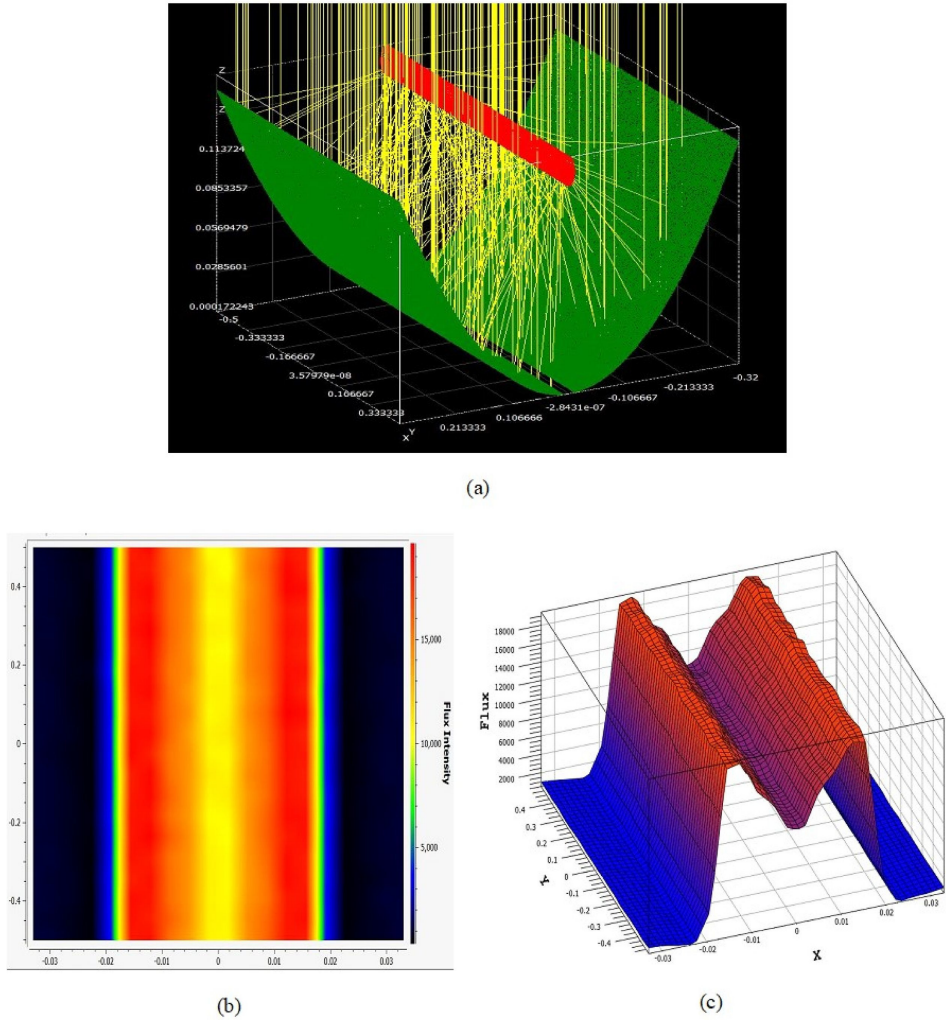


Figure 4: Effect of medium range rim angle (90 deg): (a) ray-intersection plot, (b) contour plot, (c) surface plot.

Furthermore, the ideal value of the rim angle for proper operation of the PTC system is 70–110 deg [16], which is satisfied by the result given in Table 2. Table 2 shows that the simulated values of peak and average heat flux for 70–110 deg of rim angle do not vary much. A 90-degree rim angle is most practically employed in PTC with a circular absorber tube, according to Jeter [10]. The above discussion proves that the MCRT method used

Table 2: Comparative analysis of heat flux density for different values of rim angle.

Rim angle (deg)	Peak heat flux (kW/m ²)	Uncertainty in peak heat flux (%)	Average heat flux (kW/m ²)	Uncertainty in average heat flux (%)
30	51.3	±0.86	8.55	±0.07
40	35.65	±1.04	8.56	±0.07
50	30.78	±1.12	8.56	±0.07
60	25.86	±1.2	8.57	±0.07
70	23.54	±1.2	8.56	±0.07
80	22.26	±1.32	8.56	±0.07
90	19.44	±1.4	8.58	±0.07
100	20.42	±1.37	8.57	±0.07
110	19.93	±1.39	8.56	±0.07
120	19.81	±1.39	8.55	±0.07
130	16.85	±1.51	6.52	±0.07

in this work is viable and the numerical findings obtained are reliable. So, a 90-degree rim angle is what we have selected for further numerical analysis and the fabrication of an experimental setup.

2.2 Data reduction

The different geometrical parameters are discussed mathematically as follows. The aperture of the parabolic trough collector is represented by the parabola equation [22, 23]:

$$y = \frac{x^2}{4f}, \quad (1)$$

where x and y are Cartesian coordinates and f is the focal length of the parabola.

The following is the relationship between focal length, aperture width (W_a), and rim angle (ϕ_r):

$$f = \frac{W_a}{4 \tan \frac{\phi_r}{2}}. \quad (2)$$

The minimum theoretical outer diameter of the absorber tube that can intercept all the reflected DNI is given by the relation as follows [24, 25]:

$$d_o = 2r_r \sin \frac{\alpha_D}{2}, \quad (3)$$

where r_r is the radius of the rim which can be calculated from the relation [1, 26]

$$r_r = \frac{2f}{1 + \cos \phi_r}. \quad (4)$$

Parameter α_D is the acceptance angle for maximum concentration and its value is taken as 0.53° [27].

By using Eqs. (3) and (4) for a 90-degree rim angle, we get a minimum theoretical outer diameter of 2.96 mm for the absorber tube. However, due to geometrical imperfections, misalignments, and other constraints, it is difficult to use the theoretically designed diameter for experimental analysis. In this study, we used an absorber tube with an inner diameter of 19 mm and an outer diameter of 21 mm, which is within the range of diameters used by many researchers to investigate small-sized PTC.

The height of the parabolic trough can be obtained by putting $x = \frac{W_a}{2}$ and $y = H$ in Eq. (1), which finally gives

$$H = \frac{W_a^2}{16f}. \quad (5)$$

The surface area (A_s) of the reflector is given by the relationship [17]

$$A_s = \left[\frac{W_a}{2} \sqrt{1 + \frac{W_a^2}{16f^2}} + 2f \ln \left(\frac{W_a}{4f} + \sqrt{1 + \frac{W_a^2}{16f^2}} \right) \right] l, \quad (6)$$

where l is the length of the parabolic trough.

Another important geometrical parameter for focusing type of solar collector is the concentration ratio which is given as

$$\text{CR} = \frac{\text{Effective aperture area}}{\text{Absorber tube surface area}} = \frac{(W_a - d_o)l}{\pi d_o L}, \quad (7)$$

where L is the length of the absorber tube.

2.3 Design methodology for a new parabolic trough collector

The flow chart of the design methodology and the fabrication process for a new small-sized PTC is shown step by step in Fig. 5.

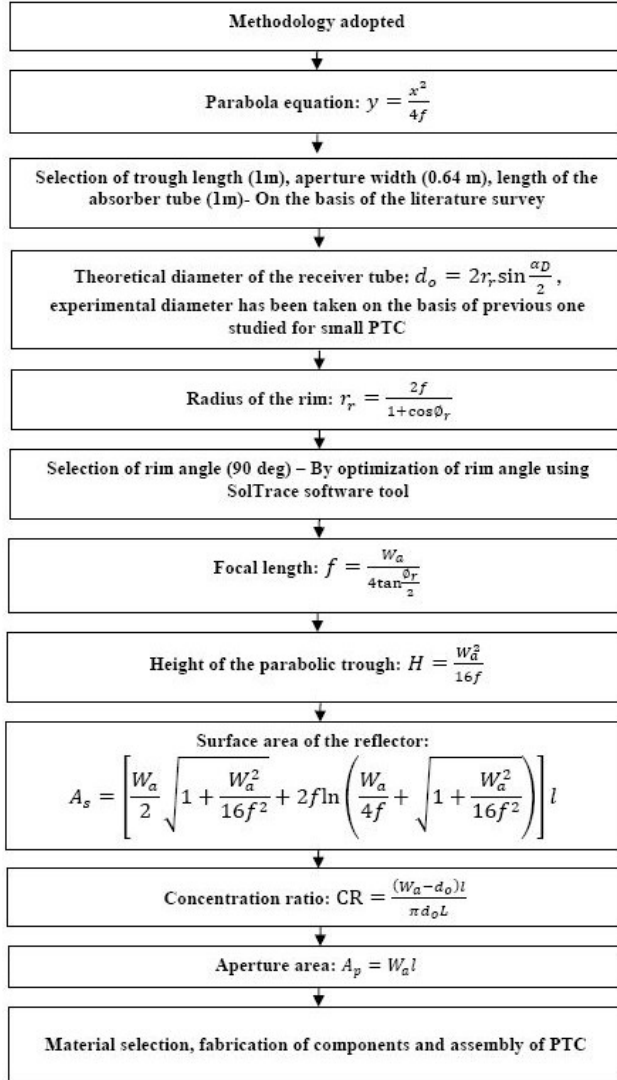


Figure 5: Flow chart for design methodology and fabrication of a new PTC.

2.4 Experimental design and fabrication of a parabolic trough collector

This section deals with the experimental process adopted for the design and fabrication of the PTC. First, a laser light test for the design of the curvature of the PTC has been done to determine the feasibility of the technique.

After that, an experimental trough with the dimensions shown in Table 1, including an optimized rim angle of 90 deg and, correspondingly, a value of the focal length of 160 mm calculated using Eq. (2), was fabricated for the further study.

2.4.1 Laser light test

This test has been performed for a smaller dimension of the parabola, for the feasibility test of the procedure, and for the ease of conducting the test. The materials and parameters used in the test are summarized in Table 3. Later, this technique was used to create actual troughs for experimentation. Their dimensions are given in Table 4.

Table 3: Parameters and material used for laser light test.

Parameters and material used	Dimensions/Property
Width of aperture	200 mm
Focal length of the parabolic aperture	50 mm
Rim angle	90 deg
Laser light	635 nm
Chrome sheet (reflector) – reflectivity	0.88
Drawing sheet	–

Table 4: Description of the components, materials and its dimensions used in the fabrication of PTC.

Components	Material	Dimension
End aperture of trough	Plywood	Width of aperture: 640 mm
Trough	Galvanised sheet	Length: 1000 mm, width: 640 mm
Absorber tube	Copper	$d_i = 19$ mm, $d_o = 21$ mm
Solar reflector film	Chrome sticker	Reflectivity: 0.88
Focal length	–	160 mm
Rim angle	–	90 deg

In this test, a 635 mm laser light was used as the light source, and a drawing sheet of 1 mm thickness has been shaped into a parabolic curve according to the coordinate points marked on the sheet, obtained by Eq. (1) for the parabola and the parabola calculator 2.0 software [28]. A chrome sheet adhered to the parabolic-shaped sheet was used to reflect the laser light

that fell on it. We can see in Fig. 6 that the laser light, after reflection from the parabolic-shaped reflector, exactly passes through the focal point made at 50 mm focal length, corresponding to a 90-degree rim angle, which proves the feasibility of the test. Sixteen segment coordinate points for designing an accurate parabolic curve have been obtained from the parabola calculator, as shown in Fig. 7. For a 50-mm focal length, the same coordinate points can also be obtained by using the parabola equation (Eq. (1)).



Figure 6: Experimental view of laser light test.

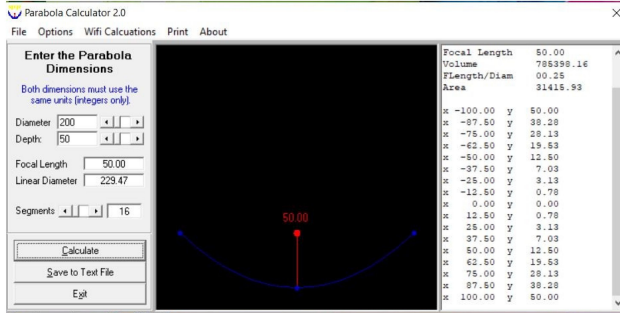


Figure 7: Snap of the parabolic curve and coordinate points in Parabola Calculator 2.0 software [28].

2.4.2 Fabrication of experimental parabolic trough collector

After a successful feasibility test of the laser light, the same procedure was used for the fabrication of experimental PTC, as shown in Fig. 8. Table 4 lists the materials and dimensions used in the fabrication of experimental PTC.

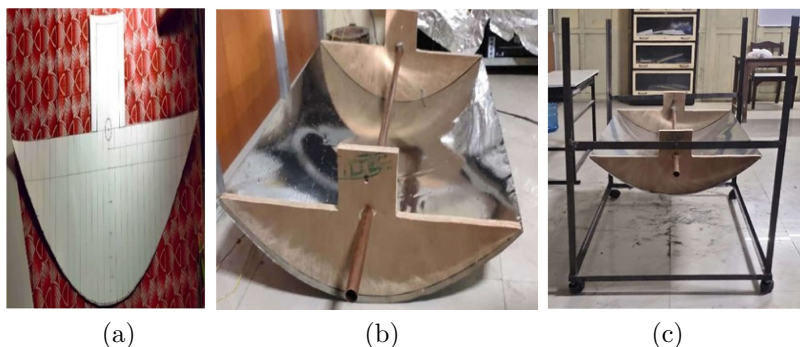


Figure 8: Experimental view of (a) parabolic aperture drawn on the sheet, (b) trough with absorber tube, (c) parabolic trough collector with supporting frame.

3 Methodology for heat flux distribution analysis using SolTrace software

The CSHFD analysis with SolTrace is carried out in the steps depicted in flow chart (Fig. 9). It is based on an optical interaction technique that uses the ray tracing method. The programme generates the scatter plot, surface plot (3D), and contour plot (2D) for the heat flux distribution profile on the circumference of the PTC absorber [29]. The first step to analysing the ray tracing is to define the sun's shape and sun position. There are three options available to define the shape of the sun, namely pillbox, Gaussian and user-defined distributions, while the position of the sun is defined either

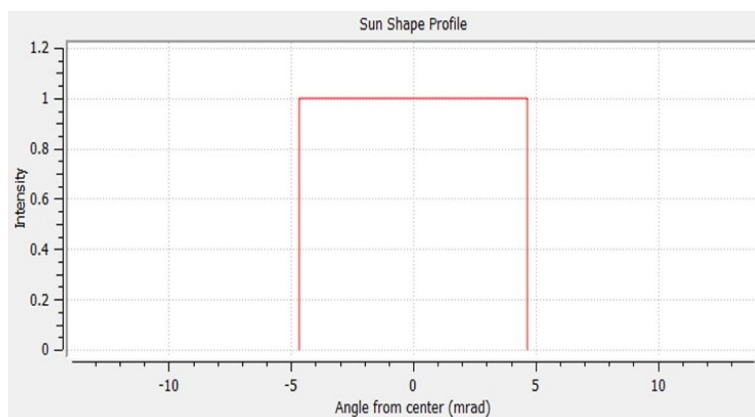


Figure 9: Flow chart of CSHFD analysis using SolTrace software version 2012.7.9.

by the global coordinate system or by defining the latitude, day and solar hour of a particular place. In the present analysis, the sun's shape is defined as a pillbox distribution with a half-angle width of 4.65 mrad as shown in Fig. 10 [11, 29, 30], and the sun position is defined by the global coordinate system. The next step is setting the optical properties of the concentrator and absorber tube as shown in Fig. 9. After defining the optical properties,

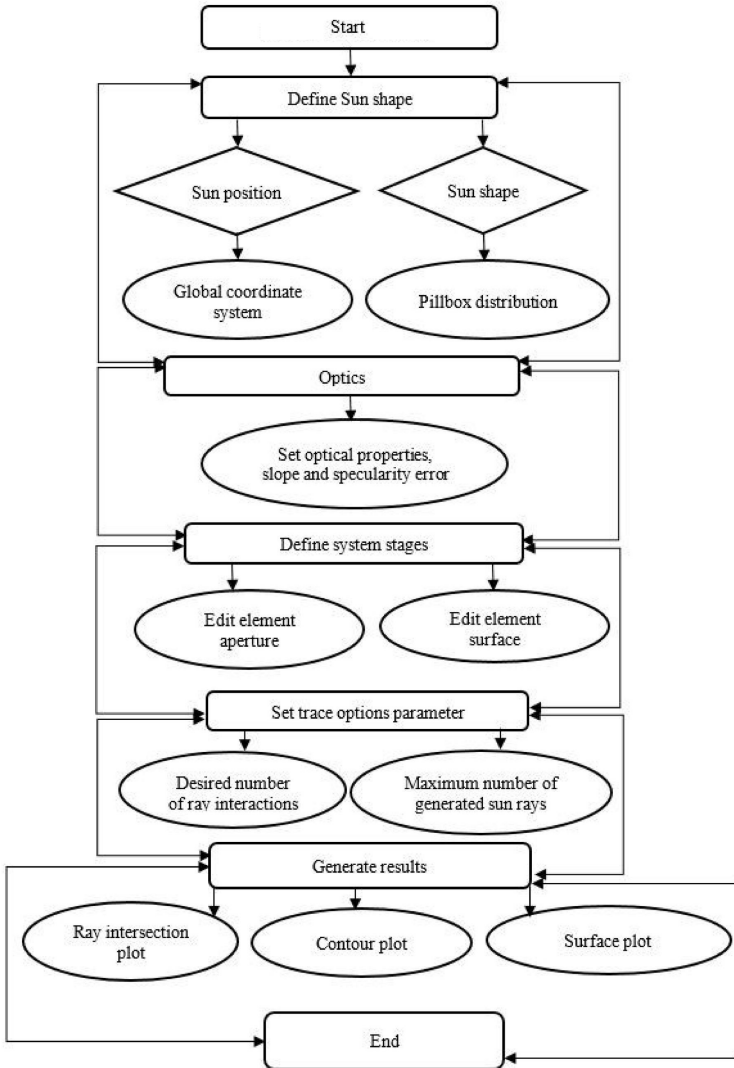


Figure 10: Pillbox sun shape profile.

the geometry of the system was developed by setting stage properties and defining the element aperture and element surface. The desired number of ray interactions of 10^6 and a maximum number of generated rays of 10^8 have been employed in the trace options parameter to obtain an accurate heat flux profile and save computational time [5]. During simulations, it has been seen that the value of heat flux changes significantly between runs when the desired number of ray interaction values is less than 10^6 . A constant value of DNI 1000 W/m^2 is employed for the simulation. The sun's rays first strike the absorber and concentrator, and the reflected rays from the concentrator fall on the absorber and are absorbed by it.

4 Results and discussion

4.1 Discussion on non-uniform heat flux profile

Figure 11 shows the surface plot of heat flux distribution along the outer periphery of the absorber tube. The surface plot actually shows the heat flux distribution on the unwrapped absorber tube, varying from 0–360 deg from left to right, where 0 deg and 180 deg stand for the top and bottom positions of the absorber tube, as illustrated in Fig. 12c. As shown in Fig. 11,

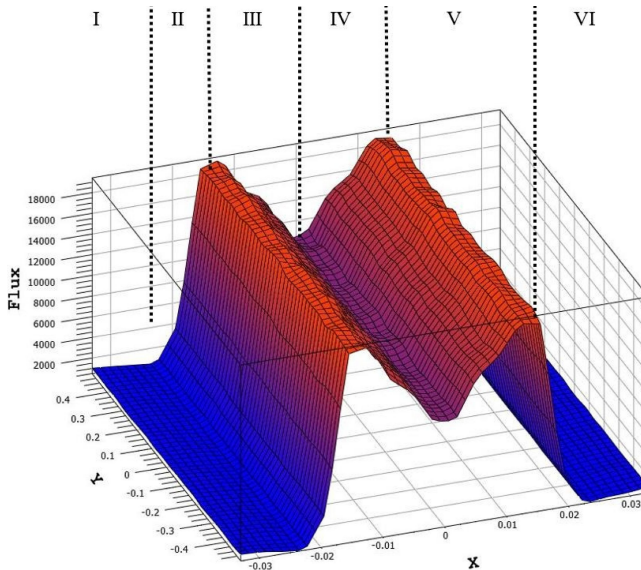


Figure 11: Surface plot of solar heat flux distribution along the absorber tube periphery.

the curve can be divided into six parts for ease of explanation of heat flux variation. In the first part of curve depicted in Fig. 11, heat flux intensity is very low, since in this part, the absorber tube only receives DNI. This is clear from the graph representing the change in heat flux distribution with the absorber tube circumferential angle (Fig. 12b) and the scatter plot shown in Fig. 12a. In the second part, heat flux increases rapidly and reaches a peak of 19.44 kW/m^2 at about 112.5 deg circumferential angles from the top of the tube, as shown in Fig. 12b, then decreases rapidly

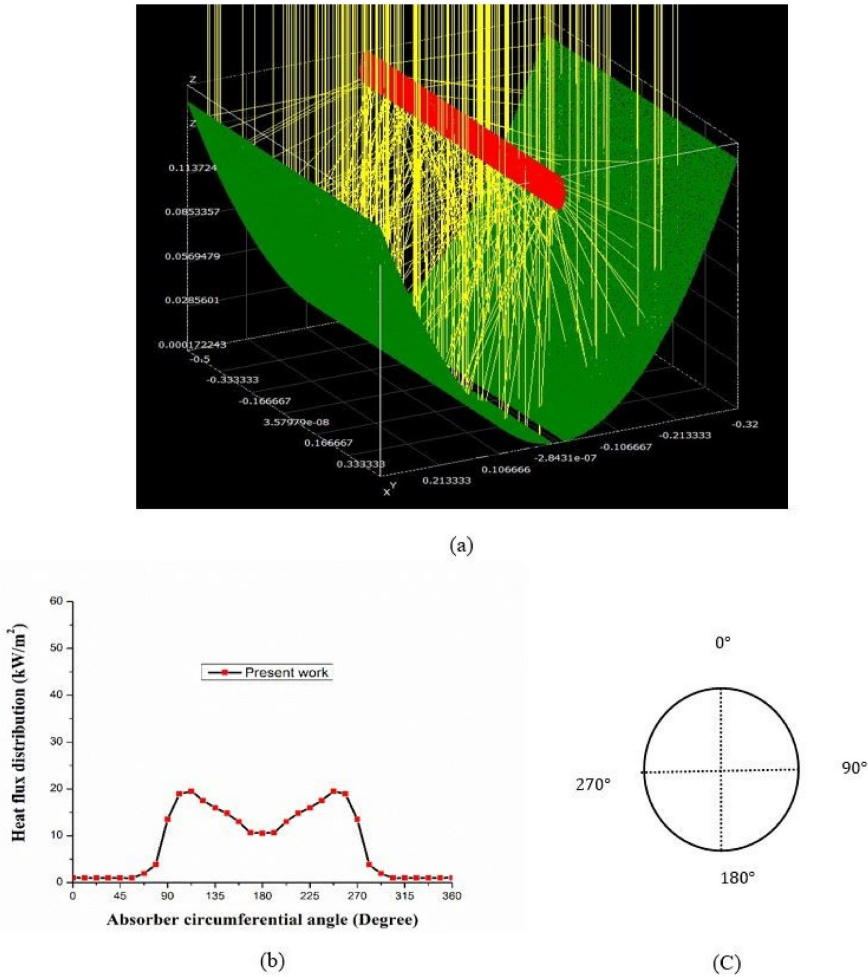


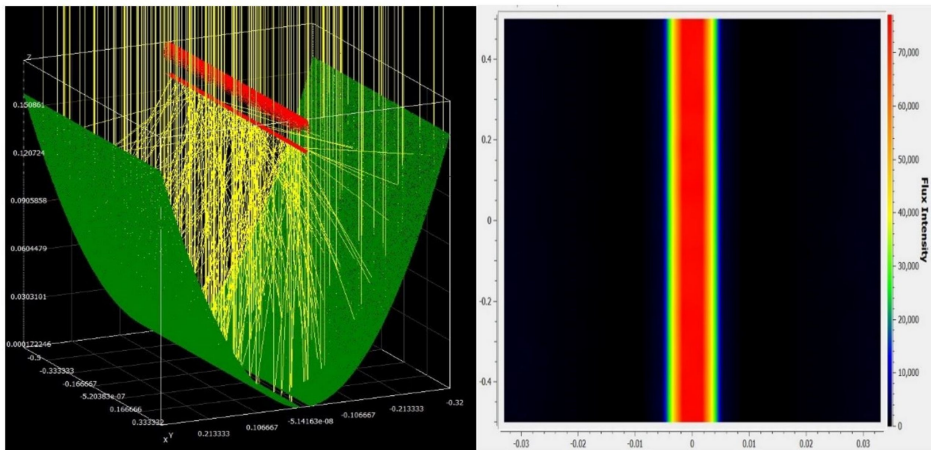
Figure 12: (a) Scatter plot for 90 deg rim angle, (b) heat flux *vs.* absorber circumferential angle, (c) absorber circumferential angle distribution.

and reaches a value of 10.55 kW/m^2 at 180° in the third part due to a decrease in reflected heat flux, which can also be seen in the scatter plot in Fig. 12a. The curve is symmetrical about 180° , and the variation of heat flux in the next part exhibits the same characteristics as in the earlier one.

These CSHFD can be used as one of the boundary conditions in the CFD simulations for further thermal analysis.

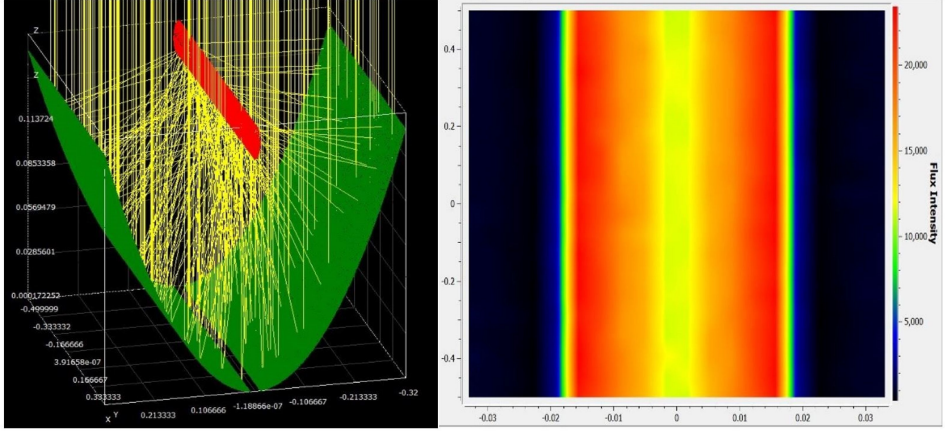
4.2 Receiver position error analysis

In this part, the numerical modelling software was used to investigate how the misalignment of the receiver along the optical axis affects the heat flux profile. For this analysis, the dimensional details have been incorporated from Table 4 without consideration of a slope or specularity error (i.e., 0.0001 mrad). As presented in Fig. 13, the centre of the absorber tube is shifted above the focal point of the parabolic trough by its outer radius (10.5 mm) in the first case (Fig. 13a), in which most of the reflected ray concentrates at the small bottom part of the absorber tube. In this case, the peak value of heat flux is 76.95 kW/m^2 , i.e., almost 77 times DNI (1 kW/m^2) which is very high, and will increase CTG in the absorber tube. The second is the case when the absorber tube is concentric with the focal point (Fig. 13b). This is the ideal case, where the peak value of

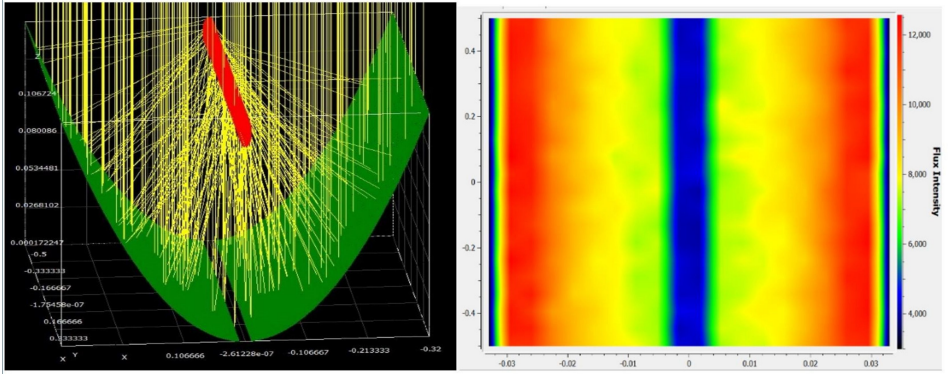


(a) Scatter plot and contour plot for absorber tube with the centre shifted by 10.5 mm above the focal point

Figure 13: For caption see next page.



(b) Scatter plot and contour plot for absorber tube concentric with the focal point



(c) Scatter plot and contour plot for absorber tube with the centre shifted by 10.5 mm below the focal point

Figure 13: Effect of receiver position misalignment along the optical axis on the heat flux profile.

heat flux is 23.5 kW/m^2 , and the average value of heat flux is 9.32 kW/m^2 , which is greater than the average value of 8.17 kW/m^2 for the first case and 8.16 kW/m^2 for the third one. The third case deals with the centre of the absorber tube being below the focal point by 10.5 mm (Fig. 13c). In this case, the absorber tube receives a poor value of peak heat flux (12.57 kW/m^2).

The above discussion reveals that the heat flux density is significantly affected by receiver misalignment along the optical axis.

4.3 Validation of numerical modelling results

For the validation of the present simulation work in SolTrace, the obtained outcome was compared with Jeter's result [10]. In his paper, the parameter local concentration ratio (LCR) is discussed [5]:

$$\text{LCR} = \frac{q}{\text{DNI}}, \quad (8)$$

where q represents the local heat flux.

Jeter's result corresponds to the parameter of the solar energy generating system (SEGS), solar collector (LS2 – Luz system 2) used in Sandia National Laboratories. Numerical simulation was carried out at the same geometrical dimensions, and optical and material properties as presented in [10] with normal irradiance, 90 deg rim angle and a uniform sun of 0.0075 mrad angular radius. The simulation results of LCR distribution at the cross-section of the absorber outer surface compared with those reported by Jeter are shown in Fig. 14. The comparison shows that the predictions agree well with Jeter's results, which also proves that the MCRT method used in the present work is viable and the numerical results are reliable.

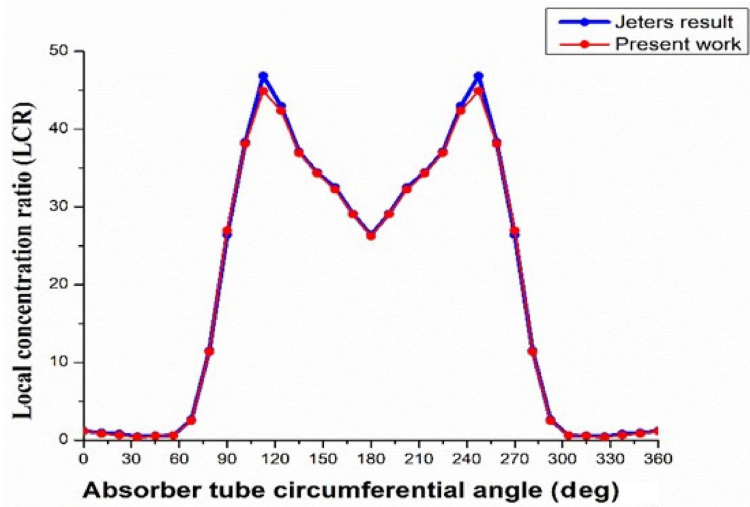


Figure 14: The LCR distribution – comparison between the present study and Jeter's results.

4.4 Sensitivity analysis

4.4.1 Influence of rim angle on the peak heat flux

The variation of the peak value of heat flux with the rim angle around the absorber tube periphery is shown in Fig. 15. Within the 30- to 130-degree rim angle, the peak value of heat flux is very large at 30 deg, with a poor value for peak heat flux at 130 deg. The peak value of heat flux for the rim angle varies little in the optimum range (70–110 deg).

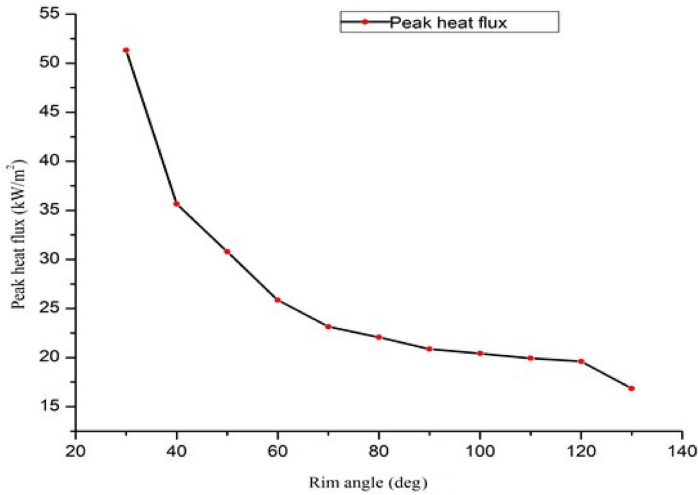


Figure 15: Peak heat flux *vs.* rim angle.

4.4.2 Heat flux variation along the receiver circumference for three different rim angles

The heat flux distributions along the absorber circumference for three different rim angles, namely 30 deg, 90 deg, and 130 deg, are compared in Fig. 16. Due to concentrated heat flux in a relatively small region of the absorber tube, a larger spike in the peak value of heat flux can be observed with a smaller rim angle of 30 deg. A poor value of peak and average heat flux is found for the relatively larger rim angle of 130 deg, while an acceptable range of peak heat flux and an optimum average heat flux is observed for the 90 deg rim angle. The heat flux profile distribution for different rim angles have been discussed in more detail in Section 2.1.

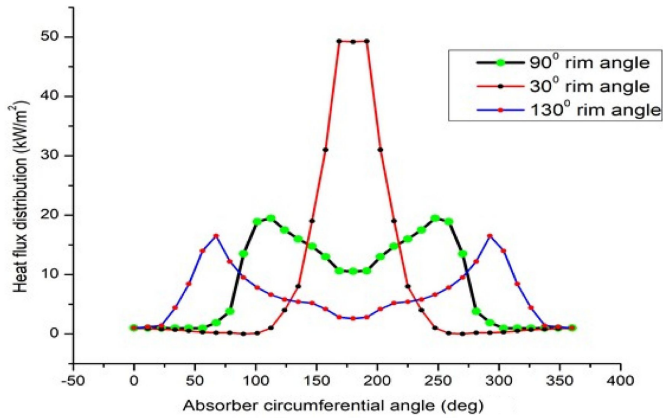


Figure 16: Comparison of heat flux profile along the absorber circumferential angle for different rim angles.

4.4.3 Effect of absorber tube outer diameter on the heat flux profile

Figure 17 depicts the variation of heat flux distribution with the absorber tube's outer diameter. For this analysis, all parameters given in Tables 1 and 4 have been adopted, except for the receiver's outer diameter. The three different values of the absorber tube's outer diameter, 21 mm, 23 mm, and

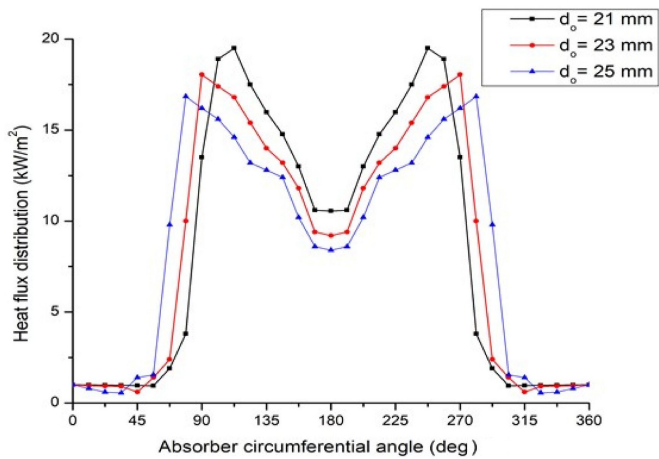


Figure 17: Variation of heat flux along absorber circumferential angle for different outer diameters of absorber tube.

25 mm, have been used while keeping the aperture width at 640 mm. As we know from Eq. (7), the concentration ratio depends on the width of an aperture as well as the outer diameter of the absorber tube. As the outer diameter increases, the concentration ratio decreases, resulting in a decrease in the value of heat flux intensity.

5 Conclusion

The present work focus on the geometrical optimization and optical analysis of a novel small-sized PTC based on the analysis of heat flux distribution around the circumference of the absorber tube using a ray tracing software called SolTrace. The outcome of this study can be summarised as follows:

- Heat flux distribution analysis was carried out for different values of rim angle within 30–130 deg, and an optimized rim angle of 90 deg was obtained on the basis of the optimum value of average heat flux and an acceptable range of peak heat flux to obtain the maximum collection of solar heat flux for a non-ideal concentrator. Also, the determined optimum rim angle falls within a range of values obtained by other researchers in the literature, which proves the Monte Carlo ray tracing method used in the present work is viable and the numerical results are reliable.
- Ray-intersection plots, contour plots and surface plots were provided. Also, the peak and average values of heat flux were presented for the different values of rim angle 30–130 deg, with a gap of 10 deg.
- An experimental model of a small-sized parabolic trough collector was designed and fabricated. The curvature of the parabolic trough was designed for an optimized value of rim angle 90 deg, and other parameters mentioned in Table 1. A laser light test of a small dimension parabolic trough was performed first for the feasibility test of the procedure before fabrication of the actual parabolic trough collector and was found successful. Also, the design methodology was presented through a flow chart.
- The heat flux around the circumference of the absorber tube is non-uniform in nature. The heat flux profile is found to be symmetrical about the bottommost point of the circular absorber tube. The maximum value of heat flux is found at the bottom part of the tube

(112.5 deg and 247.5 deg from the topmost point), and the heat flux decreases towards the top of the absorber tube due to only direct normal irradiation falling in this location.

- The effect of the receiver position error along the optical axis on the heat flux profile was analysed and found to be significant. A receiver with a centre 10.5 mm above and below the focal point of the parabolic trough increases peak heat flux by 227.44%, which is very large and decreases it by 46.8%, which is poor. A very large value of heat flux caused by concentrated rays at a very small area of absorber creates a greater value of circumferential temperature gradient, and a poor value of heat flux may decrease overall performance; hence, both large and poor values of peak heat flux are not recommended for the efficient functioning of a reliable before fabrication of the actual parabolic trough collector and was found successful.
- During the sensitivity analysis of the parabolic trough collector, it was observed that as the outer diameter of the absorber tube increases, while keeping the aperture width the same, the heat flux intensity around the circumference of the absorber tube decreases due to a decrease in the concentration ratio.
- The slope error has a significant impact on the uniformity of flux intensity and the peak heat flux at the focal point. When the slope error is low, the peak heat flux at the focal point of the trough is high. When the slope error is high, however, the peak heat flux and uniformity go down because the rays do not reflect as well off the concentrator.
- A comparison of the local concentration ratio distribution versus absorber tube circumferential angle was made between the present work and Jeter's result for the optimized value of rim angle 90 deg and the same geometrical configurations, and the profile of the curve is found to be very close. This proves that the Monte Carlo ray tracing method used in the present work is viable and the numerical results are reliable.
- The heat flux distribution profile along the absorber tube circumferential angle generated by using the Monte Carlo ray tracing method can be utilized as one of the boundary conditions in CFD.

Received 30 March 2023

References

- [1] Abdulhamed A.J., Adam N.M., Ab-Kadir M.Z. A., Hairuddin A.A.: *Review of solar parabolic-trough collector geometrical and thermal analyses, performance, and applications*. Renew. Sust. Energ. Rev. **91**(2018), 822–831.
- [2] Stanek B., Bartela Ł., Węcel D., Rulik S.: *An experimental study on parabolic trough collector in simulated conditions by metal-halide solar radiation simulator*. Arch. Thermodyn. **43**(2022), 3, 47–61.
- [3] Wang Y., Potter D., Asselineau C.A., Corsi C., Wagner M., Caliot C., Piaud B., Blanco M., Kim J.S., Pye J.: *Verification of optical modelling of sunshape and surface slope error for concentrating solar power systems*. Sol. Energy **195**(2020), 461–474.
- [4] Mwesigye A., Bello-Ochende T., Meyer J.P.: *Minimum entropy generation due to heat transfer and fluid friction in a parabolic trough receiver with non-uniform heat flux at different rim angles and concentration ratios*. Energy **73**(2014), 606–617.
- [5] Donga R.K., Kumar S., Kumar A.: *Performance evaluation of parabolic trough collector with receiver position error*. J. Therm. Eng. **7**(2021), 1, 271–290.
- [6] Zhao D., Xu E., Wang Z., Yu Q., Xu L., Zhu L.: *Influences of installation and tracking errors on the optical performance of a solar parabolic trough collector*. Renew. Energ. **94**(2016), 197–212.
- [7] Treadwell G.W.: *Design considerations for parabolic-cylindrical solar collectors*. Sandia Laboratories Energ. Rep. **9**(1976), SAND-76-0082.
- [8] Treadwell G.W., Grandjean N.R.: *Systematic rotation and receiver location error effects on parabolic trough annual performance*. Am. Soc. Mech. Eng. **104**(1981), 345–348.
- [9] Ghomrassi A., Mhiri H., Bournot P.: *Numerical study and optimization of parabolic trough solar collector receiver tube*. J. Sol. Energy Eng. Trans. ASME **137**(2015), 5, SOL-15-1068.
- [10] Jeter S.M.: *Calculation of the concentrated flux density distribution in parabolic trough collectors by a semifinite formulation*. Sol. Energy **37**(1986), 5, 335–345.
- [11] Wang Y., Liu Q., Lei J., Jin H.: *Performance analysis of a parabolic trough solar collector with non-uniform solar flux conditions*. Int. J. Heat Mass Transf. **82**(2015), 236–249.
- [12] Cheng Z.D., He Y.L., Xiao J., Tao Y. B., Xu R.J.: *Three-dimensional numerical study of heat transfer characteristics in the receiver tube of parabolic trough solar collector*. Int. Commun. Heat Mass Transf. **37**(2010), 7, 782–787.
- [13] Dudley E., Kolb J., Mahoney A., Mancini T.R., Matthews C.W., Kearney D.: *Test results: SEGS LS-2 solar collector*. Sandia Nat. Lab. Rep. **140**(1994), SAND94-1884.
- [14] He Y.L., Xiao J., Cheng Z.D., Tao Y.B.: *A MCRT and FVM coupled simulation method for energy conversion process in parabolic trough solar collector*. Renew. Energ. **36**(2011), 3, 976–985.

- [15] Upadhyay B.H., Patel A.J., Sadasivuni K.K., Mistry J.M., Ramana P.V., Panchal H., Ponnamma D., Essa F.A.: *Design, development and techno economic analysis of novel parabolic trough collector for low-temperature water heating applications*. Case Stud. Therm. Eng. **26**(2021), 100978.
- [16] Günther M., Joemann M., Csambor S., Guizani A., Krüger D., Hirsch T.: *Parabolic trough technology*. In: Advanced CST Teaching Materials, Chap. 5, 51–43. DLR, Kassel 2011,
- [17] Upadhyay B.H., Patel A. J., Sadasivuni K. K., Mistry J. M., Ramana P.V., Panchal H., Ponnamma D., Essa F.A.: *Design, development and techno economic analysis of novel parabolic trough collector for low-temperature water heating applications*. Case Stud. Therm. Eng. **26**(2021), 100978.
- [18] Özcan A., Devocioğlu A G., Oruç V.: *Experimental and numerical analysis of a parabolic trough solar collector for water heating application*. Energ. Source. Part A Recover. Util. Environ. Eff. **44**(2022), 2, 4184–4203.
- [19] Bharti A., Mishra A., Paul B.: *Thermal performance analysis of small-sized solar parabolic trough collector using secondary reflectors*. Int. J. Sustain. Energ. **38**(2019), 10, 1002–1022.
- [20] Faheem M., Jizhan L., Akram M.W., Khan M.U., Yongphet P., Tayyab M., Awais M.: *Design optimization, fabrication, and performance evaluation of solar parabolic trough collector for domestic applications*. Energ. Source. Part A Recover. Util. Environ. Eff. (2020), 1–20.
- [21] Kalogirou S.A., Lloyd S., Ward J., Eleftheriou P.: *Design and performance characteristics of a parabolic-trough solar-collector system*. Appl. Energ. **47**(1994), 4, 341–354.
- [22] Menbari A., Alemrajabi A.A., Rezaei A.: *Experimental investigation of thermal performance for direct absorption solar parabolic trough collector (DASPTC) based on binary nanofluids*. Exp. Therm. Fluid Sci. **80**(2017), 218–227.
- [23] Price H., Lüpfert E., Kearney D., Zarza E, Cohen G., Gee R., Mahoney R.: *Advances in parabolic trough solar power technology*. J. Sol. Energy Eng. Trans. ASME **124**(2002), 2, 109–125.
- [24] Sukhatme S.P., Nayak J.K.: *Solar Energy Principles of Thermal Collection and Storage*. McGraw-Hill, New Delhi 2008.
- [25] Duffie J.A., Beckman W.A., McGowan J.: *Solar engineering of thermal processes*. Am. J. Phys. **53**(1985), 382–382.
- [26] Collares-Pereira M., Gordon J.M., Rabl A., Winston R.: *High concentration two-stage optics for parabolic trough solar collectors with tubular absorber and large rim angle*. Sol. Energy **47**(1991), 6, 457–466.
- [27] Ceylan I., Ergun A.: *Thermodynamic analysis of a new design of temperature controlled parabolic trough collector*. Energ. Convers. Manag. **74**(2013), 505–510.
- [28] <http://mscirt.tripod.com/parabola/> (accessed 15 Aug. 2022).
- [29] Wendelin T.: *Soltrace: A new optical modeling tool for concentrating solar optics*. Int. Sol. Energy Conf. (2003), 253–260.
- [30] SolTrace optical modelling software, *SolTrace v.2012.7.9*. <http://www.nrel.gov/csp/soltrace/> (accessed 20 Oct. 2022).

Performance of cryogenic oxygen production unit with exhaust gas bleed for sewage sludge gasification and different oxygen purities

MAJA KASZUBA*
PAWEŁ ZIÓŁKOWSKI
DARIUSZ MIKIELEWICZ

Gdańsk University of Technology, Narutowicza 11/12, 80-233 Gdańsk,
Poland

Abstract The paper presents a thermodynamic analysis of the integration of a cryogenic air separation unit into a negative CO₂ emission gas power plant. The power cycle utilizes sewage sludge as fuel so this system fits into the innovative idea of bioenergy with carbon capture and storage. A cryogenic air separation unit integrated with the power plant was simulated in professional plant engineering and thermodynamic process analysis software. Two cases of the thermodynamic cycle have been studied, namely with the exhaust bleed for fuel treatment and without it. The results of calculations indicate that the net efficiencies of the negative CO₂ emission gas power plant reach 27.05% (combustion in 95.0% pure oxygen) and 24.57% (combustion in 99.5% pure oxygen) with the bleed. The efficiencies of the cycle without the bleed are 29.26% and 27.0% for combustion in 95.0% pure oxygen and 99.5% pure oxygen, respectively. For the mentioned cycle, the calculated energy penalty of oxygen production was 0.235 MWh/kgO₂ for the lower purity value. However, for higher purity namely 99.5%, the energy penalty of oxygen production for the thermodynamic cycle including the bleed and excluding the bleed was indicated 0.346 and 0.347 MWh/kgO₂, respectively. Additionally, the analysis of the oxygen purity impact on the carbon dioxide purity at the end of the carbon capture and storage installation shows that for the case with the bleed, CO₂ purities are 93.8% and 97.6%, and excluding the bleed they are 93.8% and 97.8%, for the mentioned oxygen purities respectively. Insertion of the cryogenic oxygen production in-

*Corresponding Author. Email: maja.kaszuba@pg.edu.pl

stallation is required as the considered gas power plant uses oxy-combustion to facilitate carbon capture and storage method.

Keywords: Thermodynamic analysis; Oxy-combustion of syngas; BECCS; Cryogenic air separation; Penalty of oxygen production

Nomenclature

c	–	velocity, m/s
ϵ_{CO_2}	–	emissivity of CO_2 , kgCO_2/MWh
ϵ_{pen}	–	energy penalty, MWh/kgO_2
g	–	gravitational acceleration, m/s^2
LHV	–	lower heating value, MJ/kg
\dot{m}	–	mass flow rate, kg/s
N_{ASU}	–	power for air separation needs, kW
N_{CCS}	–	power for CCS compressors needs, kW
N_{CP}	–	total power for own needs, kW
N_{fuel}	–	power for fuel compressor needs, kW
N_{O_2}	–	power for oxygen compressor needs, kW
$N_{\text{P}_{\text{H}_2\text{O}}}$	–	power for water pump needs, kW
$N_{\text{P}_{\text{SEC}}}$	–	power for SEC pump needs, kW
N_t	–	combined turbines power, kW
R	–	factor describing energy source as renewable
t	–	temperature, $^\circ\text{C}$
\dot{Q}_{CC}	–	chemical rate of combustion, kW
u	–	internal energy, kJ/kg
X_{CO_2}	–	volume fraction of carbon dioxide, %
z	–	height, m

Greek symbols

η_{cum}	–	cumulative efficiency, %
η_{g}	–	gross efficiency of the cycle, %
η_{net}	–	net efficiency of the cycle, %
η_{R_H}	–	gasifier efficiency, %
ρ	–	density, kg/m^3

Acronyms

ASU	–	air separation unit
BCCS	–	bioenergy with carbon capture and storage
CCS	–	carbon capture and storage
GS	–	gas scrubber
GT	–	gas turbine
HE	–	heat exchanger
nCO2PP	–	negative CO_2 emission gas power plant
PC	–	pre-cooler
SEC	–	spray ejector condenser
WCC	–	wet combustion chamber

1 Introduction

It is estimated that the production of electric power contributes to the generation of approximately 25.0% of CO₂ in the atmosphere [1, 2]. Over the years, several ways for reducing CO₂ from the atmosphere were introduced. These solutions can be divided generally into oxy-combustion, post-combustion, and pre-combustion [3]. In post-combustion technology, CO₂ is captured after the combustion process from flue gases. It can be done in several ways including sorption technologies, membrane separation, and cryogenic distillation [3–5]. A very crucial advantage of the post-combustion method is that it can be introduced to existing power plants, and a disadvantage is that CO₂ concentration in exhaust gases is very low and the exhaust pressure is near the atmospheric pressure [3]. According to the literature, the most mature way to separate CO₂ from the rest of the flue gas is absorption and its energy requirement contributes to 13.0–15.0% of the power plant efficiency [3].

The pre-combustion technology assumes carbon removal from the fuel before the combustion process. This process consists of two parts. In the first one, the mixture of H₂ and CO is obtained from gas reforming, then in the second part, CO is altered into CO₂ and separated from H₂. In the end, only H₂ is combusted. The power cycles coupled with pre-combustion technology are called integrated gasification combined cycles (IGCC) [3].

Oxy-fuel is the third carbon capture and storage method, next to post-combustion and pre-combustion. It is probably the most promising solution for power plants that require carbon capture and storage (CCS) technology. In particular, in the case of the connection between increasing global electricity production and growing CO₂ concentration in the atmosphere. Future power plants will need to feature the CCS installations [6, 7], due to the need of stopping and avoiding an increase in CO₂ concentration in the atmosphere. A typical power plant worked with oxy-combustion technology would require 20 tons of O₂ for each megawatt per day [8–10]. Oxygen can be produced in several ways. The most popular are cryogenic air distillation, followed by pressure swing adsorption, oxygen transport membranes, chemical looping air separation, and electrolysis of water [11]. For the combustion process, low-purity oxygen in the range of 85.0–98.0% is supposed to be the most appropriate. It is connected with high energy consumption while producing oxygen purer than 95.0% with the cryogenic air distillation method. This technology will be taken into consideration

in this work and will be connected with the negative CO₂ emission gas power plant.

Cryogenic air distillation is the most developed technology in oxygen production [11]. Its biggest disadvantage is that oxygen production is very energy-consuming. On the other hand, cryogenic separation is the only technology that can provide huge capacities of produced oxygen. Additionally, other air gases which are also industrial gases are possible to be obtained [10]. The minimum thermodynamic work needed to produce oxygen is 0.051 MWh/kgO₂ but in real cryogenic installations, it is approximately four times greater [12].

Conventional cryogenic double-column air separation unit consists of an air compressor considered the most energy-consuming device in the installation [9], two thermally-coupled rectification columns, and heat exchangers. In the first step, the air is compressed usually to 5.4–6.0 bar [13,14]. Next, it is cooled in a heat exchanger called a pre-cooler, then separated into two streams. One of the streams is introduced into the high-pressure column and the second into the low-pressure column. At the top of the high-pressure column, nitrogen is obtained at a pressure of 6.0 bar. At the bottom of mentioned column oxygen-enriched liquid is obtained. Obtained nitrogen is condensing because of boiling oxygen in the reboiler, which connects two columns. Both product streams obtained at the high-pressure column are depressurized and sent to the low-pressure column. In this column, gaseous nitrogen is obtained at the top of the tower, and liquid oxygen at the bottom [13,14]. The distillation process is based on differences in boiling points of air components at specified pressures [15].

The paper presents the results of an integration of a cryogenic air separation unit (ASU) into a negative CO₂ emission gas power plant (nCO₂PP) and the impact of the oxygen production installation on the power cycle. For this thermodynamic cycle, other oxygen production methods might be considered such as membrane or sorption techniques. Some of these technologies were compared with cryogenic air distillation in other works [16–18]. However, when it comes to large scale power plants with a capacity of hundreds of megawatts, cryogenic air separation is the only appropriate solution [19], because only this method is able to produce huge amounts of oxygen up to 150 000 m³/h [20]. Moreover, it is the most developed way to produce oxygen from the air. Due to its maturity, low-temperature technology was chosen.

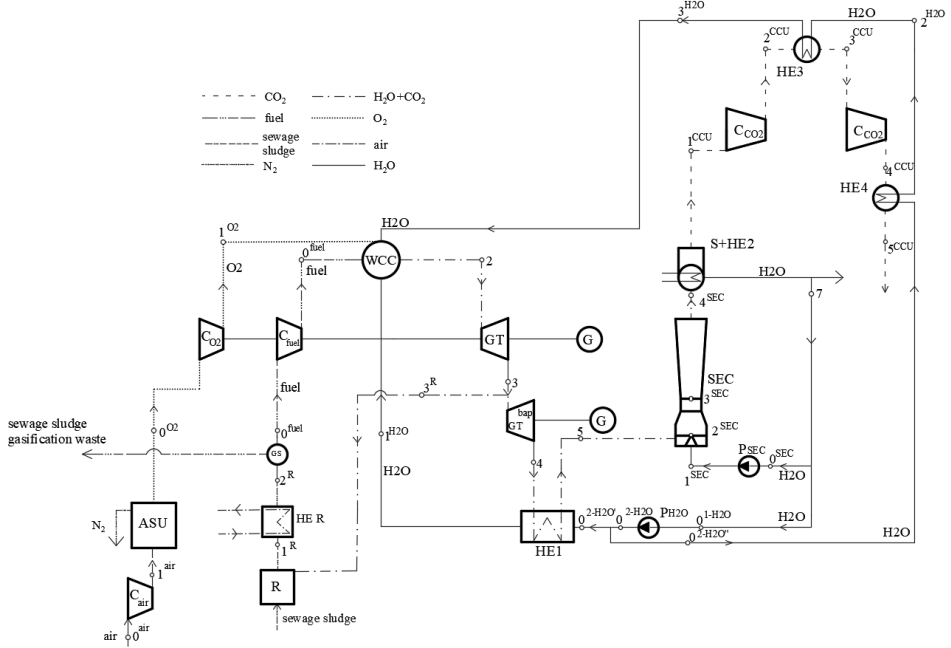
2 Negative CO₂ emission gas power plant integrated with cryogenic air separation unit

Over the years, several configurations of power cycles with oxy-fuel technology have been proposed, with either gas or coal fuels. The common entity for all these cycles was the oxygen as an oxidizer and then flue gases composed of steam and carbon dioxide. Part of the solutions recovers the carbon dioxide from exhaust gases, recirculates it to the combustion chamber, and uses it as a working medium in the cycle [21–23]. Most oxy-fuel cycles are integrated by a heat recovery steam generator with the Rankine cycle to avoid huge heat losses [24].

The scrutinised nCO₂PP cycle is a gas-steam turbine cycle integrated with a CCS installation and a cryogenic ASU. The power plant is fuelled with syngas from the gasification process of sewage sludge. The combustion process takes place in the atmosphere of pure oxygen and the combustion chamber is cooled by water injection. The considered thermodynamic cycle has been studied before in other works [25], but its integration with an ASU has not been taken into consideration.

The diagram of nCO₂PP is presented in Fig. 1. The system is equipped with two compressors. The first one forces the flow of oxidant (C_{O₂}), whereas the second one is for the fuel transport (C_{fuel}). The cycle also consists of the high-pressure gas turbine (GT), low-pressure gas turbine (GT^{bap}), wet combustion chamber (WCC), and generator (G). The main heat exchanger (HE1) heats the water supplied to the WCC with exhaust gases. The spray-ejector condenser (SEC) is a novel device for the exhaust gas condensation process. A CCS installation consists of two compressors (C_{CO₂}), two heat exchangers (HE3, HE4), and a heat exchanger connected with a water separator (S+HE2). The water pump (P_{H₂O}) increases the pressure of water, which is supplied to the WCC. Between two expanders is an exhaust bleed for the needs of the gasification process. Sewage sludge gasification takes place in the gasifier (R). A heat exchanger (HE R) and a gas scrubber (GS) are also on the fuel way to the combustion chamber.

According to the calculations, exhaust gases contain mostly steam. Indeed, oxygen and fuel are supplied by compressors, as they are present in gas turbines, but there is much more water injected into the combustion chamber by the pump. This amount of water exceeds the fuel and oxidizer streams. An additional characteristic of steam cycles is the presence of a condensation process, which is also characteristic to the considered nCO₂PP cycle.

Figure 1: Diagram of negative CO_2 emission gas power plant.

The beginning of the process in the cycle can be established when fuel and oxygen compressors (C_{fuel} , C_{O_2}) start transporting fluids to the combustion chamber (WCC). In the combustion chamber fuel, oxygen, and injected water, due to high temperature processes, create a mixture of carbon dioxide and water. Water injection is necessary, because of high temperatures, which are the effect of the oxy-combustion process. Additionally, the extra mass flow of water contributes to the increase of the turbines power, which is dependent on the mass flow. After the combustion process, expansion in two turbines (GT, GT^{bap}) takes place. Afterwards, exhaust gases are heating water, which is transported by the pump ($P_{\text{H}_2\text{O}}$) to the combustion chamber, through the heat exchanger (HE1). The spray-ejector condenser (SEC) intakes the flue gases from the heat exchanger (HE1). Provided is also water, which is a motive fluid in the SEC with the pump (P_{SEC}). The presence of motive water, which breaks up into droplets, and the mixture of steam and carbon dioxide enables the condensation process to take place. The mixture of water and carbon dioxide leaving the SEC goes to the separator connected to the heat exchanger (S+HE2). Water is isolated and directed to pumps (P_{SEC} , $P_{\text{H}_2\text{O}}$) in the separator. Subsequently, it

is used as the motive fluid in SEC or as a cooling fluid in the combustion chamber (WCC). The carbon dioxide is directed to the compressor (C_{CO_2}) and the heat exchanger (HE3).

The oxygen, which is an oxidant in the combustion process in the WCC, is supplied from the cryogenic air separation unit. Air separation in a modelled installation starts with compressing the air by a compressor (C_{air}) and then cooling in the precooler (PC). Afterwards, cooled air is introduced into the first distillation column (RCI). The separation section of the installation consists of two columns. In column RCI oxygen is obtained, and the rest of the air is transported to the second column and is separated there into low-purity nitrogen (lN_2) and high-purity nitrogen (hN_2). A diagram of modelled cryogenic ASU is presented in Fig. 2.

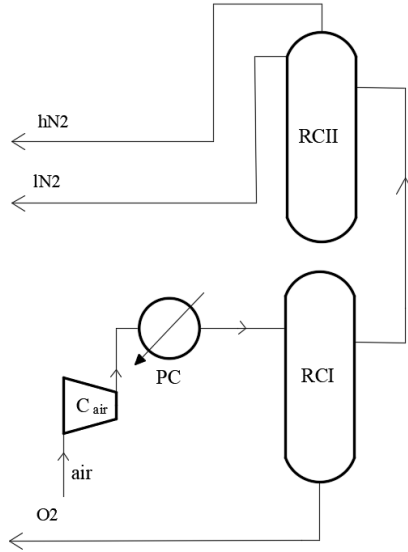


Figure 2: Diagram of modelled cryogenic unit.

3 Methodology

3.1 Cycle efficiency

The gross and net efficiencies of the power cycle have been calculated using the following formulae:

$$\eta_g = \frac{N_t}{\dot{Q}_{CC}}, \quad (1)$$

and

$$\eta_{\text{net}} = \frac{N_t - N_{CP}}{\dot{Q}_{CC}}, \quad (2)$$

where N_t is a combined power of turbines, \dot{Q}_{CC} is a chemical energy rate of combustion, and N_{CP} is the power for the cycle own needs, and which can be expressed as

$$N_{CP} = N_{\text{ASU}} + N_{C_{\text{fuel}}} + N_{C_{O_2}} + N_{P_{H_2O}} + N_{P_{\text{SEC}}} + N_{C_{\text{CCS}}}, \quad (3)$$

where N_{ASU} is the power for oxygen production, $N_{C_{\text{fuel}}}$ is the power for fuel compressor, $N_{C_{O_2}}$ is the power for oxygen compressor, $N_{P_{H_2O}}$ is the power for water pump, $N_{P_{\text{SEC}}}$ is the power for SEC and $N_{C_{\text{CCS}}}$ is the power for CCS compressors needs.

Additionally, the cumulative cycle efficiency which is a product of the net efficiency of the power cycle and gasification process efficiency (η_{R_H}) has been calculated. The gasification process inside the gasifier was not calculated in this work but its efficiency has been taken from another paper regarding nCO2PP [21]. The cumulative efficiency is expressed as

$$\eta_{\text{cum}} = \eta_{R_H} \eta_{\text{net}}, \quad (4)$$

where the gasification process efficiency (η_{R_H}) according to the literature [26] is equal to 86.52% for the nCO2PP cycle.

3.2 Energy penalty and emissivity

For cryogenic oxygen production, an important parameter is the energy penalty of oxygen production:

$$e_{\text{pen}} = \frac{N_{\text{ASU}}}{3600 \dot{m}_{O_2}}, \quad (5)$$

where N_{ASU} is the power for the needs of oxygen production and \dot{m}_{O_2} is the produced oxygen mass flow.

Due to the name of the cycle (negative CO₂ emission gas power plant), an essential factor is the emission potential of the whole system, which can be defined as [25–27]

$$e_{\text{CO}_2} = R \frac{\dot{m}_{4\text{CO}_2}}{N_t - N_{CP}} 3600, \quad (6)$$

where $\dot{m}_{4\text{CO}_2}$ is the mass flow rate of carbon dioxide at the outlet of the CCS, R is a factor describing the energy source as renewable energy (for sewage sludge is 90.0% according to Polish regulations [28]).

The emission calculations should be carried out properly and carefully if the power cycle is integrated with the carbon capture and storage unit. If an energy source is only partly considered a renewable source of energy, emissions should be multiplied by the factor that accounts for it. In this case, the relative emissions of carbon dioxide were multiplied by η_{net} . The relative emission is

$$\eta_{\text{net}} e\text{CO}_2 = \frac{N_t - N_{CP}}{\text{LHV} \dot{m}_{0\text{fuel}}} R \frac{\dot{m}_{4\text{CO}_2}}{N_t - N_{CP}} 3600 = R \frac{\dot{m}_{4\text{CO}_2}}{\dot{Q}_{CC}} 3600, \quad (7)$$

where LHV is the lower heating value.

The avoided $e\text{CO}_2$ for the negative emission power plant is a sum of emissions without CO_2 capture and the value of negative emissions obtained because of the application of renewable energy sources [27].

3.3 Ebsilon software

A numeric code for the purpose of the present analysis solves equations of mass and energy balance. According to the mass balance equation, the mass that flows into a channel is equal to the mass, which flows out of the channel [29, 30]. The mass balance is nothing else than the equation of continuity:

$$\sum_{i=1}^n \dot{m}_i = \sum_{j=1}^m \dot{m}_j, \quad (8)$$

where \dot{m} is a mass flow rate. According to the energy balance, the energy that flows into a device is equal to the energy, which outflows [29, 30] and can be written as

$$\sum_{i=1}^n \dot{m}_i \left(u_i + \frac{c_i^2}{2} + \frac{p_i}{\rho} + z_i g \right) + \dot{Q}_i = \sum_{j=1}^m \dot{m}_j \left(u_j + \frac{c_j^2}{2} + \frac{p_j}{\rho} + z_j g \right) + N_j, \quad (9)$$

where u is the internal energy, c is the velocity, p is the pressure, ρ is the density, z is the height, g is the gravitational acceleration, \dot{Q} is the heat energy rate, and N is the mechanical power, and here $i = 1, 2, \dots, n$, $j = 1, 2, \dots, m$, and m and n represent streams that flow in the channel and flow out of the channel, respectively.

There are many various equations of state, which are used in industrial calculations [31]. The system under investigation was simulated using commercial plant engineering and thermodynamic process analysis software, Ebsilon Professional [32]. Ebsilon software uses the Peng-Robinson equation of state for real gas, instead of the Clapeyron ideal gas equation of state [29]. The software predefined models are clearly expressed by thermodynamic tables for steam. Appropriate choice of the thermodynamic models of real gases has crucial importance for the critical area [33, 34]. The crucial advantage of using the Peng-Robinson equation of state is obtaining a higher accuracy of calculation, especially near the gases and mixtures critical points. This fact is important for modelling real thermodynamic cycles. The Peng-Robinson equation takes into account intermolecular forces [34]. A disadvantage of this model is the fact that not all of the factors have been fully examined at the area of their critical point. On the other hand, the Clapeyron equation allows us to obtain results very fast but it idealizes all gases.

4 Calculation conditions

In the study, four analyses have been carried out. The first one is the nCO2PP connected with cryogenic ASU and with the exhaust bleed for sewage sludge gasification. The bleed is made between GT and GT^{bap}, its pressure is 1.0 bar and temperature is 664.83°C, whereas the mass flow transported to the gasifier is 18.0 g/s. The second analysis is for the same cycle but without the bleed for gasification. Moreover, research on the cryogenic ASU model power consumption depending on the produced oxygen purity has been done. The fourth analysis refers to CO₂ purity at the end of the power cycle (point 5^{CCU} in Fig. 1). Traditionally it is assumed that the production of nitrogen oxides in gas turbines combustion chambers is connected with Zeldowicz's thermal mechanisms [35]. In order to properly model NO_x and CO₂ production in new devices, computational fluid dynamics (CFD) simulations are more convenient, because they allow us to take into account a distribution of components, production sources in particular chemical reactions, and velocity fields [36, 37]. The most important conditions for the ASU model are presented in Table 1.

Important assumptions of the nCO2PP cycle are stoichiometric combustion in oxygen as oxidizer and using sewage sludge as fuel. Fuel composition is as follows: 13.31% CO, 5.12% H₂, 11.46% CH₄, 59.29% CO₂, 8.03%

C_3H_8 , and its lower heating value (LHV) is 17.44 MJ/kg. The rest of the assumptions and boundary conditions are presented in Table 2.

Table 1: Cryogenic ASU model condition.

Description	Symbol	Unit	Value
Air initial temperature	t^{0air}	$^{\circ}C$	15.0
Air initial pressure	p^{0air}	bar	1.0
Air compression pressure	p^{1air}	bar	5.8

Table 2: The nCO2PP model input data.

Parameter	Symbol	Unit	Value
Initial fuel temperature	t_{0fuel}	$^{\circ}C$	50.0
Initial oxygen temperature	t_{0O_2}	$^{\circ}C$	40.0
Syngas fuel pressure before C_{fuel} compressor	p_{0fuel}	bar	1.0
Oxygen pressure before C_{O_2} compressor	p_{0O_2}	bar	1.0
Exhaust temperature after HE1, before SEC	t_5	$^{\circ}C$	65.42
CO_2 pressure after compressor C_{CCU}	p_{2CCU}	bar	40.0
CO_2 pressure after compressor C_{CCU}	p_{4CCU}	bar	90.0
H_2O temperature after HE4	t_{2-H_2O}	$^{\circ}C$	91.67
CO_2 temperature after HE3	t_{3-CCU}	$^{\circ}C$	110
Pressure after GT^{bap}	p_4	bar	0.078
Temperature after SEC	t_6	$^{\circ}C$	18.03
Turbine GT, internal efficiency (η_i)	η_{iGT}	–	0.89
Turbine GT^{bap} , η_i	$\eta_{iGT-bap}$	–	0.89
Fuel compressor C_{fuel} , η_i	$\eta_{iC-fuel}$	–	0.89
Oxygen compressor C_{O_2} , η_i	η_{iC-O_2}	–	0.87
Water pump P_{H_2O} , η_i	η_{iP-H_2O}	–	0.43
Water pump P_{SEC} , η_i	η_{iP-SEC}	–	0.80
CO_2 compressor C_{CO_2-1} , η_i	η_{iC-CO_2-1}	–	0.85
CO_2 compressor C_{CO_2-2} , η_i	η_{iC-CO_2-2}	–	0.85
Mechanical efficiency for all devices	η_m	–	0.99
Gasification process efficiency	η_{RH}	–	0.8652
Temperature in the WCC	t_2	$^{\circ}C$	1100
Pressure in the WCC	p_2	bar	10.5
Exhaust mass flow after WCC	\dot{m}_2	g/s	100.0

5 Results

The following studies have been accomplished:

- analysis of the nCO₂PP integrated with ASU which produces oxygen at 95.0% and 99.5% purity, and with the bleed for the gasification process;
- analysis of the nCO₂PP integrated with ASU which produces oxygen at 95.0% and 99.5% purity, and without the bleed for the gasification process;
- analysis of power consumption of an individual cryogenic ASU model dependent on produced oxygen purity. In this case, constant oxygen mass flow was established as 21.7 g/s, and C_{air} compression to 5.8 bar;
- analysis of the impact of oxygen purity on the nCO₂PP cycle efficiency;
- analysis of oxygen purity impact on the carbon dioxide purity at the end of the CCS installation.

In Table 3 the results for nCO₂PP integrated with cryogenic ASU, with the bleed and without the bleed for the gasification process are presented. Two oxygen purities were taken into consideration, namely 95.0% and 99.5%. Figure 3 presents the obtained plot of the energy penalty of the cryogenic

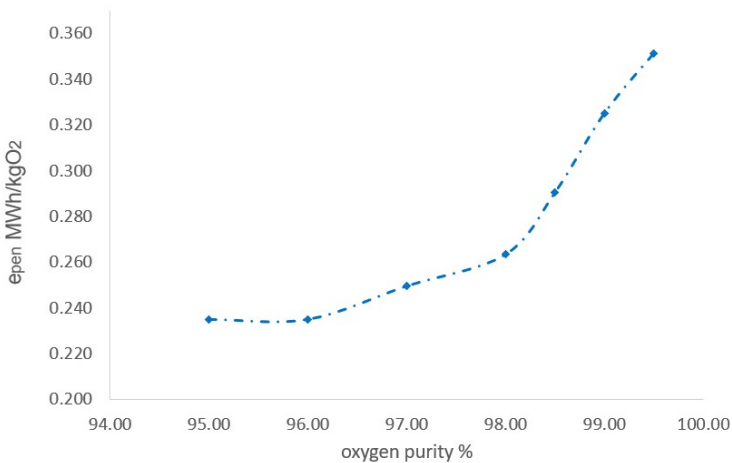


Figure 3: Results of power consumption of the modelled ASU dependent on produced oxygen purity.

Table 3: Results of the analyses of the nCO2PP integrated with the cryogenic ASU including the bleed for gasification process and excluding the bleed.

Description	Symbol	Unit	Oxygen purity			
			95.0%		99.5%	
			nCO2PP + ASU + bleed	nCO2PP + ASU	nCO2PP + ASU + bleed	nCO2PP + ASU
Air mass flow	$\dot{m}_{0\text{air}}$	g/s	98.0	97.73	94.0	93.69
Oxygen mass flow	$\dot{m}_{0\text{O}_2}$	g/s	22.64	22.48	21.7	21.55
ASU power consumption	N_{ASU}	kW	19.17	19.03	27.03	26.91
nCO2PP turbines output	N_t	kW	143.91	154.77	143.05	154.56
nCO2PP power for own needs	N_{CP}	kW	61.1	65.85	67.79	72.27
Chemical rate of combustion	\dot{Q}_{CC}	kW	306.08	303.88	306.27	304.80
nCO2PP gross efficiency	η_g	%	47.02	50.93	46.71	50.71
nCO2PP net efficiency	η_{net}	%	27.05	29.26	24.57	27.0
nCO2PP cumulative efficiency	η_{cum}	%	23.41	25.32	21.26	23.36
Emission of CO ₂	e_{CO_2}	kgCO ₂ /MWh	-782.54	-874.49	-860.98	-905.57
Relative emissivity of CO ₂	$\eta_{\text{net}} e_{\text{CO}_2}$	kgCO ₂ /MWh	-211.71	-255.89	-211.58	-244.49
Avoided emission of CO ₂	Avoid e_{CO_2}	kgCO ₂ /MWh	1652.03	1846.15	1817.63	1911.75
Energy penalty	e_{pen}	MWh/kgO ₂	0.235	0.235	0.346	0.347

ASU dependent on the produced oxygen purity. It is important to mention that the considered ASU model is the same as the one which was integrated with the nCO2PP but independent and with constant oxygen mass flow. In Fig. 4 efficiencies characteristics of the whole cycles dependent on the generated oxygen purity are shown both for the cycle including bleed and excluding bleed. In the same figure, the results of the produced CO₂ purity for two power cycle cases are presented.

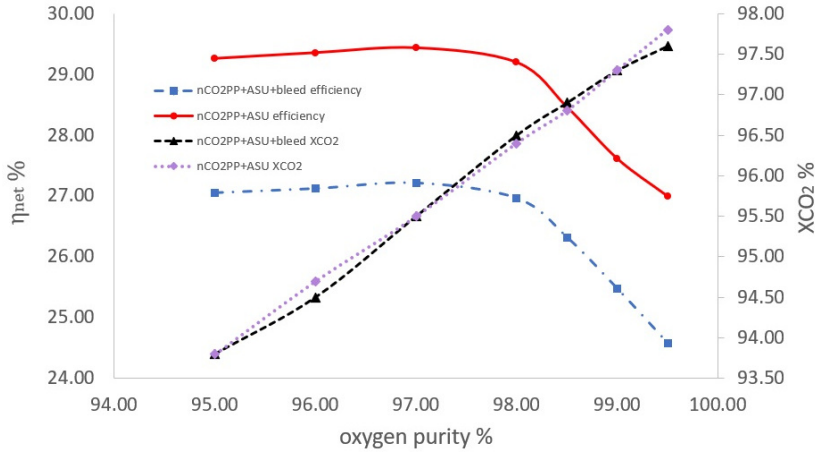


Figure 4: Results of the nCO2PP cycle efficiency and CO₂ purity in the exhaust dependent on produced oxygen purity.

6 Discussion of the results

According to the results in Table 3, the cycle net efficiency is higher for combustion in the oxygen of 95.0% purity for both cases including and excluding the bleed. Although 99.5% is an extremely high value of oxygen purity and it is desirable in some industries like metallurgy, it is too high for the nCO2PP cooperating with cryogenic ASU. This high level of purity does not have a positive impact on cycle efficiency. Its advantage might be resulting in a smaller amount of nitrogen oxides in the exhaust [38,39] but it was not considered in this work. With the enhancing oxygen purity, the temperature in the WCC should increase [40], but for the purpose of this analysis, the temperature in the WCC and exhaust mass flow were set and balanced at 1100°C and 100.0 g/s for every simulation. The analysis of the influence of oxygen purity on the nCO2PP efficiency showed (Fig. 4) that the most appropriate oxygen purity is 97.0%, because efficiency is growing until oxidizer purity reaches 97.0%. After surpassing this value, a rapid efficiency drop is observed. The most common statement is that oxygen at 95.0% purity is the most proper for the majority of the power cycles that work with oxy-fuel technology [41,42].

Regarding the independent model of cryogenic ASU, it can be seen that the energy penalty does not change significantly until it reaches a purity of 96.0% (Fig. 3). After this value, it suddenly increases. It is supposed to

be a proper behaviour. In [42] Darde showed a similar characteristic, which was increasing after exceeding the value of 95.0% oxygen purity. In [13] also the power consumption dependent on ASU can be seen but the plot is more steady. It grows but significantly slower. The obtained energy penalty values are crucial factors for this ASU model and they are 0.235 MWh/kgO₂ for 95.0% purity, 0.263 MWh/kgO₂ for 98.0% purity, and 0.351 MWh/kgO₂ for 99.5% oxygen purity. The obtained values can be compared to the results from other works. Fu claims that the power consumption for 95.0% purity is 0.229 MWh/kgO₂ [9], Janusz-Szymańska states that for 97.0% oxygen purity, the power consumption is 0.247 MWh/kgO₂ [43], Aneke says about 0.357 MWh/kgO₂ for oxygen at purity 99.9% [14], and Tafone assumes 0.370 MWh/kgO₂ for 99.5% oxygen purity [44].

Results regarding the emissivity indicate that cycles with a combustion process with 99.5% oxygen achieved higher values of negative emission and avoided emission of CO₂ than the equivalent cycles with combustion in 95.0% oxygen.

There is one more point worth mentioning. According to the calculations, CO₂ purity is different for various oxygen purities. For the cycle case with the exhaust bleed, the CO₂ composition in the last point of the cycle (5^{CCU}) is 97.6% and 93.8% for 99.5% and 95.0% oxygen purity, respectively. For the cycle case excluding the bleed, CO₂ composition in mentioned point is 97.8% and 93.8% for 99.5% and 95.0% oxygen purity. A reasonable CO₂ purity for the oxy-combustion process is in the range of 95.0–97.0% [45, 46]. In this work, this value is only achieved for 97.0% oxygen purity. Thus, as the authors [47] pointed out, in addition to electricity, the output product of the nCO2PP cycle is also carbon dioxide, and in such a context it makes as great sense as possible to raise its purity. CO₂ is a useful product and its purity for syngas from methane was examined in [47]. On the other hand, in [48] at the inlet of the carbon capture installation, the gas composition is as follows: 64.72% H₂O, 32.53% CO₂, 2.0% O₂, and 0.75% N₂. It means that in the model, the excess of oxygen and oxygen purity lower than 100.0% was assumed.

In this paper, oxy-fuel technology is considered in case of thermodynamic cycle with gas turbine. However, it would also be interesting to introduce oxy-combustion technology to piston engines. There were researches regarding piston engines with internal combustion and oxy-fuel before [49–51]. It would also be interesting to see how oxy-combustion technology can be introduced into piston engine with external combustion process e.g. Stirling engine like in [52].

7 Conclusions

In the paper, the impact of the cryogenic air separation unit on the negative CO₂ emission gas power plant was presented. As the results showed, the highest oxygen purity does not provide the most profitable cycle efficiency. Power consumption dependent on oxygen purity plot shows that attempts to obtain high purity oxygen may generate large power demand and due to that the cycle efficiency drop. However, it should be emphasized that increasing the purity of the oxygen injected into the combustion chamber has a beneficial effect on the purity of the captured carbon dioxide obtained from the CCU.

Acknowledgements

The research leading to these results has received funding from the Norway Grants 2014–2021 via the National Centre for Research and Development. This research has been prepared within the frame of the project: “Negative CO₂ emission gas power plant” – NOR/POLNORCCS/NEGATIVE-CO₂-PP/0009/2019-00 which is co-financed by the programme “Applied research” under the Norwegian Financial Mechanisms 2014–2021 POLNOR CCS 2019 – Development of CO₂ capture solutions integrated in power and industry processes.

The part of work is a result of a project realized by Maja Kaszuba and it was financed by Radium Learning Through Research Programs.

Received 4 April 2023

References

- [1] United States Environmental Protection Agency. <https://www.epa.gov/> (accessed 20 March 2022).
- [2] Our World in Data. <https://ourworldindata.org> (accessed 20 March 2022).
- [3] Chen W., van der Ham L., Nijmeijer A., Winnubst L.: *Membrane-integrated oxy-fuel combustion of coal: Process design and simulation*. J. Membrane Sci. **492**(2015), 461–470.
- [4] Merkel T., Lin H., Wei X., Baker R.: *Power plant post-combustion carbon dioxide capture: An opportunity for membranes*. J. Membrane Sci. **359**(2010), 126–139.
- [5] Blamey J., Anthony E.J., Wang J., Fennell P.S.: *The calcium looping cycle for large-scale CO₂ capture*. Prog. Energ. Combust. Sci. **36**(2010), 260–279.

- [6] Mikielwicz D., Wajs J., Ziółkowski P., Mikielwicz J.: *Utilisation of waste heat from the power plant by use of the ORC aided with bleed steam and extra source of heat.* Energy **97**(2016), 11–19.
- [7] Ziółkowski P., Mikielwicz D., Mikielwicz J.: *Increase of power and efficiency of the 900 MW supercritical power plant through incorporation of the ORC.* Arch. Thermodyn. **34**(2013), 4, 51–71.
- [8] Ye H., Zheng J., Li Y.: *Feasibility analysis and simulation of argon recovery in low oxygen-purity cryogenic air separation process with low energy consumption.* Cryogenics **97**(2019), 109–121.
- [9] Fu C., Gundersen T.: *Using exergy analysis to reduce power consumption in air separation units for oxy-combustion processes.* Energy **44**(2012), 1, 60–68.
- [10] Higginbotham P., White V., Fogash K., Guvelioglu G.: *Oxygen supply for oxycoal CO₂ capture.* Energy Proced. **4**(2011), 884–891.
- [11] García-Luna S., Ortiz C., Carro A., Chacartegui R., Pérez-Maqueda L.A.: *Oxygen production routes assessment for oxy-fuel combustion.* Energy **254**(2022), B, 124303.
- [12] Chorowski M., Gizicki W.: *Technical and economic aspects of oxygen separation for oxy-fuel purposes.* Arch. Thermodyn. **36**(2015), 1, 157–170.
- [13] Fu Q., Kansha Y., Song C., Liu Y., Ishizuka M., Tsustumi A.: *A cryogenic air separation process based on self-heat recuperation for oxy-combustion plants.* Appl. Energ. **162**(2015), 1114–1121.
- [14] Aneke M., Wang M.: *Potential for improving the energy efficiency of cryogenic air separation unit (ASU) using binary heat recovery cycles.* Appl. Therm. Eng. **81**(2015), 223–231.
- [15] Kerry F.: *Industrial Gas Handbook: Gas Separation and Purification.* Taylor and Francis, New York 2006.
- [16] Portillo E., Gallego Fernández L.M., Vega F., Alonso-Fariñas B., Navarrete B.: *Oxygen transport membrane unit applied to oxy-combustion coal power plants: A thermodynamic assessment.* J. Environ. Chem. Eng. **9**(2021), 4, 105266.
- [17] Castillo R.: *Thermodynamic analysis of a hard coal oxyfuel power plant with high temperature three-end membrane for air separation.* Appl. Energ. **88**(2011), 5, 1480–1493.
- [18] Gutiérrez F.A., García-Cuevas L.M., Sanz W.: *Comparison of cryogenic and membrane oxygen production implemented in the Graz cycle.* Energ. Convers. Manage. **271**(2022), 116325.
- [19] Fu C., Gundersen T.: *Recuperative vapor recompression heat pumps in cryogenic air separation processes.* Energy **59**(2013), 708–718.
- [20] Tesch S., Morosuk T., Tsatsaronis G.: *Comparative evaluation of cryogenic air separation units from the exergetic and economic points of view.* Low-temperature Technologies. IntechOpen, 2020. doi: [10.5772/intechopen.85765](https://doi.org/10.5772/intechopen.85765)
- [21] Yantovski E., Zvagolsky K.N., Gavrilenko V.A.: *The cooperate – demo power cycle.* Energ. Convers. Manage. **36**(1995), 6-9, 861–864.
- [22] Yantovski E.: *Zero emission fuel-fired power plants concept.* Energ. Convers. Manage. **37**(1996), 6-8, 867–877.

- [23] Sanz W., Hustad C.-W., Jericha H.: *First generation Graz cycle power plant for near-term development*. In: Proc.. ASME Turbo Expo 2011, 969–979.
- [24] Gou C., Cai R., Hong H.: *A novel hybrid oxy-fuel power cycle utilizing solar thermal energy*. Energy **32**(2007), 9, 1707–1714.
- [25] Ziółkowski P., Madejski P., Amiri M., Kuś T., Stasiak K., Subramanian N., Pawlak-Kruczek H., Badur J., Niedźwiedzki Ł., Mikielwicz D.: *Thermodynamic analysis of negative CO₂ emission power plant using Aspen Plus, Aspen Hysys, and Ebsilon software*. Energies **14**(2021), 19, 6304.
- [26] Ziółkowski P., Stasiak K., Amiri M., Mikielwicz D.: *Negative carbon dioxide gas power plant integrated with gasification of sewage sludge*. Energy **262**(2023), B, 125496.
- [27] Madejski P., Chmiel K., Subramanian N., Kuś T.: *Methods and techniques for CO₂ capture: Review of potential solutions and applications in modern energy technologies*. Energies **15**(2022), 3, 887.
- [28] Regulation of the Minister of Environment of 8 June 2016 on the technical conditions for the qualification of part of the energy recovered from thermal transformation of waste). J. Laws Republic of Poland (in Polish).
- [29] Badur J.: *Five Lectures in Modern Fluid Thermomechanics*. Wydawn. IMP PAN, Gdańsk 2005 (in Polish).
- [30] Kaszuba M., Ziółkowski P., Mikielwicz D.: *Thermodynamical analysis of integration of a negative emission power plant cycle with oxygen generation station*. In: Proc. 7th Conf. on Contemporary Problems of Thermal Engineering, CPOTE 2022. Silesian UT, Warszawa 2022, 619–630.
- [31] Ibrahim M., Skaugen G., Ertesvåg I.S.: *An extended corresponding states equation of state (EoS) for CCS industry*. Chem. Eng. Sci. **137**(2015), 572–582.
- [32] Ebsilon® Professional 15.00, Steag Energy Services GmbH, Flextek 2022.
- [33] Mikielwicz J., Bieliński H., Mikielwicz D.: *Outline of Thermodynamics* Wydawn. IMP PAN, Gdańsk 1996 (in Polish).
- [34] Peng D.-Y., Robinson D.: *A new two-constant equation of state*. Ind. Eng. Chem. Fundam. **15**(1976), 1, 59–64.
- [35] Jesionek K., Chrzczonowski A., Ziółkowski P., Badur J.: *Power enhancement of the Brayton cycle by steam utilization*. Arch. Thermodyn. **33**(2012), 3, 39–50.
- [36] Badur J., Stajnke M., Ziółkowski P., Józwick P., Bojar Z., Ziółkowski P.J.: *Mathematical modeling of hydrogen production performance in thermocatalytic reactor based on the intermetallic phase of Ni₃Al*. Arch. Thermodyn. **40**(2019), 3, 3–26.
- [37] Ziółkowski P.: *Porous structures in aspects of transpiring cooling of oxycombustion chamber walls*. In: AIP Conf. Proc. AIP **2077**(2019), 020065 .
- [38] Normann F., Andersson K., Leckner B., Johnsson F.: *Emission control of nitrogen oxides in the oxy-fuel process*. Prog. Energ. Combust. Sci. **35**(2009), 5, 385–397.
- [39] Ziółkowski P., Zakrzewski W., Kaczmarczyk O., Badur J.: *Thermodynamic analysis of the double Brayton cycle with the use of oxy combustion and capture of CO₂*. Arch. Thermodyn. **34**(2013), 2, 23–38.

- [40] Koohestanian E., Shahraki F.: *Review on principles, recent progress, and future challenges for oxy-fuel combustion CO₂ capture using compression and purification unit*. J. Environ. Chem. Eng. **9**(2021), 4, 105777.
- [41] Banaszkiewicz T., Chorowski M., Gizicki W.: *Comparative analysis of oxygen production for oxy-combustion application*. Energy Proced. **51**(2013), 127–134.
- [42] Darde A., Prabhakar R., Tranier J.-P., Perrin N.: *Air separation and fuel gas compression and purification units for oxy-coal combustion systems*. Energy Proced. **1**(2009), 527–534.
- [43] Janusz-Szymańska K., Dryjańska A.: *Possibilities for improving the thermodynamic and economic characteristics of an oxy-type power plant with a cryogenic air separation unit*. Energy **85**(2015), 45–61.
- [44] Tafone A., Dal Magro F., Romagnoli A.: *Integrating an oxygen enriched waste to energy plant with cryogenic engines and air separation unit: Technical, economic and environmental analysis*. Appl. Energ. **231**(2018), 423–432.
- [45] Goto K., Kazama S., Furukawa A., Serizawa M., Aramaki S., Shoji K.: *Effect of CO₂ purity on energy requirement of CO₂ capture process*. Energy Proced. **37**(2013), 806–812.
- [46] Murugan A., Brown R.J.C., Wilmot R., Hussain D., Bartlett S., Brewer P.J., Worton D.R., Bacquart T., Gardiner T., Robinson R.A., Finlayson A.: *Performing quality assurance of carbon dioxide for carbon capture and storage*. J. Carbon Res. **6**(2020), 4, 76.
- [47] Ertesvåg I.E., Madejski P., Ziółkowski P., Mikielewicz D.: *Exergy analysis of a negative CO₂ emission gas power plant based on water oxy-combustion of syngas from sewage sludge gasification and CCS*. Energy **278**(2023), 127690.
- [48] Kotowicz J., Job M.: *Thermodynamic and economic analysis of a gas turbine combined cycle plant with oxy-combustion*. Arch. Thermodyn. **34**(2013), 4, 215–233.
- [49] Serrano J.R., Arnau F.J., García-Cuevas L.M., Gutiérrez F.A.: *Coupling an oxygen generation cycle with an oxy-fuel combustion spark ignition engine for zero NO_x emissions and carbon capture: A feasibility study*. Energ. Convers. Manage. **284**(2023), 116973.
- [50] Wu Z., Yu X., Fu L., Deng J., Hu Z., Li L.: *A high efficiency oxyfuel internal combustion engine cycle with water direct injection for waste heat recovery*. Energy **70**(2014), 110–120.
- [51] Peng J., Li X.: *Oxyfuel combustion in IC engines. Internal Combustion Engines – Recent Advances*. IntechOpen, 2022. doi: [10.5772/intechopen.107155](https://doi.org/10.5772/intechopen.107155)
- [52] Kropiwnicki J.: *Analysis of start energy of Stirling engine type alpha*. Arch. Thermodyn. **40**(2019), 3, 243–259.

Thermodynamic analysis of hybrid ceramic bearings with metal inner rings

JIAN SUN^a
GUANGXIANG ZHANG^a
JUNXING TIAN^{a*}
YUSHENG ZHU^b

^a School of Mechanical Engineering, Shenyang Jianzhu University, Liaoning, 100084, China

^b Nanjing Metro Operation Co., Ltd., Nanjing 210000, China

Abstract For the sake of exploring the thermodynamic characteristics of hybrid ceramic bearings with metal inner rings in the application process, we established the mathematical model of bearings with metal inner rings based on the thermodynamics of bearings. The heat of the bearings, inner and outer raceway, and the deformation of bearings were calculated by the thermodynamic model. We used the bearing life testing machine to test the bearing load and speed. The consequences indicate that the temperature stability time of a hybrid ceramic bearing with the metal inner ring is about 6 hours after loading, and its temperature is about 1–2°C higher than that of a metal bearing. Under the condition of a certain speed, the stable temperature of bearing operation improves with the enlargement of the load. Under the condition of a certain load, the bearing temperature also improves with the enlargement of bearing speed. The overall temperature trend of the bearing outer ring is unanimous with the overall temperature value calculated by the model. The maximum error is between 2.2 and 2.4°C. The thermodynamic analysis of hybrid bearings with metal inner rings is conducive to a better study of the effect of bearing material characteristics on bearing performance.

Keywords: Hybrid ceramic bearing; Silicon nitride; Inner ring metal; Bearing temperature rise

*Corresponding Author. Email: tianjunxingge@163.com

Nomenclature

a	– bearing raceways contact along the half-shaft
c_n	– sliding coefficient of friction between the cage and the inner and outer rings
d_i, d_e	– bearing inner and outer ring groove diameter
D_m	– rolling element diameter
D_{pw}	– bearing pitch diameter
d_n	– bearing outer ring inner diameter
d_w	– bearing inner ring outer diameter
$E_{(\eta)}$	– second type elliptic integral of the raceway contact zone
F_n	– friction of bearing cages
f_0	– coefficient related to the bearing type and lubrication
f_1	– coefficient related to the bearing type and load
H_{bi}, H_{be}	– friction between the cage and the inner and outer ring generates heat
H_g	– frictional heat generation between the bearing rolling elements and the cage pocket bore
H_i, H_e	– heat generation in the inner and outer rings of the bearing
H_{si}, H_{se}	– heat generated in the contact zone between the inner and outer rings of the bearing
M	– frictional moment of the bearing
M_0	– frictional moment related to the bearing designation, the speed of the bearing and the lubrication medium
M_1	– load-related frictional moment
M_i, M_e	– frictional torque between the inner and outer rings of the bearing
M_s	– frictional moment generated by the spin motion of the bearing
M_{si}, M_{se}	– friction torque concerning raceway dimensions
n	– bearing speed
n_m	– rotation speed of the bearing rolling elements
P_1	– equivalent dynamic load of the bearing
Q	– normal contact load between bearing rolling elements and raceways
Q_g	– contact load between rolling elements and cages
W_c	– rolling element angular velocity
W_i, W_e	– bearing inner and outer ring angular velocity
z	– number of rolling bodies

Greek symbols

μ	– coefficient of friction between the bearing raceway and the rolling elements
μ_b	– coefficient of friction between the rolling elements and the cage
ν	– lubrication and dynamic viscosity

1 Introduction

As an important supporting component, the rolling bearing is an important part of the high-speed spindle element, and the high-speed spindle element is a critical part of the high-speed machine tool. Its performance has

an important impact on machining accuracy of high-speed machine tools. At present, engineering ceramic materials such as silicon carbide (SiC), zirconia (ZrO_2), and silicon nitride (Si_3N_4) have excellent properties such as corrosion resistance, abrasion resistance, high-temperature resistance, low-temperature resistance, high hardness, high strength, low density, low expansion coefficient and good self-lubrication [1, 2]. Silicon nitride (Si_3N_4) stands out among engineering ceramic materials due to its higher hardness, better wear resistance, and lower weight. It is considered to be the best alternative for bearing steel. Silicon nitride full ceramic ball bearings have the characteristics of high hardness, high wear resistance, lightweight, and high thermal steady state [3, 4]. Under the conditions of the same load and speed, the maximum contact area between the bearing rolling element and the inner and outer rings of steel bearings is larger than that between the bearing rolling elements and the inner and outer rings of hybrid bearings. So the contact stress is higher than that of steel bearings. And the density of silicon nitride material is smaller than that of bearing steels [5]. As the rotor system of the spindle unit is mainly metal, the assembly accuracy of full ceramic bearings is very high. Hybrid ceramic ball bearings with only ceramic balls as rolling elements cannot fully demonstrate their pressure resistance and self-lubricating characteristics. So this paper proposes a kind of hybrid ceramic ball bearing with the outer ring and ball as silicon nitride ceramic and the inner ring as metal. This type of bearing can reduce the mismatch between metal and ceramic materials and can fully utilize the performance of ceramics.

Friction between materials is a root cause of thermogenesis. The frictional thermogenesis between internal components of bearings under heavy load, high speed, and other working conditions is the main reason for the formation of a thermal field during bearing operation [6]. The formation of the thermal field directly affects the service performance and life of the bearing. Because the operation state of bearings is complex, the formation of the bearing thermal field is closely related to its operating state. The working temperature and its distribution are important aspects of bearing condition monitoring, which directly affects the service performance and life of the system.

At present, many experts and scholars have conducted an in-depth study on the performance of hybrid ceramic bearings. Ohta and Satake [7] experimentally studied the vibration characteristics of full ceramic bearings, mixed ceramic bearings, and full steel bearings respectively. They found that the factors affecting the vibration of full ceramic bearings, mixed

ceramic bearings, and steel bearings were almost identical, but the overall vibration level of mixed ceramic bearings was larger than that of full ceramic bearings and all-steel bearings. Wang *et al.* [8] built a comprehensive dynamic model of ball bearings with structural flexible deformation as the focus and deduced the ring flexibility caused by the assembly state change of the bearing housing system. They analyzed the interaction mechanism between the ring and other bearing components. Ma *et al.* [9] proposed the dynamic model of the bearing-rotor system and established the same motion differential equation as the bearing assembly. They obtained the real-time coupling and synchronization solutions for the bearing and rotor model. Fang *et al.* [10] improved the quasi-static model of ball bearings and proposed a general mathematical model of DR-ACBA in three different configurations. They compared and analyzed the influence of preload, velocity, and load on the variation of nonlinear stiffness of DR-ACBB under different configurations. Hao *et al.* [11] established a new thermal mesh model for the dynamic temperature of bearings, discussed the coupling effect between lubricant characteristics, heat generation, structural parameters, and temperature during bearing operation, and finally realized and discussed the effects of speed, load, oil temperature, and lubricant flow on the temperature rise. Zhang *et al.* [12] used the Hertz theory to establish the dynamic and thermal coupling model of ceramic bearing electric spindle, studied the influence of different temperatures, preload, and speed on bearing dynamic performance, and verified the accuracy of the dynamic and thermal coupling model through the electric spindle test platform. Tian *et al.* [13] established a bearing heating model based on silicon nitride material, measured the bearing temperature by a bearing life testing machine, verified the correctness of the model, and used the friction and wear testing machine to analyze the temperature change trend between rolling elements and raceways with different precision. Chen *et al.* [14] established a bearing lubrication and heat generation model under oil-air lubrication conditions based on the theory of high-speed rolling bearings and two-phase flow, and further studied the effects of oil supply, lubricating oil viscosity, load, and speed on bearing temperature rise.

Currently, there is relatively little research on hybrid bearings based on an inner ring of metal and an outer ring and balls of ceramic. To deeply study the thermodynamic characteristics of such bearings, it is planned to first establish a mathematical model based on the characteristics of metal and ceramic materials, predict the temperature rise of the bearing, and

then use the life testing machine to test the bearing, analyze the test results, finally establish a finite element simulation model suitable for ceramic bearings, and further analyze the test results in combination with the test.

2 Model building and test methods

For the sake of better understanding the thermodynamic characteristics of hybrid ceramic bearings during operation, a thermodynamic model of bearings was established based on the material characteristics of ceramic materials and metal inner rings. Bearing-related parameters are shown in Table 1.

Table 1: Material characteristics

Material parameter	Units	Si ₃ N ₄	GCr15
Density	g·cm ⁻³	3.2	7.85
Coefficient of thermal expansion	K ⁻¹	3.5 · 10 ⁻⁶	3 · 10 ⁻⁵
Modulus of elasticity	GPa	310	207
Poisson's ratio	—	0.26	0.30
Thermal conductivity	W·m ⁻¹ K ⁻¹	35	45

Friction torque due to lubricant viscosity when the bearing is unloaded is equal to

$$M_0 = \begin{cases} 160 \cdot 10^{-7} f_0 D_{pw}^3 & \text{for } \nu n < 2000, \\ 10^{-7} f_0 (\nu n)^{2/3} D_{pw}^3 & \text{for } \nu n \geq 2000, \end{cases} \quad (1)$$

where f_0 is the coefficient related to the bearing type and lubrication, ν is the dynamic viscosity of the lubricant, and n is the bearing speed. The load-dependent friction torque is

$$M_1 = f_1 P_1 D_{pw}, \quad (2)$$

where f_1 is the coefficient related to the bearing type and load, and P_1 refers to the bearing equivalent dynamic load. Therefore, the formula for the bearing friction torque is

$$M = M_0 + M_1. \quad (3)$$

During the operation process of angular contact ball bearings, the contact status between the rolling bodies and the inner and outer rings under the

action of centrifugal force is slightly different due to the high-speed rotation, resulting in different friction torque between the inner and outer rings [15]. Thus, according to the difference between bearing inner raceway diameter d_i and outer raceway diameter d_e , the total friction torque is divided. The friction torque of the inner ring is

$$M_i = 0.5 \frac{MD_m}{d_i} \quad (4)$$

and the friction torque of the outer ring is

$$M_e = 0.5 \frac{MD_m}{d_e}. \quad (5)$$

Because ceramic ball bearings are mostly used in high-speed rotation conditions, the spin sliding between the rolling body and the inner raceway of the bearing is one of the main movements during the working process of the bearing in addition to the inner ring rotation of the bearing and the rolling body rotation movement. The friction torque generated by spin sliding has a great effect on the total friction torque and should be considered when calculating thermogenesis. Therefore, the thermogenesis by spin sliding friction is added based on the above formula to make the empirical formula more accurate:

$$M_s = \frac{3\mu QaE_{(\eta)}}{8}, \quad (6)$$

where μ is the friction coefficient between the bearing raceway and the rolling body, and Q is the normal contact load between the bearing rolling body and the bearing raceway. The thermogenesis by the inner and outer rings and the contact area of the rolling body is related to the friction moment of the contact area and the rotation speed of the inner and outer rings and the rolling body. According to the diameter of the raceway, the spin friction moments M_s are divided into M_{se} and M_{si} related to the size of the raceway.

The thermogenesis by the inner ring is

$$H_i = 10^{-3}W_c M_i + 1.047 \cdot 10^{-4} M_{si} n_m z \quad (7)$$

and the thermogenesis by the outer ring is

$$H_e = 10^{-3}W_c M_e + 1.047 \cdot 10^{-4} M_{se} n_m z, \quad (8)$$

where z is the number of rolling bodies and W_c is the rolling element angular velocity.

Because the rolling body rotates around the centre of the bearing in the cage pocket, the angular speed of the cage is equal to the public angular speed of the rolling body. The friction thermogenesis between the rolling body and the cage pocket hole is

$$H_g = \mu_b Q_g W_c, \quad (9)$$

where μ_b is the friction coefficient between the rolling body and the cage, and Q_g is the contact load between the rolling body and the cage. Under high-speed rotation, the contact load Q_g between the rolling body and the cage is very small. So the friction thermogenesis between the rolling body and the cage can be ignored.

The movement of the cage is mainly guided by the friction between the cage and the rolling body or the inner and outer rings. When there is sliding friction between the cage and the outer ring, that is when the outer ring is guided, the thermogenesis by sliding friction between the cage and the outer ring is

$$H_{be} = 0.5d_n F_n [c_n (W_c - W_e)], \quad (10)$$

where d_n is the inner diameter of the bearing outer ring, F_n is the friction force, c_n is the sliding friction coefficient and W_e is the outer angular velocity. When there is sliding friction between the cage and the inner ring, that is when the inner ring is guided, the thermogenesis by sliding friction between the cage and the inner ring is

$$H_{bi} = 0.5d_w F_n [c_n (W_c - W_i)], \quad (11)$$

where d_w is the outer diameter of the inner ring and W_i is the inner angular velocity.

The total thermogenesis in the contact area of the inner and outer rings of the bearing is, respectively

$$\begin{aligned} H_{si} &= H_i + H_{bi}, \\ H_{se} &= H_e + H_{be}. \end{aligned} \quad (12)$$

3 Test methods

For the sake of studying the temperature variation characteristics of hybrid ceramic bearings during operation, we used the life testing machine for experimental research, as shown in Fig. 1. First of all, the test bearing

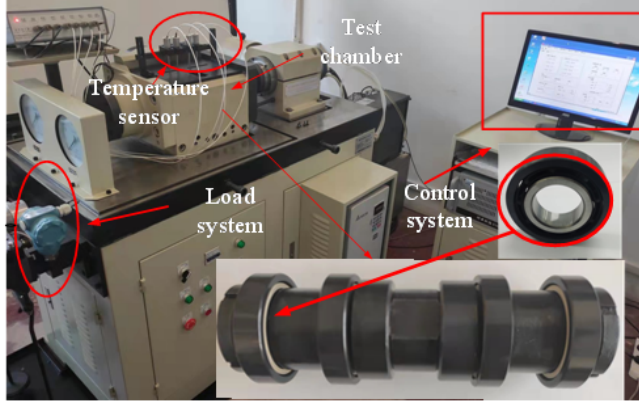


Figure 1: Life testing machine device diagram.

was soaked in the oil pollution cleaning agent to clean, to prevent pollutants from the bearing assembly process, affecting the operation state of the bearing. Then the test bearing was installed on the mandrel, and the mandrel was placed in the cavity of the bearing life testing machine. After the test bearing placement was completed, the bearing performance test was executed for the test parameters gathered in Table 2.

Table 2: Experimental parameters.

Working condition	Units	Value
Rotational speed	rpm	6000, 8000, 10000
Load	N	0, 500, 1000, 1500, 3000, 3500, 4000
Ambient temperature	°C	25
Lubrication	—	oil bath lubrication

As these hybrid ceramic bearings have the same inner ring as metal bearings, the outer ring, and balls are made of different materials, the thermal deformation of the shaft and the inner ring of the bearings are larger compared to the outer ring and balls when these bearings are used in conjunction with metal shafts. And the volume of change between the ball and the outer ring is relatively small. The thermal deformation of the shaft and bearing inner ring can be compensated by bearing clearance. However, the change of bearing clearance has a certain effect on the temperature rise of the bearing [16–20]. For the sake of studying the form of temperature change of hybrid ceramic bearing, the temperature rise of hybrid ceramic

bearing and metal bearing was compared, as shown in Fig. 2. Under the same operation condition, the initial temperature of the bearing is the same, but with the increase of operation time, the temperature of the bearing also rises. The temperature rise of metal bearings is lower than that of ceramic bearings. This is due to the relatively large thermal variables of the bearing inner ring and the shaft, while the thermal deformation of the ceramic ball and the ceramic outer ring is relatively small. Then the bearing heat dissipation space becomes smaller, and eventually, the temperature rises. In the process of operation of the bearing, its operation time is 6 hours, and the temperature of the bearing tends to be stable.

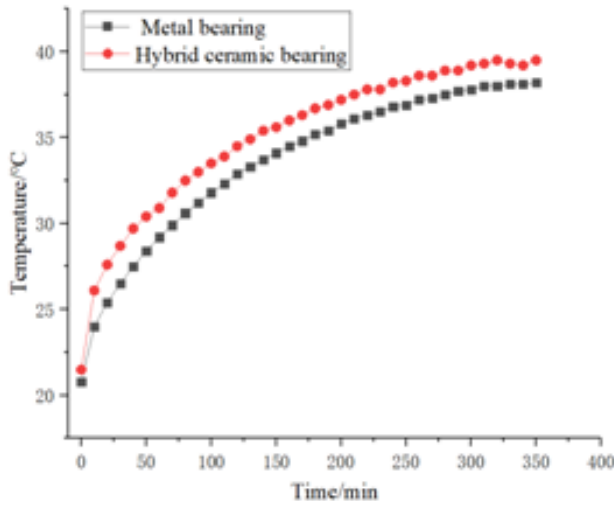


Figure 2: Test temperature of metal bearing and mixed ceramic bearing.

For the sake of studying the influence of load on the temperature of hybrid bearings, the speed of the life testing machine was set at 6000 rpm, and then the load as in Table 2 was applied. For the sake of obtaining the stable temperature of the bearings under each operation condition, each group of tests was operated for 8 h. The test consequences are indicated in Fig. 3. The consequences indicate that under the condition of a certain rotational speed, during stable operation of the bearing, its temperature increases with the increasing load. However, the heating process of the bearing is not obvious due to the influence of loading time and frequency. At bearing loads of 1500–4000 N, the stabilized temperature of the bearing during operation does not change much as the operating time increases. However, the

warming process of the bearing during operation is quite different. Under the condition that the bearing load is 4000 N, the operation temperature of the bearing rises relatively fast, and the highest temperature reaches 40°C. When the bearing is in no-load operation, the stable temperature of the bearing is about 37°C.

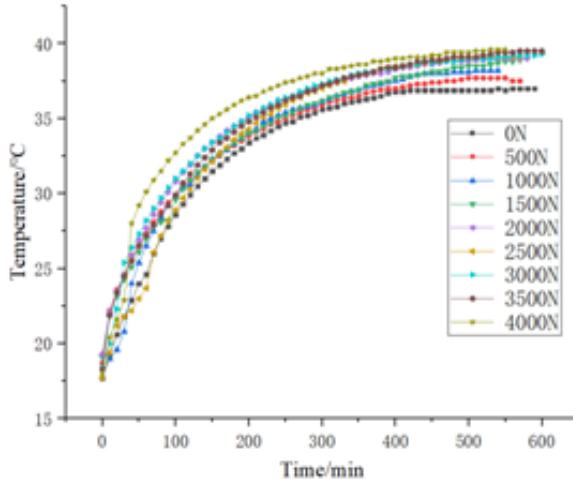


Figure 3: Influence of bearing load on temperature change.

To study the effect of the speed on the temperature of the hybrid bearing, the load of the life testing machine was assumed 1000 N, and the rotational speed was applied as in Table 2. The test consequences are indicated in Fig. 4. The consequences indicate that under a certain load, the temperature of the bearing increases with the rise of the bearing rotational speed. When the bearing speed is 10000 rpm, the highest temperature of the bearing reaches 45°C. When the bearing speed is 6000 rpm and 8000 rpm, the temperature changes are relatively smooth. This is because the friction frequency between the bearing ball and the inner and outer rings increases during the high-speed operation of the bearing, which makes the bearing temperature rise faster. However, after the bearing temperature reaches a stable value, it tends to be stable, and the temperature no longer rises, reaching a state of thermal equilibrium. The higher the rotational speed, the faster it takes to reach thermal equilibrium.

Since it is difficult to realize the test of bearing operation under high speed and heavy load conditions, the temperature change of bearing was

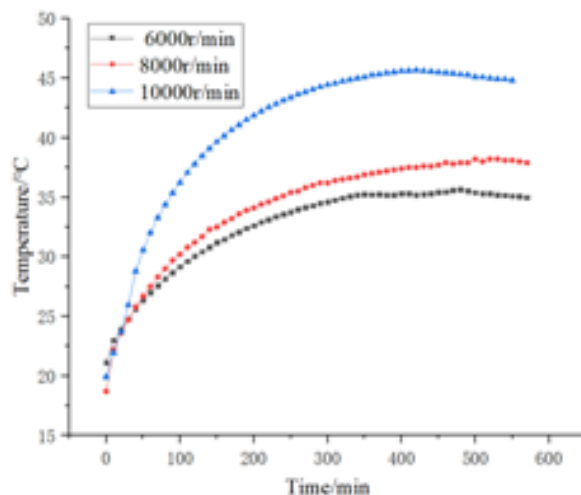


Figure 4: Influence of bearing speed on bearing temperature.

modelled, analyzed, and calculated. For the sake of verifying the accuracy of the model, we selected the rotational speed of 8000 rpm, and the load parameter as 0 N, 500 N, 1000 N, 1500 N, 2000 N, and 2500 N, and compared the obtained results with the experimental data. As can be seen from Fig. 5, the overall temperature trend of the bearing outer ring is consistent with the overall temperature value calculated by the model. The calculated

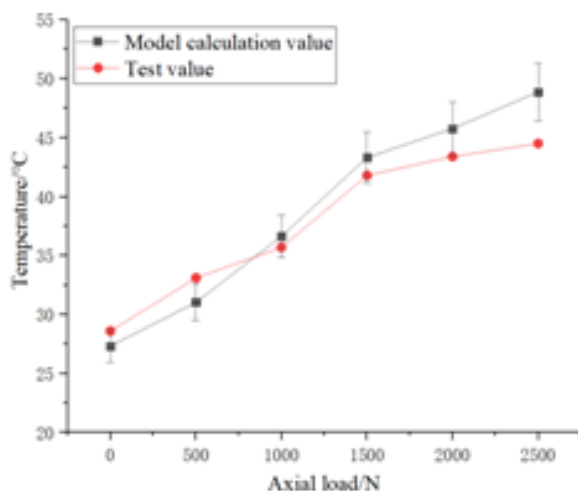


Figure 5: Analysis of test consequences and model consequences.

temperature of the bearing model and the test temperature are similar under the conditions of load 0 N, 500 N, 1000 N, and 1500 N. The error value is between 1.3 and 2°C, while the error for 2000 N and 2500 N is between 2.2 and 2.4°C. The error increases as the load increases, which is because the model has some error in calculating the amount of heat transfer in the calculation process.

The ball of the bearing, the inner raceway of the bearing, and the outer raceway of the bearing are difficult to measure during operation. The heat released in the bearing is generated under the action of torque between the ball and the inner and outer rings. To better understand the change of the temperature of the inner and outer ring of the hybrid bearing, based on the simulation model, the simulation analysis of the temperature change of the bearing under the condition of speed 8000 rpm and load 0–2500 N is made. The bearing simulation setup is shown in Fig. 6. The simulation procedure consists of the following steps:

- 1) set the material properties of each part and define the bearing assembly;
- 2) set the analysis step, power-display analysis, and turn on geometric nonlinearity;
- 3) divide the grid, using the C3D8R grid type;
- 4) set interaction, the ball is in face-to-face contact with the inner and outer ring and cage setting, the inner ring and the inner surface of the cage are coupled to the bearing centre, and the reference points RP1 and RP2 are set respectively;

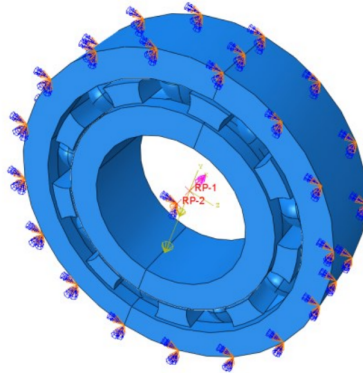


Figure 6: The bearing simulation setup.

- 5) apply load and boundary conditions, apply gravity as a whole, and apply force to the inner ring reference point RP1. The outer ring is fully fixed and angular velocity is applied to RP1 and RP2;
- 6) submit the job and run the analysis.

The simulation results are shown in Fig. 7. The temperature of the bearing ball and the inner and outer raceway increases with the increase of load. Using ABAQUS finite element analysis software, it was found that the highest temperature occurred in the position where the sphere is in contact with the channel – 65.61°C , as shown in Fig. 8. The high-temperature region of the inner and outer rings of the bearing is mainly concentrated in the raceway area. The temperature of the inner raceway is the same as that of the ball, but with the increase in load, the temperature difference between the ball and the inner raceway becomes larger, which is because of collection of heat from the inner raceway and the outer raceway. The heat generated by the ball is higher under the condition of large load. The temperature of the inner raceway of the bearing is higher than that of the outer raceway, and the maximum difference is 5°C . The overall simulation analysis of the bearing is shown in the figure, and the highest temperature point in the figure is at the position of the ball.

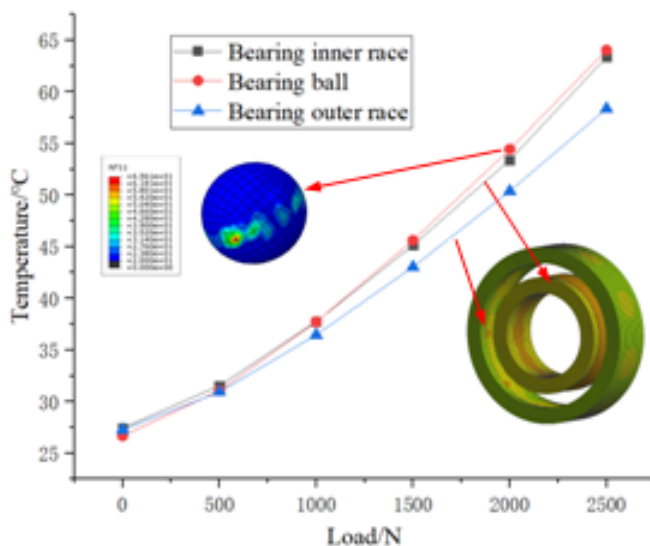


Figure 7: Analysis of temperature of bearing inner and outer rings and spheres.

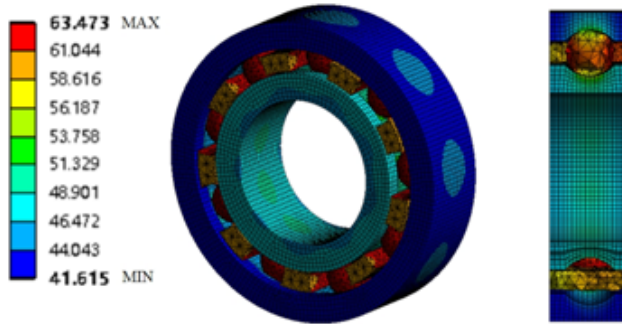


Figure 8: A Simulation analysis of the overall bearing temperature change.

4 Conclusion

The thermogenesis model of a hybrid bearing with the metal inner ring was established based on bearing thermodynamics, and the heat change of the bearing rolling body and the inner ring was analyzed. For the sake of studying the influence of bearing load and speed change on bearing thermogenesis, a bearing life testing machine was used to analyze and confirm the correctness of the simulation model.

1. Due to the relatively large thermal deformation of the inner ring and shaft of the bearing, the ceramic ball and ceramic outer ring have a relatively small thermal deformation. The clearance of the hybrid bearing becomes smaller, and then the heat dissipation space of the bearing becomes smaller, and finally, the temperature rises. Therefore, the temperature rise of hybrid bearings is relatively higher than that of metal bearings. After operation for 6 hours, the temperature of a hybrid ceramic bearing with a metal inner ring tends to be stable.
2. The stable operating temperature of the bearing increases with the rise of load. Under the condition of bearing load 4000 N, the operation temperature of the bearing rises relatively fast, and the highest temperature of the bearing reaches 40°C. When the bearing is in no-load operation, the stable temperature of the bearing is about 37°C.
3. Under the condition of a certain load, the temperature of the bearing rises with the rise of the bearing speed. When the bearing speed is 10000 rpm, the highest temperature of the bearing reaches 45°C. When the rotating speed is 6000 rpm and 8000 rpm, the temperature change is relatively smooth.

4. The temperature of the bearing ball is mainly focused on the contact position between the ball and the raceway, and the highest temperature is 65.61°C. The highest temperature of the inner and outer rings of the bearing is mainly on the raceway, and the temperature of the inner and outer raceway is the same as the temperature of the ball. However, with the rise of the load, the difference between the temperature of the ball and the inner raceway becomes larger. The temperature of the inner raceway of the bearing is higher than that of the outer raceway, and the maximum difference is 5°C.

Acknowledgments

The authors acknowledge the collective support granted by the National Natural Science Foundation of China (Grant No. 52105196), the Education Department of Liaoning Province (Grant No. LJKMZ20220936), Young and Middle-aged Innovation Team of Shenyang (Grant No. RC210343).

Received 15 March 2023

References

- [1] Li S., Wei C., Wang Y.: *Fabrication and service of all-ceramic ball bearings for extreme conditions applications*. IOP Conf. Ser. Mat. Sci. Eng. **1009**(2021), 1, 012032. doi: [10.1088/1757-899X/1009/1/012032](https://doi.org/10.1088/1757-899X/1009/1/012032)
- [2] Xia Z., Wu Y., Wei H., Ren K., Gao L., Sun J., Li S.: *Experimental research on the influence of working conditions on vibration and temperature rise of Si₃N₄ full-ceramic bearing motors*. Shock Vib. **2021**(2021), 1–16. doi: [10.1155/2021/1176566](https://doi.org/10.1155/2021/1176566)
- [3] Guo J., Wu Y., Zhang X., Zhang Y., Wang H., Bai X., Lu, H.: *Research on the influence of thermal expansion of steel shaft on dynamic characteristics of full ceramic bearing-rotor system*. Adv. Mech. Eng. **14**(2022), 7, 1–14. doi: [10.1177/16878132221109349](https://doi.org/10.1177/16878132221109349)
- [4] Yan H., Wu Y., Li S., Zhang L., Zhang, K.: *The effect of factors on the radiation noise of high-speed full ceramic angular contact ball bearings*. Shock Vib. **2018**(2018), 1–9. doi: [10.1155/2018/1645878](https://doi.org/10.1155/2018/1645878)
- [5] Han X., Xu C., Jin H., Xie W., Meng S.: *An experimental study of ultra-high temperature ceramics under tension subject to an environment with elevated temperature, mechanical stress and oxygen*. Sci. China Technol. Sc. **62**(2019), 1349–1356. doi: [10.1007/s11431-018-9501-1](https://doi.org/10.1007/s11431-018-9501-1)
- [6] Wang Y., Cao J., Tong Q., An G., Liu R., Zhang Y., Yan H.: *Study on the thermal performance and temperature distribution of ball bearings in the traction motor of a high-speed EMU*. Appl. Sci. **10**(2020), 12, 4373. doi: [10.3390/app10124373](https://doi.org/10.3390/app10124373)

- [7] Wang Y.Z., Liu H.B., Meng Y.G.: *Thermal field characteristics of lubrication under high-speed cylindrical roller bearing rings*. *Aerosp. Power* 36(2022), 5 (in Chinese). doi: [10.13224/j.cnki.jasp.20210583](https://doi.org/10.13224/j.cnki.jasp.20210583)
- [8] Wang M., Yan K., Tang Q., Guo J., Zhu Y., Hong J.: *Dynamic modeling and properties analysis for ball bearing driven by structure flexible deformations*. *Tribol. Int.* 179(2023), 108163. doi: [10.1016/j.triboint.2022.108163](https://doi.org/10.1016/j.triboint.2022.108163)
- [9] Ma S., Yin Y., Chao B., Yan K., Fang B., Hong J.: *A Real-time Coupling Model of Bearing-Rotor System Based on Semi-flexible Body Element*. *Int. J. Mech. Sci.* 245(2023), 108098. doi: [10.1016/j.ijmecsci.2022.108098](https://doi.org/10.1016/j.ijmecsci.2022.108098)
- [10] Fang B., Zhang J., Hong J., Yan K.: *Research on the nonlinear stiffness characteristics of double-row angular contact ball bearings under different working conditions*. *Lubricants*. 11(2023), 2, 44. doi: [10.3390/lubricants11020044](https://doi.org/10.3390/lubricants11020044)
- [11] Hao X., Yun X., Han Q.: *Thermal-fluid-solid coupling in thermal characteristics analysis of rolling bearing system under oil lubrication*. *Tribol.* 142(2020), 3, 031201. doi: [10.1115/1.4045377](https://doi.org/10.1115/1.4045377)
- [12] Zhang K., Wang Z., Bai X., Shi H., Wang Q.: *Effect of preload on the dynamic characteristics of ceramic bearings based on a dynamic thermal coupling model*. *Adv. Mech. Eng.* 12(2020), 1, 1687814020903851. doi: [10.1177/1687814020903851](https://doi.org/10.1177/1687814020903851)
- [13] Tian J., Wu Y., Sun J., Xia Z., Ren K., Wang H., Yao J.: *Thermal dynamic exploration of full-ceramic ball bearings under the self-lubrication condition*. *Lubricants* 10(2022), 9, 213. doi: [10.3390/lubricants10090213](https://doi.org/10.3390/lubricants10090213)
- [14] Chen C.Y., Li J.S., Yu Y.J., Xue Y.J.: *Study on temperature rise characteristics of oil-air lubrication of high-speed angular contact ball bearings*. *Mach. Des. Manu.* (2021), 9, 216–221+227 (in Chinese). doi: [10.19356/j.cnki.1001-3997.2021.09.049](https://doi.org/10.19356/j.cnki.1001-3997.2021.09.049)
- [15] Wu Y., Ren K., Xia Z., Sun J., Tian J., Li S.: *Heat generation analysis of full-ceramic angular contact ball bearings under the condition of non-lubrication*. *Mod. Mach. Tool Autom. Manufact. Techniq.* (2022), 7, 148–151 (in Chinese). doi: [10.13462/j.cnki.mmtamt.2022.07.035](https://doi.org/10.13462/j.cnki.mmtamt.2022.07.035)
- [16] Xia Z., Wu Y., Ma T., Bao Z., Tian J., Gao L., Li S.: *Experimental study on adaptability of full ceramic ball bearings under extreme conditions of cryogenics and heavy loads*. *Tribol. Int.* 175(2022), 107849. doi: [10.1016/j.triboint.2022.107849](https://doi.org/10.1016/j.triboint.2022.107849)
- [17] Wang J., Xu M., Zhang C., Huang B., Gu F.: *Online bearing clearance monitoring based on an accurate vibration analysis*. *Energies* 13(2020), 2, 389. doi: [10.3390/en13020389](https://doi.org/10.3390/en13020389)
- [18] Shi H., Li Y., Bai X., Wang Z., Zou D., Bao Z., Wang Z.: *Investigation of the orbit-spinning behaviors of the outer ring in a full ceramic ball bearing-steel pedestal system in wide temperature ranges*. *Mech. Syst. Signal Process.* 149(2021), 107317. doi: [10.1016/j.ymssp.2020.107317](https://doi.org/10.1016/j.ymssp.2020.107317)
- [19] Smolík L., Hajžman M., Byrtus M.: *Investigation of bearing clearance effects in dynamics of turbochargers*. *Int. J. Mech. Sci.* 127(2017), 62–72. doi: [10.1016/j.ijmecsci.2016.07.013](https://doi.org/10.1016/j.ijmecsci.2016.07.013)
- [20] Gu Y.K., Li W.F., Zhang J., Qiu G.Q.: *Effects of wear, backlash, and bearing clearance on dynamic characteristics of a spur gear system*. *IEEE Access* 7(2019), 117639–117651. doi: [10.1109/ACCESS.2019.2936496](https://doi.org/10.1109/ACCESS.2019.2936496)

Mixed convection heat transfer in trapezoidal lid-driven cavity with uniformly heated inner circular cylinder

ASMAA ALI HUSSEIN*

Middle Technical University, Institute of Technology/Baghdad,
Baghdad, Iraq

Abstract The present work comprises a numerical analysis using the Ansys program to solve the problem of combined free-forced convection around a circular cylinder located in a horizontal lid-driven trapezoidal enclosure. The enclosure is filled with water. The upper moving wall and lower fixed wall are cold at a constant temperature, whereas the inclined walls are adiabatically insulated. The uniformly heated cylinder is located at different positions in the cavity. The study covers three values of Richardson number (0.01, 1, and 10). The results show that the streamlines and isotherms in the enclosure, the Nusselt number and friction factor in the moving wall, hot wall and bottom wall are strongly dependent on the position of the inner hot cylinder. The results are validated with previous work, and the comparison gives good agreement.

Keywords: Cavity; Heat transfer; Mixed convection; Lid-driven

Nomenclature

Bn	–	Bingham number
C_f	–	friction coefficient
Da	–	Darcy number
g	–	gravitational acceleration
Gr	–	Grashof number
H	–	hieght of cavity
Ha	–	Hartmann number
L	–	side length of cavity
Le	–	Lewis number

*Corresponding Author. Email: asmaa31930@yahoo.com

p	–	pressure
Nu	–	Nusselt number
n	–	coordinate normal to wall
Pr	–	Prandtl number
Re	–	Reynold number
Ri	–	Richardson number
T	–	temperature
T_r	–	freezing point of the base fluid, = 273.15 K
T_0	–	reference temperature, = 310 K
U, V	–	dimensionless velocity in x - and y -direction
u, v	–	velocities in x - and y -direction
u_1	–	velocity of moving wall
x, y	–	Cartesian coordinates

Greek symbols

α	–	thermal diffusivity
β	–	thermal expansion coefficient
γ	–	inclination angle
θ	–	dimensionless temperature
κ	–	thermal conductivity
κ_f, κ_s	–	thermal conductivity for base fluid and nanoparticles
μ	–	dynamic viscosity
ϑ	–	kinematic viscosity
ρ	–	density
φ	–	nanoparticles volume fraction

Subscripts

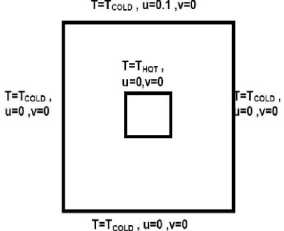
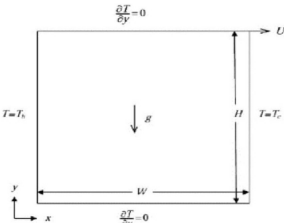

c	–	cold
h	–	hot

1 Introduction

Fluid behaviour and thermal field in lid-driven trapezoidal cavities is a topic of great importance to many researchers due to its significance in practical engineering applications. These applications include solar energy, power stations, heat exchanger devices, nuclear reactors, the technology of lubrication, combustion of atomized liquid fuels and cooling of electronic equipment [1, 2]. The forced convection process is achieved when the fluid motion is caused by using external devices such as a compressor, fan, etc. This process may be occurred by using rotating cylinder in cavity or movement of wall in the cavity (lid-driven cavity). It is characterized by the Reynolds number (Re). The heating of the system causes thermal patterns between the hot wall and the cold fluid and leads to reducing the fluid

density. As a result, the light fluid particles rise upwards while the heavy particles descend downward. The motion of fluid resulting from density changes in the fluid is called free convection. This process is characterized by the Rayleigh number (Ra) or Grashof number (Gr). The Richardson number (Ri) is the ratio between Gr and Re^2 . The value of the Richardson number determines if the process is dominated by forced convection, natural convection, or mixed convection. The mixed convection heat transfer in a lid-driven cavity with different geometries and thermal boundary conditions was studied by many authors [1–24]. The cavity with lid-driven is considered in different shapes, such as square [1–8], trapezoidal (or triangle) [9–13], rectangle [14–18], and other geometries [19–24] with various thermal and hydrodynamic boundary conditions. Tables 1–4 present a summary of these works.

Table 1: Previous works which included square lid-driven cavity.

Geometry	Conditions	Conclusions	Reference
	Air $10^2 \leq Re \leq 10^3$ $Ri = 0.01-10$	Richardson number plays an important role in fashioning of vorticity	Rosdzimin <i>et al.</i> (2010), [1]
	$H_2O-Al_2O_3$, CuO, Cu nanofluids $\varphi = 0-0.05$ $Re = 1, 10, 100$ $Ra = 10^4$	Increasing Re causes reduction of the nanoparticles concentration	Nemati <i>et al.</i> (2010), [2]
	$H_2O-Al_2O_3$ nanofluid $\varphi = 0-0.06$ $Gr = 10^4$ $Ri = 0.01-100$	The heat transfer enhances as volume fraction of nanoparticles increases	Sheikhzadeh <i>et al.</i> (2012), [3]

Continued on next page

Table 1. *Continued from previous page.*

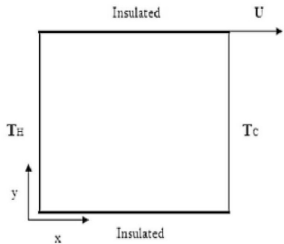
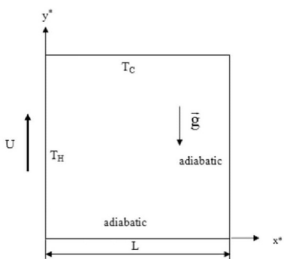
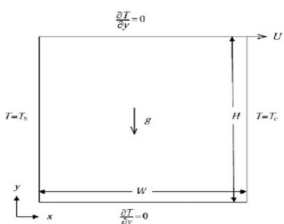
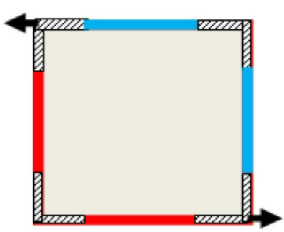
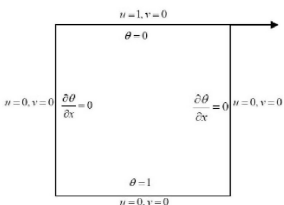
Geometry	Conditions	Conclusions	Reference
	Air $Ri = 1$ $10^{-5} \leq Da \leq 10^{-1}$	The thermal patterns and fluid field depend on the direction of moving walls with nonuniform heating	Chattopadhyay <i>et al.</i> (2014), [4]
	Al_2O_3 + ethylene glycol- H_2O nanofluid $\varphi = 0-0.08$ $Ri = 0.1-10$ $Gr = 10^4$	The thermal patterns and fluid field depend on φ	Ögüt and Kahveci (2016), [5]
	$Cu-H_2O$ nanofluid $\varphi = 0-0.05$ $Ri = 0.01-100$	The maximum heat transfer rate is produced with presence of the shear-driven and the buoyancy forces	Mastiani <i>et al.</i> (2017), [6]
	$Cu-H_2O$ nanofluid $\varphi = 0.05$ $10^3 \leq Gr \leq 10^6$ $1 \leq Re \leq 100$ $10^{-5} \leq Da \leq 10^{-2}$	The heat transfer enhances with decrease in Da	Haque Munshi <i>et al.</i> (2019), [7]
	$Gr = 10^3, 10^5$ $Re = 10-10^3$ $Al_2O_3-H_2O$ nanofluids $\varphi = 0-0.05$	The heat transfer enhances with increase in Re	Çakmak <i>et al.</i> (2020), [8]

Table 2: Previous works which included trapezoidal lid-driven cavities.

Geometry	Conditions	Conclusions	Reference
	$Pr = 0.015, 0.7, 10$ $Re = 1-100$ $Gr = 10^3-10^5$	The bottom wall produces multiple steady states in either natural or mixed convection	Bhattacharya <i>et al.</i> (2013), [9]
	$0.026 \leq Pr \leq 1000$ $10^3 \leq Ra \leq 10^6$ $Ha = 50-1000$	There is no effect of the moving lid for $Ra \geq 10^5$	Mehmod and Tabish (2016), [10]
	$Le = 0.1-50$ $0.1 \leq Ri \leq 100$	Uniform heat flux concentrated of the fixed horizontal wall has given high mass transfer	Uddin <i>et al.</i> (2016), [11]
	$H_2O-Cu, Ag, Al_2O_3, TiO_2$ $0 \leq \varphi \leq 0.02$ $0.04 \leq Ri \leq 100$ $0 \leq Ha \leq 50$	Ha and heat source location produced significant influence on Nusselt number	Ahmed <i>et al.</i> (2018), [12]
	$Pr = 0.7, 1000$ $10^3 \leq Ra \leq 10^5$ $\gamma = 45^\circ-90^\circ$	The results produced minimum entropy and maximum efficiency of any system	Monda and Mahapatra (2020), [13]

Table 3: Previous works which included rectangular lid-driven cavity.

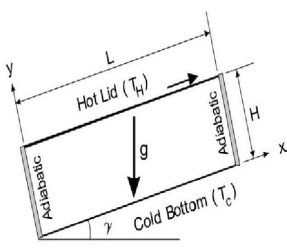
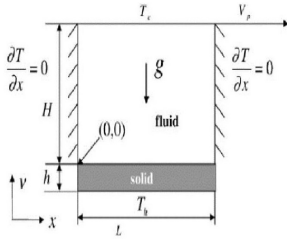
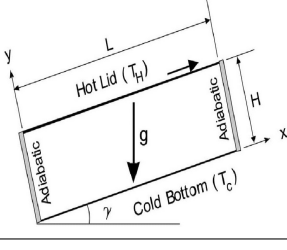
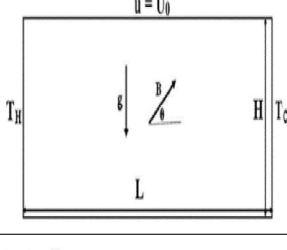
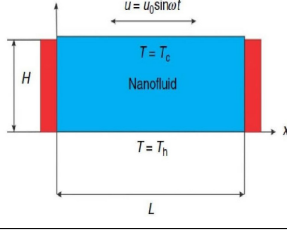
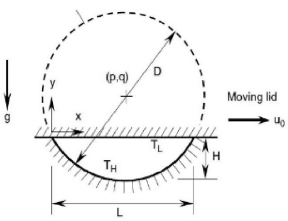
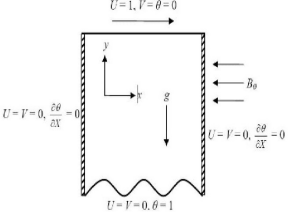
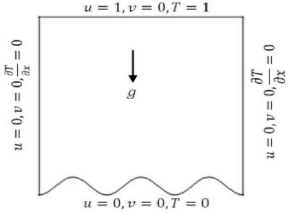
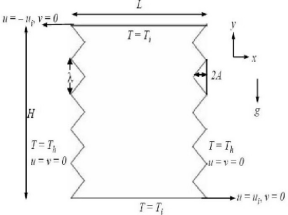
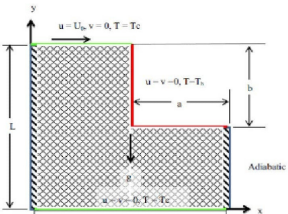
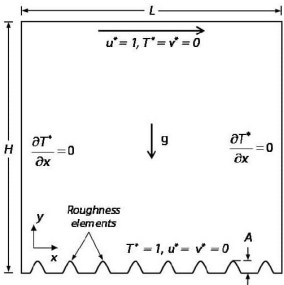
Geometry	Conditions	Conclusions	Reference
	Water $Ra = 10^5 - 10^7$ $Re = 408.21$ $\gamma = 0^\circ - 30^\circ$	The heating process increases as the tilt angle is moved from vertical to horizontal situation	Sharif (2007), [14]
	$0.1 \leq Ri \leq 10$ $0.1 \leq h/H \leq 0.5$ $0.01 \leq \kappa_f/\kappa_s \leq 10$	Nu decrease with increasing the wall thickness ratio	Oztop <i>et al.</i> (2008), [15]
	H_2O-Cu $\gamma = 0^\circ - 30^\circ$ $Ri = 0.1 - 10$ $\varphi = 0.05 - 0.08$	Nu increases strongly as tilt angle is increased for $Ri = 10$	Salahi <i>et al.</i> (2015), [16]
	$Pr = 1$ $Re = 100 - 1000$ $Gr = 10^4$ $Ha = 0 - 5$ $Bn = 1 - 10$	Nu increases with increasing Ha, and with decreasing Bn	Kefayati and Tang (2018), [17]
	Cu-H ₂ O nanofluid $Gr = 10^4$ $Ri = 0.1 - 10$	The heat transfer increases using Al ₂ O ₃ -H ₂ O nanofluid with increase in for a constant Darcy number	Ardalan <i>et al.</i> (2021), [18]

Table 4: Previous works which included other geometries of lid-driven cavities.

Geometry	Conditions	Conclusions	Reference
	$Pr = 0.71$ (air) $Gr = 0-10^6$ $Re = 0-500$	The influence of inertia force is pronounced for $Gr \leq 10^5$	Chin-Lung and Chin-Hsiang (2004), [19]
	$Pr = 0.71$ $Re = 300$ $Ra = 10^5$ $0 \leq Ha \leq 50$	The average Nu increases with increase in the number of waves and decrease in Ha	Parvin and Nasrin (2010), [20]
	$Pr = 0.71$ $Re = 10^2-5 \cdot 10^3$ $Gr = 10^3-10^6$	The parameters (Re and Gr) affect significantly on the fluid field and thermal patterns	Kumar <i>et al.</i> (2013), [21]
	CuO-H ₂ O nanofluid $Pr = 10, 1.47$ $Ri = 0.1, 1, 10$ $\varphi = 0.04-0.2$	Ri and volume fraction have significant effects on the behavior of heat transfer and fluid flow inside the triangular cavity	Nasrin <i>et al.</i> (2014), [22]
	$Pr = 0.71$ porous media $Re = 1-100$ $Gr = 10^3-10^5$ $Da = 10^{-5}-10^{-3}$	The heat transfer rate in the vertical wall is higher than that in the horizontal wall at a low Gr, higher Da and higher Re	Mojumder <i>et al.</i> (2016), [23]

Continued on next page

Table 4. *Continued from previous page.*

Geometry	Conditions	Conclusions	Reference
	$Pr = 0.7$ $0.01 \leq \varphi \leq 0.08$ $Ra = 10^3 - 10^5$ $Re = 10, 2000$	Significant effects of number and amplitude of roughness elements on the thermal and fluid patterns	Guo <i>et al.</i> (2016), [24]

The motivation of the present simulation is to enhance the heat transfer process inside the trapezoidal cavity because of its importance in mechanical engineering applications. To obtain this goal, the influence of different parameters that affect the heat transfer process should be studied. One of these important parameters is the position of an inner hot cylinder inside the trapezoidal lid-driven cavity for the same condition. Additionally, the influence of the Richardson number on the thermal pattern and fluid velocity requires further study. The working fluid is water. The parallel walls are cooled and the inclined walls are adiabatically insulated. The upper wall only moves as lid-driven at a constant speed, while the other three walls are stationary. The novelty of this work is studying the mixed convection heat transfer inside the cavity at different hot source positions. This work requires advanced computers and more patience with the run time of the program. The simulation was achieved using the Ansys commercial program (ANSYS Fluent 2021 R2).

2 Theoretical analysis

The physical domain for a trapezoidal enclosure with the movement of the top wall at velocity U is shown in Fig. 1. The heating source consists of a circular cylinder located at different positions inside the cavity. The circular hot cylinder is kept constant and the inclined walls are adiabatically insulated. The working fluid is water with $Pr = 6.2$. The combined effect of buoyancy forces due to the temperature difference throughout the fluid and the forced convection effect due to the motion of the top wall of a trapezoidal

cavity is numerically modelled. Table 5 represents the hydrodynamic and thermal boundary conditions for the problem.

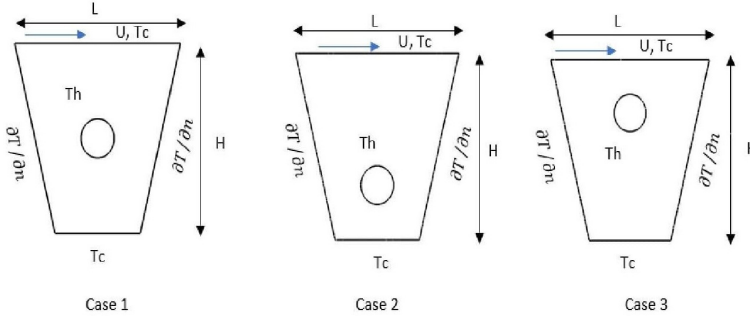


Figure 1: Schematic of physical domain.

Table 5: Boundary conditions for the present study.

Position of wall	U	V	θ
Bottom wall	0	0	0
Top wall	1	0	0
Left and right walls	0	0	$\partial\theta/\partial X = 0$
Circular cylinder wall	0	0	1

2.1 Governing equations

The two-dimensional laminar mixed convection heat transfer in the lid-driven trapezoidal cavity containing concentric and eccentric circular cylinders is represented by governing equations. The water properties are assumed constant except for the density which varies in the buoyancy term according to the Boussinesq approximation. The governing equations include continuity, momentum in x - and y -direction, and energy equations [14]:

$$\frac{\partial u}{\partial x} + \frac{\partial v}{\partial y} = 0, \quad (1)$$

$$u \frac{\partial u}{\partial x} + v \frac{\partial u}{\partial y} = -\frac{1}{\rho} \frac{\partial p}{\partial x} + \vartheta \left(\frac{\partial^2 u}{\partial x^2} + \frac{\partial^2 u}{\partial y^2} \right), \quad (2)$$

$$u \frac{\partial v}{\partial x} + v \frac{\partial v}{\partial y} = -\frac{1}{\rho} \frac{\partial p}{\partial y} + \vartheta \left(\frac{\partial^2 v}{\partial x^2} + \frac{\partial^2 v}{\partial y^2} \right) + g\beta(T - T_c), \quad (3)$$

$$u \frac{\partial T}{\partial x} + v \frac{\partial T}{\partial y} = \alpha \left(\frac{\partial^2 T}{\partial x^2} + \frac{\partial^2 T}{\partial y^2} \right). \quad (4)$$

These equations can be normalized by defining the dimensionless variables as follows:

$$X = \frac{x}{L}, \quad Y = \frac{y}{L}, \quad U = \frac{u}{u_1}, \quad V = \frac{v}{u_1}, \quad \theta = \frac{T - T_c}{T_h - T_c}, \quad \text{Re} = \frac{u_1 H}{\vartheta},$$

$$\text{Gr} = \frac{g\beta(T_h - T_c)H^3}{\vartheta^2}, \quad P = \frac{pL^2}{\rho\alpha^2}, \quad \text{Pr} = \frac{\vartheta}{\alpha}, \quad \text{Ri} = \frac{\text{Gr}}{\text{Re}^2}.$$

So, Eqs. (1)–(4) can be written in dimensionless form as shown below:

$$\frac{\partial U}{\partial X} + \frac{\partial V}{\partial Y} = 0, \quad (5)$$

$$U \frac{\partial U}{\partial X} + V \frac{\partial U}{\partial Y} = -\frac{\partial P}{\partial X} + \frac{1}{\text{Re}} \left(\frac{\partial^2 U}{\partial X^2} + \frac{\partial^2 U}{\partial Y^2} \right), \quad (6)$$

$$U \frac{\partial V}{\partial X} + V \frac{\partial V}{\partial Y} = -\frac{\partial P}{\partial Y} + \frac{1}{\text{Re}} \left(\frac{\partial^2 V}{\partial X^2} + \frac{\partial^2 V}{\partial Y^2} \right) + \text{Ri} \theta, \quad (7)$$

$$U \frac{\partial \theta}{\partial X} + V \frac{\partial \theta}{\partial Y} = \frac{1}{\text{Pr Re}} \left(\frac{\partial^2 \theta}{\partial X^2} + \frac{\partial^2 \theta}{\partial Y^2} \right). \quad (8)$$

2.2 Nusselt number and pressure drop losses

The Nusselt number expresses the average heat transfer rate in the system. In the present work, the mean Nusselt number on the moving wall is as follows [14]:

$$\text{Nu} = \int_0^L \text{Nu}_x dx, \quad (9)$$

where Nu_x is the local Nusselt number. Equation (9) can be written as follows:

$$\text{Nu} = \frac{1}{L} \int_0^L \left. \frac{\partial \theta}{\partial X} \right|_{X=0} dY, \quad (10)$$

where L is the length of wall.

2.3 Validation

The code which is used to obtain the present results is validated by taking a case study investigated by Alesbe *et al.* [25]. The results of streamlines and isotherms for both studies with three values of Richardson numbers are given in Fig. 2. Alesbe *et al.* [25] in their work used a hybrid nanofluid

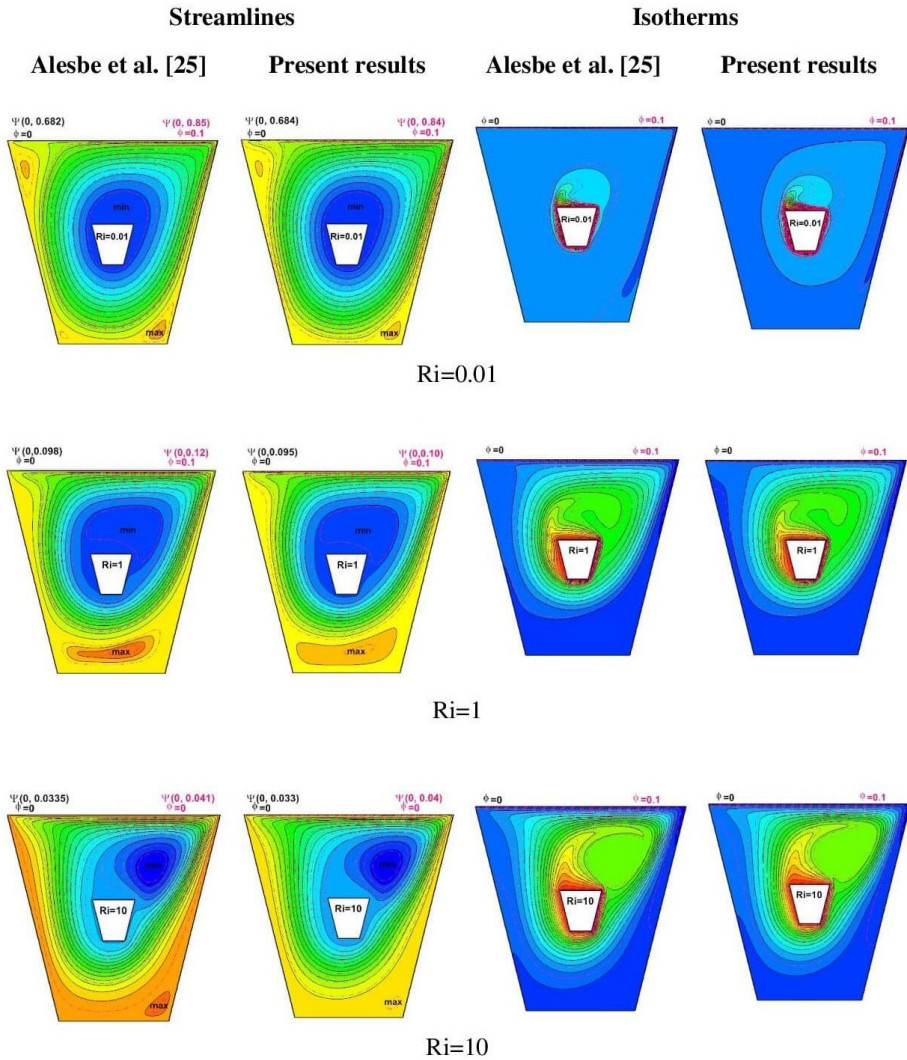


Figure 2: Code validation for the present study (Φ – nanoparticles volume fraction, Ψ – stream function).

in a trapezoidal lid-driven annulus. The comparison has been carried out by moving only the top wall. It is noticed that the comparison gives a good validation for both studies.

3 Numerical results

3.1 Flow field and thermal patterns

The effects of the inner cylinder position as in case 1: concentric annulus; case 2: lower position; case 3: upper position on the behaviour of fluid motion and thermal fields for three Richardson numbers ($Ri = 0.01, 1$, and 10) are shown in Figs. 3 and 4, respectively. Generally, the thermal distribution

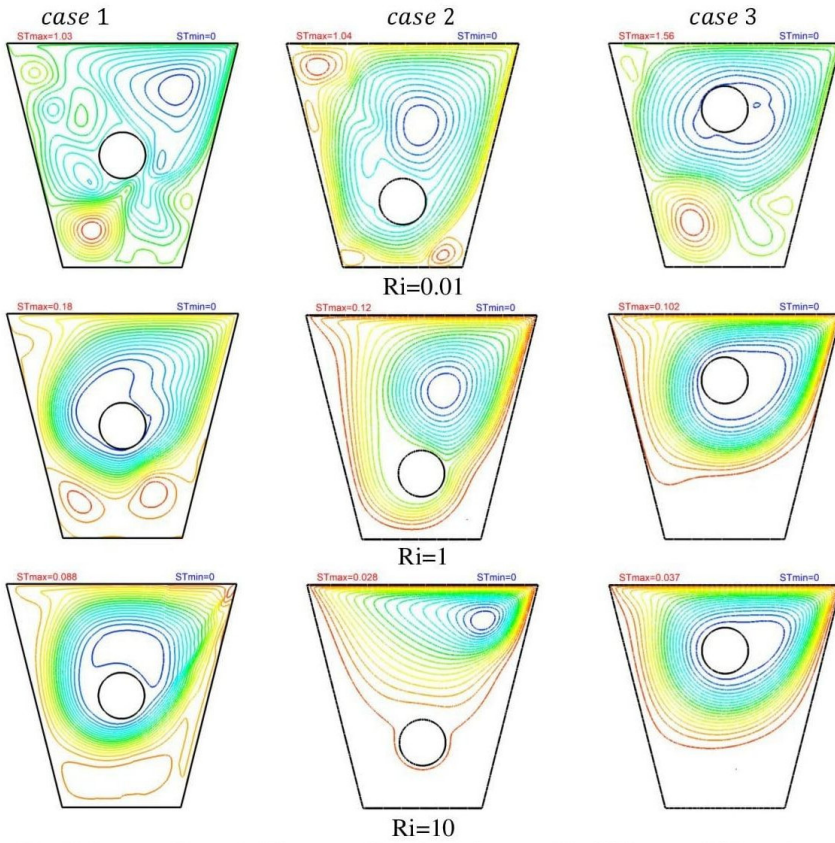


Figure 3: Streamlines in trapezoidal lid driven annulus with different Richardson numbers $Ri = 0.01, 1$, and 10 (ST_{min} , ST_{max} – minimum and maximum stream function).

inside the enclosure depends greatly on the forced convection flow resulting from moving the top wall. So, at a low Richardson number ($Ri = 0.01$), the shear effects resulting from the motion of the top lid are predominant. This motion of the top wall causes a significant recirculating eddy which will be generated in the corners of the cavity for the three investigated cases. The number of these eddies for the concentric annulus (case 1) is higher than that for the eccentric annuli (cases 2 and 3), especially on the left-hand side of the cavity. As can be seen, higher temperature gradients are formed near the hot cylinder wall. The thermal lines (isotherms) rotate about the hot cylinder. The isotherms get away from the hot cylinder. So, the region seems to be colder than nearby areas because of the dominating forced

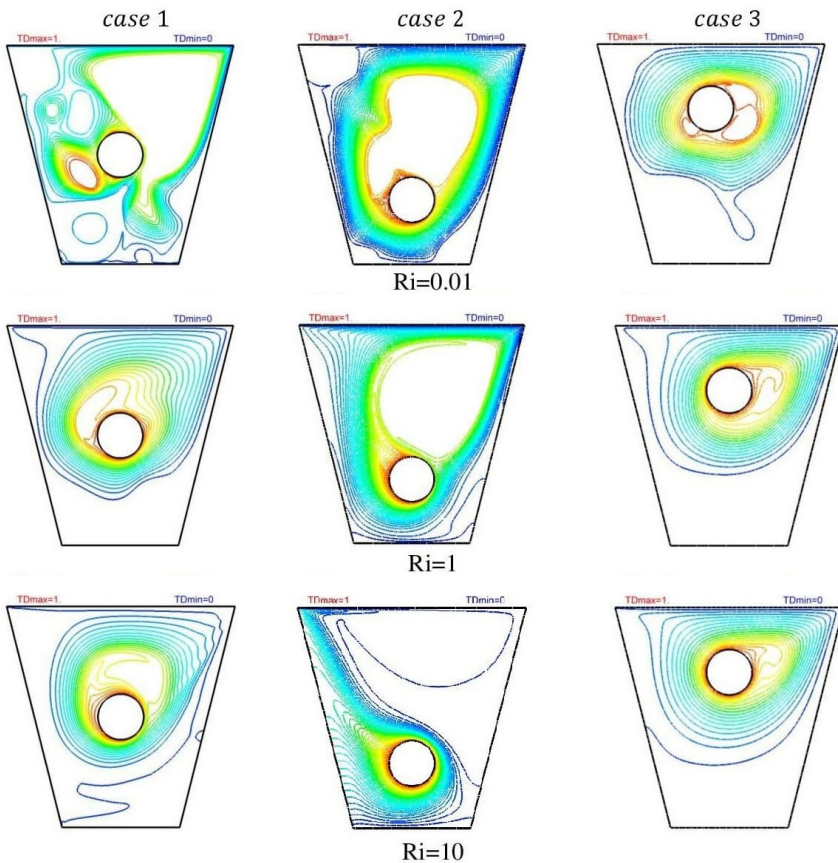


Figure 4: Isotherms in trapezoidal lid driven annulus with different Richardson numbers $Ri = 0.01$, 1 , and 10 (TD_{min} , TD_{max} – minimum and maximum temperature difference).

convection. Actually, for forced convection (low Richardson number), the vorticities are stronger at the upper region of the enclosure than those in the mixed and natural convection.

The free convection currents grow as the Richardson number increases and produce circulation. The mini vortices (eddies) diminish in the top region of the annulus at $Ri = 1$ (dominant mixed convection, i.e., the primary and secondary flows are equivalent) for case 1 and case 3 except for case 2 (bottom position of the circular cylinder). Moreover, two eddies will be formed at the lower region of the concentric annulus, while circular lines of fluid velocity will be generated around the hot cylinder in case 3 (top position of the inner cylinder). Moreover, two eddies will be formed at the lower region of the concentric annulus. It is evident that the isotherms move towards the outer cylinder. The higher velocity of the fluid close to the lid-driven wall produces a significant distortion in the thermal plume.

Increasing the buoyancy effects at the expense of inertia force reduces the shear-driven circulation. In this case, the natural convection is dominated ($Ri = 10$). It is noted that the small vortices (eddy) will be eliminated. One large vorticity will be formed. Its centre depends on the position of the inner cylinder. The maximum stream function in case 1 is higher than in case 3 and case 2, consequently. It is expected that the heat transfer rate in case 1 is better than that in case 3 and case 2, respectively. The isotherms in case 1 and case 3 are more uniform than in case 2 because higher natural convection currents in case 2 cause a high temperature gradient, and a large distortion in the thermal plume deviates towards the adiabatic left wall, while the right wall will be cold. Additionally, the bottom region of cases 1 and 3 will be colder than other regions of the cavity; leading to a high heat transfer rate in these cases. Increasing Ri from 1 to 10 leads to the thermal patterns which do not exhibit much change in cases 1 and 3 because the hot cylinder is close to the moving wall in these cases. As a result, the thermal plume will be affected by the motion of fluid near the moving wall.

3.2 Nusselt number

Figure 5 represents the relationship between the mean Nusselt number and Richardson number for three cases studied in the present work, and for three walls for each case: moving wall, bottom wall and hot circular wall. It is shown in this figure that the values of the mean Nusselt number in the moving wall are higher than that in the hot and the bottom walls. This is attributed to the effect of the lid-driven wall to improve the heat transfer

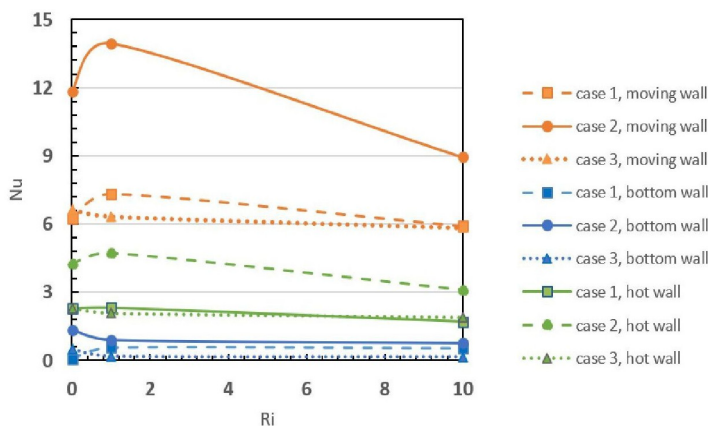


Figure 5: The relation between the mean Nusselt number and the Richardson number for all cases considered.

rate and due to the dominant inertia force in the mechanism of heat transfer. Also, the natural convection currents aid to increase the fluid velocity near the hot wall. This leads to an increase in the rate of heat transfer on the hot wall. Moreover, the maximum value of the Nusselt number in the moving and hot walls for both cases: case 1 (concentric cylinder) and case 2 (lower position of the inner cylinder) occurs at $Ri = 1$ (mixed convection), whereas for case 3 (upper position of the inner cylinder), the maximum Nusselt number occurs at $Ri = 0.01$ (forced convection) in the moving and hot walls. This behaviour will be reversed in the bottom walls for all cases. The minimum value of the Nusselt number in the three walls: hot wall, moving wall and bottom wall for all cases occurs at $Ri = 10$. This is related to the dominant buoyancy force in the mechanism of heat transfer.

4 Friction factor

Figure 6 represents the variation of skin friction with Richardson number for three cases studied in the present work, and for three walls for each case: moving wall, bottom wall and hot circular wall. The higher values of skin friction on the lid wall at $Ri = 0.01$ (dominant forced convection) compared with other values on the other walls and for other cases make these values seem to be closer to each other in the lower portion of the figure.

So, Table 6 shows the average skin friction values for the above cases. It is seen that the friction coefficients for $Ri = 0.01$ are much higher than that

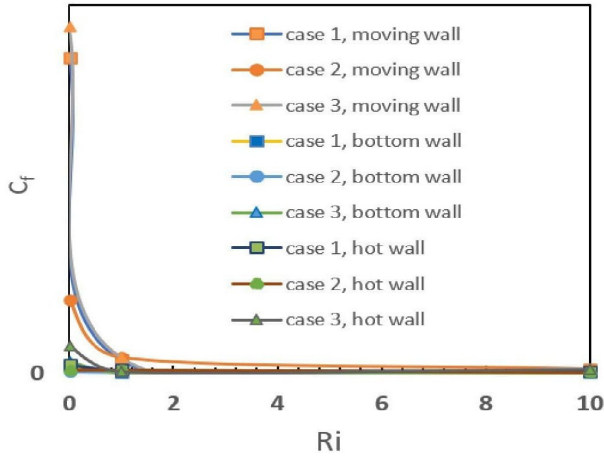


Figure 6: Average skin friction coefficient *versus* Richardson number on the moving, hot, and bottom walls.

at $Ri = 1.0$ and 10.0 , especially on the moving wall because the dominating forced convection produces an increased pressure drop on the moving wall, bottom wall and hot cylinder wall. Moreover, the values of friction coefficient on the lid wall are higher than that on the bottom wall due to the high velocity of fluid motion on the moving wall, whereas these values are higher on the hot cylinder wall with respect to the bottom cold wall because of high mixed convection in this region.

Table 6: Average skin friction on the moving, hot, and bottom walls.

Wall type	Ri	Case 1	Case 2	Case 3
Moving wall	0.01	$1.371 \cdot 10^{-3}$	$3.1536 \cdot 10^{-4}$	$1.5087 \cdot 10^{-3}$
Moving wall	1.00	$5.53 \cdot 10^{-5}$	$6.6222 \cdot 10^{-5}$	$6.5097 \cdot 10^{-5}$
Moving wall	10.00	$1.56 \cdot 10^{-5}$	$1.554 \cdot 10^{-5}$	$1.51829 \cdot 10^{-5}$
Bottom wall	0.01	$3 \cdot 10^{-5}$	$5.7376 \cdot 10^{-6}$	$4.9819 \cdot 10^{-5}$
Bottom wall	1.00	$2.29 \cdot 10^{-6}$	$2.6087 \cdot 10^{-6}$	$5.5419 \cdot 10^{-7}$
Bottom wall	10.00	$6.23 \cdot 10^{-7}$	$1.826 \cdot 10^{-7}$	$1.1374 \cdot 10^{-7}$
Hot wall	0.01	$3.4 \cdot 10^{-5}$	$1.0121 \cdot 10^{-5}$	$1.185 \cdot 10^{-4}$
Hot wall	1.00	$1.3 \cdot 10^{-5}$	$1.1176 \cdot 10^{-5}$	$4.7116 \cdot 10^{-6}$
Hot wall	10.00	$5.33 \cdot 10^{-5}$	$3.0551 \cdot 10^{-7}$	$1.53388 \cdot 10^{-5}$

Figure 7 shows the behaviour of pressure drop on the moving wall at different values of Richardson numbers. The behaviour is the same as that in the average friction factor.

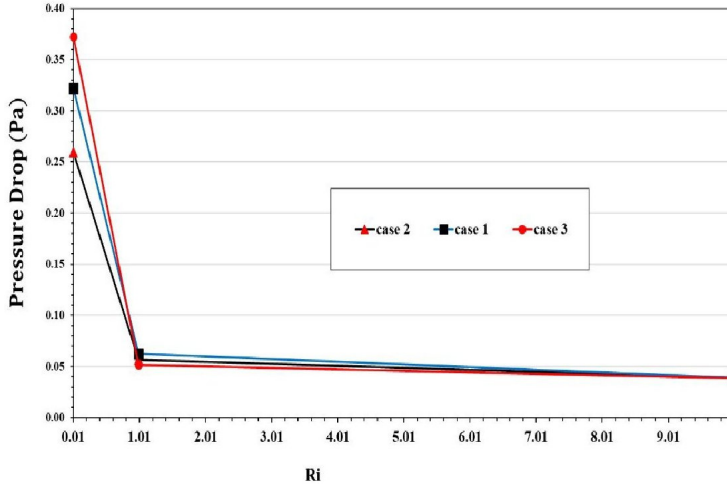


Figure 7: Pressure drop *versus* Richardson number on the moving wall.

5 Conclusions

The objective of the present study is to investigate the influences of the position of the hot circular cylinder on the behaviour of streamlines, isotherms, average Nusselt number and friction factor in a lid-driven trapezoidal cavity filled with water. The top wall moves as lid-driven with a constant speed. Three values of Richardson number ($Ri = 0.01$, 1.0 , and 10) are considered. It is concluded that:

1. At a low Richardson number ($Ri = 0.01$), the shear effects resulting from the motion of the top lid are predominant.
2. The higher velocity of fluid close to the lid-driven wall produces a significant distortion in the thermal plume.
3. When the natural convection is dominated ($Ri = 10$), the maximum stream function in case 1 (concentric cylinder) is higher than in case 3 (upper position of the inner cylinder) and case 2 (lower position of the inner cylinder), consequently.

4. The values of the mean Nusselt number in the moving wall are higher than that in the hot and bottom walls.
5. The maximum value of the Nusselt number in the moving and hot walls for both cases: case 1 and case 2 occurs at $Ri = 1$ (mixed convection).
6. The skin friction factors (frictional losses) for $Ri = 0.01$ are much higher than those at $Ri = 1$ and 10, especially on the moving wall.
7. The values of friction coefficient on the lid wall are higher than those on the hot and bottom walls.

Received 10 February 2023

References

- [1] Rosdzhimin A.R.M., Zuhairi S.M., Azwadi C.S.N.: *Simulation of mixed convective heat transfer using lattice Boltzmann method*. Int. J. Automot. Mech. Eng. (IJAME) **2**(2010), 130–143.
- [2] Nemati H., Farhadi M., Sedighi K., Fattahi E., Darzi A.A.R.: *Lattice Boltzmann simulation of nanofluid in lid-driven cavity*. Int. Commun. Heat Mass **37**(2010), 10, 1528–1534.
- [3] Sheikhzadeh G.A., Qomi M.E., Hajialigol N., Fattahi A.: *Numerical study of mixed convection flows in a lid-driven enclosure filled with nanofluid using variable properties*. Results Phys. **2**(2012), 5–13.
- [4] Chattopadhyay A., Sensarma S., Pandit S.K.: *Numerical simulations of mixed convection in a porous double lid driven cavity*. In: Proc. Int. Conf. on Mathematical Modeling And Computer Simulation with Applications, IIT Kanpur, Dec. 31, 2013 – Jan. 2, 2014.
- [5] Ögüt E.B., Kahveci K.: *Mixed convection heat transfer of ethylene glycol and water mixture based Al_2O_3 nanofluids: Effect of thermal conductivity models*. J. Mol. Liq. **224**(2016), 338–345.
- [6] Mastiani M., Kim M.M., Nematollah A.: *Density maximum effects on mixed convection in a square lid-driven enclosure filled with Cu-water nanofluids*. Adv. Powder Technol. **28**(2017), 1, 197–214.
- [7] Jahirul Haque Munshi M., Nusrat J., Golam M.: *Mixed convection heat transfer of nanofluid in a lid-driven porous medium square enclosure with pairs of heat source-sinks*. Am. J. Eng. Res. (AJER) **8**(2019), 6, 59–70.
- [8] Çakmak N.K., Durmazucar H.H., Yapici K.: *A numerical study of mixed convection heat transfer in a lid-driven cavity using Al_2O_3 -water nanofluid*. Int. J. Chem. Technol. **4**(2020), 1, 22–37.

- [9] Bhattacharya M., Basak Tanmay, Oztop H.F., Varol Y.: *Mixed convection and role of multiple solutions in lid-driven trapezoidal enclosures*. Int. J. Heat Mass Tran. **63**(2013), 366–388.
- [10] Mehmood Z., Javed T., Pop J.: *MHD-Mixed convection flow in a lid driven trapezoidal cavity under uniformly/ non-uniformly heated bottom wall*. Int. J. Numer. Method Heat Fluid Fl. **27**(2016), 6, 1231–1248.
- [11] Borhan Uddin M., Rahman M.M., Khan M.A.H., Saidur R., Ibrahim T.A.: *Hydro-magnetic double-diffusive mixed convection in trapezoidal enclosure due to uniform and nonuniform heating at the bottom side: Effect of Lewis number*. Alexandria Eng. J. **55**(2016), 2, 1165–1176.
- [12] Raizah Z.A., Ahmed S.E., Hussein A.K., Mansour M.A.: *MHD mixed convection in trapezoidal enclosures filled with micropolar nanofluids*. Nanosci. Technol.-Int. J. **9**(2018), 4, 343–372.
- [13] Mondal P., Mahapatra T.R.: *Minimization of entropy generation due to MHD double diffusive mixed convection in a lid driven trapezoidal cavity with various aspect ratios*. Nonlinear Anal.-Model. Contr. **25**(2020), 4, 545–563.
- [14] Sharif M.A.R.: *Laminar mixed convection in shallow inclined driven cavities with hot moving lid on top and cooled from bottom*. Appl. Therm. Eng. **27**(2007), 1036–1042.
- [15] Oztop H.F., Sun C., Yu B.: *Conjugate-mixed convection heat transfer in a lid-driven enclosure with thick bottom wall*. Int. Commun. Heat Mass Tran. **35**(2008), 779–785.
- [16] Salahi H., Sharif M.A.R., Rasouli S.: *Laminar mixed convective heat transfer in a shallow inclined lid-driven cavity filled with nanofluid*. J. Therm. Sci. Eng. Appl. **7**(2015), 4, 041016.
- [17] Kefayati G.H.R., Tang H.: *MHD mixed convection of viscoplastic fluids in different aspect ratios of a lid-driven cavity using LBM*. Int. J. Heat Mass Tran. **124**(2018), 344–367.
- [18] Ardalan M.V., Alizadeh R., Fattahi A., Rasi N.A., Doranehgard M.H., Karimi N.: *Analysis of unsteady mixed convection of Cu–water nanofluid in an oscillatory, lid-driven enclosure using lattice Boltzmann method*. J. Therm. Anal. Calorim. **145**(2021), 2045–2061.
- [19] Chen C.-L., Cheng C.-H.: *Experimental and numerical study of mixed convection and flow pattern in a lid-driven arc-shape cavity*. Heat Mass Transfer **41**(2004), 1, 58–66.
- [20] Parvin S., Nasrin R.: *Magnetohydrodynamic mixed convection heat transfer in a lid-driven cavity with sinusoidal wavy bottom surface*. J. Tri. Math. Soc. **12**(2010), 1–9.
- [21] Saha L.K., Monotos Chandra Somadder, Salah Uddin K.M.: *Mixed convection heat transfer in a lid driven cavity with wavy bottom surface*. Am. J. Appl. Math. **1**(2013), 5, 92–101.
- [22] Nasrin R., Alim M.A., Chamkha A.J.: *Modeling of mixed convective heat transfer utilizing nanofluid in a double lid-driven chamber with internal heat generation*. Int. J. Numer. Method Heat Fluid Fl. **24**(2014), 1, 36–57.
- [23] Mojumder S., Saha S., Rahman M.R., Rahman M.M., Khan Md. Rabbi, Ibrahim T.A.: *Numerical study on mixed convection heat transfer in a porous L-shaped cavity*. Eng. Sci. Technol.-Int. J. **20**(2017), 1, 272– 282.

- [24] Guo Z., Wang J., Mozumder A.K., Das P.K.: *Mixed convection of nanofluids in a lid-driven rough cavity*. AIP Conf. Proc. **1851**(2017), 020004.
- [25] Alesbe I., Ibrahim S.H., Sattar A.: *Mixed convection heat transfer in multi-Lid- driven trapezoidal annulus filled with hybrid nanofluid*. J. Phys.: Conf. Ser. **1973**(2021), 012065.

Investigation of thermal-flow characteristics of the minichannel heat exchanger of variable louvers height

ARTUR ROMANIAK*
MICHAŁ JAN KOWALCZYK
MARCIN ŁĘCKI
ARTUR GUTKOWSKI
GRZEGORZ GÓRECKI

Lodz University of Technology, Żeromskiego 116, 90-924 Łódź, Poland

Abstract The numerical simulation of the heat transfer in the flow channels of the minichannel heat exchanger was carried out. The applied model was validated on the experimental stand of an air heat pump. The influence of louver heights was investigated in the range from 0 mm (plain fin) to 7 mm (maximum height). The set of simulations was prepared in Ansys CFX. The research was carried out in a range of air inlet velocities from 1 to 5 m/s. The values of the Reynolds number achieved in the experimental tests ranged from 93 to 486. The dimensionless factors, the Colburn factor and friction factor, were calculated to evaluate heat transfer and pressure loss, respectively. The effectiveness of each louver height was evaluated using the parameter that relates to the heat transfer and the pressure drop in the airflow. The highest value of effectiveness (1.53) was achieved by the louver height of 7 mm for the Reynolds number of around 290.

Keywords: CFD; Heat transfer; Heat pump; Louvered fins; Minichannel heat exchanger

Nomenclature

- A – airside area of the heat exchanger, m^2
- A_c – minimum free flow area, m^2
- c_p – air specific heat, $\text{J}/(\text{kg K})$

*Corresponding Author. Email: artur.romaniak@dokt.p.lodz.pl

F_d	–	flow depth, mm
F_p	–	fin pitch, mm
f	–	friction factor
H	–	fin height, mm
h	–	mean value of heat transfer coefficient, $W/(m^2K)$
JF	–	parameter related to heat transfer and pressure drop in airflow
j	–	Colburn factor
$j_{\text{ref}}, f_{\text{ref}}$	–	reference values of j and f factors (for $L_h = 0$ mm)
L_a	–	louver angle, $^\circ$
L_h	–	louver height, mm
L_l	–	louver length, mm
L_p	–	louver pitch, mm
Nu	–	Nusselt number
Pr	–	Prandtl number
p_{in}	–	air pressure at the inlet to the evaporator, Pa
p_{out}	–	air pressure at the outlet of the evaporator, Pa
Re	–	Reynolds number
T_{in}	–	mean value of air temperature at the inlet to the evaporator, K
T_{out}	–	mean value of air temperature at the evaporator outlet, K
v_{ave}	–	mean value of airstream velocity in the air MCHE channel, m/s
v_{fr}	–	mean value of the frontal velocity of an airstream, m/s
Q	–	heat transfer rate, W
X_f	–	length of the air side section inside the fin, mm
$X_{f \text{ in}}$	–	length of the air inlet section to the fin, mm
$X_{f \text{ out}}$	–	length of the air outlet section downstream of the fin, mm
X_{in}	–	length of the air inlet section, mm
X_{out}	–	length of the air outlet section, mm
ΔT	–	cooling effect in the airstream, $= T_{\text{in}} - T_{\text{out}}$, K
ΔT_{in}	–	logarithmic mean temperature difference, K
Δp	–	pressure drop in the airstream, $= p_{\text{in}} - p_{\text{out}}$, Pa

Greek symbols

δ	–	characteristic dimension (L_p), m
ρ	–	air density, kg/m^3
λ_{air}	–	thermal conductivity of air, $W/(m K)$
ν	–	air kinematic viscosity, m^2/s
η	–	surface efficiency

Abbreviations

CFD	–	computational fluid dynamics
MCHE	–	minichannel heat exchanger

1 Introduction

Nowadays, refrigeration systems face new challenges caused by environmental standards. According to the Regulation of the European Parliament and the Council of EU No. 517/2014, developed countries are obliged to reduce greenhouse gas emissions by about 80–95% by 2050 in comparison to 1990. The fluorinated greenhouse gases on the market should be reduced by about 79% by 2030. These actions were undertaken to prevent climate change. Conventional refrigerants are replaced by new ones with an indifferent impact on the environment. This situation is also a challenge for components of refrigeration systems, like heat exchangers (evaporators and condensers). A minichannel heat exchanger (MCHE) meets these requirements. MCHE is a type of heat exchanger, built from flat tubes with minichannels and louvered fins. Minichannels improve refrigerant heat transfer by enhancing the contact area. Furthermore, louvers on the fin wall improve air heat transfer by decreasing boundary layer thickness. MCHE is made from aluminum. Due to these features, it achieves high thermal performance. MCHE is applied in the automotive industry and is more frequently used in modern refrigeration systems because of its high effectiveness. In previous years, this device was the subject of many papers focused on its exploitation and the methods of construction improvement.

A good example of experimental studies was presented by Boeng *et al.* from the Federal University of Santa Catarina [1]. They performed experimental research on a new microchannel evaporator design for ‘no frost’ household refrigerators (sixteen aluminum evaporator samples). The researchers prepared empirical correlations based on the entire data set for the Colburn factor (j) and friction factor (f). They were able to predict 90% of the experimental data within $\pm 10\%$ and $\pm 20\%$ error bounds, respectively. Considering the air-side pressure drop observed for all microchannel evaporators tested, the authors concluded that such technology seems to be suitable for household refrigerating appliances as it barely impacts the total air flow rate of the system. Another case of the MCHE studies was conducted by Huang *et al.* [2]. The thermal and hydraulic performance of a designed compact bare-tube heat exchanger prototype was experimentally evaluated in comparison with the louvered-fin and flat-tube heat exchanger (with a similar frontal surface). Based on the experimental results it was possible to show that the bare tube heat exchanger was able to achieve the same heat capacity with 72% less envelop volume and 70% less material volume than in the case of louvered-fin and flat-tube heat exchangers. As

regards the j/f ratio, the so-called coefficient of goodness, the value of the bare tube heat exchanger was 50% larger than that of the reference heat exchanger. Srisomba *et al.* [3] published experimental results showing the effect of the operating conditions on the performance of a microchannel heat exchanger under wet surface conditions. The subject of studies was an aluminum microchannel heat exchanger with a multi-louvered fin and multi-port minichannels. The tests were performed on R-134a refrigerant. The conditions were as follows: the relative air humidity in the range between 45% and 80% and the air inlet temperature of 27, 30, and 33°C. The Reynolds numbers ranged between 128 and 166. In their paper, the authors showed that when air inlet temperature and inlet relative humidity increase the heat transfer coefficient increases, but the wet fin efficiency decreases rapidly. Dogan *et al.* [4] performed the experimental comparison of double- and triple-row multi-louvered fin heat exchangers. The tests were conducted under constant thermal conditions and with identical frontal areas and depths. The tests in the wind tunnel were conducted under transient and steady-state conditions. The Reynolds number calculated based on the louvered pitch was 275. Their results showed that the heat exchanger with double-row fins had a higher thermal performance in terms of NTU (number of transfer units) and effectiveness.

The examination of automotive air conditioning systems was presented by Prabakaran *et al.* [5]. They conducted tests for two operating states (dry bulb temperature 27°C; relative humidity 40% and dry bulb temperature 40°C; relative humidity 40%) for the basic circuit (conventional serpentine evaporator with parallel flow condenser) and the enhanced (minichannel evaporator with an integrated receiver-dryer condenser). For both operating states, the coefficient of performance achieved in the test was higher for the enhanced cycle by 15% and 8%, respectively. The influence of the symmetrical and the asymmetrical pattern of the louvered fins was investigated experimentally by Vasi *et al.* [6]. The results of their work showed that the symmetrical setting of the louvers increases the values of heat transfer coefficients by 9.3% while reducing the pressure loss by 18.2% compared to the asymmetric setting. Additionally, with the set constant values of heat exchange and pressure drop for both settings, a 17.6% decrease in the weight of lamellas with symmetrical cuts can be observed. The next example of the test of compact heat exchangers with louver fins was presented by Ribeiro *et al.* [7]. They used wavy turbulators with louvers in the tubes and performed the experimental investigation for Reynolds numbers within the range 2588–7045. A new correlation for the Nusselt number in terms of

the hydraulic diameter based Reynolds number, Prandtl number, and geometric parameters has been proposed for the tubes with turbulators. They observed a gain in the performance by use of the turbulators, obtained by a significant improvement in the convection heat transfer coefficient at the cost of an increase in the friction coefficient. Ayad *et al.* [8] investigated experimentally the air-side thermal-hydraulic performance of louvered fin and flat-tube heat exchangers under dehumidifying conditions. The tested louvered heat exchanger was characterized by geometrical dimensions as a flow depth of 47 mm, a high louver angle of 50° , and a louver pitch of 1.1 mm. The heat exchanger was tested in dry and wet work conditions. They observed that, for all inlet conditions, the wet friction factor is higher than that for the dry surface (from 15 to 43%). At a low Reynolds number, the Colburn factor under wet conditions is not influenced by the inlet humidity and it does not deviate from the dry conditions. However, as the Re increases, the sensible wet j factor decreases (up to 23%) compared to the dry one. Cao *et al.* [9] investigated the condensation heat transfer and pressure drop characteristics of R600a in a multi-louvered fins compact heat exchanger. The experiments conditions included saturation pressures from 530 to 620 kPa, mass fluxes from 25 to 41.25 kg/(m²s), air temperature from 25 to 35°C, and inclined angles from 0° to 180° in horizontal and vertical directions, respectively. Based on the results, the authors noted that both the heat transfer capacity and the heat transfer coefficient of the condenser increase with an increase in mass flux. The heat transfer coefficient increases with the decrease in air temperature and the decrease in saturation pressure. However, both these parameters have opposite effects on the heat transfer capacity.

The computational fluid dynamics (CFD) methods are widely used in studies on MCHE performance. Yue *et al.* [10] used numerical simulations to evaluate MCHE heat transfer characteristics and flow mechanisms under different filling ratios in the evaporator of a microchannel separate heat pipe. The model was built in the Ansys Fluent software and it was validated in the experimental facility. The authors noticed that the optimal refrigerant filling ratio was from 68% to 100%. They found that the cooling capacity increased with the filling ratio and was as high as 4087 W at a filling ratio of 78%. They also noticed that the distribution of wall temperature and the liquid fraction both indicated that the effective heat transfer area of the two-phase region was a key parameter affecting the cooling capacity. Another numerical investigation of the louvered fin heat exchanger was developed by Zuoqin *et al.* [11]. They investigated the influence of louver fin

configurations on thermal performance. The analyzed ranges of the geometry parameters were 7.5–12.5 mm (louver length, L_l), 8–20° (louver angle, L_a), and 2.25–3.75 mm (louver pitch, L_p). The achieved range of Reynolds number was 70–350. The authors showed the optimized geometrical parameters as $L_l = 7.5$ mm, $L = 8^\circ$, and $L_p = 2.25$ mm. The best geometry increased the value of performance evaluation criterion by 19% in comparison to the reference one. Numerical studies on the air-side thermal-hydraulic performance of multi-louvered fin heat exchangers at Reynolds numbers from 30 to 500 were presented by Saleem and Kim [12]. The authors conducted parametric studies for 36 heat exchanger configurations with louver angles between 19–31°, fin pitches of 1.0, 1.2, and 1.4 mm, and flow depths of 16, 20, and 24 mm. They determined numerically the critical Reynolds number and the variation in flow physics along with the thermal and hydraulic performance of the microchannel heat exchanger. The researchers found that the critical Reynolds number rises with an increase in flow depth (F_d) and a decrease in fin pitch (F_p) values. Based on the heat transfer coefficient determined using numerical results, they reported the best air-side thermal performance for geometry with $F_p = 1$ mm, $F_d = 16$ mm, and $L_a = 19^\circ$. The other example of the numerical investigation of the louvered fin was provided by Shinde *et al.* [13]. They conducted numerical studies of aluminum heat exchangers with different fin and tube geometrical configurations in the range of Reynolds numbers from 25 to 200. Three different heat exchanger geometries were obtained for the experimental investigation purposes with constant fin pitch (14 fins per inch) but varied fin geometrical parameters (fin height, fin thickness, louver pitch, louver angle, louver length, and flow depth) were numerically investigated. The research team found that in the tested range of small Reynolds numbers, the flow is directed by fin instead of louvers. Karthik *et al.* [14] also provided a parametric analysis of the performance of a compact heat exchanger using numerical methods. The researchers modeled different frontal air velocities by changing the geometrical parameters such as fin pitch, transverse tube pitch, longitudinal tube pitch, louver pitch, and louver angle. The authors found that a decrease in fin pitch led to a higher pressure drop at a tested frontal air velocity. The effect of the increase in both transverse and longitudinal tube pitches resulted in a higher pressure drop due to an increase in the surface without louvers. The influence of these parameters on the convective heat transfer coefficient is very minimal owing to the constant of the louver configuration. The reduction of the louver pitch contributed to a higher pressure drop with only a minimal increase in heat transfer

coefficient and hence, the goodness factor of the compact heat exchanger decreased significantly. An example of the numerical investigations concerning the methods for enhancement of MCHE performance was presented by Dezan *et al.* [15]. The influence on the thermal efficiency of two geometries with a vortex generator was investigated. The geometrical differences concerned the louver height and delta-winglet frontal area. The Reynolds numbers based on the hydraulic diameter of 120 and 240 were tested. The calculation was conducted using Ansys Fluent. The authors stated that for both geometries and Reynolds numbers, the louver angle is the major contributor to the friction factor. Another numerical test was presented by Kang's research group [16] who examined a prototype minichannel heat exchanger working with fuel cells. The heat exchanger was investigated in terms of achieved heat transfer rates on the air side and pressure drops. The authors commented that the arrangement of pipes in the prototype had little effect on the pressure drop but had a large impact on the heat transfer coefficient due to the contact zone of the pipes and the lamellas with the louvers. Martinez-Ballester *et al.* [17] investigated the effect of the number of passes of the medium in the heat exchanger on its operation. They found that there is an optimal value of the number of passes, in the case studied, it was 3. With such a number, they noticed an increase in heat exchange of approx. 3%. The numerical and analytical approach to condensation in MCHE was presented by Kumar's research team [18]. The authors used an analytical approach to calculate the heat transfer and the pressure drop through the condenser. In the analytical approach, the condenser was discretized into multiple segments and the effectiveness of heat exchanger – number of heat transfer unit (ε -NTU) method was applied. In the second approach, computational fluid dynamics was used to analyze condensation phenomena inside the microchannel and it was compared with the analytical results. The maximum deviation of the heat transfer and the internal pressure drop (refrigerant side) for the analytical approach was found to be 8.3% and 9.4%, respectively compared to the experimental results. The results showed that the proposed analytical approach can be used to calculate the heat rejection and internal (refrigerant) pressure drop within the 10% accuracy range.

The literature review shows that most of the experimental and numerical research was performed for Reynolds numbers in the range of 25–500. The numerical research concerns geometrical parameters of fins, for example, fin height, fin pitch, louver pitch, louver height, etc. However, there is a lack of data due to the influence of louver height on thermal performance.

The present work focuses on the numerical investigation of minichannel heat exchangers with different louver heights based on the results from an experimental study conducted on the small heat pump system test rig. The tests were performed in the range of Reynolds numbers from 93 to 486. The JF factor was used to determine the performance of each geometry.

2 Materials and methods

The object of the tests was the MCHE with rectangular fins (shown in Fig. 1), which was working as an evaporator in a small refrigeration system (Fig. 2).



Figure 1: Tested minichannel heat exchanger.

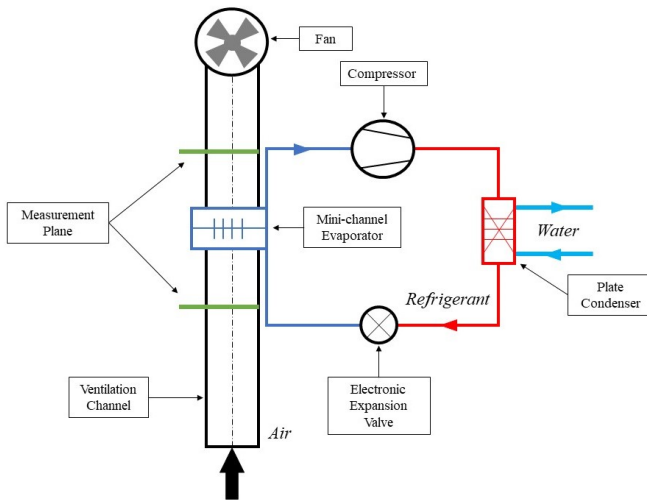


Figure 2: Scheme of the experimental stand of small air heat pump system.

The experimental rig consisted of two parts: a refrigeration system and a ventilation channel. The refrigeration system consists of a scroll compressor, water cooled plate condenser, an electronic expansion valve (EEV), and a tested minichannel evaporator. By controlling the parameters of the refrigeration system (rotation speed of the compressor, stream of water in the condenser, and percentage of opening of EEV), the evaporating conditions in MCHE can be adjusted. The second part of the experimental rig is the ventilation channel in which the tested MCHE evaporator is placed. The airflow through the channel is forced by a fan placed at the outlet of the channel. Evaluation of MCHE performance was based on the measurement of airflow parameters in the ventilation channel. These parameters included the mean velocity of the airflow in front of MCHE, the pressure drop through the heat exchanger, and the temperature distribution before and after the evaporator. The locations of the measurement points inside the ventilation channel with the dimensions are presented in Fig. 3.

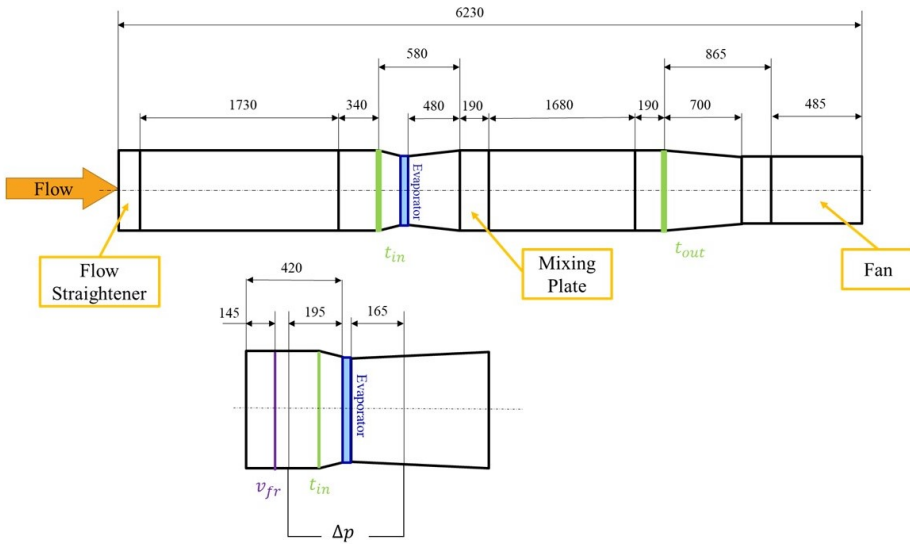


Figure 3: Scheme of ventilation channel with the location of measurement points.

The experimental rig was described in the previous paper [19]. The rig was improved by changing the expansion element and improvement of the air velocity measurement system. A change of the expansion element was implemented in the way to acquire a higher range of the evaporator capacity control. Thus, the electronic expansion valve Carel E2V 14BSF01 and Carel

EVD controller were used. To enhance the accuracy of velocity measurement, a tungsten hot-wire probe with module ATU-08 was implemented in place of the previously used climate meter. Additionally, the ventilation channel was equipped with a flow straightener and a mixing plate. Both elements were used according to the improvement of the airflow parameters.

3 Numerical methods

The numerical model was based on the dimensions of the real object. The analysis concerned air flow inside one of the louvered fins (Fig. 4). The model of the fin consisted of one fin and two flat tubes on the bottom and top (half of the thickness). The schematic drawing of the louvered fin and the dimensions are shown in Fig. 5 and Table 1.



Figure 4: The geometrical model of the tested louvered fin.

Table 1: The dimensions of the tested louvered fin.

F_d	F_p	H	L_l	L_p	L_a
15.8 mm	0.95 mm	8 mm	1.1 mm	1.13 mm	20°

The louvered height (L_h) was the parameter changed in the analysis. The simulations were performed for heights: 0, 1.5, 2.5, 3.5, 4.5, 5.5, 6.5, and 7 mm. The reference value of the louver height in the real object was 6.5 mm. The simulations with a 1 mm step were performed to the minimal value of 1.5 mm. Moreover, the simulations for 0 and 7 mm (0 mm is plain fin and 7 mm is the maximum height due to geometrical construction) were additionally carried out.

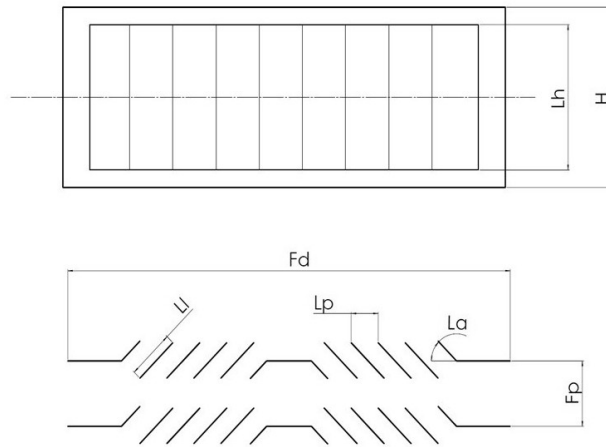


Figure 5: The schematic diagram of the tested louvered fin: H – fin height, L_h – louver height, F_d – flow depth, F_p – fin pitch, L_l – louver length, L_p – louver pitch, L_a – louver angle.

The analyzed geometry consisted of two domains: solid and fluid. The solid domain is the aluminum fin. The fluid domain is the air stream flowing through the fin. The air is modeled as an ideal gas. The thermodynamic properties of both domains are presented in Table 2. To obtain a well-distributed mesh the fluid domain was divided into five parts. The ge-

Table 2: Thermodynamic properties of the domains.

Parameter	Value
Air molar mass	$28.96 \frac{\text{kg}}{\text{kmol}}$
Air density	$1.185 \frac{\text{kg}}{\text{m}^3}$
Air specific heat	$1004.4 \frac{\text{J}}{\text{kg} \cdot \text{K}}$
Pressure	101.325 Pa
Air dynamic viscosity	$1.5 \cdot 10^{-5} \frac{\text{kg}}{\text{m} \cdot \text{s}}$
Air thermal conductivity	$2.61 \cdot 10^{-2} \frac{\text{W}}{\text{m} \cdot \text{K}}$
Aluminum thermal conductivity	$237 \frac{\text{W}}{\text{m} \cdot \text{K}}$

ometrical model and its schematic view are displayed in Figs. 6 and 7, respectively. The dimensions are described in Table 3.

Table 3: Dimensions of the air domain sections.

X_{in}	$X_{f\ in}$	X_f	$X_{f\ out}$	X_{out}
8 mm	1.9 mm	16 mm	1.9 mm	48 mm

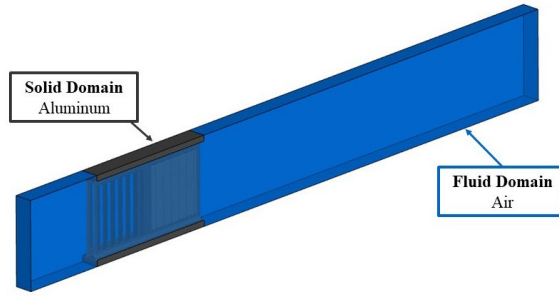


Figure 6: The geometrical model of the tested louvered fin.

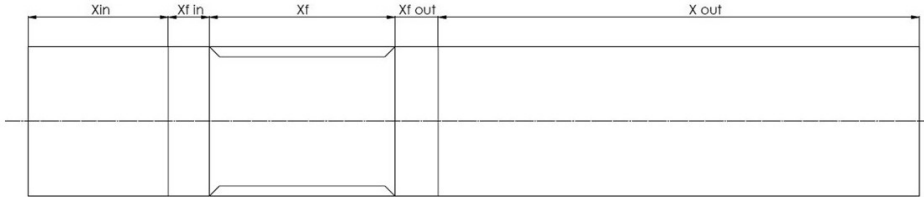


Figure 7: Schematic view of the division of air domain: X_{in} – inlet section, $X_{f\ in}$ – inlet section to the fin, X_f – fin section, $X_{f\ out}$ – outlet section downstream of the fin, X_{out} – outlet section.

After the design of the domain geometry, the mesh density independence test was performed. For 8 different densities of each grid, two simulations were conducted, for 1 and 5 m/s (minimum and maximum flow). Based on the calculation results the mesh with 2412583 elements was chosen which made it possible to achieve the required accuracy of the results while maintaining a reasonable calculation time.

The numerical model was used to simulate the phenomenon of heat transfer during air cooling by the fragment of MCHE. The measured value of air temperature and velocity at the inlet to the channel was set on the

Inlet surface. On the *Outlet* surface, the relative pressure was set at 0 Pa. In the horizontal direction, the translation periodicity was used for the fluid and the solid domains. Therefore, the right position of the louvers could be established. Additionally, on the top and bottom surfaces of the fin (purple surfaces in Fig. 8), the boundary *Wall* of constant temperature was set. For experiment validation, the values of the inlet velocity and temperatures were taken from the test conditions but in the case of parametric simulation, the values of these parameters were set. All boundaries with their location are presented in Fig. 8 and the values of each set parameter are summarized in Table 4. In the table, the parameter values are divided into two sections: the validation model (where there are parameter values entered into the numerical model from the experiment condition) and the parametric model

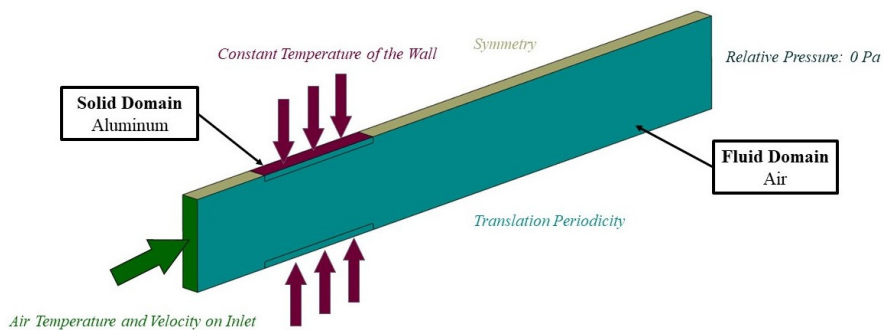


Figure 8: Boundary conditions distribution.

Table 4: Parameters used in simulation.

Parameter	Validation model	Parametric model
Temperature on the surface (<i>Inlet</i>), K	293.55 293.45 292.85 292.45	298.15
Temperature on the solid boundary (<i>Wall</i>), K	288.05 289.05 289.15 289.45	288.15
Velocity on the surface (<i>Inlet</i>), m/s	0.86 1.67 2.48 3.29	1 2 3 4 5
Relative pressure, Pa	0	0

(where there are conditions for numerical analysis of the impact of the louver height on the efficiency).

The simulations were conducted in *Ansys CFX 2021 R1* [22] with the following solver settings: a first-order turbulence model and an *SST k - ω* model of turbulence. The convergence criterion for the momentum and heat transfer was 10^{-6} .

The validation of the CFD model for the louver height of 6.5 mm (louver height for tested MCHE) is shown in Fig. 9, where a cooling effect and pressure drop are presented. Additionally, Table 5 lists the maximum values of estimated measurement uncertainties.

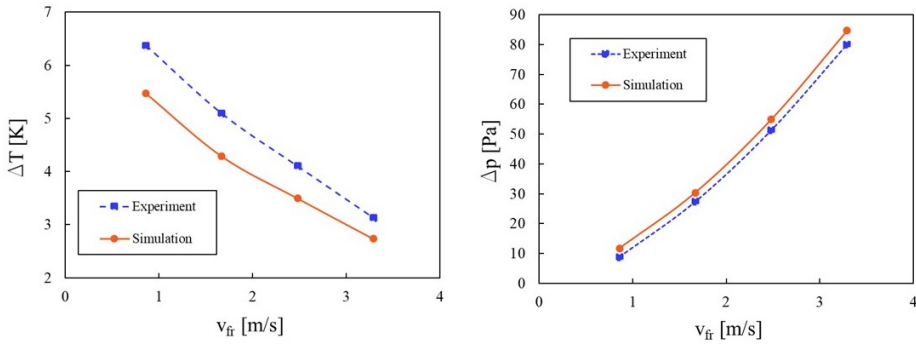


Figure 9: Validation of the simulation: the cooling effect (left picture) and the pressure drop (right picture) *vs.* the mean value of the frontal velocity of the airstream.

Table 5: The measurement uncertainties.

Parameter	Maximum value of uncertainty
Mean value of the frontal velocity of an airstream, v_{fr}	0.1 m/s
Pressure drop in the airstream, Δp	0.74 Pa
Cooling effect in the airstream, ΔT	0.4 K

The tested numerical approach compared with the experimental results is shown in Fig. 9. The cooling effect convergence is within the range of 12.8–15.8%. The differences are probably caused by the temperature in the flow channels of MCHE. The refrigerant distribution in minichannels is non-uniform, which could be caused by occlusion. The dimensions of minichannels are rather small, and they may be easily clogged with solid

impurities (for example from soldering). That phenomenon can disrupt the proper, uniform distribution of heat transfer in the contact area between the air and the aluminum flat tube. This condition raises uncertainty in the calculation of the average temperature of the fin. In terms of pressure loss, the convergence is in the range between 5.8–32.7%. The highest value of convergence was noted for the minimum velocity of the air stream (0.86 m/s), and the lowest value for the maximum velocity of the air stream (3.29 m/s). The measurement error in the case of pressure drop is constant. In other words, it had the biggest influence on the smallest measured value of pressure loss.

4 Results and discussion

Characteristics concerning changes in the pressure drop and the cooling effect with the change in the mean frontal velocity of the airstream are shown in Fig. 10. One can see that pressure drop increases with the velocity of the airflow (Fig. 10, right), and the highest values are achieved for a louver height of 7 mm. The highest value of pressure drop achieved in the test is approx. 120 Pa. As regards the cooling effect (Fig. 10, left), it is decreasing with increasing velocity of the airflow. It can be observed that the highest values of the cooling are achieved for the maximum considered louver height. One can notice that there is a linear trend of the characteristics in the range of louver height within 5.5–7 mm. The highest value of the cooling effect achieved in the test is almost 10 K.

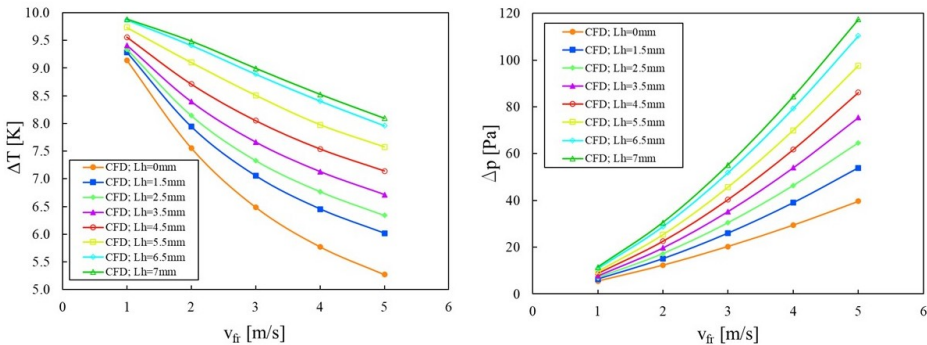


Figure 10: The influence of the mean value of the frontal airflow velocity on the cooling effect (left picture) and the pressure drop (right picture).

Further analysis was based on dimensionless numbers. The friction factor (f) and Colburn j factor were used to describe pressure drop and heat transfer. Both coefficients were presented as the function of the Reynolds number.

The Re based on the louver pitch (L_p) is calculated according to the formula [20]

$$\text{Re}_{L_p} = \frac{v_{\text{ave}} \delta}{\nu}, \quad (1)$$

where v_{ave} is the mean value of airstream velocity in the MCHE channel, δ represents the characteristic dimension ($\delta = L_p$), and ν is the air kinematic viscosity.

The Colburn and friction factors are given by, respectively:

$$j = \frac{\eta h \text{Pr}^{2/3}}{\rho v_{\text{ave}} c_p}, \quad (2)$$

$$f = \frac{2 \Delta p}{\rho v_{\text{ave}}^2} \frac{A_c}{A}, \quad (3)$$

where ρ and c_p are the density and specific heat of air, respectively, Δp denotes the pressure drop, A is the airside area of the heat exchanger, A_c represents the minimum free flow area of a heat exchanger, η is the surface efficiency, and Pr is the Prandtl number.

The heat transfer coefficient is defined as

$$h = \frac{Q}{A \Delta T_{ln}}, \quad (4)$$

where ΔT_{ln} is the logarithmic mean temperature difference and Q is the heat transfer rate.

The range of Reynolds numbers for the experiment is from 93 to 486. The friction factor for the tested geometries varies from 0.050 to 0.300 (Fig. 11, right). The characteristics show that higher louver height means a higher friction factor. In terms of the j factor (Fig. 11, left), one can observe a similar trend. But the values for louver height ranging from 0 to 4.5 are characterized by smaller differences of j factor values than in the case of other tested cases. The highest j values are obtained for 7 mm.

Additionally, based on the simulation results, the Nusselt numbers (based on the louver pitch as the characteristic dimension) were calculated using the formula

$$\text{Nu}_{L_p} = \frac{h \delta}{\lambda_{\text{air}}}, \quad (5)$$

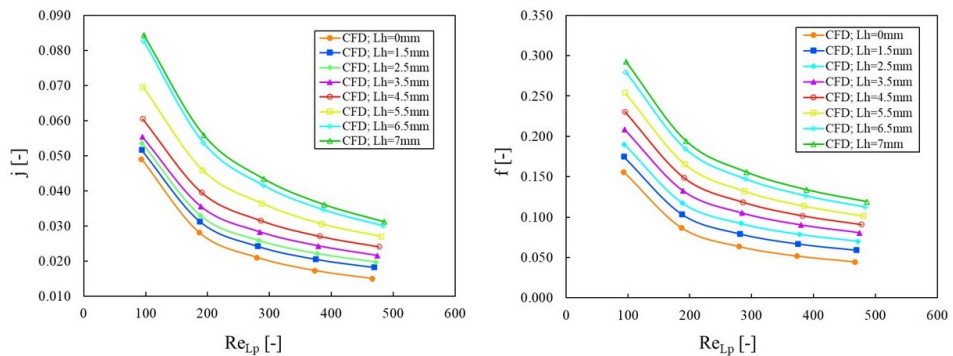


Figure 11: Characteristics of the Colburn factor (left picture) and the friction factor (right picture) *vs.* Reynolds number.

where λ_{air} is the thermal conductivity of air, and $\delta = L_p$. The characteristics of this parameter are shown in Fig. 12. The values of the Nusselt number increased with the increase in louver height. Under the tested conditions the Nusselt number was in the range from 4 to 13.

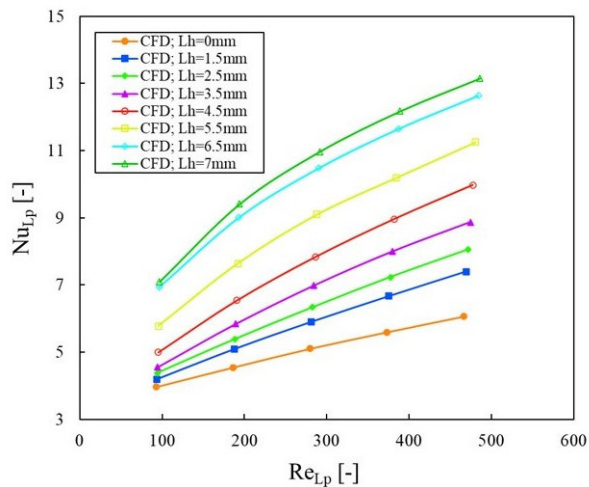


Figure 12: Characteristics of the Nusselt number *vs.* Reynold number.

The evaluation of the effectiveness is conducted based on the JF factor. This parameter refers to the heat transfer and the pressure drop in the

airflow and is calculated using the formula [21]:

$$JF = \frac{\frac{j}{j_{\text{ref}}}}{\sqrt[3]{\frac{f}{f_{\text{ref}}}}}, \quad (6)$$

where j_{ref} and f_{ref} represent the Colburn and friction factors for the reference geometry, respectively. In the present study, the reference geometry is the fin with $L_h = 0$ mm. The values of the JF factor are compared with the reference geometry.

The characteristics of the JF factor variable with the mean value of the frontal velocity of the airstream are shown in Figure 13. As one can see, the first two values of louver height (1.5 and 2.5 mm) improved effectiveness by a maximum of about 0.13. The trends of their changes are similar. The maximum value of JF was obtained for the largest airflow velocity, but for the velocity of 1 m/s, there is almost no growth at all. The geometry with the louver height of 3.5 mm shows better performance but only a slight

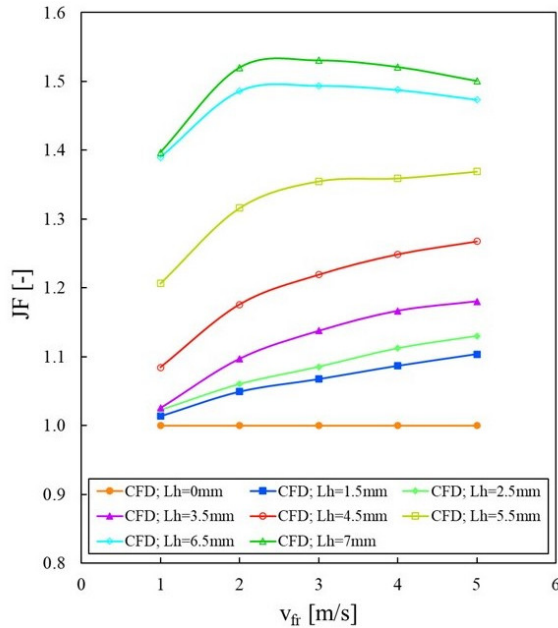


Figure 13: Characteristics of JF factor *vs.* the mean value of the frontal velocity of airstream.

improvement for small velocity (1 m/s). The maximum enhancement is observed for 5 m/s airflow ($JF = 0.181$). Next geometry ($L_h = 4.5$ mm) increased the value of JF in the range of 0.084 to 0.267. The improvement was achieved in the whole examined range of airflow velocity. A similar situation is in the case of geometry with $L_h = 5.5$ mm. The performance increased in the whole velocity range and the value of JF enhancement is from 0.206 to 0.369. The two last geometries, i.e., with louver heights of 6.5 mm (real object L_h) and 7 mm, show a similar trend. The effectiveness improved in a whole range of tested velocities and the maximum value was achieved for 3 m/s. The maximum JF improvement is observed for 7 mm geometry for the velocity of 3 m/s and it is 0.531.

Figure 14 demonstrates the effect of airflow velocity on the JF factor depending on the louver height. The trend of improvement for each height is similar but it is the worst for the velocity of 1 m/s. For this velocity, the improvements can be noted for L_h larger than 3.5 mm. The best performance is achieved for the maximum value of L_h at the velocity of 3 m/s. It can be explained by an occurrence of a flow regime in which the flow is driven by louvers, but there is a smaller pressure drop than in the case of the highest velocity. This is the reason why this area of exploitation ($L_h = 7$ mm; $v_{fr} = 3$ m/s) brings better effects.

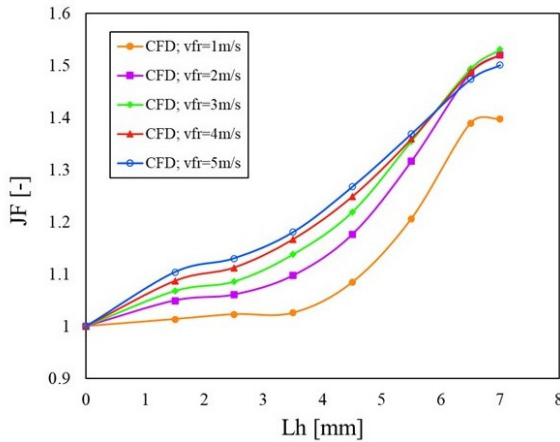


Figure 14: Characteristics of JF factor *vs.* louver height.

Figures 15 and 16 show the comparison of velocity and temperature distribution, respectively, in the air domain for $L_h = 0$ mm and 7 mm (minimum and maximum height). The comparison is based on the parameters' distri-

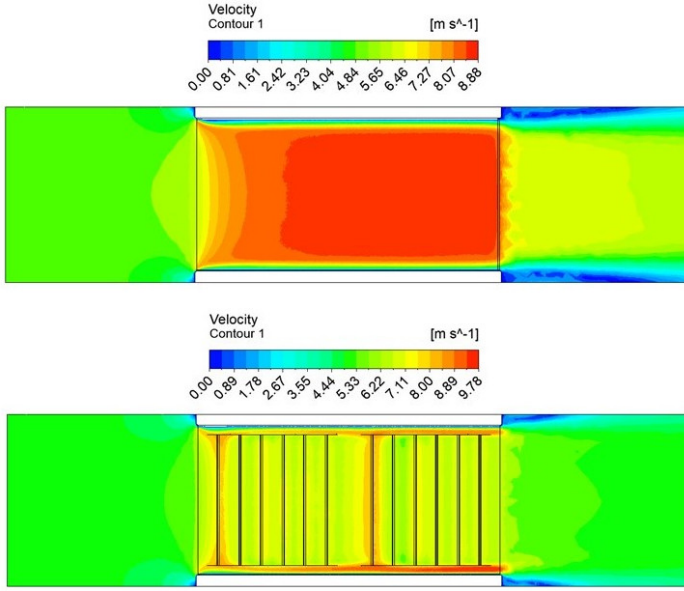


Figure 15: Distribution of velocity inside the air channel of MCHE: $L_h = 0$ mm (top), $L_h = 7$ mm (bottom).

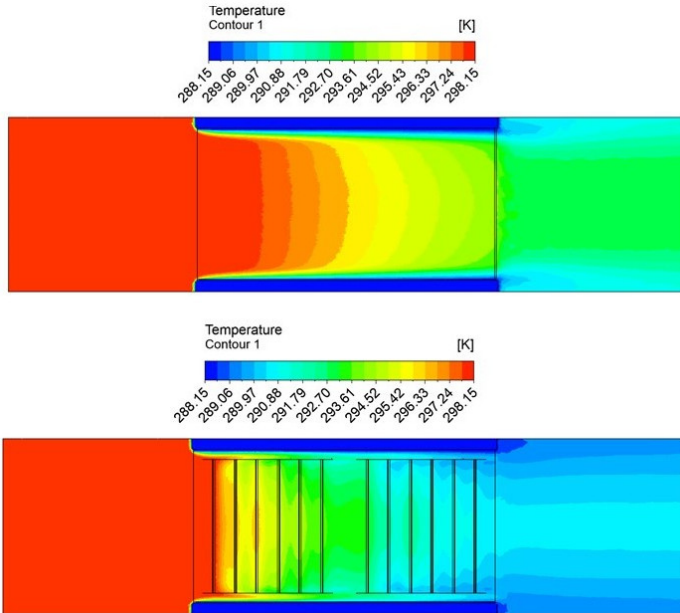


Figure 16: Distribution of temperature in the air channel of MCHE: $L_h = 0$ mm (top), $L_h = 7$ mm (bottom).

bution on the vertical plane in the center of the air channel in the flow direction, obtained for 5 m/s inlet velocity. The influence of louvers on the velocity distribution can be observed in Fig. 15. For the maximum velocity of the air stream (5 m/s), the area of maximum velocity for the plain fin geometry is much wider than for the highest louver case (7 mm). Additionally, the area of vortex below the flat tube is better observable in the plain fin. As for the temperature distribution, faster cooling can be noticed at the maximum louver height ($L_h = 7$ mm, Fig. 16 (bottom picture)). A cooling effect similar to the plate fin is observed in the half-length of the flow channel.

5 Conclusions

- The effectiveness of the cooling is rising with an increase of L_h .
- In terms of the JF factor, the highest value was achieved in the tested range for geometry with the maximum louver height ($L_h = 7$ mm).
- The best performance is achieved in the range of 2–4 m/s, where there are smaller pressure drops and louver-directed flow of the medium.

Acknowledgements

This paper has been completed while the first and second authors were Doctoral Candidates in the Interdisciplinary Doctoral School at the Lodz University of Technology, Poland.

Received 8 March 2023

References

- [1] Boeng J., Marcon A.A., Hermes C.J.L.: *Air-side heat transfer and pressure drop characteristics of microchannel evaporators for household refrigerators*. Int. J. Heat Mass Transf. **147**(2020), 2, 118913.
- [2] Huang Z., Ling J., Hwang Y., Aute V., Radermacher R.: *Airside heat transfer and friction characteristics of a 0.8 mm diameter bare tube heat exchanger*. Heat Transf. Eng. **41**(2019), 8, 1–11.
- [3] Srisomba R., Asirvatham L.G., Mahian O., Dalkilic A.S., Awad M.M., Wongwises S.: *Air-side performance of a micro-channel heat exchanger in wet surface conditions*. Therm. Sci. **21**(2017), 1, 375–385.

- [4] Dogan B.I., Altun Ö., Ugurlubilek N., Tosun M., Sariçay T., Erbay L.B.: *An experimental comparison of two multi-louvered fin heat exchangers with different numbers of fin rows*. Appl. Therm. Eng. **91**(2015), 12, 270–278.
- [5] Prabakaran R., Dhasan L.M., Prabhakaran A., Jha K.K.: *Experimental investigations on the performance enhancement using minichannel evaporator with integrated receiver-dryer condenser in an automotive air conditioning system*. Heat Transf. Eng. **40**(2018), 2, 667–678.
- [6] Vaisi A., Esmailpour M., Taherian H.: *Experimental investigation of geometry effects on the performance of a compact louvered heat exchanger*. Appl. Therm. Eng. **31**(2011), 11, 3337–3346.
- [7] Ribeiro F., de Conde K., Garcia E.C., Nascimento I.P.: *Heat transfer performance enhancement in compact heat exchangers by the use of turbulators in the inner side*. Appl. Therm. Eng. **173**(2020), 6, 115188.
- [8] Ayad F., Benelmir R., Idris M.: *Thermal-hydraulic experimental study of louvered fin-and-flat-tube heat exchanger under wet conditions with variation of inlet humidity ratio*. Appl. Therm. Eng. **183**(2021), 1, 116218.
- [9] Cao X., Wang X., Song Q., Wang D., Li Y.: *Experimental investigation on the heat transfer and pressure drop characteristics of R600a in a minichannel condenser with different inclined angles*. Appl. Therm. Eng. **196**(2021), 9, 117227.
- [10] Yue C., Zhang Q., Zhai Z., Ling L.: *CFD simulation on the heat transfer and flow characteristics of a microchannel separate heat pipe under different filling ratios*. Appl. Therm. Eng. **139**(2018), 7, 25–34.
- [11] Qian Z., Wang Q., Cheng J., Deng J.: *Simulation investigation on inlet velocity profile and configuration parameters of lower fin*. Appl. Therm. Eng. **138**(2018), 6, 173–182.
- [12] Saleem A., Kim M.H.: *CFD analysis on the air-side thermal-hydraulic performance of multi-louvered fin heat exchangers at low Reynolds numbers*. Energies **10**(2017), 6, 823.
- [13] Shinde P., Schäfer M., Lin C.: *Numerical investigation of micro-channeled lower fin aluminum heat exchangers at low Reynolds number*. ASME 2016 Heat Transfer Summer Conf., Washington 2016.
- [14] Karthik P., Kumaresan V., Velraj R.: *Experimental and parametric studies of a louvered fin and flat tube compact heat exchanger using computational fluid dynamics*. Alex. Eng. J. **54**(2015), 4, 905–915.
- [15] Dezan D.J., Salviano L.O., Yanagihara J.I.: *Interaction effects between parameters in a flat-tube louvered fin compact heat exchanger with delta-winglets vortex generators*. Appl. Therm. Eng. **91**(2015), 12, 1092–1105.
- [16] Kang H., Hyejung C., Kim J. H., Jacobi A.M.: *Air-side heat transfer performance of lower fin and multi-tube heat exchanger for fuel-cell cooling application*. J. Fuel Cell Sci. Technol. **11**(2014), 4, 041004.
- [17] Martínez-Ballester S., Corberán J.M., González-Maciá J.: *Numerical model for microchannel condensers and gas coolers: Part II – Simulation studies and model comparison*. Int. J. Refrig. **36**(2013), 1, 191–202.

- [18] Kumar R., Vijayaraghavan S., Govindaraj D.: *Numerical and analytical approach to study condensation for automotive heat exchangers*. Mater. Today: Proc. **52**(2022), 3, 556–564.
- [19] Kowalczyk M.J., Łęcki M., Romaniak A., Warwas B., Gutkowski A.N.: *Investigations of thermal-flow characteristics of minichannel evaporator of air heat pump*. Archiv. Thermodyn. **41**(2021), 4, 261–279.
- [20] Kang H., Jun G.W.: *Heat transfer and flow resistance characteristics of lower fin geometry for automobile applications*. J. Heat Transf. **133**(2011), 10, 101802.
- [21] Yun J.Y., Lee K.S.: *Influence of design parameters on the heat transfer and flow friction characteristics of the heat exchanger with slit fins*. Int. J. Heat Mass Transf. **43**(2000), 7, 2529–2539.
- [22] Ansys, Inc. *Ansys CFX-Pre User's Guide*. 2021.

Performance analysis of a lithium-ion battery of an electric vehicle under various driving conditions

SHREYA DHAWAN^a
AANCHAL SABHARWAL^b
RUPALI PRASAD^b
SHREYA SHREYA^b
AARUSHI GUPTA^b
YUSUF PARVEZ^{c*}

^a Duke University, Durham, USA

^b Indira Gandhi Delhi Technical University for Women, Mechanical and Automation Engineering, New Delhi, India

^c Maulana Azad National Urdu University, Mechanical Engineering, Cuttack, Odisha, India

Abstract Conventional fuels are the primary source of pollution. Switching towards clean energy becomes increasingly necessary for sustainable development. Electric vehicles are the most suitable alternative for the future of the automobile industry. The battery, being the power source, is the critical element of electric vehicles. However, its charging and discharging rates have always been a question. The discharge rate depends upon various factors such as vehicle load, temperature gradient, surface inclination, terrain, tyre pressure, and vehicle speed. In this work, a 20 Ah, 13S-8P configured lithium-ion battery, developed specifically for a supermileage custom vehicle, is used for experimentation. The abovementioned factors have been analyzed to check the vehicle's overall performance in different operating conditions, and their effects have been investigated against the battery's discharge rate. It has been observed that the discharge rate remains unaffected by the considered temperature difference. However, overheating the battery results in thermal runaway, damaging and reducing its life. Increasing the number of brakes to 15, the impact on the discharge rate is marginal; however, if the

*Corresponding Author. Email: parvez_yusuf01@yahoo.com

number of brakes increases beyond 21, a doubling trend in voltage drops was observed. Thus, a smoother drive at a slow-varying velocity is preferred. Experiments for different load conditions and varying terrains show a rise in discharge with increasing load, low discharge for concrete, and the largest discharge for rocky terrain.

Keywords: Clean energy; Lithium-ion battery; Discharge rate; Voltage; EV; Super-mileage; Environment

1 Introduction

Encouraging renewable and alternative energy is the need of time for sustainable development. With the current speed of globalisation and thriving industrialization, the worldwide energy demand has increased promptly. Indeed, fossil fuels have made a significant impact in the previous two centuries in worldwide development; however, global climate change and the depletion of fossil fuels have become major constraints. As per the data mentioned in the literature [1–3], it has been anticipated that with the 5% annual increment in the present production rate of oil (1.41%), coal (1.64%), and natural gas (2.69%), the fossil fuels will barely survive for next 50 years. Moreover, annual fossil fuel consumption on a global scale has increased by 1.77%. However, the spread of coronavirus disease 2019 (COVID-19) and subsequent restrictions have impacted such fuels' international supply and demand. Restricting the use of fossil fuels is one of the prime focuses of the Paris Climate Accords adopted in 2015; the committee has agreed to decrease the overall temperature below 1.5°C [3, 4].

Alternative energy sources have been promoted and commercialized to overcome environmental and other major challenges [5]. As per the latest data in the literature [6, 7], about 22 cities out of 30 most polluted cities in the world are from India. Air pollution has become a major global issue, and millions of lives are at risk due to severe air pollutants released from the transportation and industrial sectors [8, 9]. After so many cautions and various action plans, the issue is still showing an alarming trend. One such modification and action is switching towards electric or hybrid vehicles. Although there are lots of constraints, the popularity of electric vehicles is increasing. Consequently, lots of research is being processed to overcome the shortcomings and improve overall performance. Furthermore, the need for electric vehicles are even more justified, considering the environmental

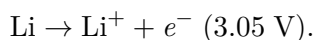
degradation. The search for alternative power sources has been a constant struggle, and electric cars can potentially be a solution. The overall cost of ownership, including battery cost, drivetrain cost, fuel prices, and maintenance costs with time, will have better pricing in the future with more research in the fields of battery technology [10].

Electric mobility is an important aspect of the energy transition. Electric vehicles (EVs), even with lower maintenance, higher well-to-wheel efficiency, and the obvious environmental and economic benefits, still have the biggest challenge of low range, low efficiency, longer charging times, limited infrastructure, and high capital cost of batteries [11, 12]. For an electric vehicle to be resourceful, the main characteristics to be focused on are that it should run entirely on cheap, small, and efficient electric motors, requires low maintenance, has a large battery for long range, and has a fast-charging capability. Consequently, battery charging conditions should be maintained to supply uninterrupted power [13]. Therefore, significant research, analysis, and optimization of batteries, which act as a portable energy reserve for an e-vehicle, are of utmost importance. The longevity of batteries is related to charging and discharging as well as ambient conditions of use.

Among many other batteries, the lithium-ion rechargeable battery has been a focal point of research and application. It has the potential to power not only electric vehicles but also various electronic consumer goods, energy storage systems, aerospace, robotic and military applications [14, 15]. Compared to traditional batteries, lithium-ion batteries charge faster, last longer, and have high power density for longer battery life in a lighter package [16, 17].

Lithium atoms at the anode get ionized and separated from their electrons during the lithium-ion battery's discharge cycle. The lithium ions then move to the cathode, recombining with electrons and getting electrically neutralized. They move through the electrolyte and are small enough to pass through a micro-permeable separator between the anode and the cathode [18]. Due to the small size of lithium-ion, lithium-ion batteries can produce a very high voltage and charge storage per unit mass and volume.

- Lithium (Li) batteries are powered by the lithium oxidation reaction:



- The oxidation potential pushes electrons generated at the anode through external circuitry, thus delivering energy.

- Different types of materials can be used as electrodes in a lithium-ion battery. One of the most typical compositions is that of lithium cobalt oxide (cathode) and graphite (anode), which can be usually discovered in compact electronic devices such as mobile phones and laptops [19]. Additional materials that can be used as cathodes include lithium manganese oxide and lithium iron phosphate. Lithium-ion batteries ordinarily use ether as an electrolyte.

1.1 Advantages

Lithium-ion cells offer a considerable advantage of low self-discharge rate compared to rechargeable cells, namely, NiMH and Ni-Cad forms. This helps deal with the concern of the range of EVs and more prolonged operations before discharge. The cell voltage of lithium-ion battery cells is higher than other standard batteries available; thus, the number of cells required for the same power generation is smaller. Lithium is the lightest of all metals, has the greatest electrochemical potential, and provides the largest energy density for its weight [20]. Two of the main reasons electric cars failed in the past were the size and weight requirements of the battery installed. Earlier, fuel-powered vehicles proved to be a more convenient and effective way of energy storage [21]. However, the development in battery technologies has made them wonderfully compact and light. With such progress, electric cars will be lighter than ever, taking the weight of the drivetrain and the energy storage together into account. Lithium-ion batteries have a reasonably high energy and power density. The broadly accepted lithium-ion battery should have a longer life along with high energy intensity [22, 23].

1.2 Disadvantages

One charge plus one discharge is known as a cycle, and the number of times a battery supports its charging and discharging without its decay is called the life cycle. The battery life of lithium-ion batteries isn't just dependent on life cycles but also on environmental conditions. Exposing them to high temperatures reduces their capacity. Also, lithium is an abundantly available resource, but its current extraction is not cost-effective [24].

The current energy densities of batteries aren't at par with the fuels used in IC engines. Battery charging infrastructure is currently under development as well. Controlled charging is an additional requirement for the safe

operation of the battery and the vehicle. To ensure continuous safe use of the battery without its degradation, a novel technique, i.e., a dynamic early recognition framework was proposed to distinguish the abnormal batteries from normally degrading batteries before their capacity drops [25].

Electric vehicles may catch fire as the Lithium-Ion battery is susceptible to a short circuit within one or more cells that make up the battery [26]. The overheating batteries could result in thermal runaway, damaging the vehicle and its life [27]. The heat can ignite the chemicals within the battery, and the fire can spread rapidly and efficiently. Various articles in the literature have discussed the way to safeguard the battery and hence the electric vehicle. Consequently, a control strategy was discussed by Dar *et al.* [28] to protect the battery and enhance its life. The article proposed an offboard charger for charging lithium-ion batteries used in EVs. The methodology used for charging safeguards the battery by protecting the battery from overvoltages. The considered charger has the ability to transfer power in two directions to transfer the additional power back to the grid and hence, protect the battery from overcharging.

1.3 Scope

It is usually difficult to predict the factors responsible for battery ageing and degradation. Some studies conclude the type of degradation, whether chemical or mechanical, by analyzing the battery's condition over time [29–32]. However, limited studies infer the ergonomic or environmental factors that may influence the said deterioration. This paper analyzes the trend of voltage drop of a lithium-ion battery as it discharges due to various factors and conditions. This paper aims to explore the multiple conditions contributing to faster discharging, which can be manipulated or evicted. The primary research concentrates on external factors affecting the discharge of the battery, namely, vehicle load, ground terrain, braking conditions, and temperature. To consolidate, the variation in the voltage of the battery has been investigated by varying each factor separately and a few factors simultaneously to understand the real-time impact on the battery.

This paper includes modifications in operational parameters to study their effect on vehicle efficiency, which is directly linked to the battery. The aim is to conduct testing of voltage drops under various conditions and understand the combined impact of these parameters. The present research will help predict the battery's efficiency and its dependency on external factors [33]. This study can further aid in optimizing the battery

and its application to its maximum potential. The enhancement and progression of battery technologies, sustainable and manufacturable battery pack, and robust design of the battery pack act as a major catalyst in the promotion of electric vehicles as a means of transportation and energy reserve [34].

The battery under observation is lithium-ion, one of the most prominent propellers for EVs. Apart from vehicles, it finds use in solar energy storage. When these two applications are combined, it will pave the way for the energy transition that will be sustainable, economical, efficient, and convenient nonetheless [35–37]. Thus, research about lithium-ion batteries, their study, analysis, and up-gradation will be a breakthrough in achieving this conclusion.

In 2021, the automobile industry aspires to have over 50 per cent of all new models equipped with EV drivetrains [38]. This is possible as many original equipment manufacturers (OEMs) have aimed to introduce models to their production lines, which is nonetheless aided by government policies. In the coming decade, the EVs produced would comprise further optimized versions of their electronic systems due to advancements in the methods of monitoring energy consumption [39].

2 Materials and method

2.1 Materials and configuration

The main focus of this work is the lithium-ion battery. The battery used in the following analysis is an essential component of an existing project that involved the design and fabrication of a supermileage vehicle. The vehicle was conceptualized and manufactured by Team Panthera for the Shell Eco-Marathon, Asia, and is illustrated in Fig. 1. The car was designed on Solidworks software [40]. The specifications of the battery cater to the vehicle. The experimental analysis for the battery performance and voltage drop conducted later in this research has been done *via* the said supermileage vehicle. The configuration of the battery has been charted in Table 1. The authors had begun taking readings with an initial voltage of 53.4 V. The observations were taken using a voltmeter enabled in the vehicle itself. The shell vehicle consists of a compact chassis with subsystems specified in Table 2.



Figure 1: Illustration of the electric vehicle used for experimental analysis.

Table 1: Custom lithium-ion battery configuration.

Custom battery configuration	
Current rating	20 Ah
Cells arrangement	13S 8P
Rated voltage	48 V
Number of batteries	1

Table 2: Supermileage vehicle subsystems.

Chassis	Structural members: Aluminium 4130	Single passenger seat
Steering	Steering assembly	
Brake assembly	Brake pedal	Braking handle mounted on the steering
Battery	Lithium-lon battery with mount and connections	
Transmission	Acceleration system, including the pedal	
Miscellaneous	Honking system	

2.2 Method

The electrical connections of the vehicle used for the present research are illustrated in Fig. 2. The positive terminal connects the battery to the kill switch, which is externally accessible so that the vehicle can be stopped

in an emergency. There are three wires connected to the motor controller. The fourth wire is a Hertz sensor which senses the frequency and sends the signal to the motor regarding the speed. The command given on the throttle is accessed by the controller and transmitted to the motor. The negative terminal connects the battery directly to the controller and speedometer. Also, the kill switch is connected directly to the speedometer and controller. The battery usually takes 5–6 h to charge to its maximum capacity. The speed reading is observed on an external speedometer software.

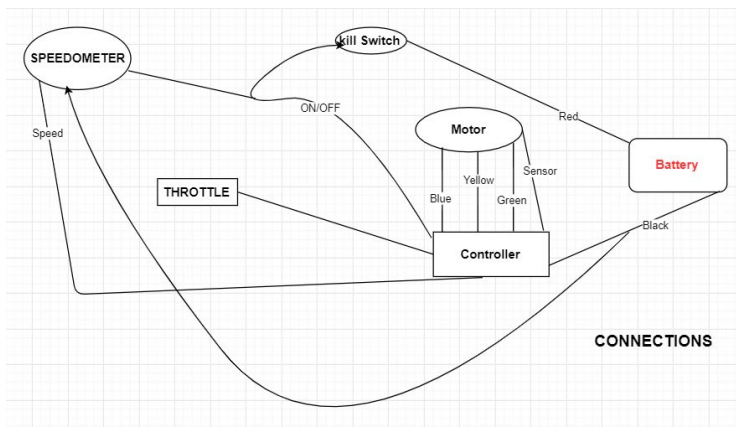


Figure 2: Illustration depicting the electrical connections of the electric vehicle.

For readings, the experiments were conducted at different times of the day to get the different environmental temperatures. Accordingly, the temperature of the battery taken and its effects were noticed. The experimentation started in the early morning when it was slightly chilly, and then based on the environment temperature, it continued to the afternoon when it was relatively hotter and then in the night when it was cold again. A thermometer was installed with the vehicle to measure the environmental temperature. Additionally, the load on the vehicle was measured from the weighing scale and varied from 49 kg to 55 kg. Also, a voltmeter was installed with the vehicle to measure the voltage drop during the experiments.

The analysis and observations have been performed from start to end on the supermileage vehicle throughout the same day. The mileage observed was approximately 119 km/kWh. The four essential parameters such as temperature, number of brakes, load and surface terrains, have been considered for experimentation as illustrated in Table 3.

Table 3: List and range of parameters evaluated during experimentation.

Parameters considered	Range defined
Temperature	6°C
Number of brakes	20 brakes
Load	6 kg
Terrain	muddy + grass, concrete

1. The first parameter, the temperature, has been varied to check the variation of the discharging of the battery. Temperature variation was achieved through changes in the temperature of the surroundings from morning to evening. The discharge at temperature differences of 2°C has been observed by keeping the load constant.
2. The second parameter, the number of brakes, has been observed by keeping the temperature, load, and distance travelled constant. The number of brakes applied is increased for a fixed distance.
3. The third parameter is load. While keeping the temperature constant and increasing the load by 6 kg, the discharge rate has been analyzed in gradual increments.
4. The final parameter, the terrain, has been changed twice to check the battery's voltage drop. The experiment was conducted on: (1) a muddy-grass road and (2) a concrete road.

3 Result and discussions

The variation of discharge with temperature, load, terrain, and the number of brakes is represented in graphs and charts for efficient visualization of results.

3.1 Temperature variation analysis

As illustrated in Fig. 3, the vehicle's voltage drops with an increase in temperature. This is associated with battery performance and its chemical reactions [41]. The initial drop is observed at 0.3 V, which is steeper till 24°C (53.8 V to 53.5 V), followed by a short phase with a reduced drop, i.e., 66% of the initial fall (53.5 V to 53.3 V). The voltage drop is observed to

get steeper again (53.3 V to 53.0 V) beyond 26°C. Low temperatures show a reduction in the ionic conductivity of the battery [42, 43]. In contrast, high temperatures tend to increase the rate of thermal ageing, thereby shortening the life of the lithium-ion battery [44, 45].

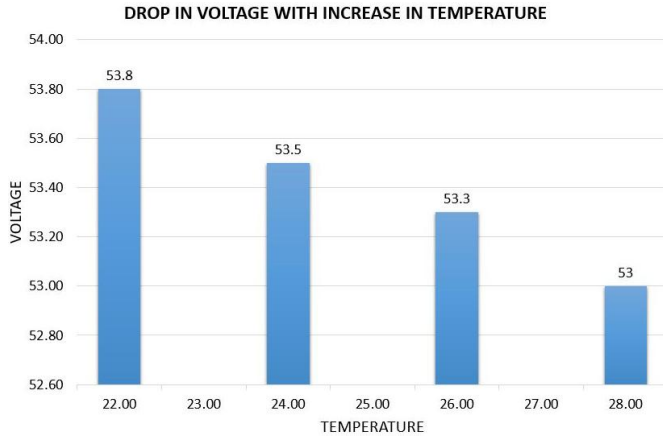


Figure 3: Battery voltage *versus* temperature in degrees Celsius to depict voltage drop with temperature.

3.2 Number of brakes variation analysis

Figure 4 shows that the voltage drop increases with the number of brakes applied due to high energy losses in the conventional braking system [46]. With nine brakes, the voltage drop is negligible, as seen from the reading change from 52.2 V to 52.1 V, i.e., 0.1 V. When the number of brakes is increased by 6 to 15 for the same distance patch, the drop observed increases by 100%, i.e., 0.2 V (from 52.1 V to 51.9 V). With another increment of 6 brakes to 21, the drop increases by another 100% to 0.4 V (from 51.9 V to 51.4 V). This doubling trend in voltage drops is inferred to be highly worrisome and causes concern in EVs. The battery powers auxiliary systems. The brakes are a crucial part of the system and have an impact on the observed voltage drop. Therefore, it is recommended to adopt energy-efficient driving practices to develop an optimal speed. This, in turn, reduces the aerodynamic drag and hence, the power consumption. Moreover, it is also recommended to install a regenerative braking system. However, existing research has proved that even with regenerative braking, optimal velocity profiles can be beneficial in reducing electromechanical energy conversion

losses [47]. Several researchers have studied the benefits of regenerative braking systems in the past. Recovering the kinetic energy evolved can substantially reduce the load on the lithium-ion battery [48–52].

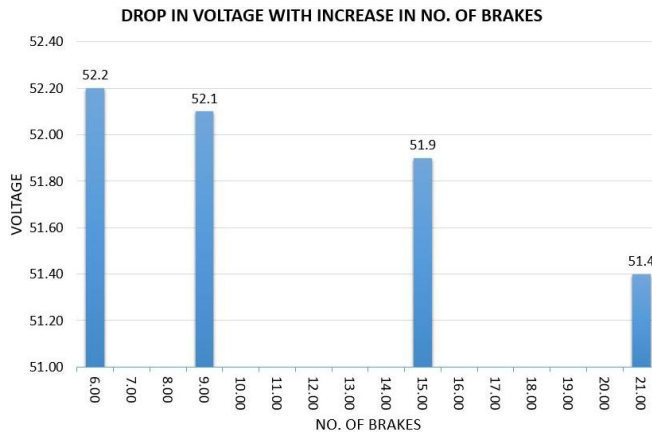


Figure 4: Battery voltage *versus* number of brakes to depict voltage drop with speed variation.

3.3 Load variation analysis

The voltage of the battery drops drastically with an increase in the load, as illustrated in Fig. 5. At 49 kg, the observed drop is 0.3 V, from 53.3 V to 53.0 V. When the load gradually increases to 55 kg, the voltage drop also

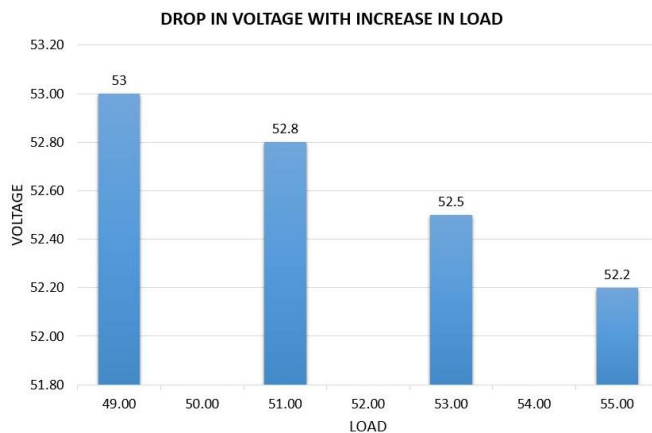


Figure 5: Battery voltage *versus* load in kg to depict voltage drop with load.

increases by 167% to 0.8 V, from 53.0 V to 52.2 V. This is because, as the load increases, the current through the battery resistance increases; thus, the voltage drop increases [53].

3.4 Terrain variation

The terrain was switched from muddy-grass to concrete to investigate the impact of road surface roughness on the change in voltage drop. As depicted in Table 4, the voltage drop observed for a concrete road and a muddy-grass, i.e., a relatively rugged road, was 0.1V (51.5 V to 51.4 V, and 51.4 V to 51.3 V, respectively) for the same distance with the same loading and environmental conditions. Therefore, the average drop is considered relatively the same across different terrains except for rocky and puddled terrains due to the added load on suspension and the difficulty of traction.

Table 4: Drop in voltage with variable terrain.

Terrain	Voltage drop (V)	Change in voltage (V)
Concrete	51.5 to 51.4	0.1
Muddy + Grass	51.4 to 51.3	0.1
Rocky	51.3 to 51.0	0.3

A group of researchers studied the performance of an EV powered by a lithium-ion battery in the hilly terrains of Vermont and found a 13% increase in energy consumption without regenerative braking [54]. It is safe to conclude that terrain is an essential, if not highly influential, characteristic that may impact the battery's performance.

4 Conclusions

In the present research, a lithium-ion battery, part of a competitive supermileage vehicle, has been considered. Various factors, such as vehicle load, temperature gradient, road surface terrain, and vehicle speed, have been analyzed to check the vehicle's overall performance in different operating conditions. The effect of these factors on the battery discharging rate has also been investigated. The following remarks have been concluded as mentioned below.

- From the analysis, it was observed that the discharge rate remained constant for the considered temperature difference of 6°C . However, warming a battery decreases internal resistance and improves the electrochemical reaction. Thus, operating a battery at a high temperature improves battery performance. Therefore, increasing temperature up to a limit will improve the performance. However, overheating batteries could result in thermal runaways, damaging the vehicle and its life. Therefore, batteries are often accompanied by cooling systems.
- Secondly, increasing the number of brakes increased discharge. With nine brakes, the voltage drop is negligible (0.1 V), however, when the number of brakes risen from 9 to 15 for the same distance patch, the drop observed increased to 0.2 V. With another increment of 15 brakes to 21, the drop increases further to 0.5 V. Hence, it is clear that starting increasing brakes will not impact much on the discharge rate, however, when the number of brakes increases beyond 15, the battery will discharge with a much faster rate.
- Lastly, a heavier load requires more energy to operate the electric vehicles; this voltage drop is more significant with a higher load, and hence, the battery will discharge more. Additionally, the average voltage drop is relatively the same across different terrains except for rocky and puddled terrains due to the added load on suspension and the difficulty of traction.

It is important to acknowledge the results validated by experimentation and make subsequent changes to our method of usage. By fabricating lightweight vehicles, the discharge rate may be controlled. This is achieved by smart weight-reduction strategies employed while choosing the chassis material, removing material without hampering the strength of the component, etc. Moreover, some additional measures taken to limit the discharge rate are mentioned below.

1. As recommended, keeping the tyre pressure maximum according to its model specifications.
2. Charging and discharging the battery to a moderate range of voltages. Extremely high and low voltages affect the battery life.
3. Usage at temperatures ranging between a few degrees of room temperature. At high temperatures, the electrochemical reactions that

power the battery occur at a higher rate as opposed to low temperatures, at which the chemical reaction rates reduce. Low temperature also causes low conductivity in lithium salts.

4. Reducing the number of brakes, especially abrupt braking, leads to a rapid drop in battery voltages which are otherwise quite slow in their discharge. Thus, a smoother drive at a slow-varying velocity keeps the battery from discharging soon.

Acknowledgements

The experiments were conducted at Indira Gandhi Delhi Technical University for Women (IGDTUW), Delhi. The authors are thankful to the entire Team Panthera for their consistent efforts during the development of the supermileage vehicle. We would also like to show our gratitude to Dr Manoj Soni, Faculty Advisor of Team Panthera, for his consistent help and support during the course of the development of the vehicle. The authors are thankful to the Head of Department, Mechanical and Automation Engineering (MAE), for supporting and allowing us to use the various departmental labs as per the requirement of the work presented. We would also like to show our gratitude to all the faculty and staff members of the MAE department who directly or indirectly helped us during the course of the present research.

Received 7 January 2023

References

- [1] Abas N., Kalair A., Khan N.: *Review of fossil fuels and future energy technologies*. Futures **69**(2015), 31–49. doi: [10.1016/j.futures.2015.03.003](https://doi.org/10.1016/j.futures.2015.03.003)
- [2] Dudley B.: *BP Statistical Review of World Energy 2019* (68th Edn.). BP p.l.c., London 2019. <https://www.bp.com/content/dam/bp/business-sites/en/global/corporate/pdfs/energy-economics/statistical-review/bp-stats-review-2019-full-report.pdf> (accessed 8 Dec. 2022).
- [3] Siram J., Sahoo N., Saha U.K.: *Changing landscape of India's renewable energy and the contribution of wind energy*. Clean. Eng. Technol. **8**(2022), 100506. doi: [10.1016/j.clet.2022.100506](https://doi.org/10.1016/j.clet.2022.100506)
- [4] Welsby D., Price P., Pye S., Ekins P.: *Unextractable fossil fuels in a 1.5° C world*. Nature **597**(2021), 230–234. doi: [10.1038/s41586-021-03821-8](https://doi.org/10.1038/s41586-021-03821-8)

- [5] Choudhary P., Sachar S., Khurana T., Jain U., Parvez Y., Soni M.: *Energy analysis of single cylinder 4-stroke diesel engine using diesel and diesel-biodiesel blends*. Int. J. Appl. Eng. Res. **13**(2018), 12, 10779–10788.
- [6] Kanaujia A., Bhati M., Lakshmanan S., Nishad S. N., Bhattacharya S.: *Air Pollution in India: A Critical Assessment and Suggestive Pathways for Clean Air. A project on Studies on Contemporary Challenges*. CSIR-NIScPR Discuss. Pap. Ser., New Delhi 2022.
- [7] Wallington T.J., Anderson J.E., Dolan R.H., Winkler S.L.: *Vehicle emissions and urban air quality: 60 years of progress*. Atmosphere **13**(2022), 5, 650. doi: [10.3390/atmos13050650](https://doi.org/10.3390/atmos13050650)
- [8] Jain U., Khurana T., Sachar S., Choudhary P., Parvez Y.: *Performance characteristics and energy analysis of a 4-stroke single cylinder diesel engine using diesel and diesel-kerosene blends*. Int. J. Res. Anal. Rev. **5**(2018), 3, 194–203.
- [9] Srivastava S., Chaubey H., Parvez Y.: *Performance evaluation of CI engine using diesel, diesel-biodiesel blends and diesel-kerosene blends through exergy analysis*. IOP Conf. Ser.-Mater. Sci. **691**(2019), 1. doi: [10.1088/1757-899X/691/1/012066](https://doi.org/10.1088/1757-899X/691/1/012066)
- [10] Kim T.H., Park J.S., Chang S.K., Choi S., Ryu J.H., Song H.K.: *the current move of lithium ion batteries towards the next phase*. Adv. Energ. Mater. **2**(2012), 7, 860–872. doi: [10.1002/aenm.201200028](https://doi.org/10.1002/aenm.201200028)
- [11] Brown S., Pyke D., Steenhof P.: *Electric vehicles: The role and importance of standards in an emerging market*. Energ. Policy **38**(2010), 7, 3797–3806. doi: [10.1016/j.enpol.2010.02.059](https://doi.org/10.1016/j.enpol.2010.02.059)
- [12] Botsford C., Szczepanek A.: *Fast charging vs. slow charging: Pros and cons for the new age of electric vehicles*. EVS24 Int. Battery, Hybrid, Fuel Cell Electric Vehicle Symp, Stavanger, May 13–16, 2009.
- [13] Kalyan R., Murali V., Pitchaimuthu R.: *Coordinate control of grid power, battery soc and LVRT protection in single VSC tied DFIG*. Distrib. Gener. Alternat. Energ. J. **37**(2022), 587–608. doi: [10.13052/Dgaej2156-3306.37310](https://doi.org/10.13052/Dgaej2156-3306.37310)
- [14] Revankar S.T.: *Chemical energy storage*. In: *Storage and Hybridization of Nuclear Energy: Techno-economic Integration of Renewable and Nuclear Energy* (H. Bindra, S. Revankar, Eds.). Elsevier, 2019, 177–227. doi: [10.1016/b978-0-12-813975-2.00006-5](https://doi.org/10.1016/b978-0-12-813975-2.00006-5)
- [15] Shastri S., Parvez Y., Chauhan N.R.: *Wireless power transfer system for scorbots Er-4u robotic arm*. Int. J. Power Energ. Sys. **40**(2020), 3, 103–111. doi: [10.2316/J.2020.203-0044](https://doi.org/10.2316/J.2020.203-0044)
- [16] Harks P.P.: *Characterization and development of high energy density Li-ion batteries*. TU Delft, 2019. doi: [10.4233/uuid:cab44efd-8a4c-4b4d-8168-bd64738adb64](https://doi.org/10.4233/uuid:cab44efd-8a4c-4b4d-8168-bd64738adb64) (accessed 8 Dec. 2022).
- [17] Salunke A.D., Chamola S., Mathieson A., Boruah B.D., Volder M.D., Ahmad S.: *Photo-rechargeable Li-Ion batteries: device configurations, mechanisms, and materials*. ACS Appl. Energ. Mater. **5**(2022), 7, 7891–7912.
- [18] Whittingham M.S.: *Introduction: Batteries*. Chem. Rev. **114**(2014), 23, 11413. doi: [10.1021/cr500639y](https://doi.org/10.1021/cr500639y)

- [19] Mekonnen Y., Sundararajan A., Sarwat A.I.: *A review of cathode and anode materials for lithium-ion batteries*. Southeast Conf. 2016, Norfolk, (2016), 1–6. doi: [10.1109/secon.2016.7506639](https://doi.org/10.1109/secon.2016.7506639)
- [20] Oswal M., Paul J., Zhao R.: *A Comparative Study of Lithium-Ion Batteries*. Univ. of Southern California, 2010.
- [21] Situ L.: *Electric vehicle development: The past, present & future*. In: Proc. 3rd Int. Conf. on Power Electronics Systems and Applications (PESA), 2009, 1–3.
- [22] Koshika K., Suzuki H.: *Performance survey for Li-Ion battery in a hybrid vehicle with 105,000 km driving*. In: Abstr. ECS Meet. **MA2020-02**, 2020, 1051. doi: [10.1149/MA2020-0261051mtgabs](https://doi.org/10.1149/MA2020-0261051mtgabs)
- [23] Husain M.A., Rajput R., Gupta M.K., Tabrez M., Ahmad M.W., Bakhsh F.I.: *Design and implementation of different drive topologies for control of induction motor for electric vehicle application*. Distrib. Gen. Altern. Energ. J. **37**(2022), 4, 999–1026. doi: [10.13052/dgaej2156-3306.3746](https://doi.org/10.13052/dgaej2156-3306.3746)
- [24] Miao Y., Hynan P., Jouanne A.V., Yokochi A.: *Current Li-Ion battery technologies in electric vehicles and opportunities for advancements*. Energies **12**(2019), 6, 1074. doi: [10.3390/en12061074](https://doi.org/10.3390/en12061074)
- [25] Wang C., Chen Y., Zhang Q., Zhu J.: *Dynamic early recognition of abnormal lithium-ion batteries before capacity drops using self-adaptive quantum clustering*. Appl. Energ. **336**(2023), 120841. doi: [10.1016/j.apenergy.2023.120841](https://doi.org/10.1016/j.apenergy.2023.120841)
- [26] Goodenough J., Kim Y.: *Challenges for rechargeable Li batteries*. Chem. Mater. **22**(2010), 3, 587–603. doi: [10.1021/cm901452z](https://doi.org/10.1021/cm901452z)
- [27] Huang Z., Liu J., Zhai H., Wang O.: *Experimental investigation on the characteristics of thermal runaway and its propagation of large-format lithium ion batteries under overcharging and overheating conditions*. Energy **233**(2021), 121103. doi: [10.1016/j.energy.2021.121103](https://doi.org/10.1016/j.energy.2021.121103)
- [28] Dar U., Siddiqui A.S., Bakhsh F.I.: *Design and control of an off board battery charger for electric vehicles*. Distrib. Gen. Altern. Energ. J. **37**(2022), 4, 959–978. doi: [10.13052/dgaej2156-3306.3744](https://doi.org/10.13052/dgaej2156-3306.3744)
- [29] Seruga D., Gosar A., Sweeney C.A., Jaguemont J., Mierlo J.V., Nagode M.: *Continuous modelling of cyclic ageing for lithium-ion batteries*. Energy B **215B**(2021), 119079. doi: [10.1016/j.energy.2020.119079](https://doi.org/10.1016/j.energy.2020.119079)
- [30] Ge M.F., Liu Y., Jiang X., Liu. J.: *A review on state of health estimations and remaining useful life prognostics of lithium-ion batteries*. Measurement **174**(2021), 109057. doi: [10.1016/j.measurement.2021.109057](https://doi.org/10.1016/j.measurement.2021.109057)
- [31] Chandran V., Patil C.K., Karthick A., Ganeshaperumal D., Rahim R., Ghosh A.: *State of charge estimation of lithium-ion battery for electric vehicles using machine learning algorithms*. World Elect. Veh. J. **12**(2021), 38, 1–17. doi: [10.3390/wevj12010038](https://doi.org/10.3390/wevj12010038)
- [32] García A., Serrano J.M., Boggio S.M., Golke D.: *Energy assessment of the ageing phenomenon in Li-Ion batteries and its impact on the vehicle range efficiency*. Energ. Convers. Manage. **276**(2023), 116530. doi: [10.1016/j.enconman.2022.116530](https://doi.org/10.1016/j.enconman.2022.116530)
- [33] Xiong R., Pan Y., Shen W., Li H., Sun F.: *Lithium-ion battery aging mechanisms*. Renew. Sust. Energ. Rev. **131**(2020), 110048. doi: [10.1016/j.rser.2020.110048](https://doi.org/10.1016/j.rser.2020.110048)

- [34] Canteros M.L., Polansky J.: *Study of the heat pump for a passenger electric vehicle based on refrigerant R744*. Arch. Thermodyn. **43**(2022), 2, 17–36. doi: [10.24425/ather.2022.141976](https://doi.org/10.24425/ather.2022.141976)
- [35] Chen T., Jin Y., Lv H., Yang A., Liu M., Chen B., Chen Q.: *Applications of lithium-ion batteries in grid-scale energy storage systems*. T. of Tianjin Univ. **26**(2020), 208–217. doi: [10.1007/s12209-020-00236-w](https://doi.org/10.1007/s12209-020-00236-w)
- [36] Singh D., Chaubey H., Parvez Y., Monga A., Srivastava S.: *Performance improvement of solar PV module through hybrid cooling system with thermoelectric coolers and phase change material*. Sol. Energy **241**(2022), 538–552. doi: [10.1016/j.solener.2022.06.028](https://doi.org/10.1016/j.solener.2022.06.028)
- [37] Zhou Y., Wang F., Xin T., Wang X., Liu Y., Cong L.: *Discussion on international standards related to testing and evaluation of lithium battery energy storage*. Distrib. Gen. Altern. Energ. J. **37**(2022), 3, 435–448. doi: [10.13052/dgaej2156-3306.3732](https://doi.org/10.13052/dgaej2156-3306.3732)
- [38] Lane B.W., Betts N.M., Hartman D., Carley S., Krause R.M., Graham J.D.: *Government promotion of the electric car: Risk management or industrial policy?*. Eur. J. Risk Regul. (EJRR) **4**(2013), 2, 227–245.
- [39] Valle J.A.D., Viera J.C., Ansean D., Branas C., Luque P., Mantaras D.A., Pulido Y.F.: *Design and validation of a tool for prognosis of the energy consumption and performance in electric vehicles*. Transp. Res. Proc. **33**(2018), 35–42. doi: [10.1016/j.trpro.2018.10.073](https://doi.org/10.1016/j.trpro.2018.10.073)
- [40] Planchard D.: *Solidworks 2018 Reference Guide*. (2018). <https://files.solidworks.com/partners/pdfs/referenceguide.pdf> (accessed 8 Dec. 2022).
- [41] Lu Z., Yu X.L., Wei L.C., Cao F., Zhang L.Y., Meng X.Z., Jin L.W.: *A comprehensive experimental study on temperature-dependent performance of lithium-ion battery*. Appl. Therm. Eng. **158**(2019), 113800. doi: [10.1016/j.applthermaleng.2019.113800](https://doi.org/10.1016/j.applthermaleng.2019.113800)
- [42] Bandhauer T.M., Garimella S., Fuller T.F.: *A critical review of thermal issues in lithium-ion batteries*. J. Electrochem. Soc. **158**(2011), 3, R1–R5. doi: [10.1149/1.3515880](https://doi.org/10.1149/1.3515880)
- [43] Kong J., Yang F., Zhang X., Pan E., Peng Z., Wang D.: *Voltage-temperature health feature extraction to improve prognostics and health management of lithium-ion batteries*. Energy **223**(2021), 120114. doi: [10.1016/j.energy.2021.120114](https://doi.org/10.1016/j.energy.2021.120114)
- [44] Ma S., Jiang M., Tao P., Song C., Wu J., Wang J., Shang W.: *Temperature effect and thermal impact in lithium-ion batteries: A review*. Pr. Nat. Sci. Mater. Int. **28**(2018), 6, 653–666. doi: [10.1016/j.pnsc.2018.11.002](https://doi.org/10.1016/j.pnsc.2018.11.002)
- [45] Liu G., Ouyang M., Lu L., Li J., Han X.: *Analysis of the heat generation of lithium-ion battery during charging and discharging considering different influencing factors*. J. Therm. Anal. Calorim. **116**(2014), 1001–1010. doi: [10.1007/s10973-013-3599-9](https://doi.org/10.1007/s10973-013-3599-9)
- [46] Miri I., Fotouhi A., Ewin N.: *Electric vehicle energy consumption modelling and estimation – A case study*. Int. J. Energ. Res. **45**(2020), 501–520. doi: [10.1002/er.5700](https://doi.org/10.1002/er.5700)
- [47] Han J., Vahidi A., Sciarretta A.: *Fundamentals of energy efficient driving for combustion engine and electric vehicles: An optimal control perspective*. Automatica **103**(2019), 558–572. doi: [10.1016/j.automatica.2019.02.031](https://doi.org/10.1016/j.automatica.2019.02.031)

- [48] Gao Y., Chen L., Ehsani M.: *Investigation of the effectiveness of regenerative braking for EV and HEV*. SAE Transactions **108**(1999), 3184–190. doi: [10.4271/1999-01-2910](https://doi.org/10.4271/1999-01-2910)
- [49] Cikanek S.R., Bailey K.E.: *Regenerative braking system for a hybrid electric vehicle*. In: Proc. 2002 Am. Control Conf. (ACC) (IEEE Cat. No. CH37301), **4**(2002), 3129–3134. doi: [10.1109/ACC.2002.1025270](https://doi.org/10.1109/ACC.2002.1025270)
- [50] Yoong M., Gan Y., Gan G., Leong C., Phuan Z., Cheah B., Chew K.: *Studies of regenerative braking in electric vehicle*. IEEE Conf. on Sustainable Utilization and Development in Engineering and Technology, Kuala Lumpur, 2010, 40–45. doi: [10.1109/student.2010.5686984](https://doi.org/10.1109/student.2010.5686984)
- [51] Fatima N., Mustafa J.: *Production of electricity by the method of road power generation*. Int. J. Adv. Elect. Electron. Eng. **1**(2016), 1, 9–14.
- [52] Raj A., Verma A., Joshi H., Gupta M., Mustafa J.: *Generation of electricity by crank mechanism method in railway track*. In: Proc. Int. Conf. on Computational and Experimental Methods in Mechanical Engineering (ICCEMME 2017), Greater Noida 8–9 Dec. 2017, 326–330.
- [53] Morcos M.M., Dillman N.G., Mersman C.R.: *Battery chargers for electric vehicles*. IEEE Power Eng. Rev. **20**(2000), 11, 8–11. doi: [10.1109/39.883280](https://doi.org/10.1109/39.883280).
- [54] Michael C., Keith P., Walter V.: *Performance of a Battery Electric Vehicle in the Cold Climate and Hilly Terrain of Vermont-Final Report*. Transp. Res. Cent. Res. Rep. **258**, Univ. of Vermont, Burlington 2008. https://rosap.ntl.bts.gov/view/dot/34424/dot_34424_DS1.pdf (accessed 8 Dec. 2022).

Emissivity measurement of black paint using the calorimetric method

EWA PELIŃSKA-OLKO*

Wrocław University of Science and Technology, Faculty of Mechanical and Power Engineering, Department of Thermodynamics and Renewable Energy Sources, Wybrzeże Wyspiańskiego 27, 50-370 Wrocław, Poland

Abstract The paper is of practical importance and describes the construction of a test rig and the measurement method for determining the relative emissivity coefficient of thermosensitive thin polymer coatings. Polymers are high-molecular chemical compounds that produce chains of repeating elements called ‘mers’. The polymers can be natural and artificial. The former ones form the building material for living organisms, the latter – for plastics. In this work, the words plastics and polymers are used as synonyms. Some plastics are thermosensitive materials with specific physical and chemical properties. The calorimetric method mentioned in the title consists of two steps. The first stage, described here, involves very accurately measuring the emissivity of black paint with the highest possible relative emissivity coefficient, which covers the surface of the heater and the inner surface of the chamber. In the second step, the thermosensitive polymer will be placed on the inner surface of the chamber, while black paint with a known emissivity coefficient will remain on the heater. Such a way of determining the properties of thermosensitive polymers will increase the error of the method itself, but at the same time will avoid melting of the polymer coating. During the tests, the results of which are presented in this work, the emissivity coefficient of the black paint was obtained in the range of 0.958–0.965.

Keywords: Calorimetric method; Emissivity; Thermosensitive materials; Polymers; Plastics

*Corresponding Author. Email: ewa.olko@pwr.edu.pl

Nomenclature

c_p	–	specific heat at constant pressure, J/(kgK)
S	–	surface, m ²
P	–	power, W
T	–	temperature, K

Greek symbols

ρ	–	mass density, kg/m ³
ε	–	emissivity coefficient
\dot{Q}	–	heat stream, W

1 Introduction

This paper presents the design of the test rig and the results of the first stage of the study of the relative emissivity coefficient, understood as the amount of thermal radiation as a form of energy transferred between solids of different temperatures – in the energy and electromagnetic wavelength range: from 1 μeV to 1 eV and 10^{-6} m to 10^{-3} m, respectively. The solids studied in the second stage will belong to a special group of materials that have a low softening point or clearly change their thermophysical properties with temperature. The measurement of certain properties, including emissivity in the method presented here, ultimately requires that samples of thermosensitive materials be placed at low temperatures, below the softening point.

This group of materials includes plastics, which are used as insulation, whether in the form of rigid surfaces, films or directly sprayed onto a specific body [1–3]. The coatings change surface heat transfer coefficients similarly to ceramic coatings in blast furnaces and exchangers operating at high temperatures [4]. Plastics appear to be the materials of the future [5]. They are both transparent and opaque. Without chemical admixtures, they generally have low thermal conductivity [6]. They are very popular in the construction industry [7, 8], and because they can also be transparent, they are used to achieve high thermal yields, in buildings with walls with so-called high optical efficiency [9]. Mention should also be made of the so-called solar energy market, where plastics are increasingly competing with glass or metal structural elements in various solar devices due to their relatively low weight and high durability. Transparent insulation increases the efficiency of devices such as solar collectors [10], built-in storage solar water heaters and others [11].

Plastic films are a group of very fast-growing materials because of the possibility of easily interfering with their properties. First of all, films can be assembled into layers with different physical and chemical properties [12], and various metals or ceramics can be sprayed onto their surface with a thickness of e.g. nanometres, thereby increasing or decreasing optical reflection or achieving selective reflection, influencing the conductivity in the layers [13] and creating other yet unexplored properties of the target materials [14], including properties affecting human health [15]. Thus, they have a variety of tasks: from reinforcing, protective - anti-burglary, increasing the insulation of building walls, and blocking UV radiation, to informative [16] and others [17]. A very good example of a common application is films used for car windows.

Such materials in general are such a rapidly growing industry that there is a need to evaluate and classify them [18].

In the practical applications of the above-mentioned ones, not only optical properties are important, but also mechanical and thermal properties, including emissivity, which justifies the topic of this paper.

In particular, some emissivity data are available in the literature, but due to the rapid development of materials, there is far too little data on these new materials. Automotive companies sometimes provide approximate emissivity values for films used for automotive glazing. However, the vast majority of such information is not published, as it is an element of commercial confidentiality. All the more so because, as mentioned earlier, plastic-polymers with relatively easily modifiable properties are increasingly used in a variety of industries, and sometimes form their basis. Therefore, topics related to the study of the properties of thin surfaces made of different types of polymers are very topical now and in the future. However, as mentioned earlier, these types of materials require a special approach when studying their properties.

Emissivity measurement methods can be briefly divided into two main groups: radiometric and calorimetric methods. The first group includes methods that use the information provided by infrared radiation in a selected range of electromagnetic waves by an infrared detector installed most often in a thermal imaging camera. This camera measures and then images the radiation coming from the object being photographed. The energy that can be measured in this way is a function not only of the object's temperature but also of its emissivity. Therefore, when using methods with thermal cameras, radiometric calibration of such devices is essential. The accuracy of the results obtained depends on the correct application of the appro-

priate measurement procedures [19–23] the authors present the design and operating principles of polarimetric imaging cameras.

The calorimetric method of measuring emissivity is classified as a conventional method. It involves direct heating of the sample and the emissivity is determined from the measured temperature and surface area of the sample, as well as the electrical power converted into radiation and consumed in the heating process under specified conditions – often in a vacuum. The system under test is brought to thermodynamic equilibrium with the measurement of specific parameters under so-called steady-state conditions. Samples should therefore be characterised by good thermal conductivity [24].

There are also variants of calorimetric methods that use measurements over a specific time interval, in transient states, the so-called dynamic methods, which require further mathematical calculations to determine the values of specific parameters in the distant future, e.g. using neural networks. Again, material samples should generally have good thermal conductivity, but practically, the method has also been shown to be effective for materials with lower thermal conductivity. In [25] a variation of the calorimetric method was used to measure the properties of non-metallic materials, which are not electrically self-heating. A Fourier transform spectrometer (FTS) was used on the test bench. One calorimetric method has also been successfully used to measure the properties of thin polyamide films, which are poor heat conductors too [26].

It is also possible to combine methods from both of these main groups [27].

In short: the advantage of the calorimetric method is that the value of the selected parameter can be determined in a steady state, the value of which is assumed to be constant in time. In addition, test stands built using this method usually have a relatively simple and logical construction. The disadvantage of this method is the high operating costs resulting from the need to create certain constant conditions both inside and outside the measuring station for a relatively long time.

The use of the calorimetric method in this work was determined by the above-mentioned advantages and the fact that most of the values of material parameters applicable in technology are determined in steady states.

The calorimetric method proposed here consists of establishing a heat balance while continuously heating a rectangular radiator inside a hexagonal chamber placed inside a desiccator, hereafter referred to as the chamber. During the test, the air is pumped out of the desiccator using a vacuum pump to eliminate heat transfer by convection. The only form of energy exchanged between the heater and the internal surface of the chamber is therefore radiant energy.

2 Theory

Heat radiation has the same properties as light waves in the spectrum visible to the eye. The condition for heat exchange in this way is the presence of a transparent medium between bodies of different temperatures exchanging energy with each other. The useful formulas used in this work are based on laws discovered in the course of radiation research. These are primarily Planck's law, formulated as a formula for the amount of radiation emitted by a blackbody as a function of the electromagnetic wavelength emitted and the temperature of the body, and Stefan-Boltzman's law, which describes the total energy flux radiated by a blackbody. In its simplest form, the amount of energy radiated from a body with temperature T expressed in kelvins into a vacuum, is proportional to the fourth power of the absolute temperature of that body. A black body is characterised by the fact that, at steady-state, it absorbs as much energy as it radiates. Grey bodies, found in the real world, radiate similarly to black bodies over the entire wavelength range, only slightly weaker. To compare the radiation properties of a gray body with a black body, the concept of relative emissivity coefficient is introduced, i.e. the quotient of the amount of energy radiated by a gray body to the amount of energy radiated by a perfect black body at a given temperature. The value of this coefficient may refer to a specific length of the emitted electromagnetic wave or to its average value determined by the appropriate temperature range. According to the literature, the emissivity of all bodies is not greater than the one.

The idea of the calorimetric measurement method shown in Fig. 1 is based on radiative heat transfer from the rectangular heater (2) to the

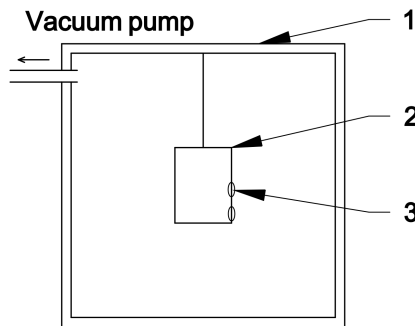


Figure 1: Conceptual outline of a test rig for testing the emission of back paint and coatings of thermosensitive materials.

cooler surface of the cubic chamber (1) surrounding it, hereinafter referred to as the chamber. The temperature will be read by means of thermocouples (3) located on the surface of the heater and the chamber. Both the chamber and the heater are placed inside the vacuum desiccator to eliminate heat transfer by convection.

Measurements will be carried out in two stages. The first stage, described here, involves measuring the emissivity of the black paint that covers both the surface of the heater and the inner surface of the chamber. The coating used, which is also an example of a polymer, has sufficient thermal resistance to be placed on the heater.

Using equations (1), (2) known from the literature [28–31], it is possible to calculate the relative emissivity coefficient under the conditions of thermal equilibrium of the system:

$$\varepsilon_z = \frac{\dot{Q}_{1-2}}{S_1 \sigma [(T_1)^4 - (T_2)^4]}, \quad (1)$$

$$\varepsilon_z = \frac{1}{\frac{1}{\varepsilon_1} + \frac{S_1}{S_2} \left(\frac{1}{\varepsilon_2} - 1 \right)}, \quad (2)$$

where: ε_z – the so-called equivalent relative emissivity coefficient obtained experimentally without taking into account the position of the surfaces exchanging heat with each other, \dot{Q}_{1-2} – heat stream exchanged between surfaces with different temperature, S_1, S_2 – the outer surface of the heater and the inner surface of the chamber respectively, T_1, T_2 – the higher and the lower average absolute temperature respectively, σ – Stefan–Boltzmann constant, $\varepsilon_1, \varepsilon_2$ – emissivity coefficients for surfaces with temperatures T_1 and T_2 respectively.

In the presence of black paint on the surface of the chamber and the heater, from (2) the following formula can be obtained (3):

$$\varepsilon_1 = \frac{1 + \frac{S_1}{S_2}}{\frac{1}{\varepsilon_z} + \frac{S_1}{S_2}}, \quad (3)$$

where: ε_1 – the relative emissivity coefficient of black paint, assuming its equal emissivity on the surface of the heater and the inner surface of the chamber.

The emissivity coefficient of the black paint determined in this way has a smaller absolute error than if the heater and the interior of the chamber were covered with different coatings. It is calculated using the differential method, which is presented later in this paper. Its smaller value is due to the smaller number of components affecting the value of the total error associated with this method. Knowledge of the relative emissivity of the black paint described above is necessary to determine the emissivity of the corresponding temperature-sensitive material in the second stage of the study.

3 The construction of the test rig

The test rig, shown schematically in Fig. 1, was originally built to assess the correctness of neural networks for predicting the temperature of heated solids in the distant future, which in practice meant determining the steady-states temperature at specific points on the body. The photograph with main components of the rig can be found in the article [32]. It has been adapted to determine the relative emissivity of black paint, mentioned in the title of the work and allows a proper thermal equilibrium to be achieved.

The ambient test conditions are a dynamic vacuum of 300 Pa (2500 μmHg). Inside the desiccator, which acts as a vacuum chamber, is a cube made of 5 mm thick sheet metal with 150 mm sides. Its interior forms a closed space, hereinafter referred to as the chamber, with an inner side length of 140 mm, made of PA11 aluminium alloy with a linear thermal expansion coefficient of $23.7 \cdot 10^{-6}$ 1/K. In its geometrical centre was placed a rectangular heater made of PA6 aluminium alloy with a linear coefficient of thermal expansion of $22.9 \cdot 10^{-6}$ 1/K. The heater was made of a rod with a square cross-section, side $a = 30$ mm. The heater has a length of $b = 40$ mm. The design of the heater is simple. A resistance wire (Fe Cr Al 135), insulated with Teflon, is wound on a threaded aluminium alloy pivot with a diameter of approximately 25 mm. The resistance wire has a diameter of $d = 0.5$ mm and a resistance of Ω/m .

The pivot is placed in a hole in a square rod, which forms the body of the heater. Its average resistance at room temperature 20°C is 9.667 Ω . The resistance of the cables connecting the heater with the power supply at 20°C is 0.037 Ω . The test rig is attached to a gauge of type KEITHLEY (hereinafter called the gauge), which provides relatively accurate readings of output signals in the form of resistance or voltage.

4 The way of performing the measurements

On the test rig, temperatures were measured at three specified locations on the heater and three specified locations on the inner surface of the chamber (Fig. 2).

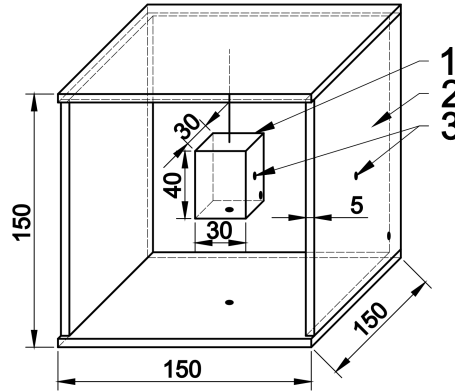


Figure 2: Axonometric mapping of the interior of the chamber (2) including the heater (1) and temperature measurement locations (3).

Temperature measuring points on the heater are located at the intersection of the diagonals: one on the side wall, one on the bottom wall, and one in the corner of the side wall. Similarly, three measurement points are defined on the inner walls of the chamber. The temperature was measured with thermocouples after they had been calibrated: [33–35]. An average temperature was then calculated on the heater and on the surface of the chamber, which was treated as a constant value, for a given power dissipated by the heater.

The reference temperature of cold ends of thermocouples in the temperature of the meter is measured by the PT-1000 resistance sensor calibrated earlier [36]. During each experiment, the voltage and resistance in the heater circuit were measured. The pressure in the desiccator was maintained at 300 Pa using a vacuum pump. This is known as a dynamic vacuum, which requires continuous operation of the vacuum pump.

Two stages of the process can be distinguished in each experiment. In the first stage, the desiccator was filled with air at ambient pressure. The temperature stabilization process after switching on the heater was relatively quick. After about 30% of the duration of the entire experiment, the second stage occurred, in which the vacuum pump was turned on and

operated until the steady state temperature was reached at selected measurement points.

5 The test results

A sample temperature evolution on selected surfaces at the test rig is shown in Fig. 3.

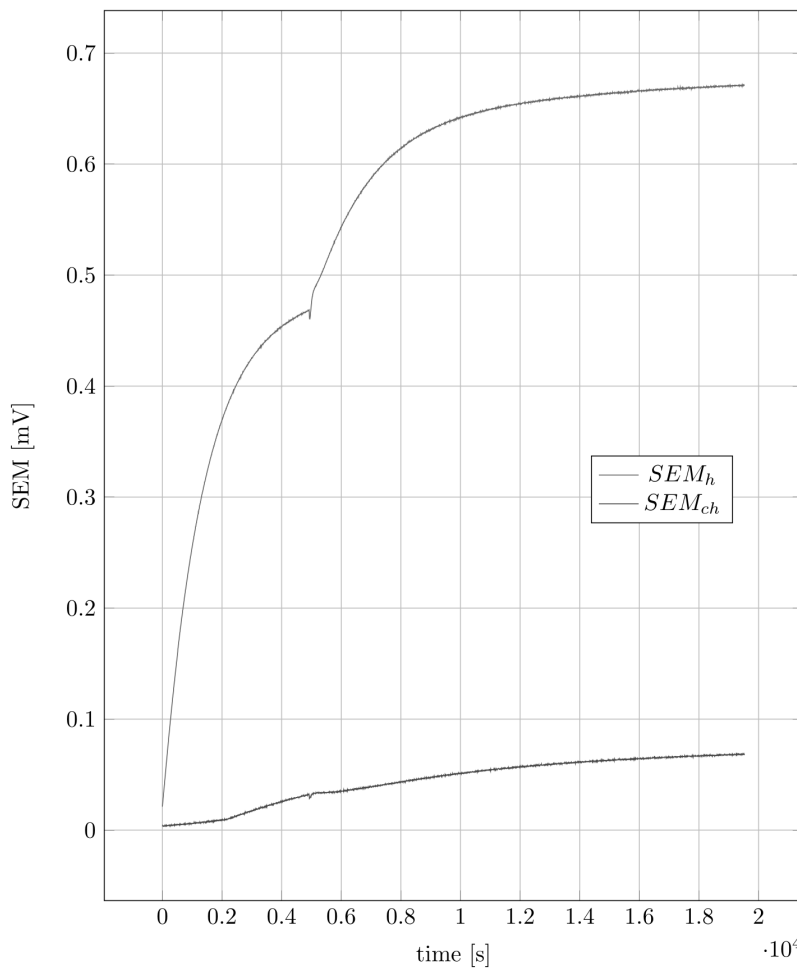


Figure 3: The dependence of the average temperature from time, expressed in SEM_h on the heater (higher values) and in SEM_{ch} on the inner surface of the chamber (lower values).

The heat flux dissipated by the heater \dot{Q}_{1-2} (4) is power on the heater P minus two kinds of losses. One is the loss on the wires \dot{Q}_w , which can be estimated using the Fourier formula, based on knowledge of the diameters of the thermocouples wires and the temperature difference between the surfaces on which the measuring junctions are placed and the environment in which the meter is located. Another one is the loss of enthalpy \dot{Q}_v in the chamber resulting from the maintenance of dynamic vacuum at 300 Pa. Therefore:

$$\dot{Q}_{1-2} = P - \dot{Q}_w - \dot{Q}_v. \quad (4)$$

Examples of experimental results are given in Table 1. Here the following information is gathered in columns from left to right: the ambient temperature where the gauge is placed, measured by Pt-1000 thermometer; the heat stream dissipated by the heater, taking into account losses (4); the resistance of the hot heater; voltage in the heater circuit; SEM of thermocouples measured in the corresponding points of the heater and the inner surface of the chamber: ΔT_1 – ΔT_6 ; the average temperature of the heater T_{avh} and the inner surface of the chamber T_{avch} ; the relative emissivity coefficient ε_z , ε_1 , $\varepsilon_2 = \varepsilon_1$; the absolute method error $\Delta\varepsilon$.

Table 1: The selected experimental results gathered during the emissivity measurement.

File		1	2	3	4	5	6
t_0	K	296.313	290.405	292.503	292.668	289.695	291.506
\dot{Q}_{1-2}	W	0.219	0.758	1.338	1.336	2.17	5.057
R	Ω	9.686	9.797	9.685	9.709	9.788	9.808
U	V	1.462	2.748	3.604	3.613	4.626	7.065
ΔT_1	mV	4.159	16.387	26.593	26.235	41.733	77.775
ΔT_2	mV	4.035	16.134	24.87	25.835	40.389	80.63
ΔT_3	mV	4.374	15.895	25.855	25.899	39.719	76.468
ΔT_4	mV	0.552	1.979	2.812	3.363	4.915	12.071
ΔT_5	mV	0.29	1.727	2.996	2.847	4.676	8.767
ΔT_6	mV	0.156	1.17	1.875	1.723	3.611	9.344
T_{avh}	K	300.543	306.583	318.632	318.699	330.349	369.837
T_{avch}	K	296.687	292.07	295.421	295.353	294.136	301.607
ε_z		1.052	0.954	0.975	0.973	0.961	0.955
ε_1		1.049	0.958	0.976	0.975	0.964	0.958
$\Delta\varepsilon$		0.102	0.027	0.017	0.017	0.012	0.07

6 Errors in determining the emissivity of black paint

The method adopted in the experiment for determining the relative emissivity coefficient is the classical calorimetric method. In the direct measurement, the temperature at the selected locations, the current and voltage supplying the heater, the vacuum level in the desiccator, the corresponding areas of the heater and the interior surface of the chamber, and the ambient temperature and pressure are measured. When both the heater and the inner surface of the chamber are covered with black paint, the formula for the relative emissivity coefficient of this material is of the form (5):

$$\varepsilon_1 = \frac{\frac{U^2}{R} \left(1 + \frac{S_1}{S_2}\right)}{CS_1 \left[\left(\frac{T_1}{100}\right)^4 - \left(\frac{T_2}{100}\right)^4 \right] + \frac{S_1 U^2}{S_2 R}}, \quad (5)$$

where: ε_1 – the relative emissivity coefficient of the black paint, U , R – the voltage and the resistance of the heater, respectively, S_1 , S_2 – the surface of the heater and the inner surface of the vacuum chamber, respectively, T_1 , T_2 – the measured average temperature of the heater and the inner surface of the chamber, respectively, $C = 5.67 \text{ W}/(\text{m}^2\text{K}^4)$.

The maximum error of the method was determined by summing the absolute values of the errors of the individual quantities occurring in the (5). The individual members generating absolute errors have the form as follows:

$$\begin{aligned} \frac{\partial \varepsilon_1}{\partial U} = & \frac{\frac{2U}{R} \left(1 + \frac{S_1}{S_2}\right) \left\{ CS_1 \left[\left(\frac{T_1}{100}\right)^4 - \left(\frac{T_2}{100}\right)^4 \right] + \frac{S_1 U^2}{S_2 R} \right\}}{\left\{ CS_1 \left[\left(\frac{T_1}{100}\right)^4 - \left(\frac{T_2}{100}\right)^4 \right] + \frac{S_1 U^2}{S_2 R} \right\}^2} \\ & - \frac{\frac{U^2}{R} \left(1 + \frac{S_1}{S_2}\right) \frac{S_1 2U}{S_2 R}}{\left\{ CS_1 \left[\left(\frac{T_1}{100}\right)^4 - \left(\frac{T_2}{100}\right)^4 \right] + \frac{S_1 U^2}{S_2 R} \right\}^2}, \quad (6) \end{aligned}$$

$$\frac{\partial \varepsilon_1}{\partial R} = \frac{-\frac{U^2}{R^2} \left(1 + \frac{S_1}{S_2}\right) \left\{ CS_1 \left[\left(\frac{T_1}{100}\right)^4 - \left(\frac{T_2}{100}\right)^4 \right] + \frac{S_1 U^2}{S_2 R} \right\}}{\left\{ CS_1 \left[\left(\frac{T_1}{100}\right)^4 - \left(\frac{T_2}{100}\right)^4 \right] + \frac{S_1 U^2}{S_2 R} \right\}^2} + \frac{\frac{U^2}{R} \left(1 + \frac{S_1}{S_2}\right) \frac{S_1 U^2}{S_2 R^2}}{\left\{ CS_1 \left[\left(\frac{T_1}{100}\right)^4 - \left(\frac{T_2}{100}\right)^4 \right] + \frac{S_1 U^2}{S_2 R} \right\}^2}, \quad (7)$$

$$\frac{\partial \varepsilon_1}{\partial S_1} = \left\langle IU \frac{\left\{ CS_1 \left[\left(\frac{T_1}{100}\right)^4 - \left(\frac{T_2}{100}\right)^4 \right] + \frac{S_1 U^2}{S_2 R} \right\}}{S_2} - \frac{U^2}{R} \left(1 + \frac{S_1}{S_2}\right) \right\rangle \cdot \frac{\left\{ C \left[\left(\frac{T_1}{100}\right)^4 - \left(\frac{T_2}{100}\right)^4 \right] + \frac{U^2}{S_2 R} \right\}}{\left\{ CS_1 \left[\left(\frac{T_1}{100}\right)^4 - \left(\frac{T_2}{100}\right)^4 \right] + \frac{S_1 U^2}{S_2 R} \right\}^2}, \quad (8)$$

$$\frac{\partial \varepsilon_1}{\partial S_2} = \frac{-\frac{U^2}{R} \frac{S_1}{S_2^2} + \left(\frac{U^2}{R}\right)^2 S_1 \left(1 + \frac{S_1}{S_2}\right) \frac{1}{S_2^2}}{\left\{ CS_1 \left[\left(\frac{T_1}{100}\right)^4 - \left(\frac{T_2}{100}\right)^4 \right] + \frac{S_1 U^2}{S_2 R} \right\}^2}, \quad (9)$$

$$\frac{\partial \varepsilon_1}{\partial T_1} = \frac{-\frac{U^2}{R} CS_1 \frac{4T_1^3}{100^4} \left(1 + \frac{S_1}{S_2}\right)}{\left\{ CS_1 \left[\left(\frac{T_1}{100}\right)^4 - \left(\frac{T_2}{100}\right)^4 \right] + \frac{S_1 U^2}{S_2 R} \right\}^2} \quad (10)$$

$$\frac{\partial \varepsilon_1}{\partial T_2} = \frac{\frac{U^2}{R} CS_1 \frac{4T_2^3}{100^4} \left(1 + \frac{S_1}{S_2}\right)}{\left\{ CS_1 \left[\left(\frac{T_1}{100}\right)^4 - \left(\frac{T_2}{100}\right)^4 \right] + \frac{S_1 U^2}{S_2 R} \right\}^2}. \quad (11)$$

When the heater and the inner surface of the chamber are covered with coatings of different materials, the relative emissivity coefficient of the material covering the cold surface of the chamber can be calculated from the

following formula:

$$\varepsilon_2 = \frac{\frac{U^2}{R} S_1 \varepsilon_1}{-S_2 \frac{U^2}{R} + C S_1 S_2 \varepsilon_1 \left[\left(\frac{T_1}{100} \right)^4 - \left(\frac{T_2}{100} \right)^4 \right] + S_1 \frac{U^2}{R} \varepsilon_1}. \quad (12)$$

The corresponding partial derivatives, generating the absolute error have the following forms:

$$\begin{aligned} \frac{\partial \varepsilon_2}{\partial U} = & \frac{\frac{2U}{R} S_1 \varepsilon_1 \left\{ -S_2 \frac{U^2}{R} + C S_1 S_2 \varepsilon_1 \left[\left(\frac{T_1}{100} \right)^4 - \left(\frac{T_2}{100} \right)^4 \right] + S_1 \frac{U^2}{R} \varepsilon_1 \right\}}{\left\{ -S_2 \frac{U^2}{R} + C S_1 S_2 \varepsilon_1 \left[\left(\frac{T_1}{100} \right)^4 - \left(\frac{T_2}{100} \right)^4 \right] + S_1 \frac{U^2}{R} \varepsilon_1 \right\}^2} \\ & - \frac{S_1 \varepsilon_1 \frac{U^2}{R} \left(-S_2 \frac{2U}{R} + S_1 \frac{2U}{R} \varepsilon_1 \right)}{\left\{ -S_2 \frac{U^2}{R} + C S_1 S_2 \varepsilon_1 \left[\left(\frac{T_1}{100} \right)^4 - \left(\frac{T_2}{100} \right)^4 \right] + S_1 \frac{U^2}{R} \varepsilon_1 \right\}^2}, \quad (13) \end{aligned}$$

$$\begin{aligned} \frac{\partial \varepsilon_2}{\partial R} = & \frac{\left(-\frac{U^2}{R^2} \right) S_1 \varepsilon_1 \left\{ -S_2 \frac{U^2}{R} + C S_1 S_2 \varepsilon_1 \left[\left(\frac{T_1}{100} \right)^4 - \left(\frac{T_2}{100} \right)^4 \right] + S_1 \frac{U^2}{R} \varepsilon_1 \right\}}{\left\{ -S_2 \frac{U^2}{R} + C S_1 S_2 \varepsilon_1 \left[\left(\frac{T_1}{100} \right)^4 - \left(\frac{T_2}{100} \right)^4 \right] + S_1 \frac{U^2}{R} \varepsilon_1 \right\}^2} \\ & - \frac{S_1 \varepsilon_1 \frac{U^2}{R} \left(S_2 \frac{U^2}{R^2} - S_1 \frac{U^2}{R^2} \varepsilon_1 \right)}{\left\{ -S_2 \frac{U^2}{R} + C S_1 S_2 \varepsilon_1 \left[\left(\frac{T_1}{100} \right)^4 - \left(\frac{T_2}{100} \right)^4 \right] + S_1 \frac{U^2}{R} \varepsilon_1 \right\}^2}, \quad (14) \end{aligned}$$

$$\begin{aligned} \frac{\partial \varepsilon_2}{\partial S_1} = & \frac{\frac{U^2}{R} \varepsilon_1 \left\{ -S_2 \frac{U^2}{R} + C S_1 S_2 \varepsilon_1 \left[\left(\frac{T_1}{100} \right)^4 - \left(\frac{T_2}{100} \right)^4 \right] + S_1 \frac{U^2}{R} \varepsilon_1 \right\}}{\left\{ -S_2 \frac{U^2}{R} + C S_1 S_2 \varepsilon_1 \left[\left(\frac{T_1}{100} \right)^4 - \left(\frac{T_2}{100} \right)^4 \right] + S_1 \frac{U^2}{R} \varepsilon_1 \right\}^2} \\ & - \frac{S_1 \varepsilon_1 \frac{U^2}{R} \left\{ C S_2 \varepsilon_1 \left[\left(\frac{T_1}{100} \right)^4 - \left(\frac{T_2}{100} \right)^4 \right] + \varepsilon_1 \frac{U^2}{R} \right\}}{\left\{ -S_2 \frac{U^2}{R} + C S_1 S_2 \varepsilon_1 \left[\left(\frac{T_1}{100} \right)^4 - \left(\frac{T_2}{100} \right)^4 \right] + S_1 \frac{U^2}{R} \varepsilon_1 \right\}^2}, \quad (15) \end{aligned}$$

$$\frac{\partial \varepsilon_2}{\partial S_2} = \frac{-S_1 \frac{U^2}{R} \varepsilon_1 \left\{ -\frac{U^2}{R} + CS_1 \varepsilon_1 \left[\left(\frac{T_1}{100} \right)^4 - \left(\frac{T_2}{100} \right)^4 \right] \right\}}{\left\{ -S_2 \frac{U^2}{R} + CS_1 S_2 \varepsilon_1 \left[\left(\frac{T_1}{100} \right)^4 - \left(\frac{T_2}{100} \right)^4 \right] + S_1 \frac{U^2}{R} \varepsilon_1 \right\}^2}, \quad (16)$$

$$\frac{\partial \varepsilon_2}{\partial T_1} = \frac{-S_1 \frac{U^2}{R} \varepsilon_1 \left(CS_1 S_2 \varepsilon_1 \frac{4T_1^3}{100^4} \right)}{\left\{ -S_2 \frac{U^2}{R} + CS_1 S_2 \varepsilon_1 \left[\left(\frac{T_1}{100} \right)^4 - \left(\frac{T_2}{100} \right)^4 \right] + S_1 \frac{U^2}{R} \varepsilon_1 \right\}^2}, \quad (17)$$

$$\frac{\partial \varepsilon_2}{\partial T_2} = \frac{-S_1 \frac{U^2}{R} \varepsilon_1 \left(CS_1 S_2 \varepsilon_1 \frac{4T_2^3}{100^4} \right)}{\left\{ -S_2 \frac{U^2}{R} + CS_1 S_2 \varepsilon_1 \left[\left(\frac{T_1}{100} \right)^4 - \left(\frac{T_2}{100} \right)^4 \right] + S_1 \frac{U^2}{R} \varepsilon_1 \right\}^2}. \quad (18)$$

7 Observations and conclusions

1. Within the heater power range of 0.21–5.06 W, the relative emissivity coefficient is in the range of 0.958 ± 0.07 to 1.049 ± 0.102 . The method error of determining the relative emissivity for black paint covering both the chamber interior and the heater increases with decreasing heater power.
2. Each test was performed for a different temperature range, depending on the heater power. If it is assumed that the relative emissivity coefficient of black paint is constant over the temperature range tested, then its value should fall within the common range of values of this coefficient for all the tests carried out, regardless of the accuracy of the measurements.

The range of common values of the coefficient sought for all tests is within the field of values (0.958–0.965).

3. If the tests will include thermosensitive materials, a sample of such material should be placed on a cold surface – the inner surface of the chamber. A layer of black paint with a known value of the relative emissivity coefficient will remain on the heater. According to preliminary calculations, the error of the method should increase, but the undertaking is necessary to avoid the melting of the polymer coating.

4. After initial attempts to apply a thin thermosensitive coating on the cooler surface of the chamber, insufficiently satisfactory results were obtained in the second stage of the research. If the technical problems related to the adhesion of coatings cannot be solved, the range of materials tested by this method will be limited to those that can only be sprayed onto surfaces.

Received 17 May 2023

References

- [1] Qu J., Song J.R., Qin J., Song Z.N., Zhang W.D., Shi Y.X., Shang T., Zhang H.Q., He Z.V., Xue X.: *Transparent thermal insulation coatings for energy efficient glass windows and curtain walls*. *Energ. Buildings* **77**(2014), 1–10.
- [2] Chen Y., Wang M.D., Xu M.D., Li L.: *Preparation of AZO/acrylic resin transparent insulation coating*. *Adv. Mat. Res.* **369-398**(2012), 229–232.
- [3] Wittwer V.: *The use of transparent insulation materials and optical switching layers in window systems*. *Renew. Energ.* **5**(1994), 318–323.
- [4] Morel S.: *The influence of a radiated heat exchanger surface on heat transfer*. *Arch. Thermodyn.* **36**(2015), 3, 161–174.
- [5] Paneri A., Wong I.L., Burek S.: *Transparent insulation materials: An overview on past, present and future developments*. *Sol. Energy* **184**(2019), 59–83.
- [6] Kaushika N.D., Sumathy K.: *Solar transparent insulation materials: a review*. *Renew. Sust. Energ. Rev.* **7**(2003), (4), 317–351.
- [7] Wong I.L., Eames P.C., Perera R.S.: *A review of transparent insulation systems and the evaluation of payback period for building applications*. *Sol. Energy* **81**(2007), 1058–1071.
- [8] Struhala K., Cekon M., Slavik R.: *Life Cycle Assessment of solar facade concepts based on transparent insulation materials*. *Sustainability-Basel* **10**(2018), 11, 4212.
- [9] Swirska-Perkowska J., Kucharczyk K., Wyrwal J.: *Energy efficiency of a solar wall with transparent insulation in Polish climatic conditions*. *Energies* **13**(2020), 4, 859.
- [10] Chaurasia PBL.: *Transparent insulation material in solar system for candle production*. *Energ. Convers. Manage.* **41**(2020), 1569–1584.
- [11] Prakash J., Garg H.P., Jha R., Hrishikesan D.S.: *Solar thermal-systems with transparent insulation*. *Energ. Convers. Manage.* **33**(1992), 987–996.
- [12] Jia H., Zhu J.J., Debeli D.K., Li Z.L., Guo J.S.: *Solar thermal energy harvesting properties of spacer fabric composite used for transparent insulation materials*. *Sol. Energ. Mat. Sol. C* **174**(2018), 140–145.
- [13] Tang J., Di F., Xu X., Xiao Y., Che J.: *Transparent conductive graphene films*. *Prog. Chem.* **24**(2012), 501–511.

- [14] Kholmanov I.N., Stoller M.D., Edgeworth J., Lee W.H., Li H.F., Lee J.H., Barnhart C., Potts J.R., Piner R., Inwande Ak D., Barrick J.E., Ruoff R.: *Nanostructured hybrid transparent conductive films with antibacterial properties*. ACS Nano **6**(2012), 5157–5163.
- [15] Vitelaru C., Parau AC., Kiss AE., Pana I., Dinu M., Constantin LR., Vladescu A., Tonofre L.E., Adochite C.S., Costinas S., Rogozea L., Badea M., Idomir M.E.: *Silver-containing thin films on transparent polymer foils for antimicrobial applications*. Coatings **12**(2022), 170.
- [16] Froyen A.A.F., Grossiord N., Heer J., Meerman T., Yang L.T., Lub J., Schenning A.P.H.J.: *Ink-deposited transparent electrochromic structural colored foils*. ACS Appl. Mater. Inter. **14**(2022), 39375–39383.
- [17] Blankenburg L., Schroedner M.: *Perhydropolysilazane derived silica for flexible transparent barrier foils using a reel-to-reel wet coating technique: Single- and multilayer structures*. Surf. Coat Tech. **275**(2015), 193–206.
- [18] Syrowa L., Ravas R., Grman J.: *The use of schlieren visualization method in the diagnostic of optically transparent polymeric foils*. J. Electr. Eng. **58**(2007), 257–263.
- [19] Hagen N.: *Review of thermal infrared polarimetry, I: theory*. Opt. Eng. **61**(2022), 7, 070902.
- [20] Hagen N.: *Review of thermal infrared polarimetry, part 2: experiment*. Opt. Eng. **61**(2022), 8, 080901.
- [21] Bieszczad G., Gogler S., Swiderski J.: *Review of design and signal processing of polarimetric imaging cameras*. Opto-Electron Rev. **29**(2021), 5–12.
- [22] Kruczek T.: *Conditions for the use of infrared camera diagnostics in energy auditing of the objects exposed to open air space at isothermal sky*. Arch. Thermodyn. **36**(2015), 1, 67–82.
- [23] Musiał D., Wyczółkowski R.: *Thermovision determination of the furnace chamber environment temperature using the technical black-body model*. Arch. Thermodyn. **31**(2010), 4, 25–35.
- [24] Fu T.R., Tan P., Duan M.H.: *Simultaneous measurements of high-temperature total hemispherical emissivity and thermal conductivity using a steady-state calorimetric technique*. Meas. Sci. Techno. **26**(2015).
- [25] Zang B., Redgrove J., Clark J.: *A transient method for total emissivity determination*. Int. J. Thermophys. **25**(2004), 423–438.
- [26] Fukuzawa K., Ohnishi A., Nagasaka Y.: *Total hemispherical emittance of polyimide films for space use in the temperature range from 173 to 700 K*. Int. J. Thermophys. **35**(2002), 319–331.
- [27] Vikhareva NA., Cherepanov VY.: *Radiation-calorimetric method of measurements for the thermal emissivity of heat radiators*. Meas. Tech.+ **59**(2016), 734–737.
- [28] Hobler T.: *Heat Movement and Exchangers*. WNT, Warszawa 1971 (in Polish).
- [29] Kostowski E.: *Heat Flow*. Wydawn. Politechniki Śląskiej, Gliwice 2006 (in Polish).
- [30] Kostowski E., Górniak H., Sikora J., Szymczyk J., Ziębik A.: *A collection of tasks related to heat flow*. Wydawn. Politechniki Śląskiej, Gliwice 2003 (in Polish).

- [31] Pudlik W.: *Heat Exchange and Exchangers*. Wydawn. Politechniki Gdańskiej, Gdańsk 2012 (in Polish).
- [32] Pelińska-Olko E., Lewkowicz M.: *Numerical prediction of steady state temperature based on transient measurements*. In: Proc. MATEC Web Conf. **240**(2018), 05024.
- [33] Wedrychowicz W.: *Thermocouple Temperature Measurement*. Wydawn. Politechniki Wrocławskiej, Wrocław 2017 (in Polish).
- [34] Liu B., Huang Q.H., Wang P.Y.: *Influence of surrounding gas temperature on thermocouple measurement*. Case Stud. Therm. Eng. **19**(2020), 100627.
- [35] Liu H.T., Shao D., Li B.Q.: *Theory analysis of thermocouple temperature measurement*. Appl. Mech. Mater. **239-240**(2013), 749–753.
- [36] Wedrychowicz W.: *Temperature Measurement with Metal and Semiconductor Resistance Thermocouples*. Wydawn. Politechniki Wrocławskiej, Wrocław 2015 (in Polish).

Alternative method of making electrical connections in the 1st and 3rd generation modules as an effective way to improve module efficiency and reduce production costs

PAWEŁ KWAŚNICKI^{a, b}
ANNA GRONBA-CHYŁA^{a, *}
AGNIESZKA GENEROWICZ^c
JÓZEF CIUŁA^d
IWONA WIEWIÓRSKA^e
KRZYSZTOF GASKA^f

^a John Paul II Catholic University of Lublin, Faculty of Natural and Technical Sciences, Konstantynów 1 H, 20-708 Lublin, Poland

^b Research & Development Centre for Photovoltaics, ML System S.A., Zaczernie 190G, 36-062 Zaczernie, Poland

^c Cracow University of Technology, Department of Environmental Technologies, Warszawska 24, 31-155 Cracow, Poland

^d State University of Applied Sciences in Nowy Sącz, Faculty of Engineering Sciences, Zamenhofa 1A, 33-300 Nowy Sącz, Poland

^e Sądeckie Wodociągi sp. z o.o., W. Pola 22, 33-300 Nowy Sącz, Poland

^f Silesian University of Technology, Faculty of Energy and Environmental Engineering, Konarskiego 18, 44-100 Gliwice, Poland

Abstract In this work, we propose a new method for manufacturing busbars in photovoltaic modules for different solar cell generations, focusing on 1st and 3rd generations. The method is based on high-pressure spray coating using nanometric metallic powder. Our focus is primarily on optimizing conductive paths for applications involving conductive layers used in 3rd generation solar cells, such as quantum dot solar cell, dye-sensitized solar cell, and silicon-based solar cells on glass-glass architecture for building-

*Corresponding Author. Email: amgronba@kul.pl

integrated photovoltaic. The advantages of the proposed method include the possibility of reducing the material quantity in the conductive paths and creating various shapes on the surface, including bent substrates.

This paper examines the influence of the proposed high-pressure spraying technique using metallic particles on the morphology of the resulting conductive paths, interface characteristics, and electrical parameters. Conductive paths were created on four different layers commonly used in photovoltaic systems, including transparent conductive oxide, Cu, Ti, and atomic layer deposition processed Al_2O_3 . The use of high-pressure technology enables the production of conductive layers with strong adhesion to the substrate and precise control of the spatial parameters of conductive paths. Furthermore, the temperature recorded during the deposition process does not exceed 385 K, making this technique suitable for various types of substrates, including glass and silicon. Additionally, the produced layers exhibit low resistance, measuring less than 0.3Ω . Finally, the mechanical resistance, as determined through tearing tests, as well as environmental and time stability, have been confirmed for the produced paths.

Keywords: Photovoltaics; Busbars; DSSC; BIPV; Solar module

Acronyms

ALD	–	atomic layer deposition
BB	–	busbar
BIPV	–	building integrated photovoltaic
DSSC	–	dye-sensitized solar cell
EDX	–	energy dispersive X-ray spectroscopy
FTO	–	fluorine-doped tin oxide
GG	–	glass-glass
IEC	–	International Electrotechnical Commission
I(U)	–	current-voltage characteristic
PV	–	photovoltaic
PVD	–	physical vapor deposition
SEM	–	scanning electron microscopy
TCO	–	transparent conductive oxide
QDSC	–	quantum dot solar cell

1 Introduction

Photovoltaic (PV) modules possess several crucial parameters that determine their performance and suitability for specific applications. The reliability and lifespan of photovoltaic modules predominantly hinge on degradation and failure modes. Therefore, comprehending the degradation mech-

anisms, including the origins of these degradation modes and their impact on PV module efficiency [1], is an essential and foundational task to enhance the reliability of PV modules [2,3].

One vital parameter relates to busbars and their stability, particularly concerning DSSC (dye-sensitized solar cell) and glass-glass modules. The issue at hand is closely linked to busbar production technology and can be refined through the technological solution proposed in this study. When subjected to cyclic bending, cracks can emerge near the points where the busbars are soldered to the silicon, potentially propagating due to fatigue [4,5]. Conversely, under cyclic axial strain, the busbars endure loads beyond the elastic limit, leading to plasticity and hysteric energy dissipation [6,7]. Kaule *et al.* demonstrated that the strength and cracking susceptibility are highly dependent on the side and direction of the load, with the lowest strength observed on the rear side loaded with tensile stress parallel to the busbars [8].

Improving module efficiency and reducing production costs are two critical objectives for the photovoltaic industry. Achieving these goals can help make solar energy more competitive with traditional energy sources and enable wider adoption of renewable energy [9–11].

In this paper, we will discuss one of the strategies that can be used to enhance module efficiency and reduce production costs by employing alternative methods for busbar production. Busbars (BBs) are essential components of photovoltaic modules [12,13] commonly used to generate electricity from solar energy. The primary purpose of busbars in PV modules is to enhance the electrical performance of the module by reducing resistive losses and improving the overall efficiency [14,15].

In a typical PV module, each solar cell generates a relatively small amount of electricity. Busbars serve to interconnect the cells, increasing the total voltage and current produced by the module. This is necessary because the voltage and current produced by a single solar cell are generally too low to be practical on their own. When solar cells are connected in series to form a module, the cumulative current flowing through each cell adds up, and any resistance in the circuit can result in power losses [16,17]. New techniques involving copper busbars offer the most efficient placement and a simplified amount of materials for PV panels [18,19]. In fact, the busbar system replaces two crucial components in a typical PV panel: the power distribution block and the connecting cables [20,21]. Lu *et al.* observed that optimizing busbars based on the uneven distribution of illumination created by the concentrator contributes to the enhancement of the electrical

parameters of the compound parabolic contractor-photovoltaic (CPC-PV) cell [22–24]. The study of the electromagnetic field distribution due to the incident photon flux demonstrates that increasing the number of busbars can generate carriers in the shaded areas under the busbars [25–27]. Several attempts have been made to reduce material costs in the production of BBs, including the application of shingled technology [28]. Shingled photovoltaic modules involve the process of creating shingled strings by splitting and gluing solar cells [29]. As an adhesive method, the application of divided cell strips across the width of the busbar is used to connect them together using electroconductive adhesive (ECA) [30]. Given the high cost of Ag paste used in the production of solar cells, efforts have been made to reduce its usage as a solar cell electrode. Oh *et al.* employed an economically effective electrode pattern that significantly reduced the amount of Ag paste used [31, 32].

In dye-sensitized solar cells (DSSCs) [33, 34], busbars are employed to connect the individual cells and create an electrical circuit. The photoactive layer consists of a semiconductor material coated with a layer of dye molecules. When light strikes the dye molecules, they absorb the energy and transfer it to the semiconductor, generating an electrical current. Given that the current generated by a DSSC is relatively low, busbars in DSSCs are typically crafted from transparent conductive materials [35], such as Indium Tin Oxide (ITO) or Fluorine-doped Tin Oxide (FTO) [36, 37], and are also used in the form of metallic paths on the edges [38]. These materials provide low-resistance paths for the current to flow through, minimizing resistive losses, and enhancing the electrical performance of the cell.

Glass-glass (GG) [39, 40] solar cells comprise two glass layers that sandwich the photovoltaic cells, typically silicon-based [41, 42]. The glass layers offer mechanical support and protection for the cells while allowing light to penetrate and reach the cells [43, 44]. Busbars are employed to collect the current generated by the individual cells and transfer it to an external load [45–47]. They also aid in distributing the current evenly across the cell, reducing hot spots and the risk of cell damage. Since GG solar cells are relatively thin [48], the busbars used in these cells are generally composed of highly conductive metals, such as copper or silver [49, 50]. These materials offer low-resistance paths for the current to flow through, minimizing resistive losses and improving the electrical performance of the cell [51, 52]. Additionally, in GG solar cells, busbars can be placed on both sides of the cells, further enhancing current collection and reducing power losses [53].

Reducing the manufacturing cost of busbars is a critical parameter, and considerable efforts have been made in this regard. Cost reduction can be achieved through various means, including:

- **Thinning the busbars:** Busbars can be made thinner while maintaining their electrical conductivity, thus reducing the required material per busbar.
- **Using alternative materials:** Instead of copper, which is commonly used for busbars, alternative materials such as aluminum or silver can be employed. These materials offer higher conductivity per unit weight than copper, allowing for a reduction in material usage.
- **Utilizing busbarless cell interconnection:** In this method, solar cells are interconnected without the need for busbars, eliminating the necessity for busbars entirely.
- **Optimizing busbar layout:** By carefully designing the layout of the busbars, it is possible to reduce the material requirements for each busbar while maintaining the necessary electrical conductivity.

All of these approaches can be achieved or improved through the high-pressure spraying process described in this paper.

2 Experimental procedure

The busbar paths under investigation have been analysed by means of contact profilometry (DektakX, Bruker) to obtain the cross-sectional shape and thickness of the busbar structures. Additionally, the elemental composition of the alloy was determined using energy-dispersive X-ray spectroscopy (EDX), and the interface between the metallic tracks and the substrate was imaged using high-resolution scanning electron microscopy (HR-SEM). Electrical measurements were conducted during the tests using a four-point probe (4-Probe, Ossila BV), an ohmmeter (Keithley), and an emission spectrometer with a glow discharge excitation source (GDS, GD-Profilor 2, Horiba).

Samples of metallic busbars made using the high-pressure spraying method on various types of glass substrates were tested. The substrates were TCO glass in the 1000 mm × 2000 mm format, covered with various nano-coatings. Two of them were created using the physical vapor deposition

(PVD) method (Kenosistec PVD system), containing coatings made of pure copper (Cu) and titanium (Ti). Aluminum (III) oxide (Al_2O_3) was deposited on glass panes using the atomic layer deposition (ALD) technique (Beneq). Additionally, one series of metallic traces was made on uncoated TCO (transparent conductive oxide) glass. The electrodes were spray-coated using a system manufactured by Ceri-com companies, following these parameters: sputtering rate between 30–40 mm/s, busbar width of 5 mm, and the process was conducted at room temperature and standard humidity.

Table 1 summarizes the information on the tested metallic tracks, including sample designations, types of coating, methods of coating deposition, and detailed descriptions of the process.

Table 1: Summary of information on tested metallic tracks.

Designation	Layer	Deposit method	Detailed description of the process
TCO-clear	No layer	–	unmodified TCO glass
TCO-Cu_a	Copper	PVD	2.4 kW, 3 number of rounds, $v = 4$ mm/s
TCO-Cu_b	Copper	PVD	1.4 kW, 3 number of rounds, $v = 4$ mm/s
TCO-Ti_a	Titanium	PVD	2.4 kW, 3 number of rounds, $v = 4$ mm/s
TCO-Ti_b	Titanium	PVD	1.4 kW, 3 number of rounds, $v = 4$ mm/s

v – speed of the substrate during deposition process.

3 Results

3.1 Determination of busbar thickness

The thickness of busbars plays a crucial role in determining the electrical performance of the module. Thicker busbars can offer lower resistance and improved current collection, leading to higher efficiency. However, thicker busbars can also increase shading effects on the cells, potentially reducing the overall power output of the module.

Samples were extracted from both the edge and the center of the glass pane. Each obtained sample, measuring approximately 50 mm × 50 mm, underwent analysis using the methods described above. Figure 1 illustrates the locations where glass fragments with electrodes were collected, exemplified by TCO-Cu_a, which features TCO glass covered with a thin copper (Cu) layer.

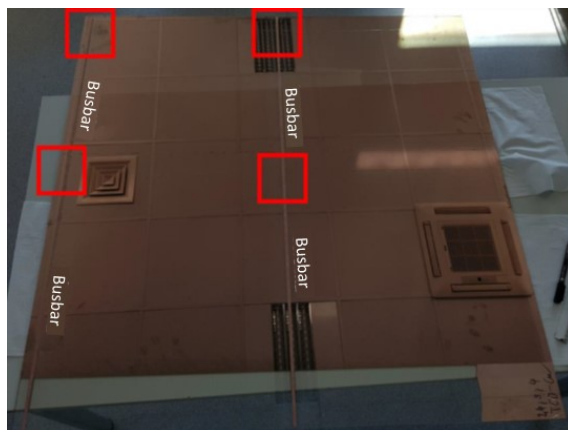


Figure 1: Photograph of TCO-Cu_a glass with marked (red) sampling points for testing.

Needle profilometry was employed to perform scans of the busbar profiles. The scans were conducted across the electrodes, resulting in the left and right sides of the scan containing the substrate profile. This allowed for the measurement of the track's height relative to the substrate. Figure 2 displays several exemplary profiles. While there is a notable difference in their heights relative to each other, the shape of each resembles a Gaussian distribution, albeit not perfectly symmetrical about the center. Due to the significant roughness of the electrodes, thickness measurements were conducted by measuring the relative height between the substrate and the one-

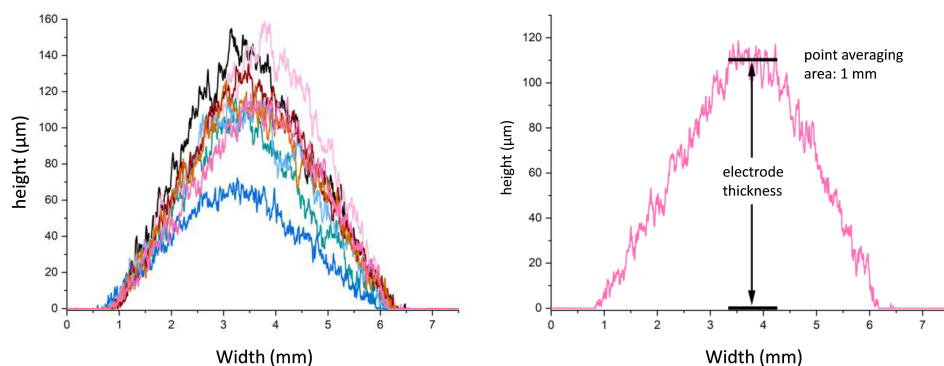


Figure 2: List of several exemplary profiles of the cross-section of metallic tracks, illustrating the method of measuring the thickness of the electrodes (averaging the height from 1 mm of the top of the profile).

millimeter average height of the top of the electrode (as depicted in Fig. 2). The width of each path fluctuated around 5 mm. The average thickness of all collected substrates was $125 \pm 16 \mu\text{m}$. However, when comparing the smallest ($65 \mu\text{m}$) and the largest ($154 \mu\text{m}$) values, it is evident that there is a significant spread.

Lower values predominantly appeared on the edge side, likely where the deposition of tracks commenced. Subsequently, the thickness stabilized, with a few exceptions. Analyzing the thicknesses for individual substrates (Fig. 3), it is apparent that these values closely align with the value determined for all samples, averaging around $125 \mu\text{m}$ and sharing similar uncertainty values. The largest deviation from the average occurred in the case of the TCO-Ti_a sample, where the average value was $113 \pm 7 \mu\text{m}$. All thickness values, along with their associated uncertainties, are presented in Table 2. The standard busbar thickness can vary depending on the specific

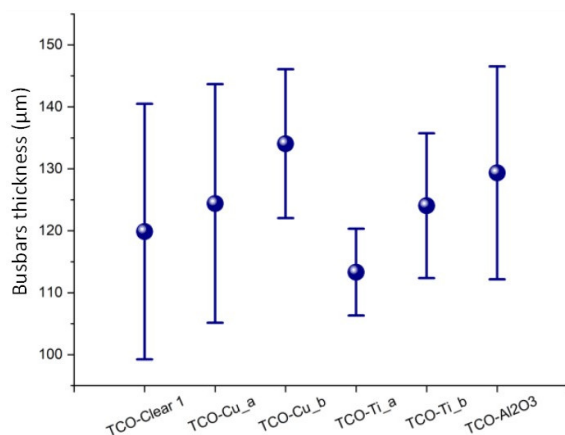


Figure 3: Determined on the basis of collected profiles of constant thickness for all substrates.

Table 2: Average thicknesses determined based on collected profiles for all substrates.

Designation	Busbar thickness (μm)
TCO-Clear	120 ± 21
TCO-Cu_a	124 ± 19
TCO-Cu_b	134 ± 12
TCO-Ti_a	113 ± 7
TCO-Ti_b	124 ± 12

module design and requirements. In general, the thickness of busbars in PV modules can range from 0.1 to 0.5 mm.

3.2 Thermal distribution during the deposition process

The deposition process took place in a room environment with a temperature of 295 K and a maximum humidity of 63%. Temperature measurements at the very surface of the contact point between the beam and the substrate were conducted using a standard pyrometer (laser pyrometer TP10) with a spot size of 1 mm and an accuracy range of ± 1 K. Measurements were performed at three different points on the sample, covering the right, center, and left sides during the deposition process. Once the process pressure stabilized, no significant temperature discrepancies were observed. The measured temperature at 7.2 ± 1 bar pressure was 377.4 ± 2 K.

A slight correlation between temperature and busbar thickness is discernible as shown in Fig. 4. Thicker busbars tend to be associated with higher temperatures. However, it is essential to note that these values fall within the measurement error range. Drawing definitive conclusions from this observed relationship necessitates further testing.

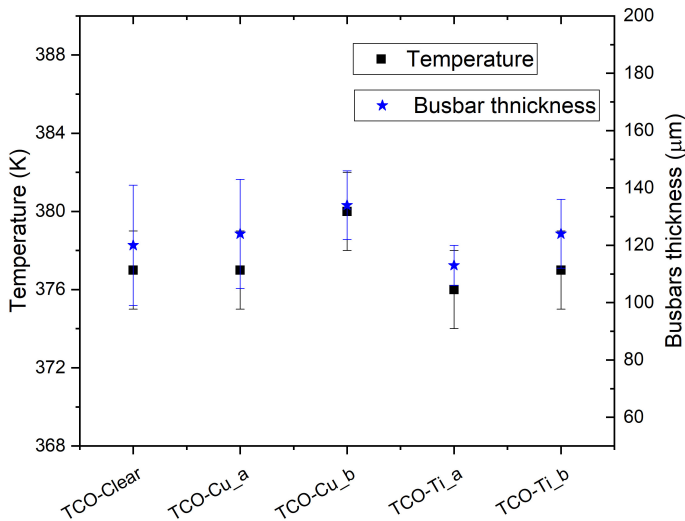


Figure 4: Temperature values for all substrates combined with the busbar thickness.

3.3 Mechanical tear and shear tests

Mechanical tear and shear tests are critical evaluations for assessing the strength and durability of busbars used in various applications, including photovoltaic modules. The tear test involves subjecting busbars to controlled tensile loads until they break or tear. Several standards outline tear test procedures for busbars in PV modules, with reference to the International Electrotechnical Commission (IEC) standard IEC 61215, which specifies requirements for the design and testing of crystalline silicon PV modules. According to IEC 61215, PV module busbars should withstand a minimum tensile force of 30 N/mm^2 without tearing. This test is typically performed on a module sample containing busbars, applying gradual load until busbar breakage occurs. The tear test serves as a crucial quality control measure to ensure the reliability and durability of busbars in PV modules. By subjecting busbars to controlled tensile loads, the test helps detect potential weaknesses or defects, enabling corrective action before deployment in the field.

Busbar shear tests assess the busbar's ability to endure mechanical stresses and loads typical of its intended application. In PV modules, busbars face various stresses, including thermal expansion, wind loads, and mechanical vibration. These stresses can lead to busbar deformation, cracking, or failure over time, resulting in reduced module efficiency or module failure. The International Electrotechnical Commission standard 61215 for terrestrial PV modules specifies a minimum requirement of 50 N for busbar shear tests. Similarly, the IEC 61646 standard for thin-film PV modules prescribes a minimum requirement of 60 N for the busbar shear test. Nonetheless, these values represent minimum requirements, and manufacturers may opt to exceed them to ensure their modules' mechanical strength and durability.

After conducting a series of measurements on each sample, the average values, regardless of the layer, were found to be 500 N/cm^2 for the tear test and 600 N/m^2 for the shear test as presented in Fig. 5. These values significantly exceed those typical for busbars made by conventional methods.

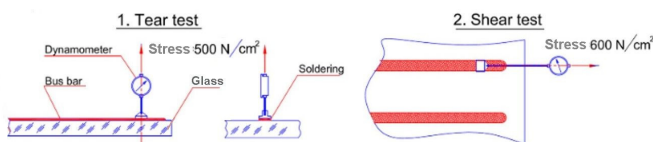


Figure 5: Schematic representation of tear and shear tests.

3.4 SEM imaging

The morphology of the tested samples was analyzed using scanning electron microscopy (SEM). Images were obtained for both the surface of the metallic tracks and the cross-section, which was achieved by cutting and fracturing the glass. Figure 6a presents an image illustrating the boundary between the metallic path (left) and the substrate (right). Upon closer examination in Fig. 6b, it becomes apparent that CuZn alloy particles are present at the boundary regions, although they do not have physical contact with the track. The electrode itself consists of fused particles, forming a highly rugged structure, as depicted in Fig. 6c. This roughness is further emphasized in images 6d to 6f. When observing the material at the nanoscale (Figs. 6g and 6h), nanoroughness becomes apparent, which may, but not necessarily, result from surface oxidation of the track. These nanoscale images reveal both darker and lighter areas, possibly indicating an inhomogeneous distribution of elements within the CuZn alloy or the presence of admixtures (estimated at < 0.5 wt%).

Figure 7a offers a general view of the cross-section of the TCO-clear sample, with a more detailed view in Fig. 7b. Figure 7c displays the interface between the glass, the FTO coating, and the metallic track, indicating a strong connection between these components. It is likely that the glass manufacturer employs an additional, very thin buffer layer of unknown chemical composition (probably SiO_2) between the glass and the FTO coating to prevent ion migration from the glass to the FTO. An inadvertently detached metallic track from the substrate (Fig. 7d) reveals that the detached surface mirrors the rough topography of the FTO coating, implying that during the initial phase of metallic track deposition, the layer is likely liquid or semi-liquid, allowing it to conform to the substrate's surface shape. Upon analyzing the interior of the cross-section (Fig. 7e), it becomes evident that the interior of the metallic path is denser (solid) compared to its surface (as seen in Fig. 6).

Similar conclusions can be drawn for samples with copper (Fig. 8) and titanium (Fig. 9) coatings. The visible cross-sections resemble Gaussian distributions. Metallic tracks exhibit strong adherence to the TCO substrate with the applied coating. During attempts to image the interface between the track and the substrate, it was challenging to directly visualize the metallic coating located between the FTO and the track (Figs. 8c and 9c). These tests were conducted on thinner (TCO-Cu_b, TCO-Ti_b) and thicker metal coatings (TCO-Cu_a, TCO-Ti_a). A slightly brighter

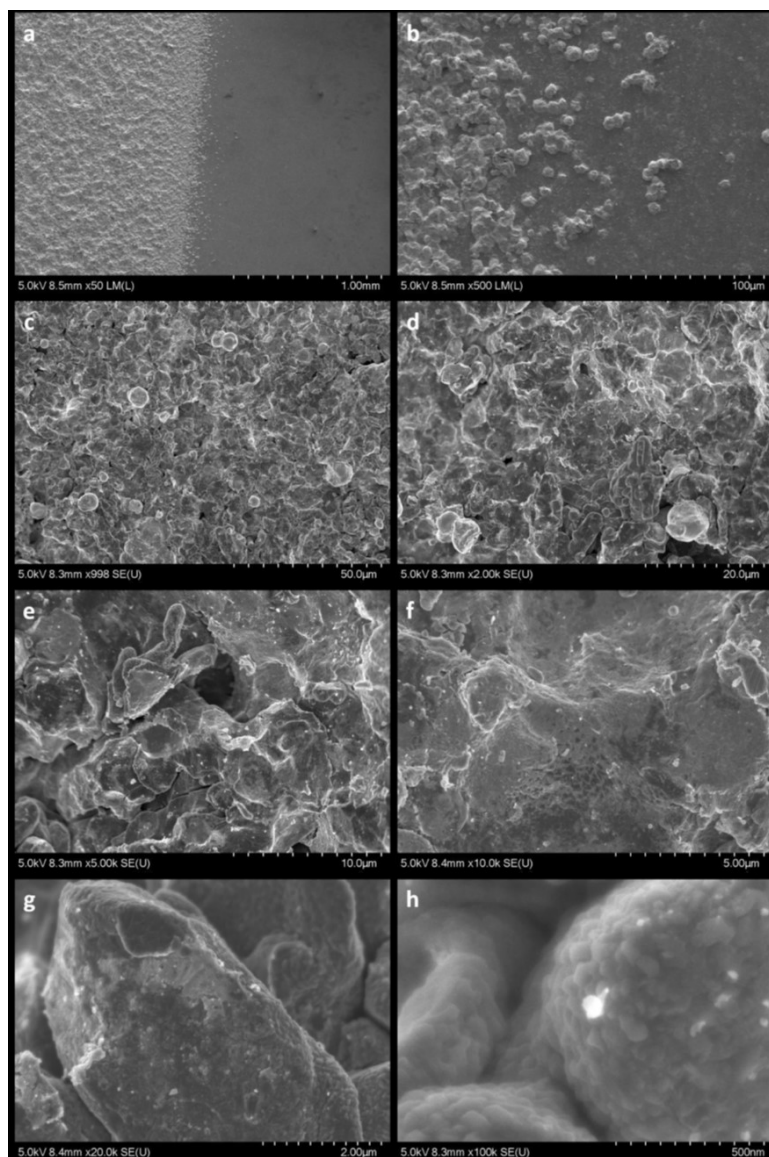


Figure 6: SEM images of the path-substrate boundary (a-b) and of the CuZn alloy surface (c-h) at different magnifications.

appearance in these areas may indicate the presence of a metallic coating, as the cross-section for secondary electron removal is correlated with the atomic number and material density.

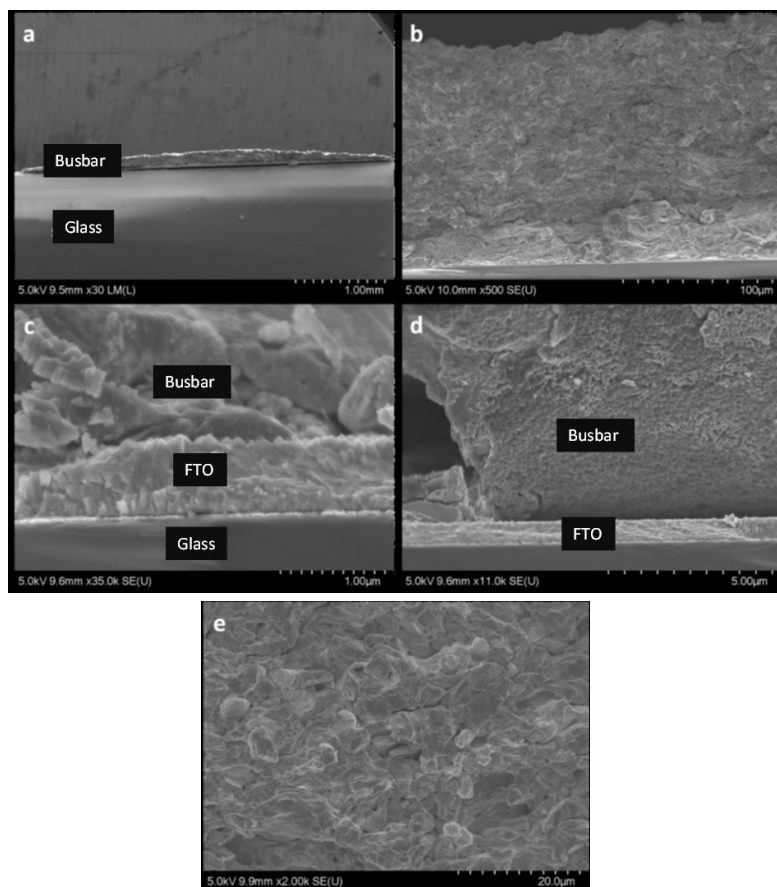


Figure 7: SEM images of the metallic path in the case of the TCO-clear sample: (a)–(b) the general cross-section, (c) the cross-section of the track-substrate interface, (d) the electrode detached from the substrate, (e) the inside of the cross-section.

The interface between the glass, FTO, Al_2O_3 , and the metallic path was also examined for the TCO- Al_2O_3 sample (Fig. 10c). In this instance, a thin layer of aluminium (III) oxide is prominently visible, appearing notably darker than the surrounding areas, and it uniformly covers the surface of the FTO along its entire length. The larger area of charge accumulation observed on the glass surface (Fig. 10a) suggests that the flow of electrons from the glass to the FTO may be hindered due to the insulating properties of Al_2O_3 . While the charging effect (bright, floating image) was observed for the other samples as well, it was particularly pronounced in this case.

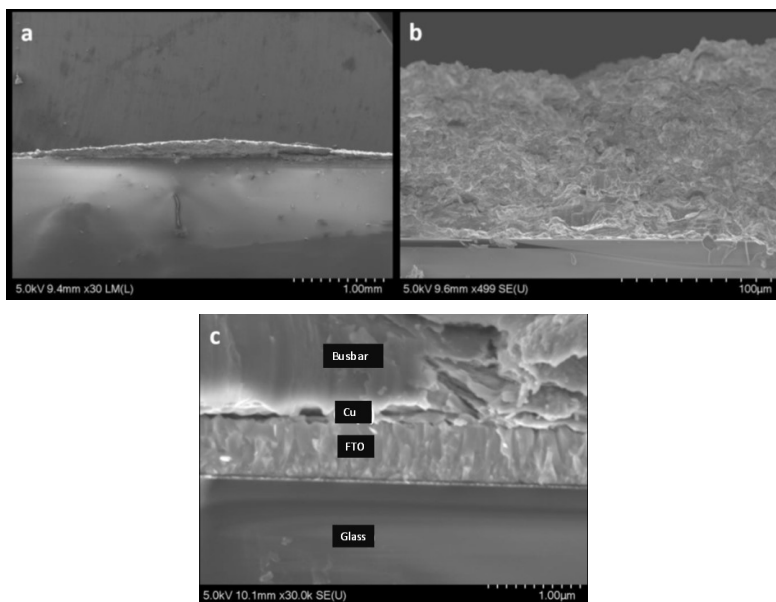


Figure 8: SEM images (a)–(b) showing the general section and (c) the path-substrate interface section obtained for the TCO-Cu_a sample.

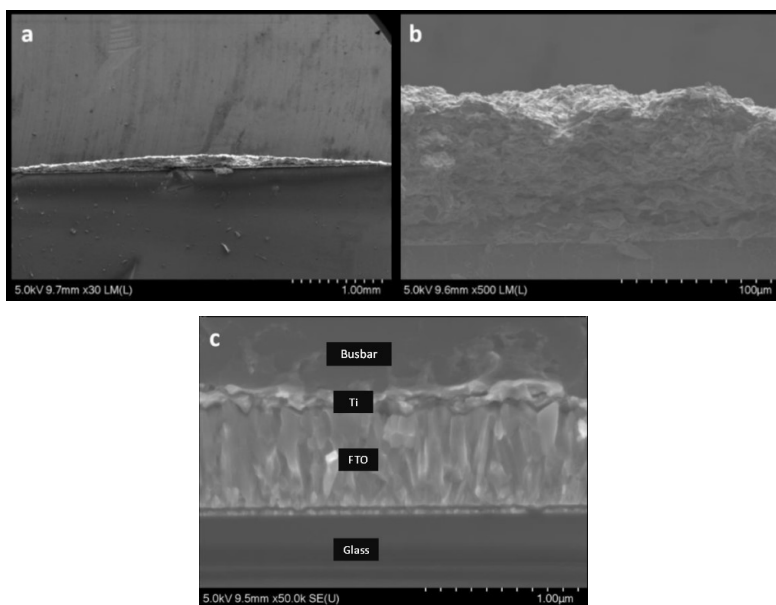


Figure 9: SEM images (a)–(b) displaying the general cross-section and (c) the cross-section of the path-substrate interface for the TCO-Ti_a sample.

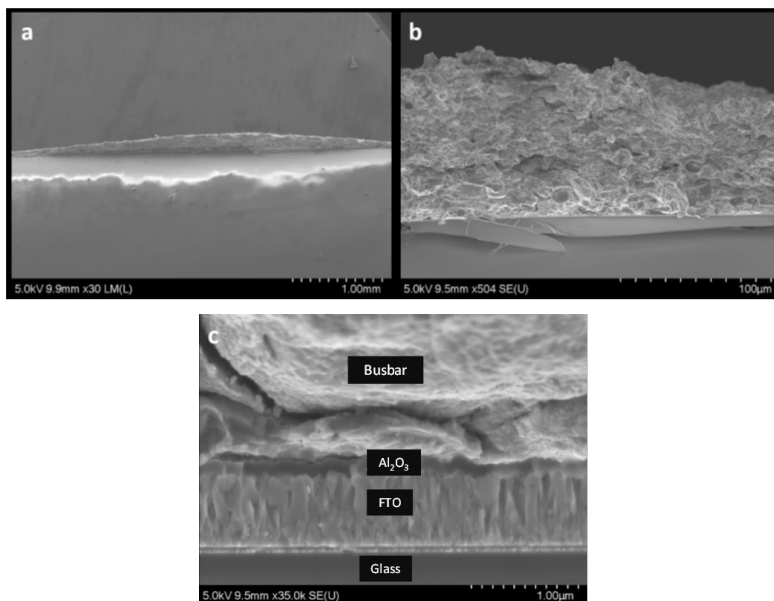


Figure 10: SEM images (a)–(b) of the general section and (c) of the path-substrate interface section obtained for the TCO- Al_2O_3 sample.

3.5 Energy-dispersive X-ray spectroscopy analysis

The elemental composition of the electrodes was analyzed using EDX spectroscopy. Figure 11 presents an example of a spectrum collected from a me-

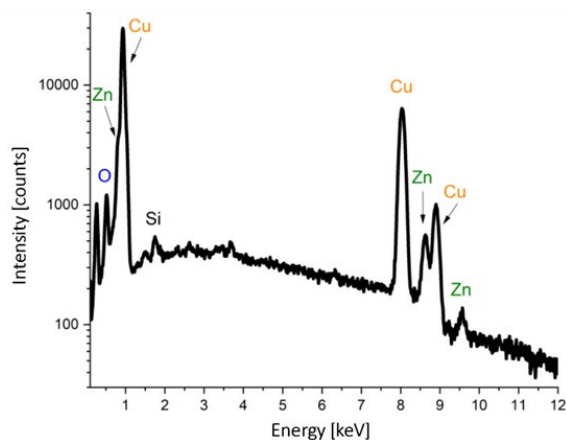


Figure 11: An example spectrum collected in the area of the metallic path from the area of $50\text{ }\mu\text{m} \times 50\text{ }\mu\text{m}$.

tallic track deposited on a TCO-clear sample. The spectrum displays characteristic peaks for copper (Cu) and zinc (Zn) atoms. Furthermore, signals from silicon (Si) and oxygen (O) are also present. While the presence of oxygen can be attributed to the oxidation of the metallic track's surface, the silicon content may result from the signal originating from the substrate (FTO glass) or a minor admixture of this element to the CuZn alloy. The former theory appears to be more plausible because, within the energy range of 3–4 keV, small peaks emerge from the noise, typical of tin (Sn) originating from the FTO ($\text{SnO}_2\text{:F}$) coating on the glass.

The weight percentage of the elemental composition is presented in Table 3. Upon analysis of the data, it is evident that the metallic traces primarily consist of copper with a notable admixture of zinc. The weight ratio of copper to zinc (Cu/Zn) varies and falls within the range of 2.33 to 3.37.

Table 3: Summary of the percentage by weight elemental compositions for individual samples of metallic paths determined from the collected EDX spectra.

Designation	% by weight				Ratio Cu/Zn
	C	O	Cu	Zn	
TCO-clear	8.1	2.7	68.7	20.4	3.37
TCO-Cu_a	5.6	2.1	68.7	23.7	2.90
TCO-Cu_b	4.7	1.8	71.1	22.4	3.17
TCO-Ti_a	6.8	1.9	70.0	21.3	3.29
TCO-Ti_b	4.9	1.9	70.6	22.6	3.12
TCO-Al ₂ O ₃	5.0	2.1	64.5	27.7	2.33

3.6 Electrical measurements

The resistance of the busbar is an important electrical parameter that affects the overall efficiency of the module. Lower resistance leads to lower power losses due to Joule heating and results in higher module efficiency. Attempts to measure the electrical properties were made on a device for determining the surface resistance with four probes and a Keithley multimeter. In both cases, the results were unclear and difficult to interpret.

A measurement made with a multimeter showed a resistance of around $0.3\ \Omega$. However, this value is lower than the resistance on the measuring probes, because when shorting them together, the device showed a resistance of about $0.4\ \Omega$. This value indicates the resistance of the test probe leads themselves, since the internal resistance of a device of this class is

negligible. Another measurement was made on a device for measuring the surface resistance. In this case, the measurement of the current from the voltage $I(U)$ between the two probes is performed and the measurement of the voltage from the current $U(I)$ between the other two probes. Both values should be linear so that the algorithm can handle the calculation of the resistance and conductivity values of the material. Attempts with different parameters and measurement locations failed because the $I(U)$ relationship was exponential. The reason for this state of affairs may be ballistic, and not diffusion, charge transport in the metallic path resulting from nanometric channels between sintered CuZn alloy particles. The counterargument to this theory are the particles visible in the SEM images, the size of which exceeds $1\text{ }\mu\text{m}$, and the radius of their sintering is significant (large sintering area between the particles). However, from the measurements carried out and the $I(U)$ characteristic obtained in the four-probe mode, it can be approximated that the resistance of the material is less than $0.4\text{ }\Omega$, which indicates that it achieves the conductivity of pure metals.

4 Summary

In summary, this research investigated the deposition of metallic busbars using a high-pressure spraying process on various substrates for photovoltaic modules. The key findings and observations from this study include:

- **Substrate variety:** The study examined six different types of substrates for busbar deposition. These substrates included TCO glass, TCO glass with metallic copper (Cu) and titanium (Ti) coatings, and insulating alumina (III) (Al_2O_3) coatings prepared using physical vapor deposition and atomic layer deposition processes.
- **Busbar thickness:** The average thickness of the busbars was determined to be approximately $125 \pm 16\text{ }\mu\text{m}$. There were slight variations in thickness between different substrates, with the smallest thickness of around $65\text{ }\mu\text{m}$ observed at the beginning of one of the busbars.
- **Surface topography:** The busbars exhibited rough surface topography at both micro- and nanometer scales. Despite this roughness, they displayed low resistivity, making them suitable for photovoltaic applications.

- Good adhesion: SEM images showed that the CuZn alloy of the busbars adhered well to the fluorine-doped tin oxide surface, as well as to fluorine-doped tin oxide surfaces covered with Cu, Ti or Al₂O₃ nanocoatings.
- Material reduction: The study demonstrated that it is possible to reduce the amount of copper (Cu) and silver (Ag) used in busbar production while maintaining low resistance values. This reduction in material usage can lead to cost savings in production.
- Versatile deposition technique: The presented high-pressure spraying process is effective for depositing conductive busbars on various surfaces, including glass, glass with a conductive layer (TCO), and polymer substrates. The relatively low deposition temperature allows for its use on different types of substrates, such as glass, TCO-coated glass, or silicon.
- Low resistance: The conductive busbars produced through this method exhibited low resistance, making them suitable for use in photovoltaic modules where efficient electrical conduction is essential.

Overall, the research suggests that the high-pressure spraying process is a promising technique for manufacturing cost-effective and efficient busbars for photovoltaic modules. It offers good adhesion, low resistance, and the potential for reducing material costs, which are all important factors for improving the performance and cost-effectiveness of solar energy generation.

Acknowledgments

This study was supported by the National Centre for Research and Development under the project No. POIR.01.02.00-00-0265/17-00.

Received 20 July 2023

References

- [1] Bouraiou A., Hamouda M., Chaker A., Lachtar S., Neçaibia A., Boutasseta N., Mostefaoui M.: *Experimental evaluation of the performance and degradation of single crystalline silicon photovoltaic modules in the Saharan environment*. Energy **132**(2017), 22–30. doi: [10.1016/j.energy.2017.05.056](https://doi.org/10.1016/j.energy.2017.05.056)

- [2] Sharma V., Sastry O.S., Kumar A., Bora B., Chandel S.S.: *Degradation analysis of a-Si, (HIT) hetero-junction intrinsic thin layer silicon and m-C-Si solar photovoltaic technologies under outdoor conditions*. Energy **72**(2014), 536–546. doi: [10.1016/j.energy.2014.05.078](https://doi.org/10.1016/j.energy.2014.05.078)
- [3] Ding K., Chen X., Weng S., Liu Y., Zhang J., Li Y., Yang Z.: *Health status evaluation of photovoltaic array based on deep belief network and Hausdorff distance*. Energy **262**(2023), 125539. doi: [10.1016/j.energy.2022.125539](https://doi.org/10.1016/j.energy.2022.125539)
- [4] Paggi M., Berardone I., Infuso A., Corrado M.: *Fatigue degradation and electric recovery in Silicon solar cells embedded in photovoltaic modules*. Sci. Rep. **4**(2014), 4506–4512. doi: [10.1038/srep04506](https://doi.org/10.1038/srep04506)
- [5] Borri C., Gagliardi M., Paggi M.: *Fatigue crack growth in Silicon solar cells and hysteretic behaviour of busbars*. Sol. Energ. Mat. Sol. C **181**(2018), 21–29. doi: [10.1016/j.solmat.2018.02.016](https://doi.org/10.1016/j.solmat.2018.02.016)
- [6] Infuso A., Corrado M., Paggi M.: *Image analysis of polycrystalline solar cells and modelling of intergranular and transgranular cracking*. J. Eur. Ceram. Soc. **34**(2014), 11, 2713–2722. doi: [10.1016/j.jeurceramsoc.2013.12.051](https://doi.org/10.1016/j.jeurceramsoc.2013.12.051)
- [7] Köntges M., Kunze I., Kajari-Schröder S., Breitenmoser X., Bjørneklett B.: *The risk of power loss in crystalline silicon based photovoltaic modules due to micro-cracks*. Sol. Energ. Mat. Sol. C **95**(2011), 4, 1131–1137. doi: [10.1016/j.solmat.2010.10.034](https://doi.org/10.1016/j.solmat.2010.10.034)
- [8] Kaule F., Wang W., Schoenfelder S.: *Modeling and testing the mechanical strength of solar cells*. Sol. Energ. Mat. Sol. C **120**(2014), 441–447. doi: [10.1016/j.solmat.2013.06.048](https://doi.org/10.1016/j.solmat.2013.06.048)
- [9] Taler J., Dzierwa P., Taler D., Harchut P.: *Optimization of the boiler start-up taking into account thermal stresses*. Energy **92**(2015), 160–170. doi: [10.1016/j.energy.2015.03.095](https://doi.org/10.1016/j.energy.2015.03.095)
- [10] Thomas M., Białecka B., Zdebik D.: *Removal of organic compounds from wastewater originating from the production of printed circuit boards by UV-Fenton method*. Arch. Env. Prot. **43**(2017), 4, 39–49. doi: [10.1515/aep-2017-0044](https://doi.org/10.1515/aep-2017-0044)
- [11] Vogt T., Boden S., Andruszkiewicz A., Eckert K., Eckert S., Gerbeth G.: *Detection of gas entrainment into liquid metals*. Nucl. Eng. Des. **294**(2015), 16–23. doi: [10.1016/j.nucengdes.2015.07.072](https://doi.org/10.1016/j.nucengdes.2015.07.072)
- [12] Braun S., Hahn G., Nissler R., Pönisch C., Habermann D.: *The multi-busbar design: an overview*. Energy Procedia **43**(2013), 86–92. doi: [10.1016/j.egypro.2013.11.092](https://doi.org/10.1016/j.egypro.2013.11.092)
- [13] Schneider A., Rubin L., Rubin G.: *Solar cell efficiency improvement by new metallization techniques – the day4 electrode concept*. In: Proc. 2006 IEEE 4th World Conf. on C Photovoltaic Energy Conversion, Waikoloa, 2006, Vol. 1, 1095–1098. doi: [10.1109/WCPEC.2006.279333](https://doi.org/10.1109/WCPEC.2006.279333)
- [14] Braun S., Hahn G., Nissler R., Pönisch C., Habermann D.: *The Multi-busbar Design: An Overview*. Energy Proced. **43**(2013), 86–92. doi: [10.1016/j.egypro.2013.11.092](https://doi.org/10.1016/j.egypro.2013.11.092)
- [15] Wang B., Jia X., Yang J., Wang Q.: *Numerical study on temperature rise and structure optimization for a three-phase gas insulated switchgear busbar chamber*. Energy **254**(2022), 124463. doi: [10.1016/j.energy.2022.124463](https://doi.org/10.1016/j.energy.2022.124463)

- [16] Braun S., Hahn G., Nissler R., Pönisch C., Habermann D.: *Multi-busbar solar cells and modules: higher efficiencies and low silver consumptions*. Energy Proced. **38**(2013), 334–339. doi: [10.1016/j.egypro.2013.07.286](https://doi.org/10.1016/j.egypro.2013.07.286)
- [17] Haverkamp H., Dastgheib-Shirazi A., Raabe B., Book F., Hahn G.: *Minimizing the electrical losses on the front side: development of a selective emitter process from a single diffusion*. In: Proc. 33rd IEEE Photovoltaics Specialist Conf. (PVSC), San Diego, 11–16 May 2008, **1**(2008), 4. doi: [10.1109/PVSC.2008.4922443](https://doi.org/10.1109/PVSC.2008.4922443)
- [18] Chen C., Pei X., Chen Y., Kang Y.: *Investigation, evaluation, and optimization of stray inductance in laminated busbar*. IEEE T. Power Electr. **29**(2014), 7, 3679–3693. doi: [10.1109/TPEL.2013.2282621](https://doi.org/10.1109/TPEL.2013.2282621)
- [19] Plesca A.: *Thermal analysis of busbars from a high current power supply system*. Energies **12**(2019), 2288. doi: [10.3390/en12122288](https://doi.org/10.3390/en12122288)
- [20] Smirnova L., Juntunen R., Murashko K., Musikka T., Pyrhönen J.: *Thermal analysis of the laminated busbar system of a multilevel converter*. IEEE T. Power Electr. **31**(2016), 1479–1488. doi: [10.1109/TPEL.2015.2420593](https://doi.org/10.1109/TPEL.2015.2420593)
- [21] Varivodov V.N., Kovalev D.I., Zhulikov S.S., Golubev D.V., Romanov V.A., Mirzabekyan G.Z.: *Technological aspects of the use of cast polymer insulation for high-voltage switchgear and busbars*. Power Technol Eng. **54**(2021), 915–922. doi: [10.1007/s10749-021-01306-2](https://doi.org/10.1007/s10749-021-01306-2)
- [22] Lu Y., Li G., Akhlaghi Y.G., Xuan Q., Pei G., Ji J., Zhao X.: *Effect of grid and optimization on improving the electrical performance of compound parabolic concentrator photovoltaic cells*. Sol. Energy **196**(2020), 607–615. doi: [10.1016/j.solener.2019.12.065](https://doi.org/10.1016/j.solener.2019.12.065)
- [23] Kyranaki N., Smith A., Yendall K., Hutt D.A., Whalley D.C., Gottschalg R., Betts T.R.: *Damp-heat induced degradation in photovoltaic modules manufactured with passivated emitter and rear contact solar cells*. Prog. Photovoltaics **30**(2022), 9, 1061–1071. doi: [10.1002/pip.3556](https://doi.org/10.1002/pip.3556)
- [24] Panda T., Sadhukhan S., Acharyya S., Banerjee P., Nandi A., Bose S., Mondal N., Das G., Maity S., Chaudhuri P., Saha H.: *Impact of multi-busbar front grid patterns on the performance of industrial type c-Si solar cel*. Sol. Energy **236**(2022), 790–801. doi: [10.1016/j.solener.2022.03.051](https://doi.org/10.1016/j.solener.2022.03.051)
- [25] Zhang Z., Zeng Y., Jiang C-S., Huang Y., Liao M., Tong H., Al-Jassim M., Gao P., Shou C., Zhou X., Yan B., Ye J.: *Carrier transport through the ultrathin silicon-oxide layer in tunnel oxide passivated contact (TOPCon) c-Si solar cells*. Sol. Energ. Mater. Sol. Cell. **187**(2018), 113–122. doi: [10.1016/j.solmat.2018.07.025](https://doi.org/10.1016/j.solmat.2018.07.025)
- [26] Schneider A., Harney R., Aulehla S., Lemp E., Koch S.: *Progress in interconnection of busbar-less solar cells by means of conductive gluing*. Energy Proced. **38**(2013), 387–394. doi: [10.1016/j.egypro.2013.07.294](https://doi.org/10.1016/j.egypro.2013.07.294)
- [27] Park J., Park N.: *Wet etching processes for recycling crystalline silicon solar cells from end-of-life photovoltaic modules*. RSC Adv. **4**(2014), 34823–34829. doi: [10.1039/C4RA03895A](https://doi.org/10.1039/C4RA03895A)
- [28] Zarmai M.Z., Ekere N.N., Oduoza C.F., Amalu E.H.: *A review of interconnection technologies for improved crystalline silicon solar cell photovoltaic module assembly*. Appl. Energ. **154**(2015), 173–182. doi: [10.1016/j.apenergy.2015.04.120](https://doi.org/10.1016/j.apenergy.2015.04.120)

- [29] Tyagi V.V., Rahim N.A.A., Rahim N.A., Selvaraj J.A.J.: *Progress in solar PV technology: Research and achievement*. Renew. Sustain. Energ. Rev. **20**(2013), 443–461. doi: [10.1016/j.rser.2012.09.028](https://doi.org/10.1016/j.rser.2012.09.028)
- [30] Jung T., Song H., Ahn H., Kang G.: *A mathematical model for cell-to-module conversion considering mismatching solar cells and the resistance of the interconnection ribbon*. Sol. Energy **103**(2014), 253–262. doi: [10.1016/j.solener.2014.01.032](https://doi.org/10.1016/j.solener.2014.01.032)
- [31] Oh W., Jee H., Bae J., Lee J.: *Busbar-free electrode patterns of crystalline silicon solar cells for high density shingled photovoltaic module*. Sol. Energ. Mater. Sol. Cell. **243**(2022), 11802. doi: [10.1016/j.solmat.2022.111802](https://doi.org/10.1016/j.solmat.2022.111802)
- [32] Oh W., Park J., Jeong C., Park J., Yi J., Lee J.: *Design of a solar cell electrode for a shingled photovoltaic module application*. Appl. Surf. Sci. **510**(2020), 145420. doi: [10.1016/j.apsusc.2020.145420](https://doi.org/10.1016/j.apsusc.2020.145420)
- [33] Grätzel M.: *Dye-sensitized solar cells*. J. Photochem. Photobiol. C: Photochem. Rev. **4**(2003), 2, 145–153. doi: [10.1016/S1389-5567\(03\)00026-1](https://doi.org/10.1016/S1389-5567(03)00026-1)
- [34] O'Regan B., Grätzel M.: *A low-cost, high-efficiency solar cell based on dye-sensitized colloidal TiO₂ films*. Nature **353**(1991), 737–740. doi: [10.1038/353737a0](https://doi.org/10.1038/353737a0)
- [35] Fortunato E., Ginley D., Hosono H., Paine D.C.: *Transparent conducting oxides for photovoltaics*. MRS Bull. **32**(2007), 3, 42–47. doi: [10.1557/mrs2007.29](https://doi.org/10.1557/mrs2007.29)
- [36] Noh S.I., Ahn H.-J., Riu D.-H.: *Photovoltaic property dependence of dye-sensitized solar cells on sheet resistance of FTO substrate deposited via spray pyrolysis*. Ceram. Int. **38**(2012), 5, 3735–3739. doi: [10.1016/j.ceramint.2012.01.018](https://doi.org/10.1016/j.ceramint.2012.01.018)
- [37] Kwak D.-J., Moon B.-H., Lee D.-K., Park C.-S., Sung Y.-M.: *Comparison of transparent conductive indium tin oxide, titanium-doped indium oxide, and fluorine-doped tin oxide films for dye-sensitized solar cell application*. J. Elec. Eng. Techn. **6**(2011) 5, 684–687. doi: [10.5370/JEET.2011.6.5.684](https://doi.org/10.5370/JEET.2011.6.5.684)
- [38] Daghsen K., Lounissi D., Bouaziz N.: *A universal model for solar radiation exergy accounting: Case study of Tunisia*. Arch. Thermodyn. **43**(2022), 2, 97–118. doi: [10.24425/ather.2022.141980](https://doi.org/10.24425/ather.2022.141980)
- [39] Singh J., Guo S., Peters I.M., Aberle A., Walsh T.: *Comparison of glass/glass and glass/backsheet PV modules using bifacial silicon solar cells*. IEEE J. Photovolt. **5**(2015), 99, 783–791. doi: [10.1109/JPHOTOV.2015.2405756](https://doi.org/10.1109/JPHOTOV.2015.2405756)
- [40] Generowicz A., Gronba-Chyła A., Kulczycka J., Harazin P., Gaska K., Ciula J., Ocioń P.: *Life Cycle Assessment for the environmental impact assessment of a city' cleaning system. The case of Cracow (Poland)*. J. Clean. Prod. **382**(2023), 135184. doi: [10.1016/j.jclepro.2022.135184](https://doi.org/10.1016/j.jclepro.2022.135184)
- [41] Ciula J., Kowalski S., Wiewiórska I.: *Pollution indicator of a megawatt hour produced in cogeneration – the efficiency of biogas purification process as an energy source for wastewater treatment plants*. J. Ecol. Eng. **24**(2023), 3, 232–245. doi: [10.12911/22998993/158562](https://doi.org/10.12911/22998993/158562)
- [42] Deng S., Zhang Z., Ju C., Dong J., Xia Z., Yan X., Xu T., Xing G.: *Research on hot spot risk for high-efficiency solar module*. Energy Proced. **130**(2017), 77–86. doi: [10.1016/j.egypro.2017.09.399](https://doi.org/10.1016/j.egypro.2017.09.399)

- [43] Kim K.A., Krein P.T.: *Photovoltaic hot spot analysis for cells with various reverse-bias characteristics through electrical and thermal simulation*. In: Proc. 2013 IEEE 14th Workshop on Control and Modeling for Power Electronics (COMPEL), Salt Lake City, 2013, 1–8. doi: [10.1109/COMPEL.2013.6626399](https://doi.org/10.1109/COMPEL.2013.6626399)
- [44] Alwaeli M.: *Investigation of gamma radiation shielding and compressive strength properties of concrete containing scale and granulated lead-zinc slag wastes*. J. Clean. Prod. **166**(2017), 157–162. doi: [10.1016/j.jclepro.2017.07.203](https://doi.org/10.1016/j.jclepro.2017.07.203)
- [45] Solheim H.J., Fjær H.G., Srheim E.A., Foss S.E.: *Measurement and simulation of hot spots in solar cells*. Energy Proced. **38**(2013), 183–189. doi: [10.1016/j.egypro.2013.07.266](https://doi.org/10.1016/j.egypro.2013.07.266)
- [46] Tomtas P., Skwiot A., Sobiecka E., Obraniak A., Ławińska K., Olejnik T.: *Bench tests and CFD simulations of liquid–gas phase separation modeling with simultaneous liquid transport and mechanical foam destruction*. Energies **14**(2021), 6, 1740. doi: [10.3390/en14061740](https://doi.org/10.3390/en14061740)
- [47] Ocloń P., Chin H.H., Kozak-Jagiela E., Taler J., Ścisłowicz F., Czamara M.: *33-Photovoltaic-Thermal Waste Heat Integration with Underground Thermal Energy Storage and Heat Pump Systems*. Handbook of Process Integration (2nd Edn.). Woodhead, 2023, 1017–1042. doi: [10.1016/B978-0-12-823850-9.00005-0](https://doi.org/10.1016/B978-0-12-823850-9.00005-0)
- [48] Hadjidj M.S., Bibi-Triki N., Didi F.: *Analysis of the reliability of photovoltaic-microwind based hybrid power system with battery storage for optimized electricity generation at Tlemcen, north west Algeria*. Arch. Thermodyn. **40**(2019), 1, 161–185. doi: [10.24425/ather.2019.128296](https://doi.org/10.24425/ather.2019.128296)
- [49] Hocine M., Abdessalam O.: *Simulation of photovoltaic panel cooling beneath a single nozzle based on a configurations framework*. Arch. Thermodyn. **42**(2021), 1, 115–128. doi: [10.24425/ather.2020.136950](https://doi.org/10.24425/ather.2020.136950)
- [50] Thomas M., Białecka B., Zdebik D.: *Removal of organic compounds from wastewater originating from the production of printed circuit boards by UV-Fenton method*. Arch. Environ. Protect. **43**(2017), 4, 39–49. doi: [10.1515/aep-2017-0044](https://doi.org/10.1515/aep-2017-0044)
- [51] Vogt T., Boden S., Andruszkiewicz A., Eckert K., Eckert S., Gerbeth G.: *Detection of gas entrainment into liquid metals*. Nucl. Eng. Des. **294**(2015), 16–23. doi: [10.1016/j.nucengdes.2015.07.072](https://doi.org/10.1016/j.nucengdes.2015.07.072)
- [52] Bogdanowicz K.A., Augustowski D., Dziedzic J., Kwaśnicki P., Malej W., Iwan A.: *Preparation and characterization of novel polymer-based gel electrolyte for dye-sensitized solar cells based on poly(vinylidene fluoride-co-hexafluoropropylene) and poly(acrylonitrile-co-butadiene) or poly(dimethylsiloxane) bis(3-aminopropyl)*. Copolymer. Mater. **13**(2020), 12, 2721. doi: [10.3390/ma13122721](https://doi.org/10.3390/ma13122721)
- [53] Abdulghafor I.A., Mnati M.J.: *Design of thermoelectric radiant cooling – photovoltaic panels system in the building*. Arch. Thermodyn. **43**(2022), 4, 85–108. doi: [10.24425/ather.2022.144407](https://doi.org/10.24425/ather.2022.144407)

Off-grid power supply – the future of district heating

ROBERT WIŚNIEWSKI^a
AGATA KANIA^a
WIESŁAW ZIMA^{b*}
JAN TALER^b

^a Municipal Heat Supply Company, Jana Pawła II 188, 30-969 Kraków, Poland

^b Cracow University of Technology, Department of Energy, Jana Pawła II 37, 31-864 Kraków, Poland

Abstract The paper presents the first off-grid system designed to supply electricity to the equipment mounted on components of the district heating network in district heating chambers. The proposed off-grid system is equipped, among other things, with a turbine and a generator intended for electricity production. On-grid power supply is a common way of providing electricity with strictly defined, known and verified operating parameters. For off-grid power supply, however, there are no documented testing results showing such parameters. This paper presents selected results of tests and measurements carried out during the operation of an off-grid supply system powering the equipment installed in a district heating chamber. The values of voltage obtained from a turbine-driven generator are analysed in detail. The analysis results can be used as the basis for further works aiming to optimize the off-grid system of electricity supply to devices installed in district heating chambers.

Keywords: District heating networks; District heating chamber and its modernization; Off-grid supply; Preliminary results of measurements

*Corresponding Author. Email: wieslaw.zima@pk.edu.pl

1 Introduction

District heating has been faced with increasing goals and developments over the years [1]. This is largely the effect of increasing environmental requirements. The year 2014 marked the introduction of the 4th generation (4G) district heating [2], which is characterized by low supply temperatures (below 70°C) and digitization of district heating systems and nodes. The premise of the 4G district heating was to increase the efficiency of the district heating system and reduce the use of fossil fuels by integrating the network with low-temperature energy sources, such as geothermal sources, waste heat or solar collectors. Research projects on the 5th generation (5G) district heating networks were performed as early as in 2015 [3]. This generation assumes an additional cooling function and supply temperatures below 50°C. In addition, the 5G network will no longer have a central source but distributed sources. An example work with a focus on 5G networks is [4], dedicated to a 5G heating and cooling network for a residential district. It presents the design and a thermal and economic analysis of such a novel network.

The technical and economic aspects of the application of adsorption refrigeration devices to generate cool using hot water from a district heating network are the subject of [5]. The paper studies the operation of adsorption air-conditioning units co-operating with a dry cooler.

The future of district heating necessitates the introduction of new energy sources (such as renewable sources), as well as other modern solutions integrating and controlling parameters of transmitted thermal energy. The authors of [6] note that with the development of renewable energy sources and their application in district heating, district heating systems will become increasingly complex. They present the results of an analysis conducted, among others by means of artificial neural networks, and concerning optimization of the operation of combined heat and power (CHP) plants. A combined heat and power plant is also the subject of [7]. The paper emphasizes that for efficient operation of such a cogeneration system, it is necessary to provide short-term prediction of the heat demand within the horizon of the next day. A method of hourly forecasting of the heat load was proposed. The results of such off-season forecasting in a real district heating system are presented. Optimization issues are also addressed in [8]. Two mathematical models for the network operation optimization are presented. A detailed analysis is conducted of thermal energy storage in pipelines. Energy storage in district heating systems is also the focus

of [9], which presents the concept and implementation of droop control for a district heating network. The characteristics of the droop between the heated water temperature and the share of power in the thermal energy storage tank are developed for a district heating network using the analogy with the droop control in a direct current (DC) electrical network.

The development of district heating networks also requires the ability to simulate heat and pressure losses in the network. For this purpose, power companies use simulation software. Such software must include fast and efficient numerical methods that produce accurate and stable results [10].

In recent years, the topical issue has been smart district heating networks (SDHNs), in which the processes of the operation management (through data monitoring and gathering) and control are improved. In order to build, and first of all operate a SDHN, it is necessary to equip it with automatic devices and elements for monitoring and regulation. However, such devices need to be supplied with power, and the access of district heating network facilities (such as district heating chambers) to the power grid is often difficult. This involves the need to create an alternative source of power supply, referred to as off-grid power supply [11], characterized by no access to the power grid, but having its own local source of voltage. The literature survey indicates that so far off-grid power supply has not been analysed, let alone utilized to supply electricity to devices of district heating facilities, such as the district heating chamber. Consequently, there is no experience related to the selection of electrical components making up an off-grid power supply system. There are also no verified algorithms for the control of the operation of an off-grid system being an alternative source of power supply.

The structure of a SDHN requires transition from district heating and power grid networks being traditionally independent to systems which are actively coupled. The district heating network thus has to be increasingly co-ordinated with the power grid. The expected outcome is a smart system integrating industries that have up till now been independent [2]. The authors of [12] indicate that SESs will fulfil an important role in implementing sustainable energy systems. A method of technical assessment of actively coupled district heating and power grid networks is proposed in [13].

The processes of integration and optimization of multiple energy networks (electricity grid, district heating grid, gas grid) are important issues in the building industry as well. This will help to increase the flexibility of future SESs that also use renewable energy [14].

The need to construct a SDHN contributed to the construction of the first off-grid system supplying power to a district heating chamber using

a turbine-based pressure controller (TPC) [15]. The turbine was installed on a pipeline belonging to the Municipal Heat Supply Company in Krakow. This paper presents the results of measurements performed during the operation of the first district heating chamber supplied with electricity by an off-grid power supply system. As indicated by the literature survey, this issue has not been analysed yet.

2 Technological description of the modernized district heating chamber

The off-grid power supply system located in the heating chamber of the Municipal Heat Supply Company in Krakow (Fig. 1) is the facility for the testing and analysis of the off-grid system operation. The district heating chamber (Fig. 2) was retrofitted to satisfy the needs of the tested off-grid power supply system. It was equipped with a TPC mounted on the pipeline. The turbine drives the generator. The main turbine and generator parameters are shown in Tables 1 and 2, respectively.

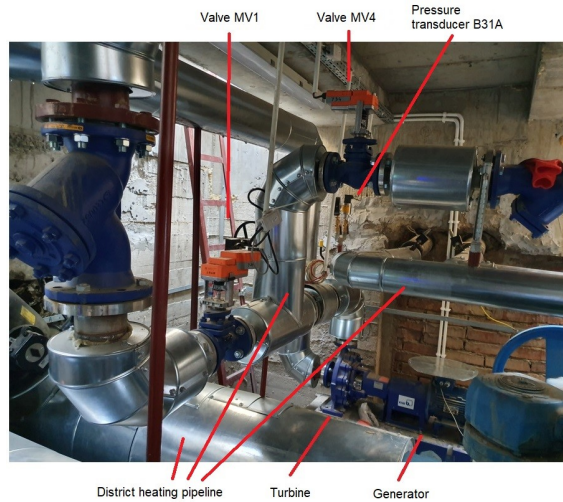


Figure 1: Fragment of the system in the district heating chamber.

The system located in the district heating chamber was extended by a bypass of the main return pipeline (DN 350). The bypass has the DN 250 diameter and branches into three pipelines:

- DN 100 pipeline, on which the turbine is located along with the generator and the MV1 valve,
- DN 100 pipeline, on which the MV2 valve is located,
- DN 250 pipeline, which is equipped with the MV3 valve.

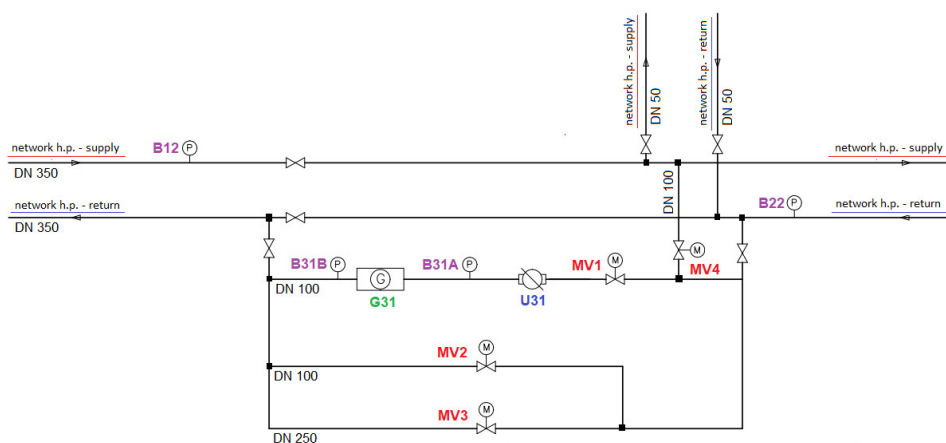


Figure 2: Flowchart of the district heating chamber: G31– generator with the turbine; MV1, MV2, MV3, MV4 – valves; U31 – flowmeter; B12, B22, B31A, B31B – pressure transducers.

Table 1: Turbine parameters.

Type	Etanorm 32-250
Capacity	19 m ³ /h
Delivery head	30 m
Rotational speed	1020 min ⁻¹

Table 2: Generator parameters.

Type	GV 100L8
Rated power	2 kVA
Rated voltage	28 V
Rated current	41.9 A
Rotational speed	1020 min ⁻¹
Frequency	68 Hz

To protect the off-grid power supply system against too low a flow rate of the heating medium driving the turbine, a DN 100 pipe was added to connect the supply and the return of the district heating network. The pipe connects the main feed pipeline (DN 350) to the DN 100 pipeline on which the turbine is installed. The medium flow through this connection is opened when the turbine is not operating (due to a small flow on the bypass) and at the risk of discharging the accumulators.

The pipeline in the district heating chamber is fitted with four pressure transducers (B12, B22, B31A, B31B), a flowmeter (U31) and four electrically driven control valves (MV1, MV2, MV3, MV4). These elements are powered by the off-grid supply system. The B12 pressure transducer measures the pressure on the main DN 350 feed pipeline, transducer B22 is used to measure the pressure on the main DN 350 return pipeline of the district heating network, while transducers B31A and B31B, respectively, measure the pressure upstream and downstream of the turbine. Flow meter U31 is used to measure the heating medium volume flow rate through the turbine. The task of valves MV1, MV2 and MV3 is to maintain the set value of the pressure in the return pipeline. Valves MV2, and MV3 maintain the set disposition and do not allow the return pressure B22 to be exceeded. Valve MV1 determines the appropriate operating point of the turbine. The medium flowing through valve MV1 drives the turbine located after it (G31). Valve MV4 operates only if a threat arises of complete discharge of the accumulators and no energy production by the generator due to too low a flow through the turbine. The MV4 valve is only opened for emergency charging of the accumulators.

The reason for installing the turbine on the bypass of the return pipeline was the medium lower temperature. The assumed mass flow rate through the chamber totals 97.22 kg/s in the winter period and 5.56 kg/s in summer. The main DN 350 return pipeline is closed and the entire heating medium flows through valves MV1, MV2 and MV3, i.e. through the bypass created during the chamber modernization.

3 Description of the tested facility electric system

The tested facility electric system (Fig. 3) includes the system of the electricity generator, the system of the valve drives, the system of the dewatering pump, the system of the cabinets with the control and measuring ap-

paratus and the lighting system. Measurements of the following quantities are performed on the off-grid power supply system: pressure, the medium volume flow rate through the turbine, the desired degrees of opening of the valves along with their actual positions, the voltage coming out of the generator after passing through the bridge rectifier, and the voltage supplying the equipment through the off-grid system. Trend logs are created for the measured quantities for data archiving.

The analysed off-grid power supply electric system (Fig. 3) is built based on an alternating current (AC) generator with voltage in the range of 24–28 V, driven by a water turbine mounted on the return pipeline of the district heating network. The supply from the electric current generator is fed to the controller through an alternating current/direct current (AC/DC) system. The system was built using the maximum power point tracking (MPPT) solar charge controller intended for off-grid photovoltaic (PV) systems, where voltage is obtained from PV panels. Two in-series configured 12 V 24 Ah accumulators are connected to the charge controller. The system is equipped with an accumulator protection module which ensures continuity of the 24 V DC supply and appropriate control of the charging of the accumulators. The maximum consumption power of the devices installed in the chamber, i.e. the electric drives of the valves, the dewatering pump,

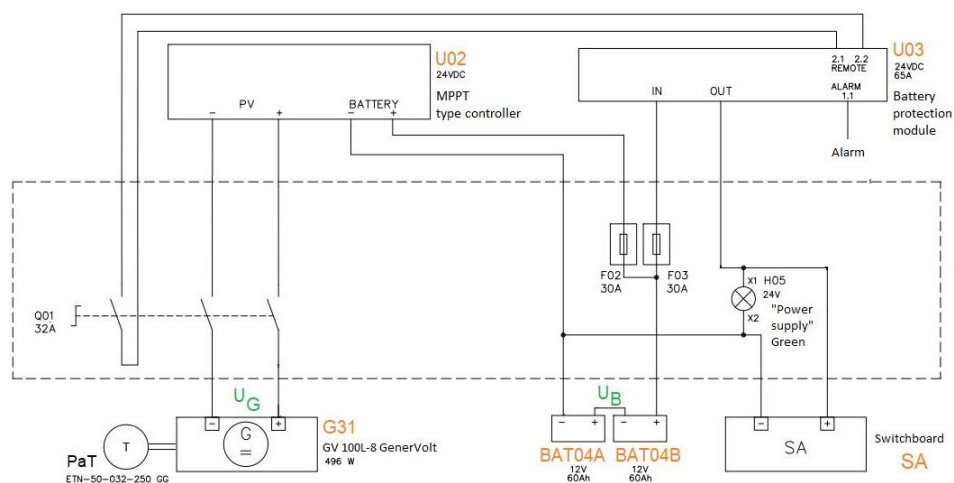


Figure 3: Diagram of the electric system of the generator connection to the controller: G31 – turbine with generator, U02 – MPPT controller, U03 – accumulator protection module, BAT04A, BAT04B – accumulators, SA – switchgear, Q01 – circuit breaker, F02, F03 – fuses, H05 – lamp.

the chamber lighting and the control system, totals 440 W at the supply voltage of 24 V DC.

3.1 Characteristics of the electric system elements

The off-grid power supply system consists of two main parts: the generation-storage and the power-receiving components. The generation-storage section includes a synchronous generator with permanent magnets, a charge controller, an accumulator protection module, and accumulators. The power-receiving part encompasses valve drives, a dewatering pump, a lighting system, and electrical cabinets.

A charge controller with the MPPT function is integrated into the off-grid system. The MPPT function continuously monitors the voltage and current intensity generated by the generator (at the controller input). Unlike conventional pulse width modulation (PWM) controllers, the MPPT controller can harness the maximum power produced by the generator. This maximizes the efficiency of energy utilization for charging the accumulators and powering other devices. The charge controller used in the system is designed with a maximum open-circuit voltage of 100 V, a rated charging current of 50 A, an accumulator voltage of 24 V, and a nominal power output of 1400 W at this voltage. The operating temperature range extends from -30°C to $+60^{\circ}\text{C}$. To ensure safety, the off-grid system adheres to safe DC voltage parameters. Safe voltage refers to a voltage level that does not pose a risk to human health or life. Considering that the heating chamber can be classified as a wet environment, the safe voltage threshold is set at 30 V DC.

The installed accumulator protection module serves the dual purpose of preventing the accumulators from complete discharge, which could potentially damage them, and safeguarding them against a power drop below the level required for the engine to start. The accumulator protection function operates by disconnecting the accumulators from less critical power consumers. This module automatically detects the system voltage and provides overvoltage protection to prevent damage to power receivers. Additionally, it includes an alarm system that notifies users when the accumulator voltage falls too low. The initial off-grid system installed in the district heating chamber was constructed using two 12 V 60 Ah gel accumulators connected in series to store electricity.

Below, you will find an overview of the analysed operational parameters of the off-grid power supply system during real chamber operations.

3.2 Quantities measured in the district heating chamber

The quantities measured in the off-grid power supply system in the district heating chamber are provided at the beginning of Section 3 above. Pressure is measured using pressure transducers, where the measuring element is a piezoresistive silicon sensor, separated from the fluid by a diaphragm and a selected manometric liquid. The pressure transducer's measuring range is from 0 to 2.5 MPa, and the output signal falls within the range of 4–20 mA. The intrinsic error of such transducers amounts to $\pm 0.1\%$. The medium volume flow rate through the turbine is measured using an Axonic ultrasonic flow transducer with a measuring range of $0.1 \text{ m}^3/\text{h}$ to $55 \text{ m}^3/\text{h}$ and Class 2 accuracy, compliant with the PN-EN 1434 standard. The positioning tolerance of the valves installed in the chamber is $\pm 5\%$. Voltage is measured using MB-1U-1 voltage transducers [16], which have a maximum measurement error of 0.5% , with a processing error totaling $\pm 0.5\%$.

3.3 Archiving of measurement data

All measured quantities are systematically archived in the supervisory control and data acquisition (SCADA) system. Additionally, a synoptic diagram of the district heating chamber has been created in the system (Fig. 4).

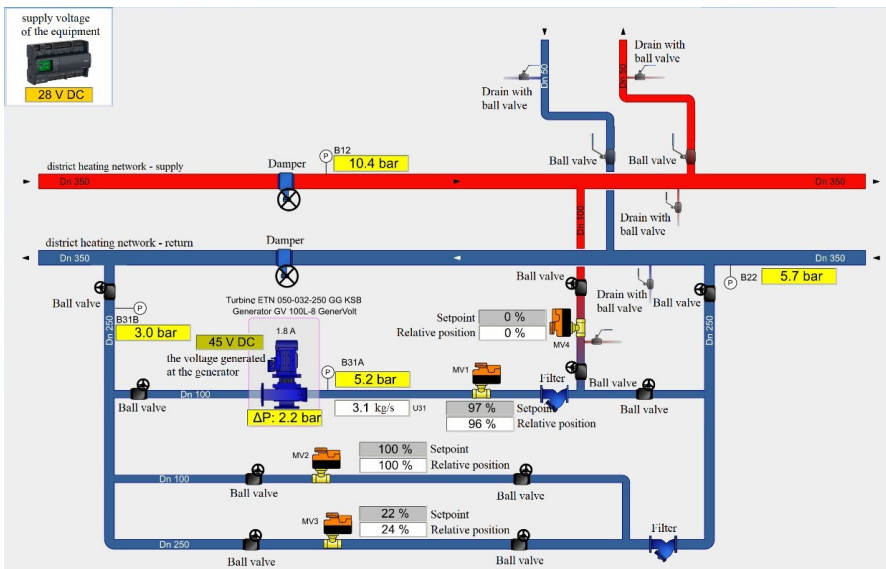


Figure 4: District heating chamber synoptic diagram in the SCADA system.

This diagram allows for the online tracking of various parameters related to the chamber's operation.

4 Measurement results and their analysis

The operation of the off-grid power supply system during the heating season is shown in Figs. 6, 8, 10, and 12, while Figs. 5, 7, 9, and 11 illustrate operation beyond the heating season. Figures 5–11 show the 24-hour measurement series at one-minute intervals, while Fig. 12 represents the 24-hour measurement series at five-minute intervals. Figures 5 and 6 show the

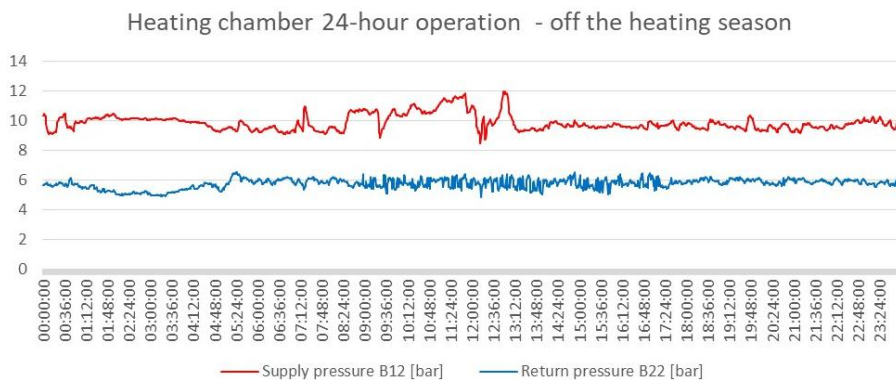


Figure 5: Supply and return pressure values of the district heating network main pipeline in the chamber – off the heating season.

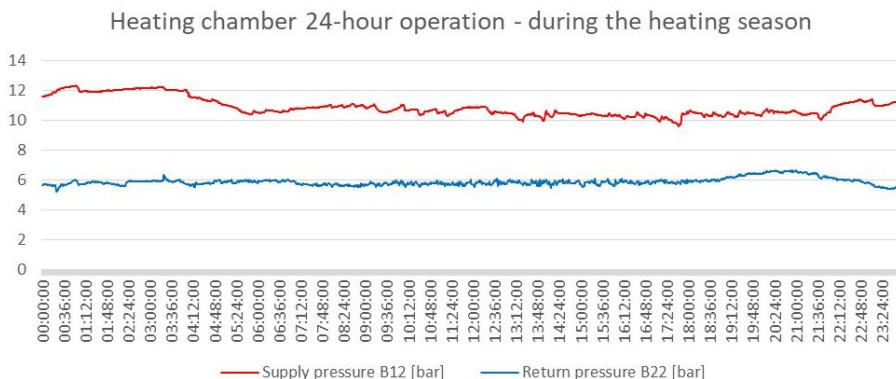


Figure 6: Supply and return pressure values of the district heating network main pipeline in the chamber – during the heating season.

supply and return pressures of the district heating network main pipeline. The pressure on the supply beyond the heating season (Fig. 5) oscillates around the value of 9.5 bar, whereas during the heating season (Fig. 6) it is between 10 and 12 bar. It can be observed that both the supply and the return pipeline of the district heating network operate with greater stability during the heating season.

The values shown in Figs. 7 and 8 represent the pressures upstream and downstream of the TPC on the return pipeline, beyond and during the heating season, respectively. The pressure upstream of the turbine both during and beyond the heating season totals about 5.5 bar. More frequent

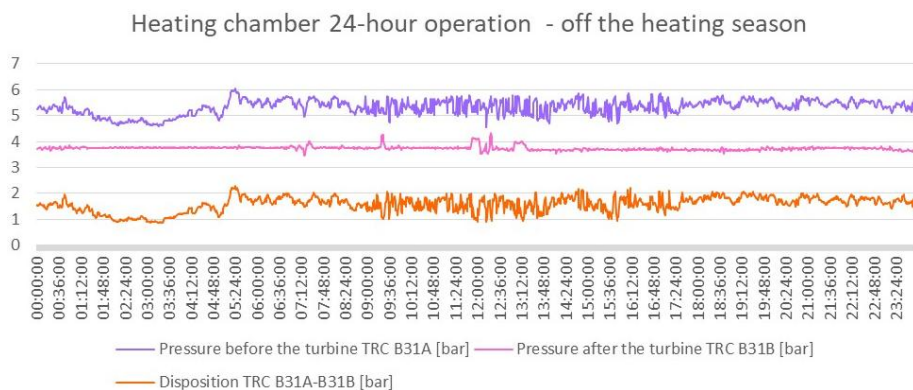


Figure 7: Pressure changes upstream and downstream of turbine, and disposition in the heating chamber (off-heating season).

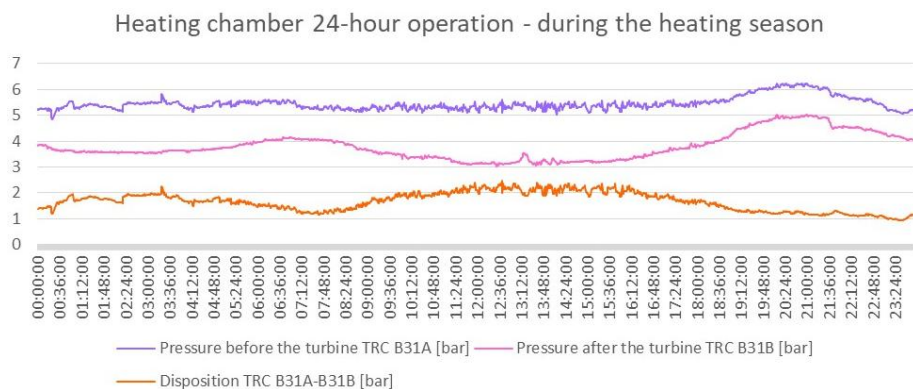


Figure 8: Pressure changes upstream and downstream of turbine, and disposition in the heating chamber (heating season).

and larger fluctuations in the pipeline pressure are visible off the heating season compared to the network operation in the heating season. Off the heating season, the district heating network supplies the heating medium mainly to the domestic hot water (DHW) system. The discontinuous nature of the operation of the domestic hot water system can cause pressure fluctuations in the district heating network off the heating season. The pressure downstream of the turbine beyond the heating season is more stable and oscillates around 3.8 bar (Fig. 7). During the heating season, the pressure downstream of the turbine also looks stable (Fig. 8). However, mild changes from about 3 bar to about 5 bar can be seen over a period of 5 h of operation. The so-called disposition, i.e. the difference between the pressure value upstream and downstream of the turbine, both in and beyond the heating season, varies between 0.9 bar and 2.2 bar.

Figures 9 and 10 show the curves illustrating changes in the heating medium volume flow rate through the turbine, the history of changes in the generator output voltage (after passing through the bridge rectifier) and in the accumulator voltage beyond and in the heating season, respectively.

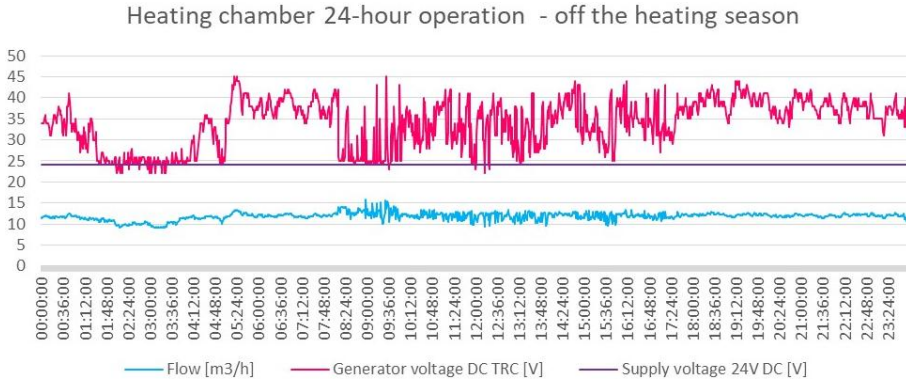


Figure 9: Turbine flow rate, generator voltage, and accumulator supply voltage (off-heating season).

The voltage at the accumulator output supplies the receivers included in the equipment of the district heating chamber and being a part of the off-grid power supply system. It follows from the analysis of the figures that the accumulator voltage beyond the heating season is 24 V DC (Fig. 9), while during the heating season it is 28 V DC (Fig. 10). This is a correct range of changes in the value of the device supply voltage, which is maintained by the MPPT controller. The voltage value at the generator output beyond

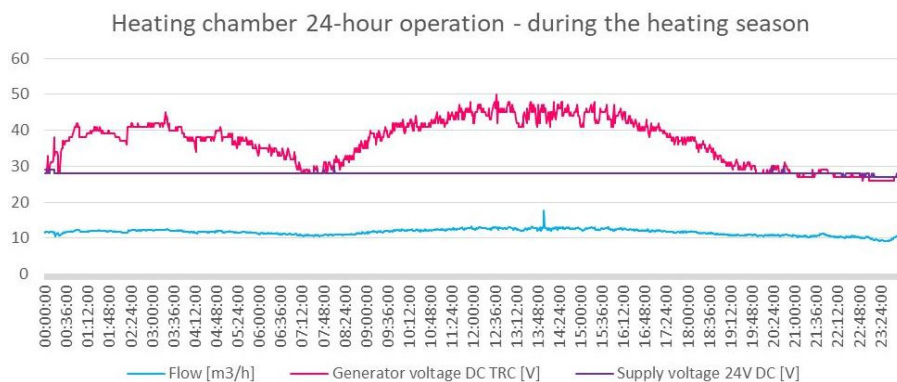


Figure 10: Turbine flow rate, generator voltage, and accumulator supply voltage (heating season).

the heating season varies strongly and ranges from 23 V to 40 V DC, with occasional measurement results between 40 V and 45 V DC (Fig. 9). During the heating season, on the other hand, the generator voltage is characterized by slightly more stable values, but in a higher range of values from about 30 V to about 48 V DC (Fig. 10). The fluctuations in the generator output voltage are caused by fluctuations in the volume flow rate and pressure of water in the district heating network. Even a slight change in these parameters involves a change in generated voltage, which can clearly be seen especially in the case of changes in the water volume flow rate. In the range of about 9 m³/h the water volume flow rate results in the generation of voltage of about 25 V DC. An increase in this quantity to about 12 m³/h translates into a much higher voltage, oscillating around 48 V DC.

The next two figures (Figs. 11 and 12) present the operation of valves under real conditions of the chamber operation. It is very useful to take advantage of the capability of the actuators to provide a feedback signal representing the valve actual position. By comparing the set value to the value from the positioner, it is possible to detect an emergency condition of the network. Such a condition can be seen in the part of Fig. 12 marked with the letter A, when, for example, a foreign object not captured by the filter gets under the valve and blocks the actuator operation. Beyond the heating season (Fig. 11), the MV3 valve is mostly in the closed position, with minor adjustments made within a 24-hour cycle. However, it plays a much bigger part in the regulation of the network operation during the heating season. Both off and during the heating season valves MV1 and MV2 are usually in the open position.

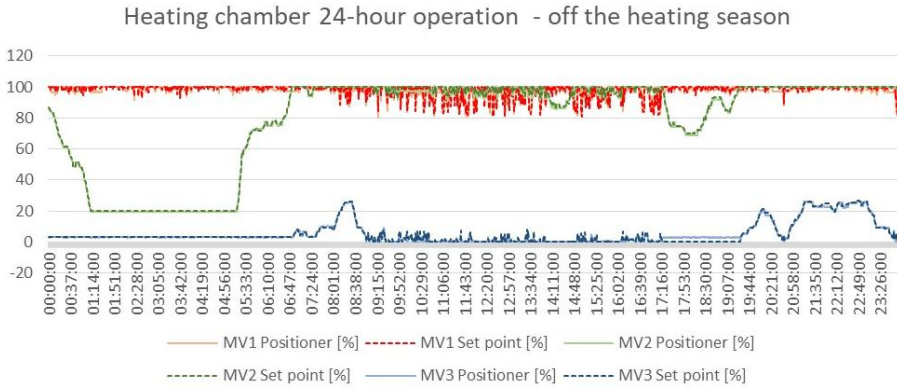


Figure 11: Valve set point and positioner (off-heating season).

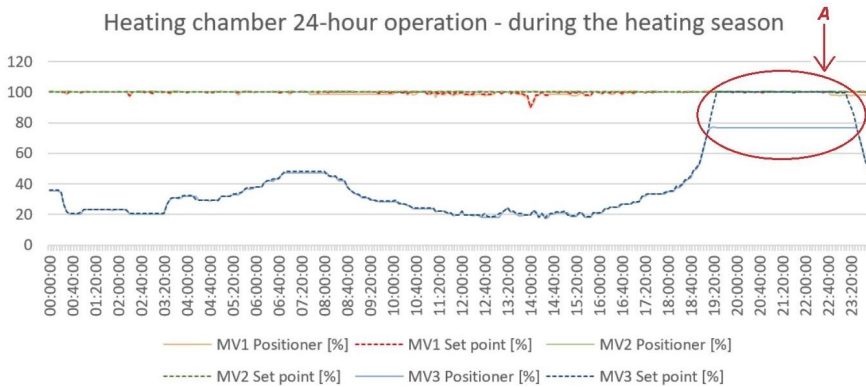


Figure 12: Valve set point and positioner in the district heating chamber (heating season).

5 Conclusions

The conducted analyses of the off-grid power supply of the district heating chamber show how much the voltage generated by the permanent magnet synchronous generator is affected by the flow rate of the medium through the turbine. The biggest problem is the high voltage values at the generator output and their considerable variability. This raises the question of where the problem lies. The solution may be selection of a turbine with parameters more suited to the operating conditions of the district heating network. On the other hand, the problem solution can just as well be found on the generator side. Measurements carried out in different periods of the district heating network operation (in and beyond the heating season) provide a lot

of information that should help in further works aiming to improve off-grid power supply.

The result of the work on the off-grid supply of the district heating chamber is local power generation. It enables visualisation of district heating network parameters at a given point and its control. It has been observed that the equipment selection (such as a turbine and generator) for an off-grid power system requires an individual approach. Namely, it is necessary to take into account the operating parameters of the grid at the off-grid location and to determine the electricity demand of the equipment supplied by the off-grid system.

Off-grid electricity generation to supply the district heating network facilities, such as heating chambers in the first place, offers great opportunities for the development of district heating. The off-grid power supply technology will not only enable but also speed up the development of smart district heating networks.

Received 31 May 2023

References

- [1] Turski M., Sekret R.: *The need to reorganize district heating systems in the light of changes taking place in the building sector*. Rynek Energii **119**(2015), 4, 27–34 (in Polish).
- [2] Joniec W.: *District heating on the way to 5G generation*. Rynek Instalacyjny (2022), 3, 36–38 (in Polish).
- [3] EU H2020 FLEXYNETS Project: Fifth Generation, Low Temperature, High Exergy, District Heating and Cooling Networks, 2015.
- [4] Calise F., Liberato Cappiello F., Cimmino L., Dentice d'Accadia M., Vicidomini M.: *Optimal design of a 5th generation district heating and cooling network based on seawater heat pumps*. Energ. Convers. Manage. **267**(2022), 115912.
- [5] Grzebielec A., Rusowicz A., Jaworski M., Laskowski R.: *Possibility of using adsorption refrigeration unit in district heating network*. Arch. Thermodyn. **36**(2015), 3, 15–24.
- [6] Frotscher O., Oppelt T., Urbanck T., Otto S., Heinrich I. Schmidt A., Göschel T., Uhlig U., Frey H.: *Software-in-the-loop-simulation of a district heating system as test environment for a sophisticated operating software*. In Proc. 9th Int. Conf. on Simulation and Modeling Methodologies, Technologies and Applications – SIMULTECH, Prague, 2019, 223–230.
- [7] Bujalski M., Madejski P., Fuzowski K.: *Day-ahead heat load forecasting during the off-season in the district heating system using generalized additive model*. Energ. Buildings **278**(2023), 112630.

- [8] Leško M., Bujalski W.: *Modeling of district heating networks for the purpose of operational optimization with thermal energy storage*. Arch. Thermodyn. **38**(2017), 4, 139–163.
- [9] Lan T., Strunz K.: *Droop control for district heating networks: Solution for temperature control of multi-energy system with renewable power supply*. Int. J. Electr. Power Energ. Syst. **146**(2023), 108663.
- [10] Lindgren J.: *Numerical modelling of district heating networks*. MSc thesis, Umeå University, Umeå 2017.
- [11] Rzewuski M.: *On-grid, off-grid and hybrid installations*. Automatyka B2B (2021) (in Polish). <https://automatykab2b.pl/fotowoltaika/55360-instalacje-on-grid-off-grid-i-hybrydowe> (accessed 8 Dec. 2022).
- [12] Lund H., Østergaard P.A., Connolly D., Mathiesen B.V.: *Smart energy and smart energy systems*. Energy **137**(2017), 556–565.
- [13] Leitner B., Widl E., Gawlik W., Hofmann R.: *A method for technical assessment of power-to-heat use cases to couple local district heating and electrical distribution grids*. Energy **182**(2019), 729–738.
- [14] Zhang Y., Campana P.E., Yang Y., Stridh B., Lundblad A., Yan J.: *Energy flexibility from the consumer: Integrating local electricity and heat supplies in a building*. Applied Energy **223**(2018) 430–442.
- [15] Mazurek M., Piękoś M.: *New controllers based on water turbines – recovery of mechanical energy from mains water*. Polski Instalator (2017) (in Polish). <https://www.polskiinstalator.com.pl/artykuly/doradca-energetyczny/2065-nowe-regulatory-wzorowane-na-turbinach-wodnych-%E2%80%93-odzysk-energii-mechanicznej-z-wody-sieciowej> (accessed 8 Nov. 2022).
- [16] <https://www.fif.com.pl/pl/przetworniki-pomiarowe-moduly-rozszerzen/421-przetwornik-napiecia-mb-1u-1.html> (accessed 15 Jan. 2023).

Experimental and numerical analysis of vortex generators designed for utility vehicles

RAMESH KUMAR CHIDAMBARAM^a
RAJESH KANNA^{b*}
POOMANANDAN GOPAL^c
SENTHIL KUMAR ARUMUGAM^d

^a Vellore Institute of Technology, Automotive Research Centre, Vellore – 632014, India

^b Vellore Institute of Technology, CO₂ Research and Green Technologies Center, Vellore – 632014, India

^c Anna University, Department of Automobile Engineering, BIT Campus, Tiruchirappalli, 620024, India

^d VIT Bhopal University, Bhopal, 466114, India

Abstract The main goal of today's car designers is to minimize fuel consumption in all possible ways at the same time maintaining the vehicle's performance as usual. The goal of this work is to study the effect of adding a vortex generator (VG) on the aerodynamics of the vehicle and fuel economy. Both theoretical and experimental works were carried out and the outcomes of the numerical simulations are contrasted with those of the experimental results. A utility vehicle model with a scale ratio of 1:15 was used as a test model. Experimental research has been done on the fluctuation of the coefficient of pressure, dynamic pressure, and coefficients of lift and drag with and without VG on the roof of a utility vehicle. The delta-shaped VG was put to the test both numerically and experimentally. At a velocity of 2.42 m/s, it is observed that the addition of VG can raise the pressure coefficient by about 17%. When compared to the vehicle model without vortex generators, the velocity profile of the computational fluid dynamics analysis shows that at the back end of the vehicle, the wake has been minimized with VG.

Keywords: Vortex generator; Pressure coefficient; Numerical simulation; Drag force

*Corresponding Author. Email: prkanna@gmail.com

Nomenclature

A	–	projected area, m^2
C_D	–	coefficient of drag
C_L	–	coefficient of lift
C_p	–	pressure coefficient
D	–	drag force, N
H	–	height, m
I/H	–	interval to height ratio
L	–	lift force, N
p	–	static pressure, N/m^2
P_d	–	dynamic pressure, N/m^2
p_∞	–	total pressure, N/m^2
Re	–	Reynolds number
S_i	–	user-defined source term
S_{ij}	–	strain tensor
t	–	time, s
U_∞	–	velocity of air, m/s
u	–	relative speed of air, m/s
u_i	–	components of velocity in x_i -direction, m/s
x	–	coordinate along scale model centreline, mm
x_i	–	Cartesian coordinates, m

Greek symbols

α	–	yaw angle, deg
ρ_∞	–	density of air, kg/m^3
δ_{ij}	–	stress tensor
μ	–	viscosity

Acronyms

CFD	–	computational fluid dynamics
VG	–	vortex generator

1 Introduction

An aerodynamic component known as a vortex generator (VG) is a tiny vane attached to a body to produce a vortex. They are used in a variety of applications, including those in road vehicles, ships, turbines, and aircraft wings [1]. To keep the airflow constant over the control surfaces at the back of the moving wing or a body, vortex generators are used. They are often made in a rectangular or triangular shape to a size of 10 to 20 mm [2]. For passive control of shock Wave/boundary-layer interactions, vortex generators are researched by both theoretical and experimental methods by

researchers [3, 4]. The exact methods by which they operate at high speeds are still a debate [5, 6].

The review of the literature shows that vortex generators (VGs) alter the boundary layer's internal structure to increase its resistance to separation. Some researchers contend that the mixing of the free stream with the trailing vortices energizes the boundary layer [7, 8]. However, it would appear that no experimental or computational findings have been made to back up this assertion. The compactness of VGs provides a practical advantage over their conventional counterparts [9, 10].

Generally, analyzing the flow over an object with add-on devices like a vortex generator in a wind tunnel is expensive [11, 12]. The cost of the wind tunnel, measuring equipment and the number of test runs necessary for add-on device optimization for drag reduction is money and time-consuming. These expenses can be eliminated by using computational fluid dynamics (CFD) simulations. Aerodynamic simulation utilising offers a quicker turnaround time and will only cost a fraction of the price of the wind tunnel or road testing today due to the decrease in computational cost as well. The Reynolds-averaged Navier-Stokes equations (RANS equations) and turbulence modelling equations can thus be solved to analyse the flow over vehicles and produce results that are close to realistic [13, 14].

The amount of power needed for a car travelling at constant speed on a flat road to overcome tyre rolling resistance is about 20% of engine output and aerodynamic drag is about 80% of engine output. While the rolling resistance nearly stays constant as speed increases, the power required to overcome aerodynamic resistance (drag) increases dramatically with the vehicle speed as shown by the relationship

$$\text{Power}_{(\text{Required})} = \frac{1}{2} C_D \rho_{\infty} A U_{\infty}^3. \quad (1)$$

Though fuel-saving technology has been the main focus of both vehicle manufacturers and researchers, studying the aerodynamic impacts of vehicles is crucial given the considerable increase in passenger cars around the world. So this study's main goal is to look at the influence of adding a VG on aerodynamics and fuel consumption. Before conducting the experimental studies, to check the merit of the VGs to reduce drag, a CFD analysis of the flow above utility vehicles with vortex generators with different interval to height (I/H) ratios was also carried out. Followed by the theoretical study, the fluctuation of the static pressure, dynamic pressure, and coefficients of lift and drag with and without vortex generators (VG) on the roof

of a utility vehicle has been experimentally explored in the current work at varied I/H ratios of VG. This work focuses on researching aerodynamic drag as well as generated lift caused by airflow over the vehicle at various free-stream velocities.

2 Experimental details

2.1 Design of vortex generator

To establish a feasible configuration of a vortex generator the determination of the design aspects (variables) for the construction of a VG is essential. Based on the analysis and suggestions from earlier studies, most of the variables were fixed or the degrees of freedom is limited [15]. The shape selected for this study was a single vane-type delta (triangular). Due to their simplicity and widespread usage vane type VGs are more appropriate for installing to the vehicle body. The most typical application of delta-shaped VGs was on aircraft wings [16]. Based on the presumption that the ideal height of the VG would be almost equal to the boundary layer thickness, the thickness of the boundary layer is measured in relation to height [17]. The velocity profile on the car's roof is depicted in Fig. 1. According to Fig. 1, the boundary layer thickness is found to be around 2 mm at the roof end directly in front of the separation point. The ideal height for the VG is therefore thought to be up to about 2 mm. To create a stiffer construction, the VG thickness was maintained at 0.5 mm. The length was measured in relation to the VG's height. In these experimental VGs, the length-to-height

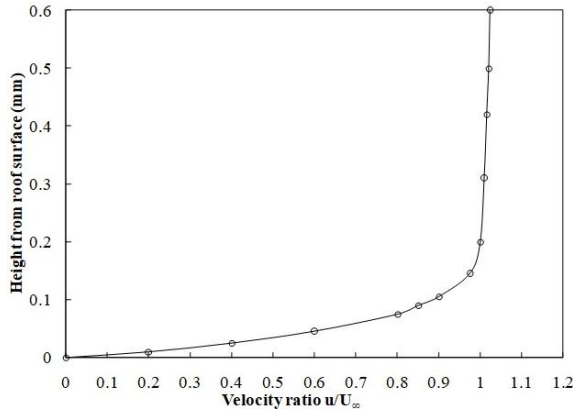


Figure 1: Velocity profile on roof.

ratio is 2, and the yaw angle is 15° to the direction of the airflow. This ratio was used to arrange a single row of VG with 8 members of VG on the roof, as illustrated in Fig. 2.

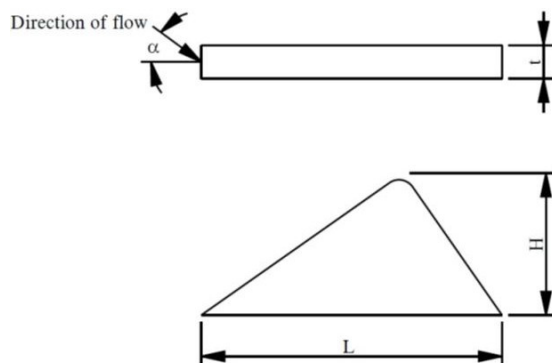


Figure 2: Dimensions of the vortex generator.

The distance (I) between each VG in a row is described in this paragraph. At 5 mm from the end of the roof, one row of VG was mounted. Based on measurements of the boundary layer and the streamline's separation point on the roof, this position was fixed. To reduce weight and potential production costs, there was only one row installed with different I/H ratios of 5, 6, and 7, the delta-shaped VGs. However, it was observed that the direction of wind varied at the side points on the roof. At the centre of a vehicle, the airflow is parallel to the backward direction and gradually deviates towards the centre as the measurement point moves away from the centre. Figure 3 depicts the way of arrangement of vortex generators.

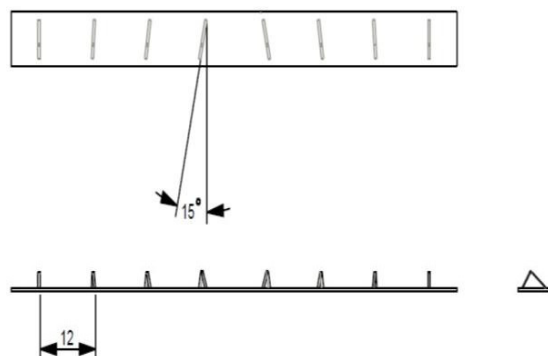


Figure 3: Arrangement of vortex generators in a row.

2.2 Experimental model

A utility vehicle model with a scale ratio of 1:15 was the test model used for this study. Figure 4 depicts the vehicle's scale model. The scaled model measured 0.290 m in length, 0.108 m in width, and 0.1 m in height. A 0.5 mm thick galvanised sheet metal was used to make this model. The same sheet metal was used to create the vortex generators, which were cut into pieces and gas welded onto a base plate. A fastener was used to secure the base plate to the scaled model's roof.

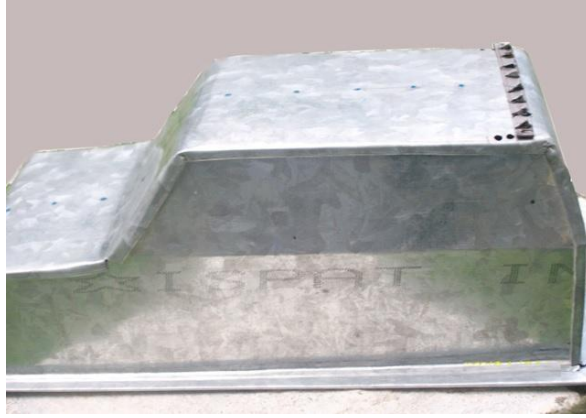


Figure 4: Scale model.

As illustrated in Fig. 5, 0.2 mm diameter holes were made on the vehicle body's centre line starting from the front end to the back end of the vehicle to measure the static pressure above the body. There are 15 pressure tapings

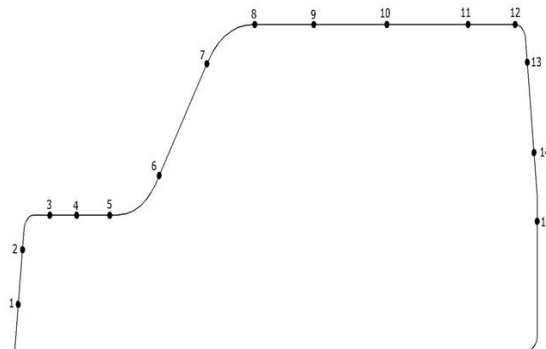


Figure 5: Location of pressure taps.

randomly employed, the roof of the car had five tapings, three of them on the back, and seven on the front. These tapings are bonded with the help of metal paste from the bottom side of the model with the sheet metal surface. Silicone tubes are used to connect the pressure tapings to a 20-way single selection box (like a multiplexer), which is followed by a digital manometer, where the pressure difference is then measured.

The test section of an open circuit wind tunnel (Altech, India) [18] was 0.09 m^2 . Figure 6 depicts the wind tunnel's schematic layout. The test section's length was 1 m, while the wind tunnel's overall length was 6 m. For suction, a 2.5 HP electric motor was employed. The yaw angles used in the wind tunnel testing ranged from 15° in both directions. The scale model of the car has a frontal area of 0.0108 m^2 . Concerning the model, it is estimated that the blockage ratio is around 9.2% of the test section. In the test part of a wind tunnel, a micromanometer (Furnace Control Ltd.) was used to measure the relative airspeed. The dynamic pressure fluctuations along the centre line of the vehicle body were calculated using this relative air speed measurement. The accuracy of a micromanometer is 0.5%. According to the SAE Wind Tunnel Test protocol, the velocity uniformity is 0.96% or 1% [19].

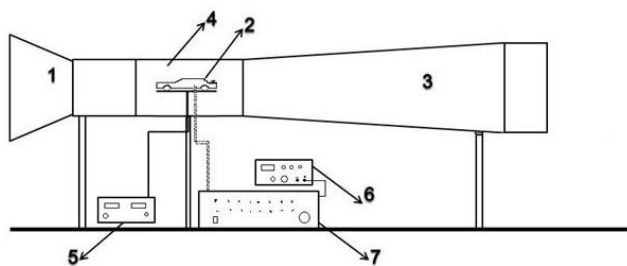


Figure 6: Experimental setup: 1 – air filter, 2 – car model, 3 – axial fan duct, 4 – test section, 5 – force display unit, 6 – micromanometr, 7 – 20-line single way selection box.

The experiment's main goal was to evaluate the drag force, pressure fluctuations, and relative speed on the front, roof, and back along the centre line at different wind speeds. The test model is mounted on a platform which is fastened to a three-axis load cell which enables the measurement of drag and lift force. Figure 7 shows the photographic view of the mount. This load cell converts the variation in position caused by force into an equivalent change in resistance. The output of the load cell is connected to a display unit.

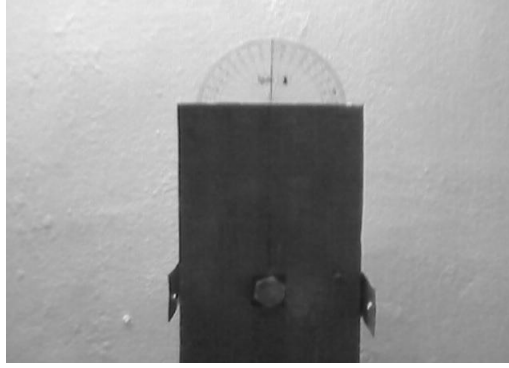


Figure 7: Platform on which model is fixed.

2.3 Experimental analysis

The pressure coefficient (C_P) which is a dimensionless quantity characterises the relative pressures present throughout a flow field. For the study of the low-speed flow of compressible fluids like air, the pressure coefficient is a helpful metric. The relationship between the dimensional parameters and the dimensionless coefficient is as follows:

$$C_p = \frac{p - p_\infty}{\rho_\infty U_\infty^2}, \quad (2)$$

where p_∞ , U_∞ , and ρ_∞ are the total pressure, air velocity and density of air, respectively.

The Bernoulli equation for incompressible flow yields the dynamic pressure (P_d), which is given by

$$P_d = p + \frac{\rho_\infty}{2} u^2. \quad (3)$$

In the equation above, pressure (p) and speed (u) along a streamline are related. The total pressure, according to Bernoulli's equation, is the sum of static and dynamic pressure. In places with high local velocities, the equation predicts low pressure, and *vice versa*. The resultant force that is parallel to and opposes the flow is known as the drag force (D). The drag coefficient (C_D) is calculated empirically, which allows the results to be independent of the actual vehicle dimensions. Drag is related to the drag coefficient as follows:

$$D = \frac{1}{2} C_D \rho_\infty A U_\infty^2. \quad (4)$$

The part of the resulting force that is perpendicular to and in opposition to the flow is known as the lift force (L). The relationship between lift force and the force of the relative fluid,

$$L = \frac{1}{2} C_L \rho_\infty A U_\infty^2, \quad (5)$$

is represented by the value of C_L .

2.4 Computational fluid dynamics analysis

Without much expense and time, CFD techniques can be effectively used to visualize the flow pattern of the geometry or fluid flow over a surface when the flow is laminar. When the flow becomes turbulent, it is impossible to solve the Navier–Stokes and continuity equations analytically. Reynolds stress originating from the time averaging process was a problem that required a time-averaged Navier–Stokes equation (Reynolds averaged Navier–Stokes equations, RANS), along with turbulent models, to resolve. The fundamental mathematical equations that control computational fluid dynamics are the equations of continuity (conservation of mass), the equation of momentum (Navier–Stokes equation), and the equation of energy (conservation of energy). Only the continuity and momentum equations out of these governing equations are important for automotive flow problems involving external aerodynamic flow. Combining the transient term with the advection/convection term results in the following representation of the continuity equation:

$$\frac{\partial \rho_\infty}{\partial t} + \frac{\partial(\rho_\infty u_j)}{\partial x_j} = 0, \quad (6)$$

where ρ_∞ is the density of air, t is the time, x_j are the Cartesian coordinates and u_j are the components of air velocity in x_j -direction ($j = 1, 2, 3$).

The transient, advection/convection, diffusion, and source terms can be used to present the momentum equation as

$$\frac{\partial \rho_\infty u_i}{\partial t} + \frac{\partial(\rho_\infty u_j u_i)}{\partial x_j} = \frac{\partial}{\partial x_j} \left(\mu \frac{\partial u_i}{\partial x_j} \right) + S_i, \quad (7)$$

where μ is the viscosity and S_i is the user-defined source term.

The mean flow impact is more prominent in a real-world automobile flow problem. Therefore, a statistical method is employed for the vast majority of flow issues including turbulence by time averaging the momentum

and continuity equation to account for the mean velocity of the flow. The instantaneous flow velocity is split into mean velocity (U_i) and variable velocity (u'_i) components using the time-averaging approach as

$$u_i = U_i + u'_i. \quad (8)$$

The Navier–Stokes equation is then created by converting the momentum equation to its simpler conserved version, which is

$$\frac{\partial u_i}{\partial t} + u_j \frac{\partial(\rho_\infty u_i)}{\partial x_j} = -\frac{1}{\rho_\infty} \frac{\partial p}{\partial x_i} + \frac{1}{\rho} \frac{\partial}{\partial x_j} \left(\mu \frac{\partial u_i}{\partial x_j} \right) + S_i, \quad (9)$$

where the diffusion term in its original form is written as

$$\frac{1}{\rho_\infty} \frac{\partial}{\partial x_j} \left(\mu \frac{\partial u_i}{\partial x_j} \right) = \frac{1}{\rho_\infty} \frac{\partial}{\partial x_j} \left(2\mu S_{ij} - \frac{2}{3}\mu \frac{\partial u_i}{\partial x_i} \delta_{ij} \right), \quad (10)$$

where S_{ij} denotes the strain tensor components and δ_{ij} is the stress sensor. The last term on the right side of the equation denotes the impact of volume dilation.

After averaging the mean and variable velocity components over time, the Reynolds averaging Navier–Stokes equation is produced and is represented as

$$\begin{aligned} \frac{\partial \bar{u}_i}{\partial t} + \overline{u_j \frac{\partial(\rho_\infty \bar{u}_i)}{\partial x_j}} &= -\frac{1}{\rho_\infty} \frac{\partial \bar{p}}{\partial x_i} \\ &+ \frac{1}{\rho_\infty} \frac{\partial}{\partial x_j} \left(2\mu S_{ij} - \frac{2}{3}\mu \frac{\partial \bar{u}_i}{\partial x_i} \delta_{ij} \right) + \frac{\partial}{\partial x_j} \left(-\rho_\infty \overline{u'_i u'_j} \right) + S_i, \end{aligned} \quad (11)$$

where $-\overline{u_i u_j}$ is the Reynolds stress term, here the over-bar denotes a time averaged quantity and prime denotes the deviation from the average.

The corresponding time-averaged continuity equation can then be written as

$$\frac{\partial \bar{u}_j}{\partial x_j} = 0. \quad (12)$$

The system of equations for a three-dimensional flow consists of three RANS equations and a continuity equation, for a maximum of four equations. Four equations, however, require the system to be closed up for ten unknowns. One mean pressure, three mean velocities, and six Reynolds stresses make up this. As a result, more equations are required to finish the

system. By simulating the Reynolds stress factor in the RANS equation, the closure of the system can be achieved. This also goes by the name of ‘turbulence modelling’. The turbulence model employed will have an impact on how realistically the RANS equations represent the flow [15]. The governing equations for kinetic energy and dissipation in the RNG k - ε model are as follows:

Equation of turbulent kinetic energy

$$\begin{aligned} \frac{1}{\sqrt{g}} \frac{\partial}{\partial t} (\rho_{\infty} x \sqrt{g}) + \frac{\partial}{\partial u_j} \left(\rho_{\infty} \bar{u}_j x - \frac{u_{\text{eff}}}{\sigma_k} \frac{\partial x}{\partial x_j} \right) \\ = \mu_t (P + P_B) - \rho_{\infty} \varepsilon - \frac{3}{2} \left(\mu_t \frac{\partial u_i}{\partial x_i} + \rho_{\infty} x \right) \frac{\partial u_i}{\partial x_i}, \end{aligned} \quad (13)$$

where

$$\begin{aligned} \mu_{\text{eff}} &= \mu + \mu_t, \\ P &= 2S_{ij} \frac{\partial u_i}{\partial x_j}, \\ P_B &= -\frac{g_i}{\sigma_{h,t}} \frac{1}{\rho_{\infty}} \frac{\partial \rho_{\infty}}{\partial x_i} \end{aligned}$$

and \sqrt{g} is the determinant of the metric tensor, g_i is the component of the gravitational vector in the i th direction, x is the coordinate along X -axis, μ_{eff} is the effective viscosity, and μ_t is the turbulent viscosity, σ_k is the turbulent Prandtl numbers for k , $\sigma_{h,t}$ is the k - ε turbulence model coefficient, ε is the rate of dissipation, and ρ_{∞} is the density of air:

$$\begin{aligned} \frac{1}{\sqrt{g}} \frac{\partial}{\partial t} (\sqrt{g} \rho_{\infty} \varepsilon) + \frac{\partial}{\partial u_j} \left(\rho_{\infty} \bar{u}_j \varepsilon - \frac{u_{\text{eff}}}{\sigma_{\varepsilon}} \frac{\partial \varepsilon}{\partial x_j} \right) \\ = C_{\varepsilon l} \frac{\varepsilon}{x} \{ \mu_t (P + C_{\varepsilon 3} P_B) \} - C_{\varepsilon 4} \rho_{\infty} \varepsilon \frac{\partial u_i}{\partial x_i} \\ - \frac{2}{3} C_{\varepsilon 1} \frac{\varepsilon}{x} \left(\mu_t \frac{\partial u_i}{\partial x_i} + \rho_{\infty} x \right) \frac{\partial u_i}{\partial x_i} \\ - C_{\varepsilon 2} \frac{\varepsilon^2}{x} - \frac{C_{\mu} \eta^3 \left(1 - \frac{\eta}{\eta_0} \right)}{1 + \beta \eta^3} \frac{\rho_{\infty} \varepsilon^2}{x}, \end{aligned} \quad (14)$$

where $\eta = S \frac{x}{\varepsilon}$, $S = (2S_{ij}S_{ij})^{1/2}$, S is the magnitude of the rate of strain, σ_{ε} is the turbulent Prandtl number for ε , $C_{\varepsilon l}$, $C_{\varepsilon 1}$, $C_{\varepsilon 2}$, $C_{\varepsilon 3}$, and $C_{\varepsilon 4}$ are constants, η_0 is the creeping viscosity, β is the coefficient of thermal expansion. The RNG theory gives values of the constants [16].

Ansys software was used for the numerical analysis [20]. In order to create a three dimensional CAD model Solidworks software was used [21]. Complete surface and wireframe data were produced. The Initial Graphics Exchange Standard (IGES) format was then used to translate this data [21]. The vehicle used in the CFD simulations is depicted in detail in Fig. 8.

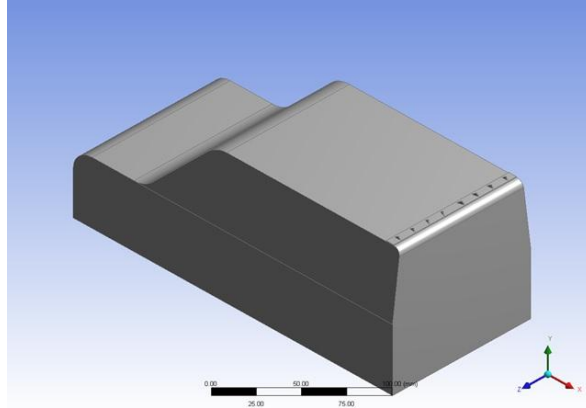


Figure 8: CAD model of the vehicle.

The CAD model of the car was improved using Ansys geometry modeller because the model had an excessive number of intersecting surfaces and free edges. The computational space has the following measurements: 1.5 times the height above the ground, 3 times the breadth sideways, 5 times the body length downstream, and 3 times the length upstream. A suitable number of grid points were assigned to each subblock of the computational domain after it had been partitioned into many logical blocks. The domain was split in half using a symmetry plane to reduce calculation time, and the resulting meshes had 1.1 million fluid cells. For each of the many wind tunnel domains, a different meshing characteristic was used.

Despite the varied approaches, both domains utilised the same arrangement of hexahedral core cells. These components are easily adaptable to the intricate bodies used in aerospace and automotive bodies. The utility vehicle utilised in the experiment's original 1/15th scale model was utilised. The ICEM Meshing tool from Ansys was used to complete the meshing. The vehicle's meshed geometry is depicted in Fig. 9.

Before starting the simulations, the solver setup must be finished for the numerical analysis issue. The viscosity model, boundary condition, solution controls, and solver type (3D or 2D) are all included in the solver settings.

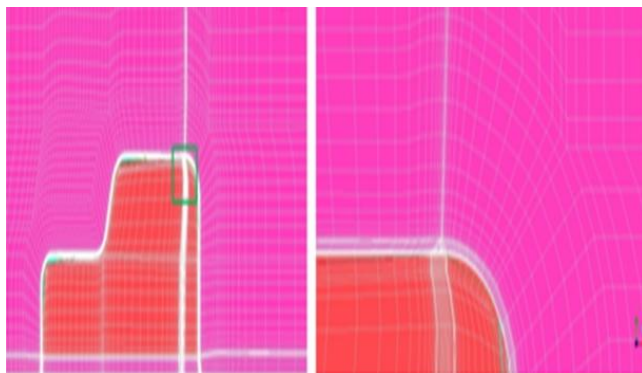


Figure 9: Meshed geometry of the vehicle.

The terms ‘velocity inlet’ and ‘pressure outlet’ are used to describe the inlet and outlet of a wind tunnel, respectively. The temperature and density of the typical ambient environment were taken into consideration when calculating the fluid characteristics. In the near-wall region, a typical wall function was used. At the input of the flow domain, the mass flow rate and static pressure were imposed. When the total momentum residuals had decreased by at least three orders of magnitude and the monitored flow velocities and flow characteristics had not significantly changed after additional iterations, the calculations were stopped. On a machine with 32 GB of RAM and 16 parallel processors, the typical solution time for a mesh with 1.1 million cells was roughly 36 hours.

3 Results and discussions

3.1 Experimental results

Variations of pressure coefficient, dynamic pressure, coefficient of drag and coefficient of lift for different arrangements of VG’s with different I/H ratios at different free stream velocities are presented in this section.

3.1.1 Pressure coefficient

Figure 10 depicts the pressure coefficient change along the scale model’s x coordinates at a free stream velocity of 2.42 m/s. From the figure, it can be seen that the pressure coefficient value without VG is lowest at the x coordinate of around 240 mm, while it is at its highest when VG has an

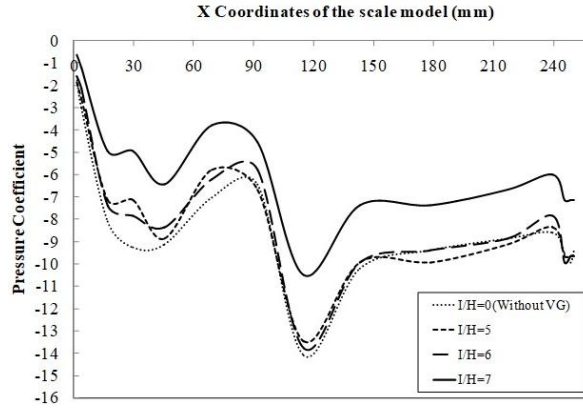


Figure 10: Variation of C_p at $U_\infty = 2.42$ m/s for different values of I/H ratio.

I/H ratio of 6. This is because the boundary layer's thickness is almost identical to the I/H ratio of 6. Figures 11, 12, and 13 depict the pressure coefficient change along the scale model's x coordinates at corresponding free stream velocities of 3.7, 5.42, and 7.14 m/s. It is clear that for different values of the I/H ratio, the values of the pressure coefficient do not change appreciably as the velocity increases. This is due to the inverse relationship between the boundary layer thickness and Reynolds number, which means that at higher velocities, or higher Reynolds number, the boundary layer thickness becomes too tiny and prevents the effect of the I/H ratio of VG from being realised.

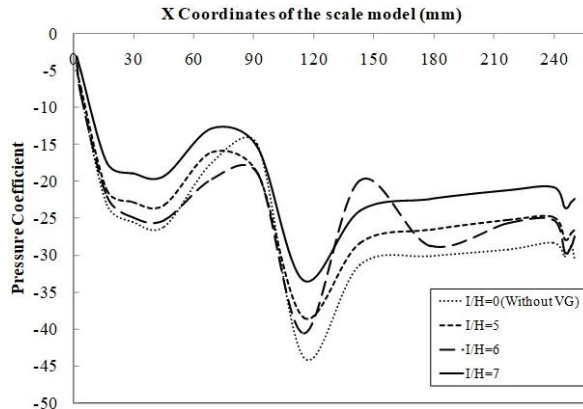


Figure 11: Variation of C_p at $U_\infty = 3.7$ m/s for different values of I/H ratio.

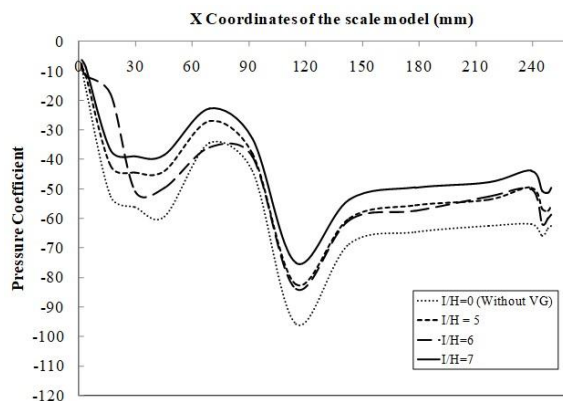


Figure 12: Variation of C_p at $U_\infty = 5.42$ m/s for different values of I/H ratio.

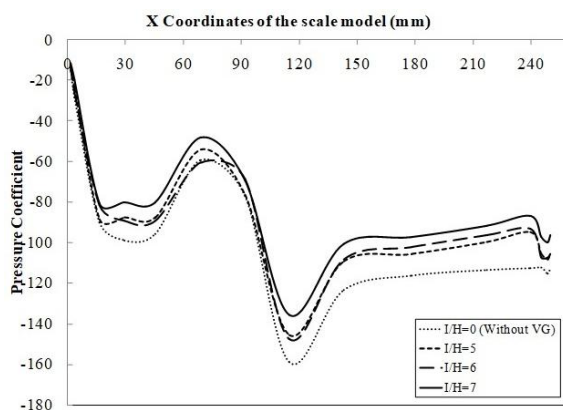


Figure 13: Variation of C_p at $U_\infty = 7.14$ m/s for different values of I/H ratio.

It is intriguing to note that the presence of VG can raise the pressure coefficient by about 18% at a speed of 7.14 m/s. Similarly, with an I/H ratio of 6, adding VG can raise the pressure coefficient to a maximum of approximately 26% and 20% at velocities of 5.42 and 3.7 m/s, respectively.

3.1.2 Dynamic pressure

Figure 14 depicts the dynamic pressure variation along the scale model's x coordinates at a free stream velocity of 2.42 m/s. From the figure, it can be seen that dynamic pressure without VG is largest at the x coordinate of around 240 mm, whereas dynamic pressure with VG having an I/H ratio

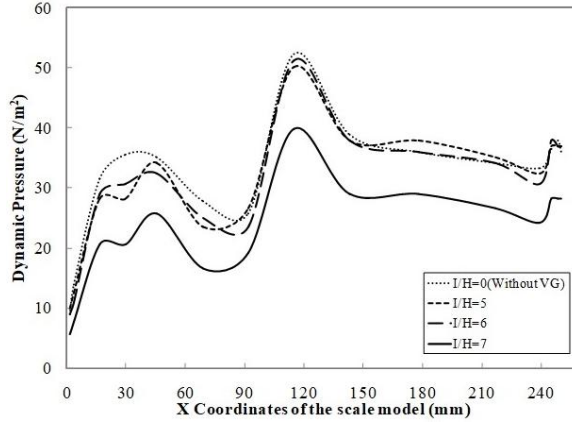


Figure 14: Variation of P_d at $U_\infty = 2.42$ m/s for different values of I/H ratio.

of 6 is smallest. The findings demonstrate that adding VG enhances the dynamic pressure over the surface of the car roof, which is advantageous for preventing flow separation and the ensuing losses. Figures 15, 16, and 17 illustrate the dynamic pressure change along the scale model's x coordinates at different free stream velocities of 3.7, 5.42, and 7.14 m/s. It is clear that for different values of the I/H ratio, the dynamic pressure values do not change considerably as the velocity increases. It is intriguing to note that the incorporation of VG can raise the dynamic pressure by about 21% at a speed of 7.14 m/s. Similar to this, the presence of VG can raise

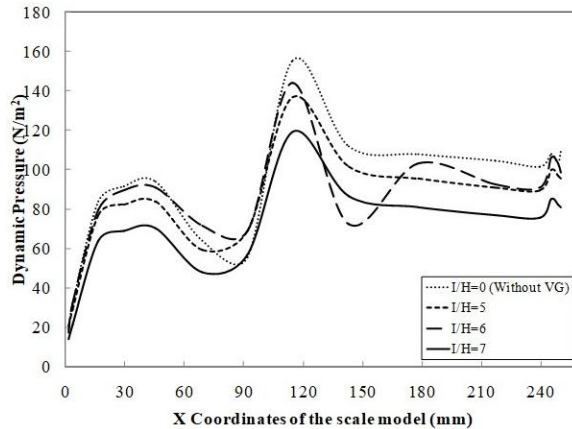


Figure 15: Variation of P_d at $U_\infty = 3.7$ m/s for different values of I/H ratio.

the dynamic pressure to a maximum of approximately 24% and 18% at velocities of 5.42 and 3.7 m/s, respectively, for an I/H ratio of 6.

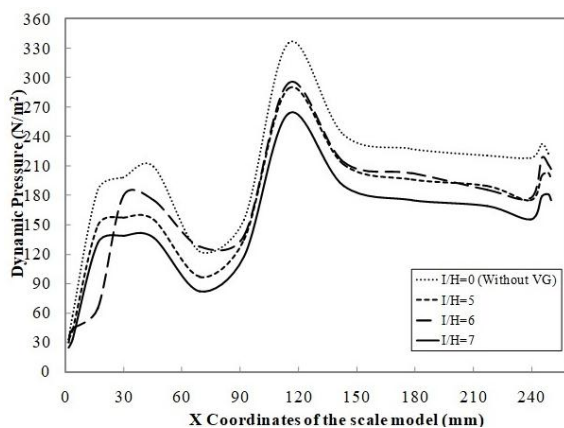


Figure 16: Variation of P_d at $U_\infty = 5.42$ m/s for different values of I/H ratio.

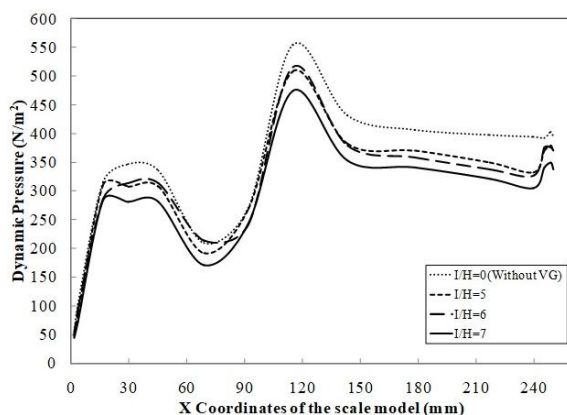


Figure 17: Variation of P_d at $U_\infty = 7.14$ m/s for different values of I/H ratio.

3.1.3 Coefficient of drag

Figure 18 depicts the variance in C_D values for various I/H ratio values at various free stream velocities along the scale model's longitudinal centre line. The graphic makes it very clear that the addition of VG lowers the value of C_D . This can be attributable to the use of VG to prevent flow separation. For instance, using VG with an I/H ratio of 6 reduces the

coefficient of drag at a velocity of 2.42 m/s by up to 90% compared to the results obtained without VG. For VG with an I/H ratio of 5, a minimum 20% reduction in drag is obtained at the same velocity. The C_D stays constant as velocity increases for changing I/H ratio values. However, when the I/H ratio is raised, the C_D values change as the velocity rises. We conclude that VG with an I/H ratio of 6 will be effective at lower speeds.

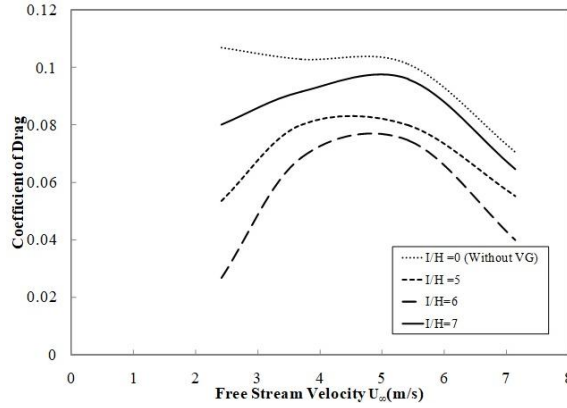


Figure 18: Variation of C_D for different values of I/H ratio along the centre plane.

3.1.4 Coefficient of lift

Figure 19 depicts the change in C_L values along the scale model's longitudinal centre line for various I/H ratio values and free stream velocities.

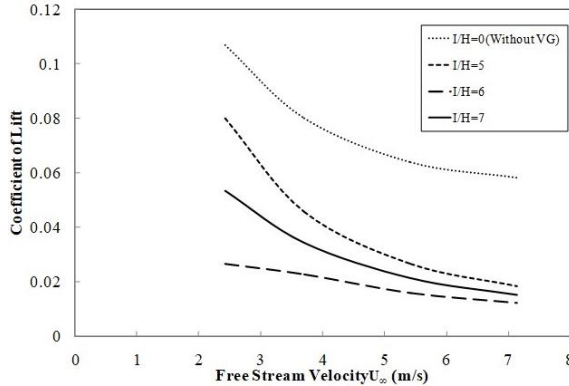


Figure 19: Variation of C_L for different values of I/H ratio along the centre plane.

The graphic makes it very clear that the inclusion of VG lowers the value of C_L . This can be attributable to the use of VG to prevent flow separation. For instance, when VG with an I/H ratio of 6 is utilised, the coefficient of lift is lowered by up to 87% at a velocity of 2.42 m/s compared to the results obtained without VG. For VG with an I/H ratio of 5, a minimum loss in the lift of 50% is attained at the same velocity. However, as velocity increases both with and without VG, C_L 's value declines. The findings showed that for all VGs of I/H ratios at greater velocities, C_L remained constant.

3.2 CFD simulations

The variation of pressure contour and velocity contour along the x/L ratio at different free stream velocities for different arrangements of VG's with different I/H ratios are presented.

3.2.1 Validation of CFD results

Experimental absolute pressure measurement from baseline testing (experiments without VG) at 7.14 m/s was compared with the simulated results for validation purposes. The front body absolute pressure shows a minor variance, but the pattern of the plot is comparable, even though the findings of the absolute pressure on the roof surface closely match the experimental data as in Fig. 20. The front windshield of the car model has the highest

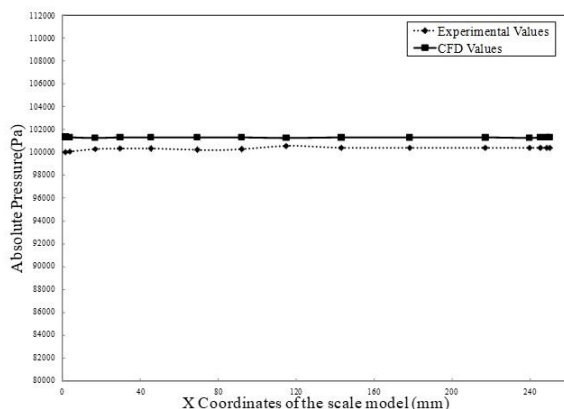


Figure 20: Comparison of experimental and CFD values of absolute pressure along the centre line of vehicle surface at a velocity of 7.14 m/s.

absolute pressure value. The simulation's calculation of the maximum absolute pressure on the front windshield came out at 101.676 kPa, which is fairly close to the experimental measurement of 100.586 kPa.

3.2.2 Pressure contour

The results of the CFD simulation of the variation in absolute pressure at the utility vehicle's rear top surface with and without VG are shown in Fig. 21a and 21b, respectively. It may be concluded that there is little difference between the two scenarios in the absolute pressure value at the utility vehicle's rear top surface. According to the analysis, the vortex generator energises the flow and causes it to separate at a distance that is comparatively greater than that of the vehicle model without a vortex generator, which lowers the drag of the vehicle.

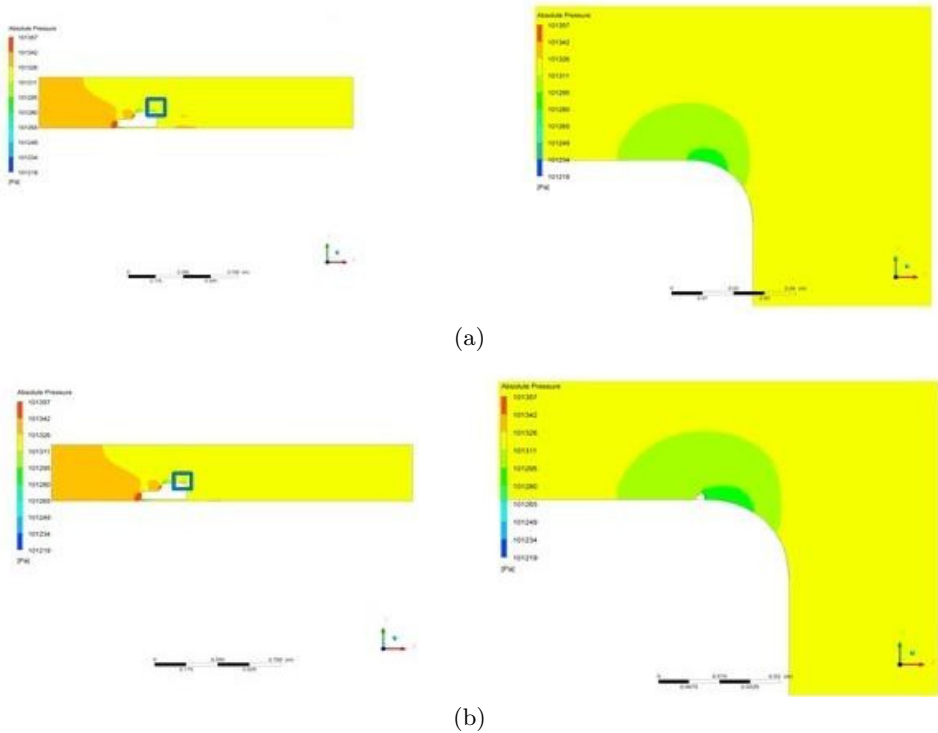


Figure 21: Pressure contour on the vehicle without (a) and with (b) vortex generators at a velocity of 7.14 m/s.

3.2.3 Velocity contour

The results of the CFD simulation (using Ansys Tool Package 2020) of the fluctuation in velocity at the utility vehicle's rear top surface with and without VG are shown in Fig. 22a and 22b, respectively. The velocity at the front end of the car is assumed to be relatively low, however, it is discovered that the velocity at the rear end of the car is higher than that at the front end. This demonstrates how low the pressure is at the vehicle's back. It has been accomplished with the help of the incorporation of vortex generators, and the drag has also been decreased. The velocity at the rear of the car will be minimized if the pressure drop is lowered. When compared to the vehicle model without vortex generators, the graphic depicts the velocity at the rear end that has less wake. This always results in the vehicle's drag being reduced. This backs up the experimental results covered in Section 3.1.2 that the addition of VG is beneficial for preventing flow separation and the ensuing losses.

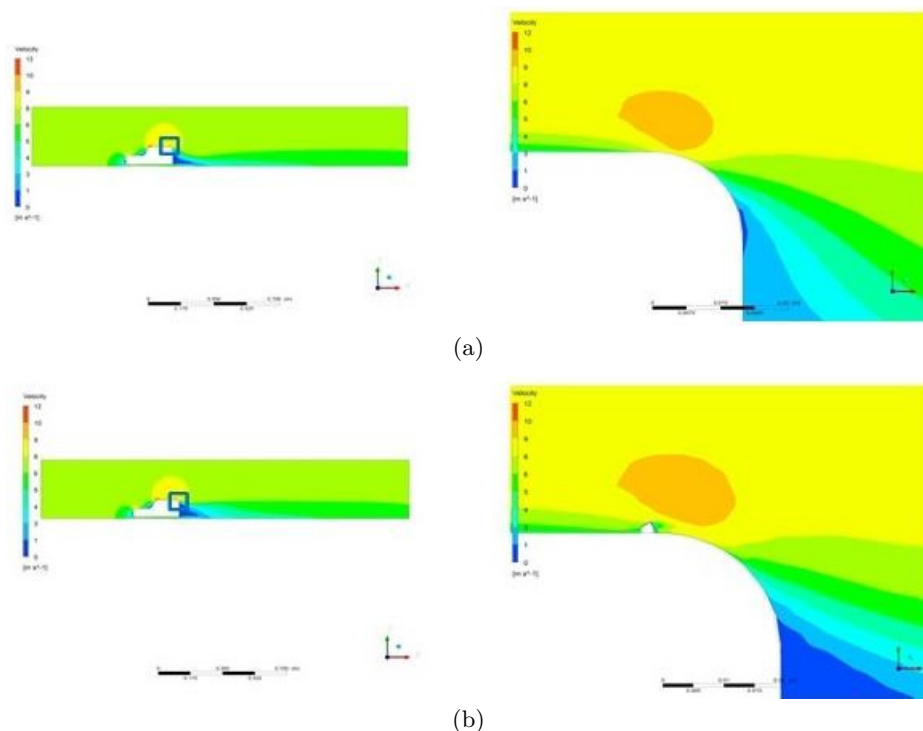


Figure 22: Velocity contour on vehicle without (a) and with (b) vortex generators at a velocity of 7.14 m/s.

4 Conclusion

The following conclusions were drawn from an experimental study on the measurement of the variation of dynamic pressure and pressure coefficient on the roof of a utility vehicle with and without vortex generators (VG).

The value of the pressure coefficient without vortex generators VG is minimum, whereas its value was observed to be maximum with VG having an I/H ratio of 6. The addition of VG can raise the pressure coefficient by roughly 17% at a speed of 2.42 m/s. For different values of the I/H ratio, the values of the pressure coefficient do not change all that much as the velocity increases.

The addition of VG raises the dynamic pressure over the surface of the vehicle roof, which is advantageous for preventing flow separation and the ensuing losses. At a velocity of 2.42 m/s, the inclusion of VG reduces the value of C_D by 90%, and VG achieves a minimum drag reduction of 20% with an I/H ratio of 5. It is noted that VG with a 6 I/H ratio will be helpful at lower velocities. The results showed that at a higher velocity, the value of C_L remains constant for VG with varied values of the I/H ratio. The value of C_L declines with the rise in velocity both with and without VG.

The pressure contour of the CFD analysis demonstrates that the vortex generator energises the flow and causes the flow to separate at a distance that is significantly greater than that of the vehicle model without the vortex generator, which lowers the drag of the vehicle. When compared to the vehicle model without vortex generators, the velocity contour of the CFD study demonstrates that the velocity at the rear end has reduced wake.

Received 17 April 2023

References

- [1] Lishu H., Bao H., Yongwei G., Binbin W.: *Effect of vortex generator spanwise height distribution pattern on aerodynamic characteristics of a straight wing*. Adv. Aerodyn. **5**(2023), 1, 1–15. doi: [10.1186/s42774-023-00137-1](https://doi.org/10.1186/s42774-023-00137-1)
- [2] Nilavarasan T, Joshi G.N., Misra A., Manisankar C., Verma S.B.: *Spatial and temporal alterations due to vortex generators in a flare induced shock-boundary layer interaction*. Eur. J. Mech. B-Fluid. **99**(2023), 3, 98–115. doi: [10.1016/j.euromechflu.2023.01.007](https://doi.org/10.1016/j.euromechflu.2023.01.007)

- [3] Jana T., Kaushik M.: *Survey of control techniques to alleviate repercussions of shock-wave and boundary-layer interactions*. Adv. Aerodyn. **27**(2022), 4, 1–30. doi: [10.1186/s42774-022-00119-9](https://doi.org/10.1186/s42774-022-00119-9)
- [4] Kung M.C., Kao C.S., Keh C.C.: *The effect of vortex generators on shock-induced boundary layer separation in a transonic convex-corner flow*. Aerospace **157**(2021), 8, 1–11. doi: [10.3390/aerospace8060157](https://doi.org/10.3390/aerospace8060157)
- [5] Hadi B., Seyed Ali A.M., Seyed Amir A.O., Mohammad R.S.: *Effects of micro-vortex generators on shock wave structure in a low aspect ratio duct, numerical investigation*. Acta Astronaut. **178**(2021), 1, 616–624. doi: [10.1016/j.actaastro.2020.08.012](https://doi.org/10.1016/j.actaastro.2020.08.012)
- [6] Neeraj K.G., Nirmal K.S.: *Control of shock-induced separation inside air intake by vortex generators*. Heat Transfer **51**(2022), 1, 766–788. doi: [10.1002/hlj.22329](https://doi.org/10.1002/hlj.22329)
- [7] Azam C.I., Mohd R.S., Konstantinos K.: *Potential of micro-vortex generators in enhancing the quality of flow in a hypersonic inlet-isolator*. J. Adv. Res. Fluid Mech. Therm. Sci. **77**(2021), 1, 1–10. doi: [10.37934/arfmnts.77.1.110](https://doi.org/10.37934/arfmnts.77.1.110)
- [8] Tian L., Hao L., Jie Z., Jiye Z.: *Numerical study on aerodynamic resistance reduction of high-speed train using vortex generator*. Eng. Appl. Comput. Fluid Mech. **17**(2023), 1, 1–17. doi: [10.1080/19942060.2022.2153925](https://doi.org/10.1080/19942060.2022.2153925)
- [9] Arunvinthan S., Raatan V.S., Nadaraja Pillai S., Amjad A.P., Rahman M.M., Khalid A.J.: *Aerodynamic characteristics of shark scale-based vortex generators upon symmetrical airfoil*. Energies **14**(2021), 1808, 1–22. doi: [10.3390/en14071808](https://doi.org/10.3390/en14071808)
- [10] Gnatowska R., Gajewska K., Kańtoch R.: *Numerical calculations of VGs influence on aerodynamic characteristics of airfoil*. Acta Phys. Pol. A **139**(2021), 5, 1, 586–589. doi: [10.12693/APhysPolA.139.586](https://doi.org/10.12693/APhysPolA.139.586)
- [11] Tavernier D., Ferreira C., Viré A., LeBlanc B., Bernardy S.: *Controlling dynamic stall using vortex generators on a wind turbine airfoil*. Renew. Energ. **172**(2021), 7, 1194–1211. doi: [10.1016/j.renene.2021.03.019](https://doi.org/10.1016/j.renene.2021.03.019)
- [12] Wu Z., Chen T., Wang H., Shi H.: *Investigate aerodynamic performance of wind turbine blades with vortex generators at transition area*. Wind Eng. **46**(2022), 615–629. doi: [10.1177/0309524X211038542](https://doi.org/10.1177/0309524X211038542)
- [13] Reza B., Milad R., Mohammad R.S.: *Numerical simulations of spoiler's effect on a hatchback and a sedan car exposed to crosswind effect*. J. Appl. Comput. Mech. **9**(2023), 2, 346–356. doi: [10.22055/JACM.2021.36955.2937](https://doi.org/10.22055/JACM.2021.36955.2937)
- [14] Viswanathan H.: *Aerodynamic performance of several passive vortex generator configurations on an Ahmed body subjected to yaw angles*. J. Braz. Soc. Mech. Sci. Eng. **43**(2021), 2, 1–23. doi: [10.1007/s40430-021-02850-8](https://doi.org/10.1007/s40430-021-02850-8)
- [15] Popp M., White C.F., Bernal D., Wainwright D.K., Lauder G.V.: *The denticle surface of thresher shark tails: Three-dimensional structure and comparison to other pelagic species*. J. Morphol. **281**(2020), 6, 938–955. doi: [10.1002/jmor.21222](https://doi.org/10.1002/jmor.21222)
- [16] SAE: *Wind tunnel test procedure for trucks and buses, Recommended practice*. SAE J. **1252_201207**(2012).
- [17] Li X., Yang K., Wang X.: *Experimental and numerical analysis of the effect of vortex generator height on vortex characteristics and airfoil aerodynamic performance*. Energies **12**(2019), 5, 1–19. doi: [10.3390/en12050959](https://doi.org/10.3390/en12050959)

- [18] Szwaba R., Hinc K., Ochrymiuk T., Krzemianowski Z., Doerffer P., Kurowski M.: *Open low speed wind tunnel – design and testing*. Arch. Thermodyn. **42**(2021), 1, 57–70. doi: [10.24425/ather.2021.136947](https://doi.org/10.24425/ather.2021.136947)
- [19] Barlow J.B., Rae Jr. W.H., Pope A.: *Low-Speed Wind Tunnel Testing* (3rd Edn.). Wiley, 2010.
- [20] Koprowski A., Rzadkowski R.: *Computational fluid dynamics analysis of 1 MW steam turbine inlet geometries*. Arch. Thermodyn. **42**(2021), 1, 35–55. doi: [10.24425/ather.2021.136946](https://doi.org/10.24425/ather.2021.136946)
- [21] Pazouki A., Radu S., Dan N.: *A high performance computing approach to the simulation of fluid-solid interaction problems with rigid and flexible component*. Arch. Mech. Eng. **61**(2014), 2, 227–251. doi: [10.2478/meceng-2014-0014](https://doi.org/10.2478/meceng-2014-0014)

Exergetic performance analysis of solar air heater with inverted L-shape ribs as roughness element

MANMOHAN CHAUDHARI^a
SOHAN LAL SHARMA^{b*}
AJJOY DEBBARMA^b

^a Maya Institute of Technology and Management, Selaqui, Dehradun, Uttarakhand-248007, India

^b National Institute of Technology, Hamirpur, Himachal Pradesh, 177005, India

Abstract Improvement in the exergetic efficiency of a solar air heater (SAH) can be done by enhancing the rate of heat transfer. In this work, the exergetic efficiency optimization of an artificially roughened solar air heater having an inverted L-shape rib has been performed. The numerical analysis of the exergetic performance of the solar air heater was carried out at a constant heat flux of 1000 W/m^2 . The study was conducted to investigate the effect of different relative roughness pitch (7.14–17.86) on the exergy losses, under the Reynolds number range of 3000 to 18 000. The roughness parameter of this geometry has been optimized and found to be among functional operating parameters like average solar intensity and temperature rise across the collector. The optimized value of relative roughness pitch is 17.86 at the isolation of 1000 W/m^2 , and the parameter of temperature rise ranges from 0.005 to 0.04.

Keywords: Solar air heater; Heat transfer; Exergy loss; Exergy efficiency; Thermal efficiency

Nomenclature

A_c – cross-sectional area of the rectangular duct, m^2
 A_p – area of absorber plate, m^2
 C_p – specific heat, kJ/kgK

*Corresponding Author. Email: sohansh@nith.ac.in

D_h	–	hydraulic diameter of duct, mm
E_x	–	exergy, J
$E_{x\text{loss}, \text{El}}$	–	exergy loss, J
e	–	height of L-shape rib, mm
e/D_h	–	relative roughness height
f	–	friction factor
f_s	–	friction factor for smooth duct
h	–	convection coefficient, W/m ² K
k	–	thermal conductivity of air, W/m K
L, L_2	–	length of test section, mm
L_t	–	total length of the duct, mm
L_1	–	length of inlet section, mm
L_3	–	length of outlet section, mm
\dot{m}	–	rate of mass flow, kg/s
Nu	–	Nusselt number
Nu _s	–	Nusselt number for smooth duct
Q_u	–	useful heat gain, W
q, I	–	heat flux applied on absorber surface, W/m ²
P	–	pitch between two successive ribs, mm
P/e	–	relative roughness pitch
ΔP	–	pressure drops, N/m ²
Re	–	Reynolds number
THPF	–	thermohydraulic performance factor of roughened SAH
T_{fi}	–	fluid inlet temperature, K
T_{fo}	–	fluid outlet temperature, K
T_{fm}	–	fluid mean temperature, K
T_{pm}	–	mean absorber temperature, K
ΔT	–	temperature rise of air, K
$\Delta T/I$	–	temperature rise parameter, K/W
El _a	–	exergy loss by the absorber
El _{Δp}	–	exergy loss by friction
El _{ΔT}	–	exergy loss by the air
v	–	velocity, m/s

Greek symbols

η_{exe}	–	exergetic efficiency
η_{eff}	–	effective efficiency
η_{th}	–	thermal efficiency
μ	–	dynamic viscosity of air, kg/m s
ρ	–	density of air, kg/m ³

Subscripts

i	–	inlet
o	–	outlet
fi	–	fluid inlet
fo	–	fluid outlet
u	–	useful

a	–	absorber
s	–	smooth
pm	–	plate mean
fm	–	fluid mean
exe	–	exergetic
eff	–	effective

Acronyms

CFD	–	computational fluid dynamics
HT	–	heat transfer
SAH	–	solar air heater

1 Introduction

It was during the 1973 oil crisis that scientists began looking for ways to balance energy requirements and consumption. 81% of the world's energy needs are met by traditional energy sources like fossil fuels and coal, etc. Traditional fuels and wood burning cause air pollution in agricultural countries. Therefore, it is important to create a heating and cooling system for indoor environments and factories that uses hot air efficiently, sustainably, and cheaply [1, 2]. Because of rising industrialization and population, conventional resources are dwindling and cannot keep up with the rising energy needs of the world. These traditional energy sources are detrimental to humans and have harmed the environment [3, 4]. Although it has been demonstrated that conventional energy sources are limited, monetarily out of reach for many developing nations, and cause environmental damage, the current energy future is heavily weighted toward these sources. The pattern of energy consumption in emerging nations like India predicts a future that is likewise skewed toward the energy that is concentrated in urban centres. A large disparity exists between energy demand and supply because of the lack of access to reliable energy sources in rural regions.

Our natural environment provides a plethora of solar energy that might be harnessed in large quantities. Solar air heaters (SAHs) that use solar energy are common to harness solar energy because of their low cost and ease of use. The SAH is used for a wide variety of heating needs, including crop drying and space heating, etc. The thermal efficiency of SAHs is low in comparison to that of solar water heaters because of the weak heat transfer (HT) capability of air over water. Therefore, increasing the HT coefficient will increase its thermal efficiency. Sharma and Debbarma [5]

reviewed several strategies employed to boost the thermal performance of flat plate SAHs. These techniques mainly include artificial roughness like fins or other geometries. By disrupting the laminar boundary layer, these alterations generate more turbulence and boost heat transmission.

To improve the SAHs' thermal performance several roughness geometries were examined in previous research. Artificially roughened absorber plates enhance the local wall turbulence and create secondary flow. Secondary recirculation flow is responsible for improving the convective HT. Transverse ribs, V-shaped, inclined, W-shaped, and multi-V-shaped ribs are all examples of ribs that may be used to generate turbulence. The height of roughness elements is often maintained at a lower value than the height of ducts. Some characteristics are utilized to determine the geometry and placement of roughness. Prasad and Mullick [6] experimentally examined the impact of protruding wire ribs of circular cross-section on the performance of SAH, used for drying crops. High mass flow rates are employed to generate turbulence in the ducts by introducing protruding wires of 1 mm diameter. The performance of roughened air heaters was enhanced by 14% and increased the HT coefficient from 0.63 to 0.72 using the present wire geometry. Sahu and Bhagoria [7] studied the impact of 900 broken ribs on the thermal performance of a SAH. The fixed roughness height of 1.5 mm and pitch varying from 10 to 30 mm for the range of Re from 3000 to 12000 were examined. The heat transmission coefficient enhanced from 1.25 to 1.40 times. The roughness pitch of 20 mm yielded the highest Nusselt number (Nu) value, and a thermal efficiency of about 51% to 83.5% was obtained according to the findings. Gupta *et al.* [8] experimentally tested the thermohydraulic performance of a roughened SAH using inclined ribs. The HT and friction factor (f) enhancement for roughened SAH were reported about 1.79 and 2.69 times respectively, for the angle of 70° and 60°. The optimum thermohydraulic performance was recorded for a relative height of roughness 0.023 and Re of 14000. Karwa *et al.*, [9] conducted experimental research to study the impact of repetitive, 60° inclined rectangular ribs on HT and f for duct aspect ratio varying from 7.19 to 7.75 and Re range from 2800 to 15000. According to the findings the increase in f about 1.12 to 1.16 times, and enhancement in Stanton number about 22% to 32% were reported as compared to the transverse ribs for 0.0467 to 0.050 relative pitch of roughness. Aharwal *et al.* [10] experimented to study the impact of the width and spacing of square-cross-sectional inclined broken ribs on heat transmission and f . Under the same conditions, the increase in heat transmission for a continuous rib was about 1.48 and 2.26 times, and for

a split rib was about 1.71 and 2.59 times as compared to the smooth duct. For the range of parameters studied, the optimal values of heat transmission, f ratio, and thermohydraulic parameter were found to be associated with a relative gap position of 0.25 and a relative gap width of 1 under Re values 3000 to 18 000. Saini and Saini [11] conducted an experimental study to better understand the impact of the wire mesh absorber on SAH performance under a range of Re varying from 1900 to 3000. The optimum enhancement in the rate of HT was achieved about 4 times concerning the plain duct and the f was claimed to be at its maximum value.

Momin *et al.* [12] tested the effect of V-shaped ribs on the fluid flow and HT properties of the rectangular duct SAH. At 60° attack angle, the result reveals that the Nu and f increase about 2.30 and 2.83 times respectively concerning the plain duct. The Nusselt number was increased by 1.14 and 2.30 times, respectively, when a V-shaped rib pattern was used instead of inclined ribs and a smooth absorber plate. Muluwork *et al.* [13] examined and compared the thermal efficiency of staggering discrete down ribs and V-apex up with equivalent transverse staggered discrete ribs. Effects of various roughness parameters on heat transmission and f were studied including the angle of attack. According to the findings, the maximum heat transmission and f were observed at an attack angle of 60° and 70° respectively. Karwa *et al.* [14] examined heat transmission and f characteristics of SAH using an aspect ratio of 4.8 and 12 and repeated chamfered ribs. The Re range from 3000 to 20 000, the pitch of 4.5 to 8.5, roughness height of 0.014 to 0.0328, and a chamfer angle of 15° to 18° were considered. The Stanton number and the f rose when the chamfer angle was raised and the highest value was achieved at 15° chamfer angle. Bhagoria *et al.* [15] conducted experimental research for SAH using transverse wedge-shaped ribs to analyze the HT and flow properties. Relative roughness height of 0.015 to 0.033 and a rib wedge angle of 80° to 120° were used at the Re range from 3000 to 18 000 for this study. The Nu and f over smooth duct rose by 2.4 and 5.3 times respectively. Saini and Saini [16] looked at how adding arc-shaped ribs to the SAH absorber affected its HT efficiency and frictional resistance. According to the results, the Nu was found to be increased when the relative arc angle decreased, and f decreased with the arc angle. Both Nu and f were observed to increase by a factor of 3.6 and 1.75 respectively at a relative arc angle of 0.3333 and a roughness height of 0.0422 as compared to a plain duct. Saini and Verma [17] examined the impact of dimple-shaped roughened geometry on HT and f . The Re range from 2000 to 12 000 was selected for the investigation. The highest Nu was determined

to correspond to the relative roughness height and pitch of 0.0379 and 10 respectively. At constant relative roughness pitch (i.e., 10) the highest and lowest f were achieved about 0.0289 and 0.0189 respectively. Karmare and Tikekar [18] conducted an experimental investigation for an absorber plate roughened with the grit of metal ribs of a circular cross-section with the goals of heat transmission and friction characteristics enhancement. Nu and f rose by 187%, and 213% with maximum performance at a relative roughness height and pitch of 0.044 and 17.86 respectively.

Hwang and Liou [19] studied the impact of perforated turbulators on the heat transport behaviour of SAH. They examined and compared the thermal efficiency for solid, perforated, and slit turbulence promoters. They employ fences that are either half or perforated, with open area ratios of 0, 10, 22, 38, and 44%. They found that the thermal performance of the permeable fence was superior to the solid-fenced. Sara *et al.* [20] compared the HT from a plate with and without blocks as well as with solid and perforated rectangular blocks, affixed on a flat absorber surface in a SAH. They determined that utilizing perforated blocks might increase energy production by as much as 20%. Increasing the hole diameter, perforation index, and slope of perforated holes can boost HT performance. Sara *et al.* [21] further examined perforated rectangular cross-sectional blocks connected to their surface to enhance heat transmission and found that the rate of heat transmission increased with an increase in the perforation index and that blocks with inclined holes, transfer the heat more efficiently than blocks with straight holes. Greater heat transmission and potential pressure losses are observed with higher f and more compact yields. Buchlin [22] conducted experimental research on the flow through a conduit with perforated ribs at the Re range of 30 000 to 60 000. They conducted experiments with five different Plexiglas rib designs and concluded that a rib pitch ratio of 5 and an open area ratio of 0.53 produce the best results. Moon and Lau [23] performed experimental research with Re varying from 10 000 to 30 000, to investigate heat transmission and pressure drop between two obstructions with the hole in a flow channel. The pressure drop was higher, but the heat transmission was boosted by 4.6–8.1 times due to the obstructions. Though they allow for more heat transmission, smaller holes also result in a greater pressure drop. Karwa *et al.* [24] investigate the impact of perforated baffles integrated into the heated surface on HT and f with Re varying from 2,850 to 11,500. Nu was found to be 60.6 to 62.9, and 45% to 49.7% higher for perforated baffles than for smooth ducts and decreasing with increasing open area ratio from 18.4% to 46.8%, and 73.7% to 82.7% higher for solid

baffles than for smooth ducts. We discovered that the f for solid baffles was 9.6–11.1 times that of a smooth duct, but that it began to fall significantly for perforated baffles as the perforation index increased. Karwa and Maheshwari [25] experimentally investigated the heat transmission and f characteristics of SAH using fully and partially perforated baffles under the Re range of 2700 to 11 150. The perforation index for half and fully perforated baffles were 26% and 46.8%, respectively. The Nu was increased by 79–169% and 133–274% as compared to the smooth duct with fully and half-perforated baffles respectively. On the flip side, the f was found to be 2.98–8.02% higher with fully perforated baffles than with a smooth duct and 4.42–17.56% higher with half perforated baffles. Half-perforated baffles with a relative pitch of 7.2 are found to provide the highest performance about 51.6% to 75.0% as compared to a smooth duct under the same pumping conditions. Liu and Wang [26] did the numerical investigation for semi-attached ribs in SAH under the Re range of 10 000 to 25 000. Results showed that the semi-connected rib design not only outperformed the completely attached and detached rib channels but also considerably improved local HT and fluid flow characteristics. The 45°-angled-rib design with a hole radius to channel width ratio of 0.125 provides the best thermal performance. Nuntadusit *et al.* [27] studied the heat transmission and flow properties of the SAH duct with perforated ribs. They selected the rib hole positions about 0.2H, 0.5H, and 0.8H, and attack angles of 15° and 30° at Re of 60 000. They discovered that angled perforated ribs significantly improved heat transmission in comparison to standard ribs. Ghildyal *et al.* [28] performed a numerical analysis to study the thermo-hydraulic performance of SAH roughened with D-shaped, reverse D-shaped, and U-shaped roughness. Out of the investigated parameters the SAH equipped with U-shaped turbulators exhibited the most favorable thermo-hydraulic performance, achieving the highest factor of 1.76 at a Reynolds number of 4000.

From the foregoing literature study, it can be stated that various investigations have been undertaken on roughened SAHs. However, less research work is done on exergy analysis. The purpose of this study is to analyze the exergetic performance of SAHs having inverted L-shape ribs.

1.1 Novelty and objective of the study

Energy analysis is essential for estimating the performance of the system, while exergy analysis is necessary for investigating how internal irreversibility and systems with varying energy losses actually behave in practice. Ex-

ergy analysis is a crucial method for designing SAHs that make the optimal utilization of the sun's energy. By considering exergy efficiency, researchers may identify the major sources of irreversibility and optimize the system for improved performance.

Therefore, the novelty of this study is to evaluate the exergy efficiency of an SAH with inverted L-shape ribs, which was already examined experimentally and numerically for their thermal efficiency by Gawande *et al.* [29]. This approach provides valuable insights into the system's thermodynamic behaviour, enabling the identification of potential areas for improvement and optimization in terms of energy conversion and overall performance. The comparison plot of exergy efficiency obtained by the proposed model with existing research is shown in Fig. 17 under Section 4 (comparison of the present study with existing research), which shows its novelty over the many previous work.

The primary objective of the present work is to evaluate the exergetic performance of SAH with inverted L-shape ribs as a roughness element by evaluating the various exergy losses. Exergy losses by friction, by the absorber, by working fluid (air), and by convection and radiation are the major losses that are evaluated in this study to analyze the exergy efficiency of the system. The present study has been taken up to explore the effect of relative roughness pitch (P/e), Nusselt number (Nu), friction factor (f), and Reynolds number (Re) on the flow passage as well as on inverted L-shaped ribs. Further subdivisions of the objective are given below:

- to investigate the exergetic losses in inverted L-shaped ribs,
- to determine the effect of these parameters on artificially roughened SAHs,
- to determine the roughness parameter that maximizes exergetic efficiency.

2 Exergy analysis and methodology

The schematic diagrams of the present SAH and the test section with inverted L-shape ribs are shown in Fig. 1a and 1b respectively as explained in existing experimental and numerical studies performed by Gawande *et al.* [29]. The geometry of the SAH duct with three section lengths L_1 , L_2 (or L), and L_3 is selected for exergy analysis. By making the duct 20 mm in height and 100 mm in width, the duct has an aspect ratio of 5. The SAH

duct has a hydraulic diameter of $D_h = 33.33$ mm. The top wall of the test portion (L_2) is an aluminium absorber plate. The underside of the duct's top rib is a potential location for an inverted L-shaped rib. The roughness element remains on a plane that is always perpendicular to the flow. Investigated parameters were selected as per the previous research, such as roughness pitch (P/e) varying from 7.14 to 17.86, Re varying from 3000 to 18 000, 1000 W/m^2 heat flux, and constant roughness height (e/D) of 0.042. The geometrical parameters for the inverted L-shape rib considered for the analysis are given in Table 1.

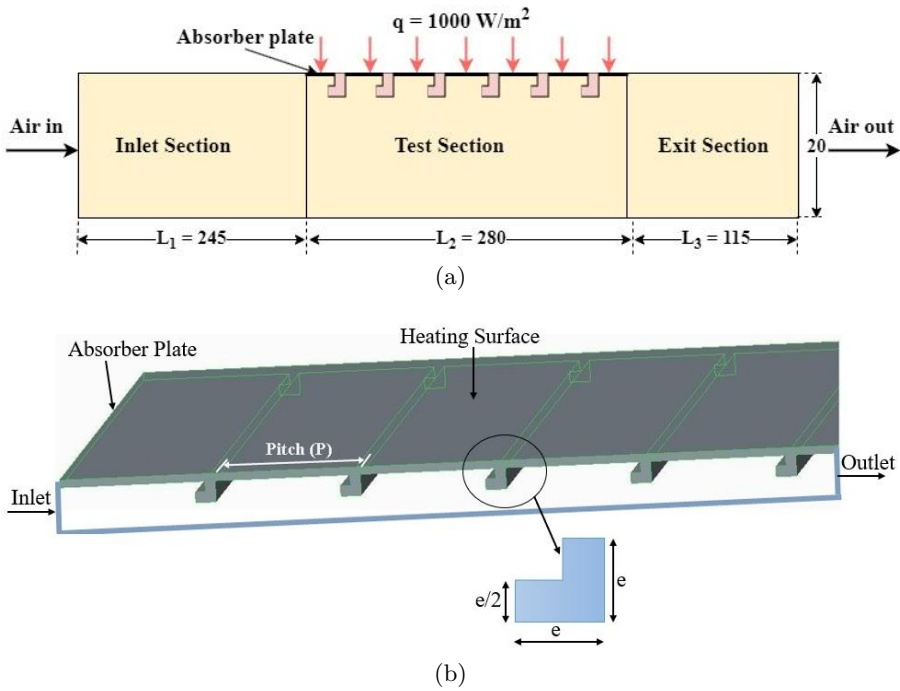


Figure 1: Schematic diagram of roughened SAH duct (a), and the test section with inverted L-shape ribs (b).

To evaluate the SAH's efficiency considering the second law of thermodynamics [31,32], it is necessary to analyze the exergy lost and the entropy created in a heat exchanger as a result of heat transfer between two media and friction. Total exergies connected with thermal systems may be expressed mathematically as

$$E_{xT} = {}^{Phy}_T E_x + {}^K_T E_x + {}^P_T E_x + {}^{Ch}_T E_x, \quad (1)$$

Table 1: Dimensional details of model and roughness parameters [29].

Roughness and flow parameters	Range of parameters
Hydraulic diameter (D_h)	33.33 mm
Length of inlet section (L_1)	245 mm
Length of test section (L_2)	280 mm
Length of outlet section (L_3)	115 mm
Rib pitch (P)	10 mm, 15 mm, 20 mm, and 25 mm
Rib height (e)	1.4 mm
Relative roughness height (e/D_h)	0.042 (fixed)
Relative roughness pitch (P/e)	7.14, 10.71, 14.29, 17.86

were the physical, kinetic, potential, and chemical constituents of total exergy are denoted as $^{Phy}_T E_{xT}$, KE_x , PE_x , and $^{Ch}_T E_x$, respectively. Under the assumption that all exergy components other than the physical components are insignificant, the balancing equation is expressed as

$$E_{xw} = E_{xout} - E_{xin} + E_{xloss}, \quad (2)$$

where E_{xin} , E_{xout} and E_{xloss} represent the entrance, outflow and loss in exergy:

$$E_{xin} = \dot{m} [(h_{in} - h_o) - T_o(S_{in} - S_o)], \quad (3)$$

$$E_{xout} = \dot{m} [(h_{out} - h_o) - T_o(S_{out} - S_o)], \quad (4)$$

$$E_{xloss} = T_o S_{gen}. \quad (5)$$

In exergy calculation a dead state condition is required. In equation 5, the term T_o is the dead state temperature (300 K) which is required to calculate the exergy losses, and reference point ‘O’ represent the dead state. At entry, outflow, and reference point, the enthalpy and entropy are all expressed by: h_{in} , S_{in} , h_{out} , S_{out} , and h_o , S_o respectively, \dot{m} is the mass flow rate of air, S_{gen} and T_o represent the entropy generation and reference temperature at dead state.

The exergetic efficiency (η_{exe}) and the energy loss (e) are calculated as follows [33]:

$$\eta_{exe} = \frac{E_{xout} - E_{xin}}{E_{xout} - E_{xin} + E_{xloss}}, \quad (6)$$

$$El = \frac{E_{xloss}}{\dot{m}(E_{xin} - E_{xout})}. \quad (7)$$

The exergy analysis flow chart is shown in Fig. 2.

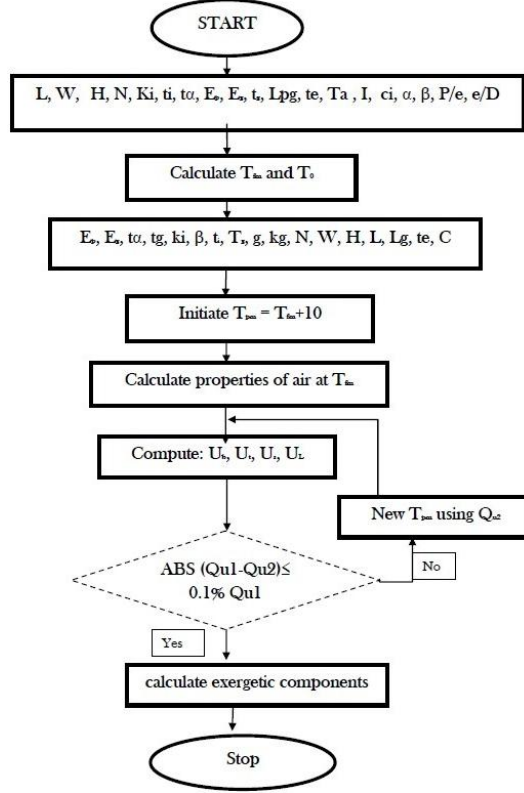


Figure 2: Flow chart for exergy analysis.

All the parameters are assumed to be noticed at steady state conditions and with the help of these parameters we can calculate the Nusselt number (Nu) and friction factor (f). To calculate the rate of mass flow (\dot{m}), useful heat gain (Q_u) by the air to raise their temperature T_{fi} to T_{fo} , and the convection coefficient (h) between air and heated plate, the following equations are used:

$$\dot{m} = C_d A_o \sqrt{\frac{2\rho_w \Delta P_o}{(1 - \beta^4)}}, \quad (8)$$

where the orifice plate calibration using a Pitot tube gave a coefficient of discharge (C_d) value equal to 0.608, the pressure drops across the orifice ($\Delta P_o = 9.81\rho_w$) was calculated by a U-tube manometer, ρ_w is the density of

the manometric fluid, A_o is the area of orifice plate, and $\beta = \frac{D_o}{D_p}$ is defined as the ratio of orifice diameter (D_o) and the blower pipe diameter (D_p).

$$Q_u = \dot{m}C_p(T_{fo} - T_{fi}), \quad (9)$$

where C_p is the specific heat capacity of air at constant pressure of 101325 Pa, T_{fi} and T_{fo} represent the temperature of working fluid (air) at the inlet and outlet, respectively, and

$$h = \frac{Q_u}{A_p(T_{pm} - T_{fm})}, \quad (10)$$

where A_p is the area of the absorber surface used to transfer the heat to the air, $T_{fm} = \frac{T_{fi} + T_{fo}}{2}$ is the mean temperature of flowing air and T_{pm} is plate mean temperature. These equations determined the Nu and the f in both experimental and computational fluid dynamics (CFD) investigations, mathematically expressed as

$$Nu = \frac{hD_h}{k}, \quad (11)$$

$$f = \frac{\Delta PD_h}{2\rho Lv^2}, \quad (12)$$

where k is the thermal conductivity of air, $D_h = \frac{2WH}{W+H}$ is the hydraulic diameter, H – height, W – width of a rectangular duct, $L = L_2$ – length of test section, and ρ is the density of air. It is necessary to calculate the hydraulic diameter for a non-circular duct for proper results. The Reynolds number formula can be expressed by

$$Re = \frac{\rho D_h v}{\mu}, \quad (13)$$

where v and μ are known as the flow velocity and dynamic viscosity of air.

The optimum performance of roughened SAH is decided by a factor called thermohydraulic performance factor (THPF) and expressed as

$$THPF = \frac{\frac{Nu}{Nu_s}}{\left(\frac{f}{f_s}\right)^{\frac{1}{3}}}. \quad (14)$$

The standard Dittus–Bolter correlation is used to calculate the Nu_s for smooth ducts in CFD analysis, mathematically expressed as

$$Nu_s = 0.023Re^{0.8} Pr^{0.4}. \quad (15)$$

Similarly, for CFD analysis, the standard Blasius correlation to calculate the friction factor for smooth ducts is utilised:

$$f_s = 0.0791Re^{-0.25}. \quad (16)$$

Here we see the crucial correlation for forecasting thermohydraulic performance, which is necessary for selecting the best possible geometric parameters in each context. The Nu and f are shown to be effectively influenced parameters with changing P/e and Re during evaluation at a fixed value of e/D [29]:

$$Nu = 0.023Re^{0.8332} \left(\frac{P}{e}\right)^{0.3479} \exp^{-0.1004 \ln\left(\frac{P}{e}\right)^2}, \quad (17)$$

$$f = 0.2805Re^{-0.2617} \left(\frac{P}{e}\right)^{0.0815} \exp^{-0.0319 \ln\left(\frac{P}{e}\right)^2}. \quad (18)$$

2.1 Validation of the proposed model

Comparisons have been made between the Nu obtained from the present study and those from previously conducted experimental study by Gawande *et al.* [29]. For the experimental validation, the input parameters used in the proposed model were carefully matched with the ones employed in the experimental study. These parameters included boundary conditions, material properties, and operating conditions. The predicted Nu from the present study is compared with the corresponding values obtained from the experimental study as shown in Fig. 3. The mean deviation in the results is obtained in the acceptable range of about 5%. By conducting this validation process, we can assess the agreement between the proposed model and the previously performed experimental model.

The proposed numerical model of SAH with inverted L-shape rib roughness for exergetic analysis is validated under the same operating conditions proposed by Chamoli *et al.* [30]. Fig. 4 shows the plot for exergetic efficiency enhancement across the full range of system and operating parameters corresponding to the temperature rise parameter ($\Delta T/I$). The exergetic efficiency obtained from the proposed model has deviated from the previous research by about $\pm 2\%$. This comparison shows the justification of the proposed numerical model for further investigation.

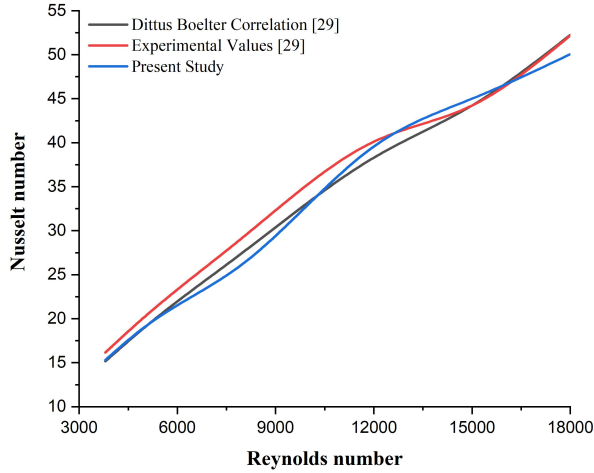


Figure 3: Experimental validation of the proposed model.

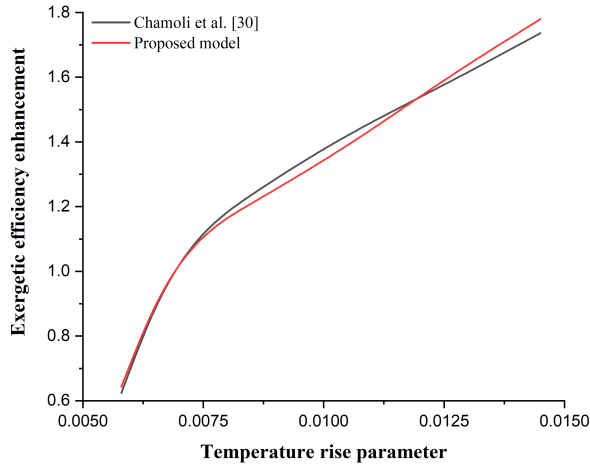


Figure 4: Validation of the proposed numerical model with the work of Chamoli *et al.* [30].

3 Results and discussion

The exergetic performance analysis of SAH having inverted L-shape ribs has been done at a fixed amount of heat flux, i.e. 1000 W/m^2 , variable P/e (7.14 to 17.86), and Re from 3000 to 18 000. The results obtained from the exergy analysis are explained as follows:

3.1 Effect of pitch ratio on exergy loss components

3.1.1 Effect of pitch ratio on exergy losses by friction

The conditions that lead to increased friction losses determine the exergy loss. High friction losses and a greater mass flow rate are the results of a lower temperature increase parameter ($\Delta T/I$). Therefore, the lowest possible pitch ratio (P/e) results in the greatest possible exergetic losses. Exertional losses due to friction ($El_{\Delta p}$) were shown to be positively correlated with the rate of temperature increase shown in Fig. 5.

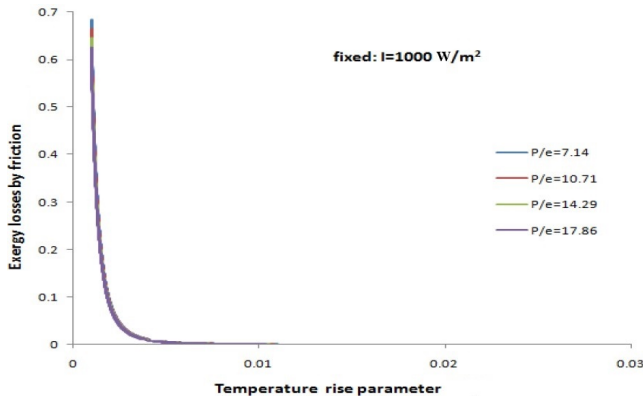


Figure 5: Variation of exergy losses by friction ($El_{\Delta p}$) with temperature rise parameter ($\Delta T/I$).

3.1.2 Effect of pitch ratio on exergy losses by an absorber

Mean plate temperature (T_{pm}) is used to calculate exergy losses through the absorber (El_a). The El_a decreases with increasing temperature increase parameter ($\Delta T/I$) as illustrated in Fig. 6. For the simple reason that there is more exergy in the energy present at higher temperatures. Raising the temperature of the absorber reduces the exergy loss through the absorber.

3.1.3 Effect of pitch ratio on exergy losses by working fluid

Exergy losses rise in proportion to the quantity of irreversibility, which grows when the temperature increase parameter is increased. An increase in the temperature increase parameter causes the absorber temperature to rise. That's why the parameter for the temperature increase where the

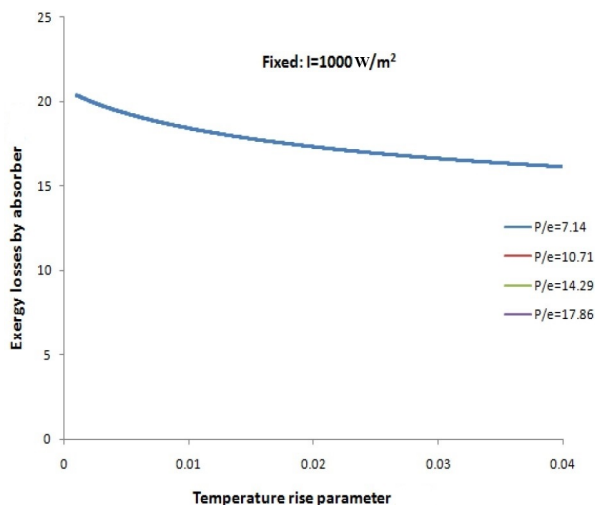


Figure 6: Variation of exergy losses by an absorber (El_a) with temperature rise parameter ($\Delta T/I$).

exergetic losses by air ($El_{\Delta T}$) are the greatest is the one with the highest values. As can be seen in the losses of exergy due to friction increase with a pitch ratio (P/e) of 7.86, but thereafter they drop and reach a minimum for all pitch ratios considered as shown in Fig. 7.

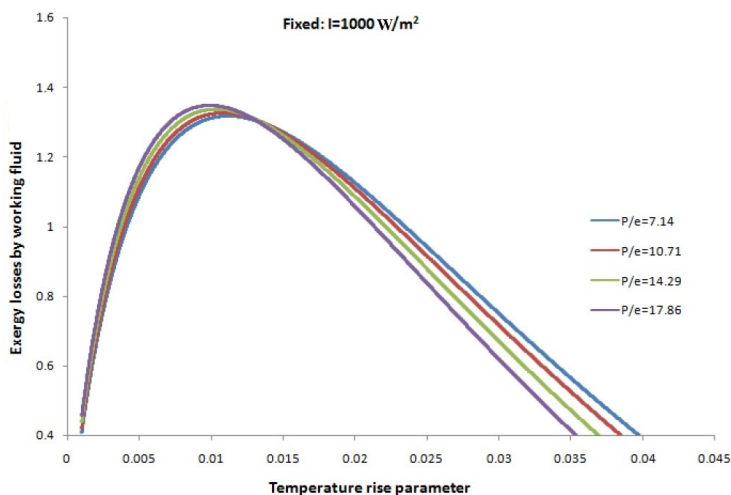


Figure 7: Loss of exergy by air ($El_{\Delta T}$) corresponds to temperature rise parameter ($\Delta T/I$).

3.1.4 Effect of pitch ratio on the loss of exergy by convection and radiation

Increasing the temperature increase parameter ($\Delta T/I$) results in a greater temperature difference between the absorber and surrounding, and hence a greater exergy loss, as shown in Fig. 8. It follows that the smallest temperature increase parameter results in the smallest exergy losses due to heat transmission to the surrounding environment. The exergy loss by the convection and radiation is denoted by El_e , and the values of El_e are highest at pitch ratios (P/e) of 14.29 and lowest at 7.14.

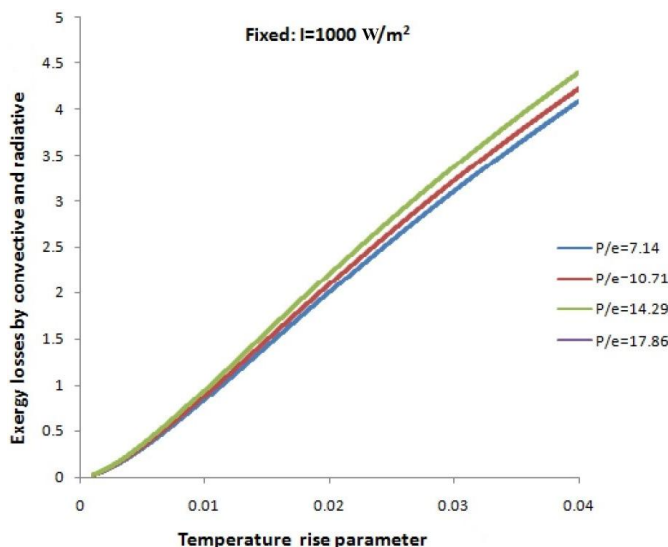


Figure 8: Variation of exergy losses by convection and radiation (El_e) with temperature rise parameter ($\Delta T/I$).

3.1.5 Effect of pitch ratio on exergetic efficiency

Exergetic efficiency is a function of temperature rise parameter. Exergetic efficiency is negative for low values of the temperature increase parameter ($\Delta T/I$) due to the extremely high mass flow rate, but it rises as $\Delta T/I$ rise. Exergetic efficiency (η_{exe}) is illustrated in Fig. 9 for a range of relative pitch (P/e) values, with low values seen for pitch ratios of 17.86 and 7.14, respectively.

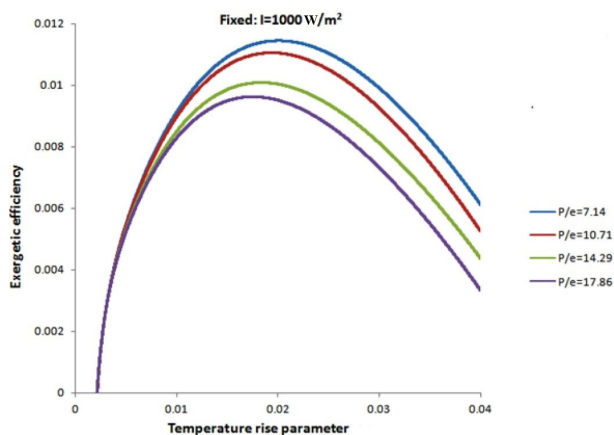


Figure 9: Variation of exergetic efficiency (η_{exe}) with temperature rise parameter ($\Delta T/I$).

3.1.6 Effect of pitch ratio on effective efficiency

Early on, as the Reynolds number rises, effective efficiency improves; it reaches a peak, and then it begins to decline. The domination of mechanical power is what's needed to overcome the forces of friction. The effective efficiency (η_{eff}) drops down dramatically as the temperature increase parameter ($\Delta T/I$) is increased. As can be seen in Fig. 10, it reaches its peak when the temperature rise is rather modest.

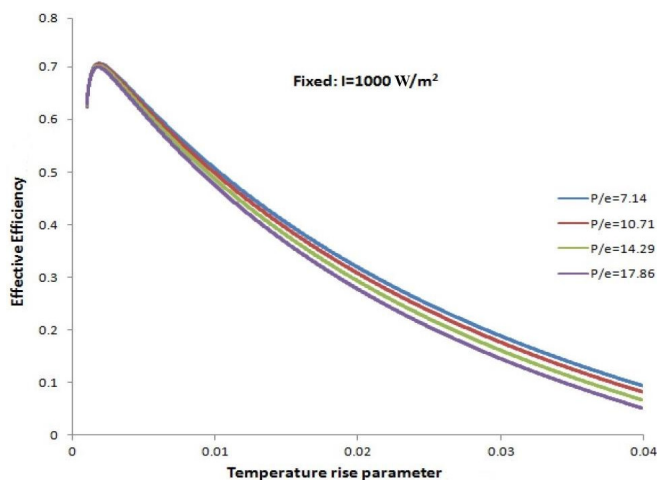


Figure 10: Variation of the effective efficiency (η_{eff}) with temperature rise parameter ($\Delta T/I$).

3.1.7 Effect of pitch ratio on thermal efficiency

When referring to heat transfer, thermal efficiency is measured as the amount of usable heat gained divided by the amount of radiation incident on the absorber. Because of this, it stands to reason that the roughened surface which is accountable for maximizing the usable heat uptake would have the highest thermal efficiency (η_{th}). As the temperature increase parameter ($\Delta T/I$) increases, thermal efficiency deteriorates. When the pitch ratio is at its lowest, $P/e = 7.14$, the thermal efficiency is at its highest as presented in Fig. 11.

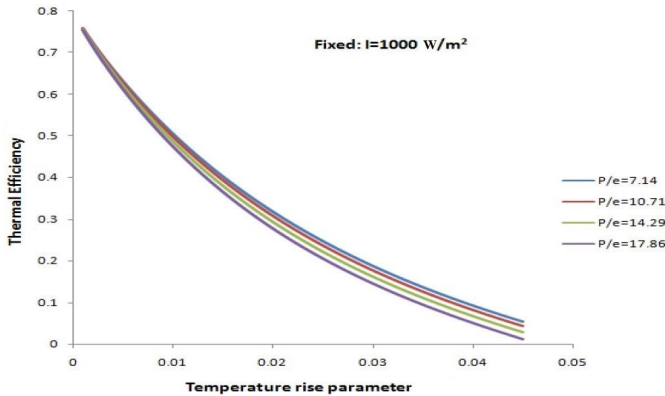


Figure 11: Variation of thermal efficiency (η_{th}) with temperature rise parameter ($\Delta T/I$).

3.1.8 Effect of pitch ratio on pressure drop

A significant pressure decrease over the test portion is the price we must pay for optimizing heat transfer. The first law of thermodynamics states that the only allowed change in energy is a change in its form. The turbulence in the test portion is therefore stimulated by a reduction in pressure. As the mass flow rate (\dot{m}) increases, the pressure drop (Δp) over the absorber plate does as well, reaching a maximum value for 0.02 kg/s as presented in Fig. 12.

3.1.9 Effect of pitch ratio on the mass flow rate

The mass flow rate is a function of the Reynolds number (Re), and when the value of the Re is increased from 3000 to 18 000, the mass flow rate also rises as shown in Fig. 13.

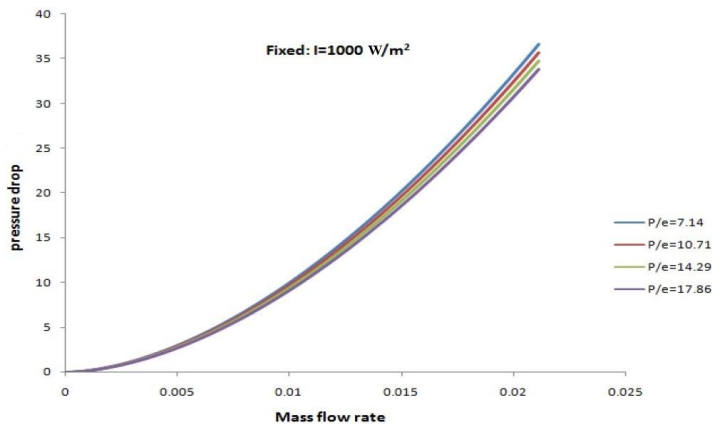


Figure 12: Variation of pressure drop (Δp) with mass flow rate (\dot{m}).

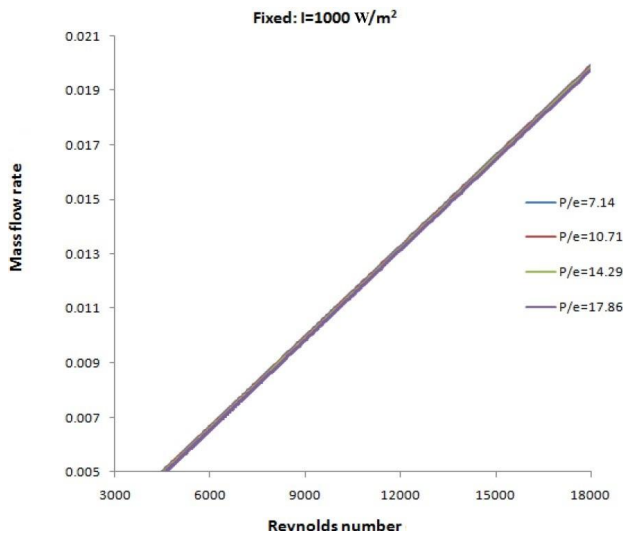


Figure 13: Variation of mass flow rate (\dot{m}) with Reynolds number (Re).

3.1.10 Effect of pitch ratio on Nusselt number

In most cases, an increase in the Reynolds number is accompanied by a corresponding rise in the Nusselt number. The value of the Nu concerning the Re attained its maximum for inverted L-shaped roughness at a pitch ratio of 7.14, while concurrently achieving its minimum at a pitch ratio ($P/e = 17.86$) as shown in Fig. 14.

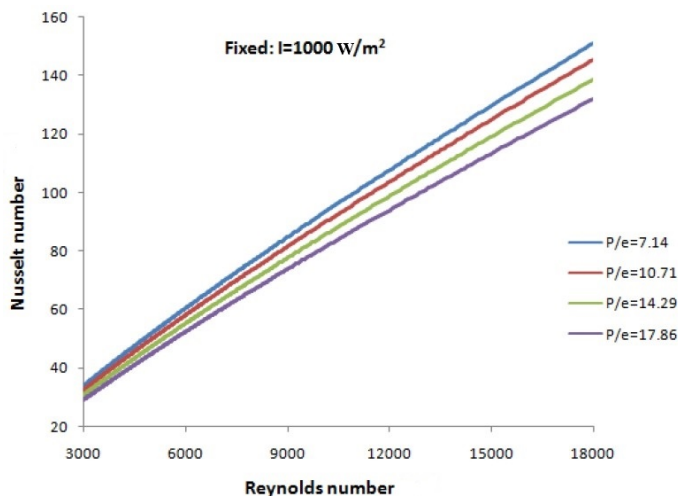


Figure 14: Variation of Nusselt number with Reynolds number.

3.1.11 Effect of pitch ratio on friction factor

The friction factor (f) has a minimum value of $P/e = 17.86$ and a maximum value of $P/e = 7.14$, and its value decreases as the Reynolds number increases as in Fig. 15.

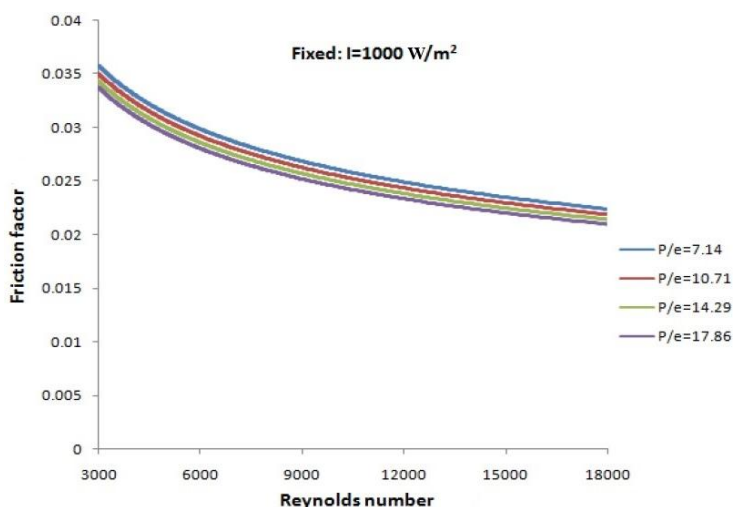


Figure 15: Variation of friction factor (f) with Reynolds number (Re).

3.1.12 Optimization of system parameters

Figure 16 clearly shows that the value of the pitch ratio (P/e) is optimised at an insulation of 1000 W/m^2 , and that the value of the temperature rise parameter ($\Delta T/I$) ranges from 0.005 to 0.03, with 17.86 being the optimum value for the relative pitch, as has been shown.

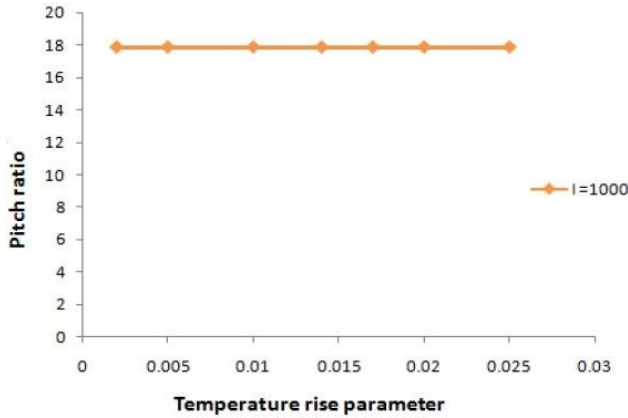


Figure 16: Variation of pitch ratio (P/e) with temperature rise parameter ($\Delta T/I$).

4 Comparison of the present study with existing research

A comparison was made between the results in the literature acquired using different shapes to make it evident how much of an improvement might be made by the proposed numerical model. Exergetic efficiency obtained from the present study is compared to the existing research by Chamoli *et al.* [30]. This comparison of the plot between the present study and previous literature is presented in Fig. 17. Present study offers higher exergetic efficiency at a small temperature rise parameter ($\Delta T/I$) and starts decreasing with a further increase in $\Delta T/I$ when compared to existing literature. After the comparison is concluded that the exergetic efficiency found from the proposed model with an inverted L-shape rib on the absorber plate is larger as compared to the existing work by Chamoli *et al.* [30] at a higher range of $\Delta T/I$, which shows the novelty of the proposed model.

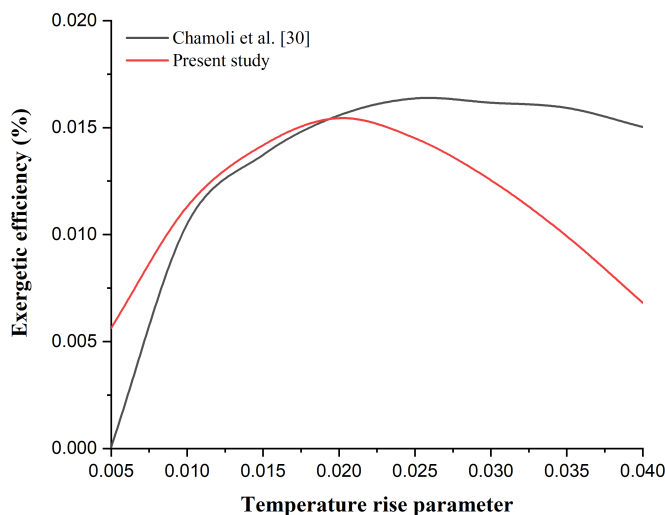


Figure 17: Comparison of the present study with existing research by Chamoli *et al.* [30].

5 Conclusions

In this work, we do a numerical analysis of an inverted L-shape rib on the absorber plate of solar air heater that has been intentionally roughened. Heat transfer improvement and flow friction characteristics as a function of relative roughness pitch and Reynolds number are investigated. Using the exergetic efficiency requirements, the roughness parameters for a given operating state of a SAH were optimized using a Matlab based analytical model.

The following are the study's most significant findings:

- As the Re rises the average value of the Nu increases and the friction factor decreases in general. A fixed value of relative roughness height (e/D_h) and a decrease in relative roughness pitch (P/e) leads to an increase in the average Nusselt number and friction factor.
- At a Re of 15 000, P/e of 7.14, and e/D_h of 0.042, the highest improvement in Nusselt number has been to be about 2.827 times over the smooth duct.
- At P/e of 7.14, the exergetic efficiency of the inverted L-shaped rib is at its highest point, and at P/e of 17.86, it is at its lowest.

- Exergy losses (El) from the absorber plate by convection and radiation heat transfer are the smallest at $P/e = 7.14$ and the largest at $P/e = 14.29$.
- As the temperature increase parameter ($\Delta T/I$) rises, the working fluid's exergy losses from the absorber plate decrease. Exergy losses due to the working fluid are the greatest for $P/e = 17.86$ and the lowest for $P/e = 7.14$.
- As the $\Delta T/I$ increase, the exergy losses *via* absorber (El_a) from the absorber plate decrease, and they become nearly equal for all P/e ratios.
- The maximum effective efficiency (η_{eff}) of the inverted L-shaped rib was seen at $P/e = 7.14$ and the minimum efficiency was observed at $P/e = 17.86$, both as a function of the $\Delta T/I$.
- The maximum thermal efficiency (η_{th}) is achieved at $P/e = 7.14$, while the minimal efficiency is achieved at $P/e = 17.86$.
- Gaining a mass flow rate of 0.02 kg/s produces a maximum pressure drop (Δp) from the absorber plate.

The research outcomes of exergy analysis of SAH with inverted L-shape ribs have significant industrial relevance. They provide valuable insights for optimizing system performance, improving energy efficiency, guiding system design and retrofitting, conducting techno-economic assessments, and promoting sustainability in industrial processes.

Received 22 April 2023

References

- [1] Singh I., Singh S.: *A review of artificial roughness geometries employed in solar air heaters*. Renew. Sust. Energ. Rev. **92**(2018), 405–425. doi: [10.1016/j.rser.2018.04.108](https://doi.org/10.1016/j.rser.2018.04.108)
- [2] Singh I., Singh S.: *CFD analysis of solar air heater duct having square wave profiled transverse ribs as roughness elements*. Sol. Energy **162**(2018), 442–453. doi: [10.1016/j.solener.2018.01.019](https://doi.org/10.1016/j.solener.2018.01.019)
- [3] Kalogirou S.A.: *Solar thermal collectors and applications*. Prog. Energ. Combust. Sci. **30**(2004), 3, 231–295. doi: [10.1016/j.pecs.2004.02.001](https://doi.org/10.1016/j.pecs.2004.02.001)

- [4] Omer A.M.: *Energy use and environmental impacts: A general review*. J. Renew. Sustain. Ener. **1**(2009), 5, 053101. doi: [10.1063/1.3220701](https://doi.org/10.1063/1.3220701)
- [5] Sharma S.L., Debbarma A.: *A review on thermal performance and heat transfer augmentation in solar air heater*. Int. J. Sustain. Energ. **41**(2022), 11, 1973–2019. doi: [10.1080/14786451.2022.2125518](https://doi.org/10.1080/14786451.2022.2125518)
- [6] Prasad K., Mullick S.C.: *Heat transfer characteristics of a solar air heater used for drying purposes*. Appl. Energ. **13**(1983), 2, 83–93. doi: [10.1016/0306-2619\(83\)90001-6](https://doi.org/10.1016/0306-2619(83)90001-6)
- [7] Sahu M.M., Bhagoria J.L.: *Augmentation of heat transfer coefficient by using 90 broken transverse ribs on absorber plate of solar air heater*. Renew. Energ. **30**(2005), 13, 2057–2073. doi: [10.1016/j.renene.2004.10.016](https://doi.org/10.1016/j.renene.2004.10.016)
- [8] Gupta D., Solanki S.C., Saini J.S.: *Thermohydraulic performance of solar air heaters with roughened absorber plates*. Sol. Energ. **61**(1997), 1, 33–42. doi: [10.1016/S0038-092X\(97\)00005-4](https://doi.org/10.1016/S0038-092X(97)00005-4)
- [9] Karwa R.: *Experimental studies of augmented heat transfer and friction in asymmetrically heated rectangular ducts with ribs on the heated wall in transverse, inclined, V-continuous and V-discrete pattern*. Int. Commun. Heat Mass **30**(2003), 2, 241–250. doi: [10.1016/S0735-1933\(03\)00035-6](https://doi.org/10.1016/S0735-1933(03)00035-6)
- [10] Aharwal K.R., Gandhi B.K., Saini J.S.: *Experimental investigation on heat-transfer enhancement due to a gap in an inclined continuous rib arrangement in a rectangular duct of solar air heater*. Renew. Energ. **33**(2008), 4, 585–596. doi: [10.1016/j.renene.2007.03.023](https://doi.org/10.1016/j.renene.2007.03.023)
- [11] Saini R.P., Saini J.S.: *Heat transfer and friction factor correlations for artificially roughened ducts with expanded metal mesh as roughness element*. Int. J. Heat Mass Tran. **40**(1997), 4, 973–986. doi: [10.1016/0017-9310\(96\)00019-1](https://doi.org/10.1016/0017-9310(96)00019-1)
- [12] Momin A.M.E., Saini J.S., Solanki S.C.: *Heat transfer and friction in solar air heater duct with V-shaped rib roughness on absorber plate*. Int. J. Heat Mass Tran. **45**(2002), 16, 3383–3396. doi: [10.1016/S0017-9310\(02\)00046-7](https://doi.org/10.1016/S0017-9310(02)00046-7)
- [13] Muluwork K.B.: *Investigations on fluid flow and heat transfer in roughened absorber solar heaters*. Ph.D. thesis, IIT Roorkee, 2000.
- [14] Karwa R., Solanki S.C., Saini J.S.: *Heat transfer coefficient and friction factor correlations for the transitional flow regime in rib-roughened rectangular ducts*. Int. J. Heat Mass Tran. **42**(1999), 9, 1597–1615. doi: [10.1016/S0017-9310\(98\)00252-X](https://doi.org/10.1016/S0017-9310(98)00252-X)
- [15] Bhagoria J.L., Saini J.S., Solanki S.C.: *Heat transfer coefficient and friction factor correlations for rectangular solar air heater duct having transverse wedge shaped rib roughness on the absorber plate*. Renew. Energ. **25**(2002), 3, 341–369. doi: [10.1016/S0960-1481\(01\)00057-X](https://doi.org/10.1016/S0960-1481(01)00057-X)
- [16] Saini S.K., Saini R.P.: *Development of correlations for Nusselt number and friction factor for solar air heater with roughened duct having arc-shaped wire as artificial roughness*. Sol. Energy **82**(2008), 12, 1118–1130. doi: [10.1016/j.solener.2008.05.010](https://doi.org/10.1016/j.solener.2008.05.010)
- [17] Saini R.P., Verma J.: *Heat transfer and friction factor correlations for a duct having dimple-shape artificial roughness for solar air heaters*. Energy **33**(2008), 8, 1277–1287. doi: [10.1016/j.energy.2008.02.017](https://doi.org/10.1016/j.energy.2008.02.017)

- [18] Karmare S.V., Tikekar A.N.: *Heat transfer and friction factor correlation for artificially roughened duct with metal grit ribs*. Int. J. Heat Mass Tran. **50**(2007), 21–22, 4342–4351. doi: [10.1016/j.ijheatmasstransfer.2007.01.065](https://doi.org/10.1016/j.ijheatmasstransfer.2007.01.065)
- [19] Hwang J.J., Liou T.M.: *Heat transfer in a rectangular channel with perforated turbulence promoters using holographic interferometry measurement*. Int. J. Heat Mass Tran. **38**(1995), 17, 3197–3207. doi: [10.1016/0017-9310\(95\)00065-H](https://doi.org/10.1016/0017-9310(95)00065-H)
- [20] Şara O.N., Pekdemir T., Yapici S., Erşahan H.: *Thermal performance analysis for solid and perforated blocks attached on a flat surface in duct flow*. Energ. Convers. Manage. **41**(2000), 10, 1019–1028. doi: [10.1016/S0196-8904\(99\)00163-6](https://doi.org/10.1016/S0196-8904(99)00163-6)
- [21] Sara O.N., Pekdemir T., Yapici S., Yilmaz M.: *Heat-transfer enhancement in a channel flow with perforated rectangular blocks*. Int. J. Heat Fluid Fl. **22**(2001), 5, 509–518. doi: [10.1016/S0142-727X\(01\)00117-5](https://doi.org/10.1016/S0142-727X(01)00117-5)
- [22] Buchlin J.M.: *Convective heat transfer in a channel with perforated ribs*. Int. J. Therm. Sci. **41**(2002), 4, 332–340. doi: [10.1016/S1290-0729\(02\)01323-6](https://doi.org/10.1016/S1290-0729(02)01323-6)
- [23] Moon S.W., Lau S.C.: *Heat transfer between blockages with holes in a rectangular channel*. J. Heat Transf. **125**(2003), 4, 587–594. doi: [10.1115/1.1576812](https://doi.org/10.1115/1.1576812)
- [24] Karwa R., Maheshwari B.K., Karwa N.: *Experimental study of heat transfer enhancement in an asymmetrically heated rectangular duct with perforated baffles*. Int. Commun. Heat Mass **32**(2005), 1–2, 275–284. doi: [10.1016/j.icheatmass-transfer.2004.10.002](https://doi.org/10.1016/j.icheatmass-transfer.2004.10.002)
- [25] Karwa R. Maheshwari B.K.: *Heat transfer and friction in an asymmetrically heated rectangular duct with half and fully perforated baffles at different pitches*. Int. Commun. Heat Mass **36**(2009), 3, 264–268. doi: [10.1016/j.icheatmass-transfer.2008.11.005](https://doi.org/10.1016/j.icheatmass-transfer.2008.11.005)
- [26] Liu H., Wang J.: *Numerical investigation on synthetical performances of fluid flow and heat transfer of semi attached rib-channels*. Int. Commun. Heat Mass **54**(2011), 1–3, 575–583. doi: [10.1016/j.ijheatmasstransfer.2010.09.013](https://doi.org/10.1016/j.ijheatmasstransfer.2010.09.013)
- [27] Nuntadusit C., Wae-Hayee M., Bunyajitradulya A., Eiamsa-ard S.: *Thermal visualization on surface with transverse perforated ribs*. Int. Commun. Heat Mass **39**(2012), 5, 634–639. doi: [10.1016/j.icheatmasstransfer.2012.03.001](https://doi.org/10.1016/j.icheatmasstransfer.2012.03.001)
- [28] Ghildyal A., Bisht V.S., Bhandari P., Rawat K.S.: *Effect of D-shaped, reverse D-shaped and U-shaped turbulators in solar air heater on thermo-hydraulic performance*. Arch. Thermodyn. **44**(2023), 2, 3–20. doi: [10.24425/ather.2023.146556](https://doi.org/10.24425/ather.2023.146556)
- [29] Gawande V.B., Dhoble A.S., Zodpe D.B., Chamoli S.: *Experimental and CFD investigation of convection heat transfer in solar air heater with reverse L-shaped ribs*. Sol. Energy **131**(2016), 275–295. doi: [10.1016/j.solener.2016.02.040](https://doi.org/10.1016/j.solener.2016.02.040)
- [30] Chamoli S., Thakur N.S.: *Energetic performance evaluation of solar air heater having V-down perforated baffles on the absorber plate*. J. Therm. Anal. Calorim. **117**(2014), 909–923. doi: [10.1007/s10973-014-3765-8](https://doi.org/10.1007/s10973-014-3765-8)
- [31] Kumar S., Kumar R., Goel V., Bhattacharyya S., Issakhov A.: *Energetic performance estimation for roughened triangular duct used in solar air heaters*. J. Therm. Anal. Calorim. **145**(2021), 3, 1661–1672. doi: [10.1007/s10973-021-10852-w](https://doi.org/10.1007/s10973-021-10852-w)

- [32] Yadav S., Kaushal M.: *Exergetic performance evaluation of solar air heater having arc shape oriented protrusions as roughness element*. Sol. Energy **105**(2014), 181–189. doi: [10.1016/j.solener.2014.04.001](https://doi.org/10.1016/j.solener.2014.04.001)
- [33] Zheng N., Liu P., Shan F., Liu Z., Liu W.: *Heat transfer enhancement in a novel internally grooved tube by generating longitudinal swirl flows with multi-vortexes*. Appl. Therm. Eng. **95**(2016), 25, 421–432. doi: [10.1016/j.applthermaleng.2015.11.066](https://doi.org/10.1016/j.applthermaleng.2015.11.066)

Use of reinforced ice as alternative building material in cold regions: an overview

JELENA BOSNJAK*
NATALIA BODROZIC COKO
MISO JURCEVIC
BRANKO KLARIN
SANDRO NIZETIC

University of Split, Faculty of Electrical Engineering, Mechanical Engineering and Naval Architecture, Rudera Boskovic 32, 21000 Split, Croatia

Abstract The design of suitable thermophysical properties of reinforced ice as well as employing the novel material in feasible ways represent key aspects towards alternative building sustainability. In this overview research studies dealing with reinforced ice structures have been presented with an emphasis on construction parameters and reinforcement materials of the structures. The main focus of the study is directed to the identification of the main issues related to the construction of reinforced ice structures as well as the environmental and economic impact of such structures. Obtained research data shows that the compressive, tensile, and bending strength of reinforced ice can be increased up to 6 times compared to plain ice. The application of reinforcement materials decreases creep rate, enhances ductility, and reduces brittle behaviour of ice. Assessed reinforced ice structures were mainly found to be environmentally friendly and economically viable. However, in most of the analysed studies construction parameters and physical properties were not defined precisely. The conducted overview indicates the necessity for more comprehensive and more accurate data regarding reinforced ice construction, applied methods, and processes, and preparation of ice composites in general.

Keywords: Ice structures; Reinforced ice; Ice composite

*Corresponding Author. Email: Jelena.Bosnjak.00@fesb.hr

1 Introduction

With growing concerns over carbon dioxide pollution, ways are being sought to reduce the emissions. Innovative abundant earth materials could play a significant role in that challenge. In 2009 the global construction sector generated 5.7 billion tons of carbon dioxide, both from energy use and cement production [1]. That equals to 23% carbon dioxide emissions from global economic activities [1]. In cold areas construction is very costly and time consuming, as transportation of building materials to cold remote regions is a difficult and expensive process [2]. Hence, it is of great importance for cryogenic environments to consider the use of indigenous natural materials, like ice and frozen soil, as well as the latest developments and techniques in producing novel materials [3]. With water being the most common compound on Earth, renewable, abundant, and clean, it has a strong potential of being used in sustainable, clean technologies. It is crucial to have reliable data on thermophysical properties of ice and frozen soil in order to widen their application in cryogenic environments. Frozen soil effects on concrete have been examined in [4] but there is still space to broaden the investigations of ice.

Structures made of ice are known since ancient times when people were building ice shelters to protect themselves from cold weather. Nonetheless, it has been stated that there is still insufficient understanding of ice as a material [5]. Ice has a couple of downsides when compared to conventional engineering materials: it is brittle, relatively weak, and prone to creep behaviour [6]. Because of its natural origin, it is not as homogeneous nor workable as conventional building materials. However, ice can become much more applicable with the use of reinforcement. First known structure made from reinforced ice was an igloo – a combination of ice, snow, and lichen [6], after which no progress was made until World War II when reinforced ice has started to be utilized for building bridges and roads for military purposes. Bridge over Dnieper River in Ukraine and ice roads on Ladoga Lake in Russia were made of ice reinforced with logs, branches, and twigs [6]. At the time project Habakkuk took place – it was a plan to construct an aircraft carrier out of ice strengthened with wood pulp (pykrete) [7]. Although the project never came to life, it gave rise to the research of possibilities and applications of ice reinforcement. During Cold War, project Ice Way was conducted in Greenland with a goal to make an airstrip out of sea ice strengthened with fibreglass. Ice was treated as a readily available and inexhaustible local construction material [8]. Ice domes

were first made at the University of Calgary, Canada. Unlike igloos, no blocks were used but a thin-walled structure was created by spraying water on an inflatable formwork with a network of fibreglass yarn [3]. Since then, ice domes and similarly shaped structures have been made in the cryogenic environments around the globe, as a part of winter festivals and experimental projects, like pykrete dome [9], and Sagrada Familia [10], in Juuka, Finland, Candela pavilion in Ghent, Belgium [11], Flamenco Ice Tower, ice pavilion THRICE [12], and Koi-fish ice shell in Harbin, China [13], all made of ice reinforced with some type of cellulose fibres. In 2019 first restaurant made of paper-reinforced ice was built in Harbin, China [14]. Ice roads crossing rivers in Arkhangelsk region in Russia have been reinforced with geonets from fibreglass [15]. Reinforced ice has been used in the form of cryogels to seal a leakage at the base of a dame at the Russian Irelyakh hydro system [16]. Reinforced ice as a sustainable and often fully recyclable building material could be used for all kinds of temporary constructions in cold areas, ice events, the Winter Olympics and even Mars missions [9].

Research demonstrated that there is a wide range of possibilities for ice reinforcement and the reinforcement methods are constantly developing and progressing [6]. However, applications of reinforced ice were not covered well and nor were the problems arising from the processes of producing ice composites and building the structures.

The main objective of this work is focused on those aspects and offers an encompassing study of achievable applications considering the construction parameters (method of construction, wall thickness, cooling method) and reinforcement method (material, mass fraction, particle size). Although numerous studies have dealt with reinforced ice, possibilities of reinforcement and properties of ice composites, not many have used reinforced ice in practice. In this work only ice composites that have been put in practice have been presented along with building techniques and issues that appeared in the process. The economic and environmental aspects of the novel materials have also been discussed. Hence, the analysis of herein presented reinforced ice structures provides a useful basis for comparisons and problems identification.

1.1 Review methodology

Reviewed articles were obtained mainly from Elsevier's Scopus database. According to the Elsevier's Scopus database and based on targeted keywords, research work done in the area from 1988 until today has been very

modest with a total of 41 publications, including articles and conference papers, dealing with reinforced ice and ice composites, Fig. 1 [17].

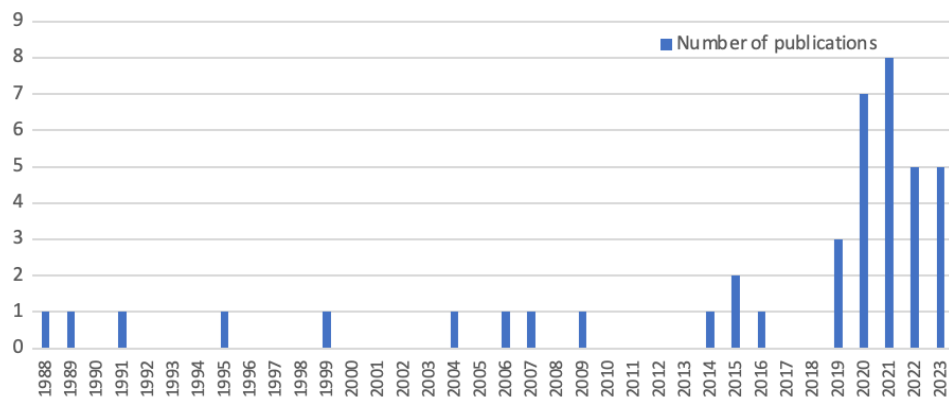


Figure 1: Number of publications dealing with reinforced ice through the years [17].

However, a rise in the number of publications can be observed from the year 2019 onwards. Specifically, from 2019 until today the sum of 28 publications was released which is almost 70% of a total number of publications associated with ice reinforcement possibilities and applications. It is a clear indicator that the interest of the research community for reinforced ice, although still low, is on the rise. Most of the research studies related to the investigation of ice were done in the fields of engineering and material science which suggests the interest in the usage of reinforced ice for engineering purposes.

The selection process consisted of two stages. The primary selection was made with respect to the targeted keywords. The subject area was limited to engineering, material science, earth and planetary sciences and environmental science. Document type was chosen to be papers only and written in English. Time range was not taken because overall a limited number of research papers are related to the herein considered search topic. In the second step, papers focused on ice reinforcement and those that cover reinforced ice structures were selected.

The aim of this work is to introduce and compare the possibilities of using reinforced ice as a building material. Thus, an overview of different reinforced ice structures is given with emphasis on construction parameters and environmental and economic aspects of the structures.

2 Comparison of thermophysical properties of pure ice and reinforced ice

2.1 Thermophysical properties of pure ice

Ice has many crystal structures, but in nature it can be found in 12 crystalline and 2 amorphous forms [18]. Under standard conditions (0°C , $101\,325\text{ Pa}$), it has a hexagonal crystal lattice (I_h). Ice is less dense than water with a density of 916.4 kg m^{-3} at 0°C , and the value increases as the temperature decreases [18].

2.1.1 Thermal properties of pure ice

In Table 1 thermal properties of pure ice (I_h) at -20°C [18] and 0°C [19] are presented. It is apparent that the thermal conductivity of ice is about 4 times greater than that of water and increases with the decrease of temperature. On the contrary, the specific heat of ice decreases with temperature decreasing and it is more than two times lower than the specific heat of the water [20].

Table 1: Thermal properties of pure ice (I_h) at -20°C [18] and 0°C [19].

Property	Symbol	Unit	Value	
			-20°C	0°C
Thermal conductivity	λ	$\text{Wm}^{-1}\text{K}^{-1}$	2.4	2.2
Specific heat capacity	c	kJkg^{-1}K	1.96	2.01
Latent heat of fusion	r	kJkg^{-1}	333.5	334
Linear expansion coefficient	α	K^{-1}	5.3×10^{-5}	10^{-6}

Measured thermal conductivities of pure ice found in literature depend largely on specific chemical composition of water used, and the temperature of ice specimens. Most notable conducted measurements were summarized by Fukusako [21], Fig. 2. Variations between the values is due to the fact that each researcher used different preparation methods and different ways to collect the experimental data.

Latent heat of fusion of ice represents a change in enthalpy as a unit mass of ice coverts into water isothermally and reversibly [21]. Measured values showed that the latent heat of fusion for ice at 0°C under atmospheric pressure is 333.9 kJkg^{-1} and decreases with temperature decreasing [21].

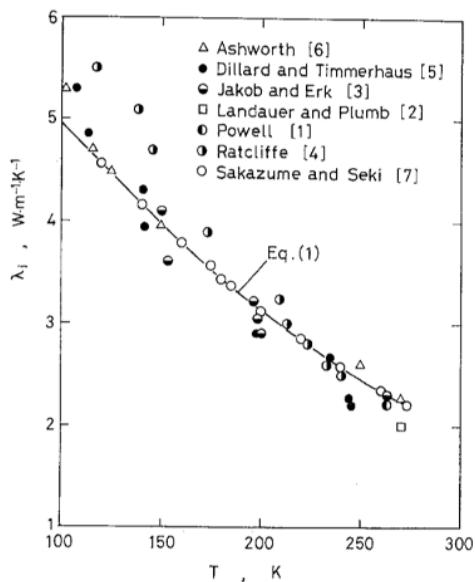


Figure 2: Thermal conductivity of pure ice in the range from -173.15°C to approx. 0°C [21].

Linear thermal expansion coefficient is a fractional change in length per one kelvin change in temperature. It increases with the temperature increase, as well as coefficient of cubic expansion of ice, Fig. 3. Yen gave an adequate

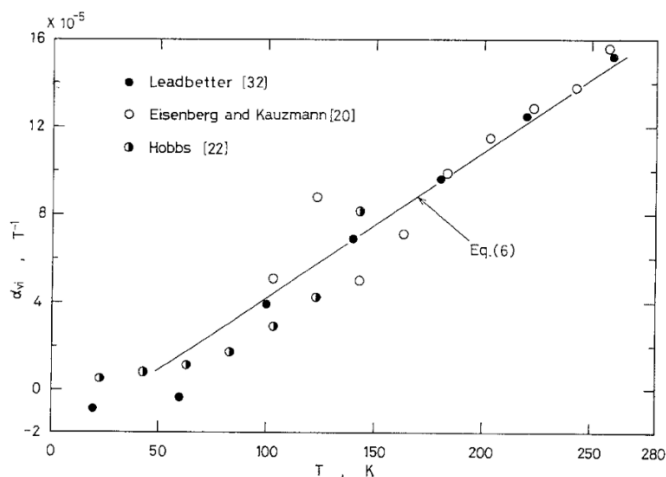


Figure 3: Cubic expansion coefficient as a function of temperature [21].

expression to calculate cubic expansion of ice [22]:

$$\alpha_{vi} = (0.67 T - 24.86) \times 10^{-6}, \quad (1)$$

where T is the temperature in K.

2.1.2 Elastic properties of pure ice

When compared to conventional building materials, ice is more of an insulator than a conductor [19]. Main elastic properties of I_h are shown in Table 2 [19]. Ice can be observed quite isotropic elastically but is meaningfully anisotropic plastically [18]. Its noteworthy mechanical properties are elasticity, viscoelasticity, viscoplasticity, creep rupture, and brittle failure [18]. Both ductile and brittle behaviour is noticeable when dealing with ice. Ice behaves ductile at low strain rates, but when the strain increases it becomes exceptionally brittle [20]. Aside from it demonstrating brittle and creep behaviour, it is also distinctly weak when compared to conventional building materials [6]. Ice strength has shown to be dependent on temperature, freezing process, presence of impurities, structure, chemical composition, load, application rate, etc. [2]. Shear and tensile strength of pure ice have almost identical values while compressive strength is nearly 3 times greater than the latter [2]. The compressive strength of the meteoritic ice demonstrates a notable decrease in temperature, from a maximum of ~ 40 MPa at -50°C to a minimum of ~ 3 MPa at 0°C . The tensile strength of the meteoritic ice is an order of magnitude lower than the compressive strength (between ~ 1 and 3 MPa) and exhibits an insignificant temperature dependence in comparison. Empirical data insinuates that ice is less rigid than many widespread materials such as glass [20]. As stated by the parameter provided by code GB 51202-2016 [23], the linear expansion coefficient of

Table 2: Elastic properties of pure ice (I_h) [19].

Property	Symbol	Unit	Value
Young's modulus	E	Nm^{-2}	9.33×10^9
Compressibility	K	m^2N^{-1}	112.4×10^{-12}
Bulk modulus	B	Nm^{-2}	8.9×10^9
Shear modulus	G	Nm^{-2}	3.52×10^9
Poisson's ratio	n	—	0.325

ice is approximately $50 \times 10^{-6}^{\circ}\text{C}$, meaning 5 times higher than that of the concrete [23].

2.2 Thermophysical properties of reinforced ice and comparison with pure ice

Reinforced ice has been examined mostly mechanically, whilst its thermal properties remain unknown. Only data available in literature are measurements made on pykrete, whose thermal conductivity and diffusivity were examined and subsequently compared to the measured values for pure ice [24]. Values of thermal conductivity were shown to vary between $1.637 \text{ Wm}^{-1}\text{K}^{-1}$ at -15°C to $1.749 \text{ Wm}^{-1}\text{K}^{-1}$ at -33°C what is calculated to be approx. 21% lower than values measured for pure ice with the same technique [24]. When it comes to thermal diffusivity, measured data ranged from $0.877 \text{ mm}^2\text{s}^{-1}$ at -15°C to $1.107 \text{ mm}^2\text{s}^{-1}$ at -33°C , showing a drop of approx. 23% when compared with values obtained for pure ice with same method [24].

When considering the overall properties of reinforced ice, more than a few advantages over plain ice can be identified. The reinforcement makes ice more deformable and can decelerate the creep rate [6]. Adding reinforcement can shorten the freezing time which is a major financial advantage when significant amounts of water need to be frozen. Compared to pure ice, reinforced ice is less affected by thermal shock [5]. Obtained experimental data shows that the use of different kinds of reinforcement can provide a significant improvement in the mechanical properties of ice. It has been investigated that the compressive strength of ice reinforced with pulp fibres can reach up to 3 times that of the plain ice [6]. Conducted research shows that introduction of fillers like basalt fibres leads to an increase in tensile strength by a factor of 2–3 [25], and an increase in bending strength by 1.5 times [2]. Even better results were obtained by Buznik *et al.* [26], who reinforced pure ice both chemically with dopants, and physically with basalt rovings and showed an increase in the strength properties of the reinforced ice specimens by 4–6 times compared to freshwater ice samples. Still, the most approved ice composite is a mixture of ice and some forms of wood pulp, such as wood chips, shavings, and sawdust, known as pykrete, Fig. 4.

Pykrete displays a low thermal conductivity which decreases ice melting rate. Its ductility has shown to be 10 times higher than of the plain ice [6]. Several authors have examined the mechanical properties of the



Figure 4: Pykrete samples [9].

pykrete, varying the type of wood pulp and the percentage used. According to Vasiliev *et al.*, the best mechanical properties were accomplished with pykrete reinforced with 10% sawdust [6]. In comparison to plain ice up to 4 times higher compressive and flexural strength was attained with the values of 12 MPa, Fig. 5, and 3.7 MPa, Fig. 6, respectively.

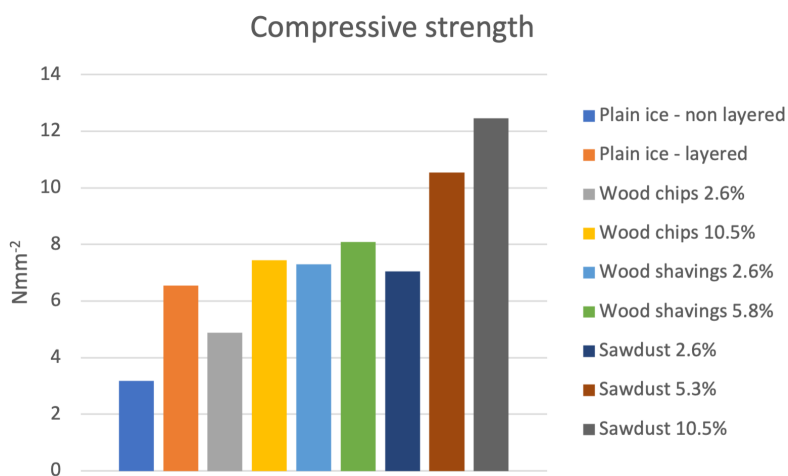


Figure 5: Compressive strength of plain ice and pykrete samples [6].

Pykrete bending tests, Fig. 7, were carried out by the group of students to check mechanical properties of specimens with different fibre percentage. The results have shown plentiful dissipation, i.e., the average compressive strength measured on specimens with 10.5% of fibres was in the range from 3.74 MPa on prisms to 12.45 MPa on cubic specimens [10]. Cryogel composites have shown to be capable of resolving issues in the freezing-thawing

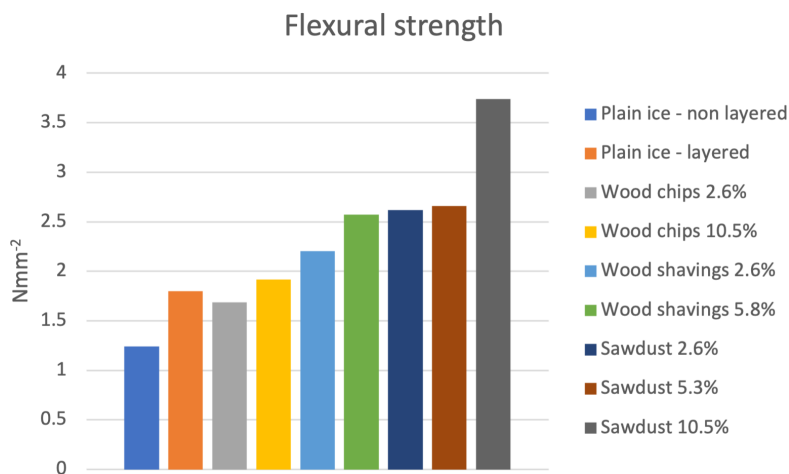


Figure 6: Flexural strength of plain ice and pykrete samples [6].

contact zones that occur in the hydraulic engineering and transport structures [6]. Prior to being used as watertight elements, cryogel solutions made with polyvinyl alcohol (PVA) were examined in the laboratory experiments as described in [16]. It was observed that subsequent freezing-thawing cycles improve the strength of cryogels.






Figure 7: Sample casting (a) and bending test (b) on pykrete specimen [10].

Also, modulus of elasticity can be increased by increasing the concentration of polyvinyl alcohol and cross-linking agent, as well as the by adding electrolyte. The properties of ice reinforced with spun fibreglass yarn were first investigated in late 20th century [3]. Shear strength tests were executed by Glockner [3] on specimens with different quantities of yarn strands. It

was observed that all specimens failed by brittle failure after 3–5 s at stress levels between 2.2 MPa and 2.7 MPa, Table 3.

Table 3: Results of sheer strength tests for ice reinforced with spun fiberglass yarn [3].

Number of strands of fiberglass yarn	Failure stress, MPa	Average failure stress, MPa	Placement of yarn in cross-section
0	2.59 2.61 2.25 2.35	2.45	
1	2.45 2.48 2.55 2.44	2.48	
4	2.70 2.29	2.49	

Therefore, the spun fibreglass did not improve the shear strength of ice when subjected to short duration loads. The author stated that it was expected as fibreglass itself has no shear strength. Short load-duration elastic tests were also carried out by varying amounts and forms of spun fibreglass yarn reinforcement. Failure of specimens happened 3–4 s after the loading started. While in plain ice the initial cracking stress was also the ultimate, it was not the case with reinforced ice, Fig. 8.

The average initial tensile cracking stress for the reinforced specimens turned out to be about 25% larger than the corresponding stress for plain ice specimens, 1.82 MPa and 2.33 MPa, respectively. That indicated that reinforcement prevents crack initiation and propagation, thereby increasing the tensile strength. In the long-term (creep) tensile strength test, both plain and reinforced ice specimens exhibited a typical creep deformation curve with failure taking place towards the end of decelerating creep stage. At the stress of 1.02 MPa unreinforced specimens crept to failure whilst reinforced specimen continued to creep at a steady rate until the load was removed. When the stress rate was reduced to 0.68 MPa plain ice specimens continued to creep without failure. Consequently, it was concluded that between 0.68 MPa and 1.02 MPa there is a critical stress level below which plain ice does not creep to failure. More details about the size, structure, and preparation of the samples can be found in the paper by Glockner [3]. Based on the results of the tests carried out by Vasiliev and Gladkov [9],

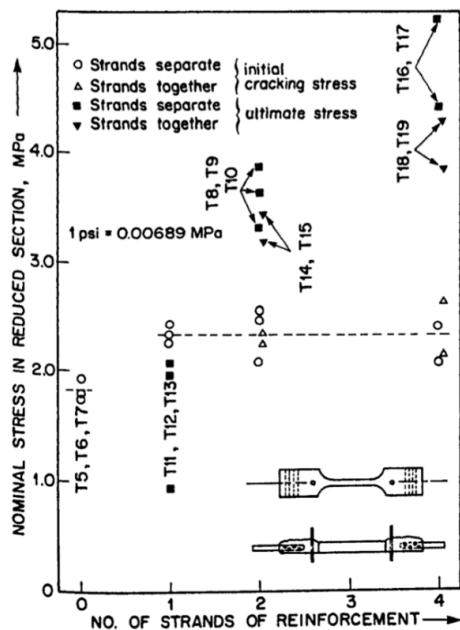


Figure 8: Tensile test results of fibreglass reinforced ice [3].

Table 4, it can be concluded that ice reinforced with fibreglass shows a significant increase both in compression and flexural strength, and a slight increase in dynamic elastic modulus. Ice with 4% fibreglass cloth has shown better properties in all categories than ice with 2% fibreglass net. All test materials have shown an increase in strength as the temperature decreased.

Table 4: Mechanical properties of reinforced ice examined by Vasiliev and Gladkov [9].

Test material*	Temperature, °C	Dynamic elastic modulus, GPa	Compression strength, MPa	Relative compression strength	Flexural strength, MPa	Relative flexural strength
Plain ice	-5	7.0	1.5	1.0	1.8	1.0
	0	8.0	2.5	1.0	2.5	1.0
Ice with 2% fibreglass net	-5	8.0	2.9	2.0	5.1	2.9
	-20	8.8	5.0	2.0	8.5	3.4
Ice with 4% fibreglass cloth	-5	8.2	3.2	2.1	5.2	3.0
	-20	9.2	6.0	2.4	10.0	4.0

*Ice specimens reinforced with fibreglass net or cloth uniformly distributed through the thickness of the ice.

By changing its temperature, differences in the mechanical properties of ice occur. At temperatures close to 0°C , ice has shown ductile and creep behaviour. The crystal structure, stress level, impurities, size of grains and temperature have an influence on creep behaviour. Creep behaviour was analysed by Kokawa [27], where in ice shell construction, linear increase of creep deflection was spotted at the beginning (stationary stage), but as time progresses the deflection rate accelerate until collapse, Fig. 9.

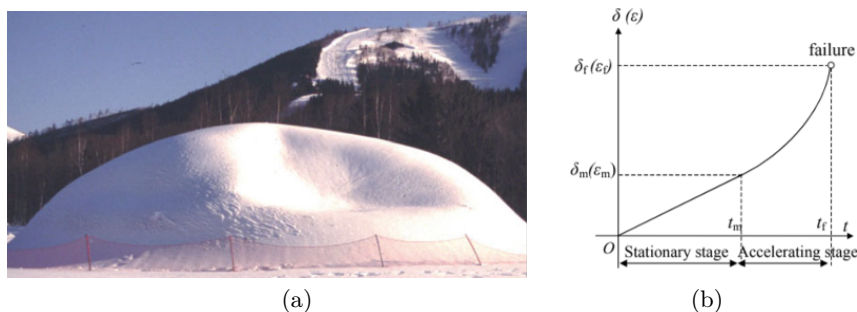


Figure 9: (a) Creep deformation just before the collapse [27]. (b) Model of creep deflection-time curve [27]: $\delta(\varepsilon)$ – creep deflection (mm/day), t – time (day), ε – uniaxial strain rate, f – complete failure, m – end of stationary stage.

Plain ice properties can be considerably improved by using suitable reinforcement. The percentage and the type of the reinforcement material directly influence the thermophysical and the mechanical properties of the composite [5]. When compared to conventional building materials, a lack of uniformity of pure ice can be noticed which leads to the inability to manage and anticipate its behaviour. By developing a systematic and formal knowledge of the ways and mechanisms of the reinforcement and the properties of reinforced ice, many ambiguities concerning ice behaviour could be diminished. Appropriate reinforcement used comprehensively in the construction of reinforced ice structures has yet to be established and/or embraced.

3 Possibilities of using reinforced ice as a building material

There are only two design codes for ice and snow structures that can be found: the first one is the Finland snow construction – general rules for design and construction [28], and the other is Chinese Technical standard

for ice and snow landscape buildings [23]. Ice reinforcement can be divided into two categories: macroscopic and microscopic reinforcement, Fig. 10.

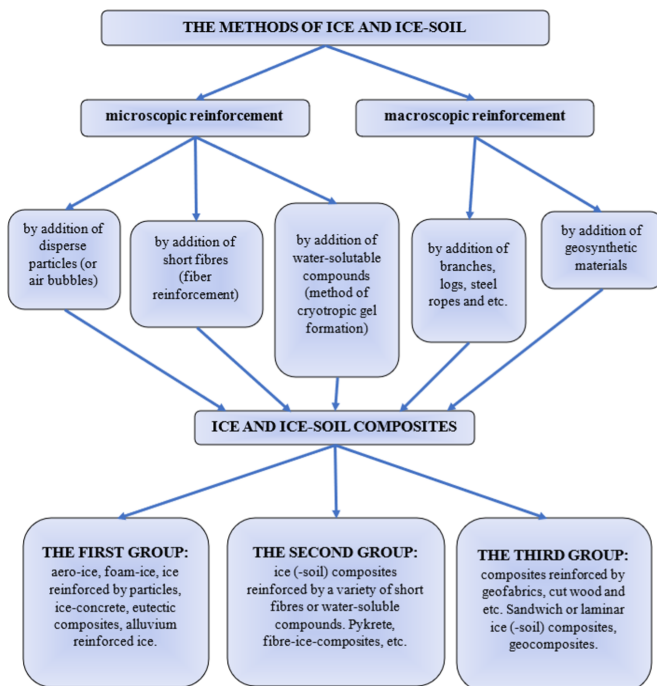


Figure 10: The methods of ice and ice-soil reinforcement [6].

Macroscopic reinforcement indicates that the size of the reinforcement particles is larger than that of the ice grains, such as rebar and trunk. Microscopic reinforcement means that the reinforcement particles size is comparable to the ice grains, such as sawdust, blast furnace slag, straw, etc. [6]. The most investigated reinforcement materials with the matching type of reinforcement are shown in Table 5. Among organic materials, sawdust and wood pulp were the most explored while glass fibre and geogrid were utilized the most among inorganic materials [6].

Several impacts that influence the performance of reinforcement can be listed: fibre-matrix stiffness, strain compatibility between the fibre and the matrix and fibre-matrix interfacial bond. It is of crucial importance to secure appropriate bonding between the matrix and reinforcement to transfer the load from one to another. It is recommended to use hydrophilic fibres rather than hydrophobic ones [6].

Table 5: Reinforcement materials and type of reinforcement [6].

Reinforcement material	Reinforcing type*	Frequency of use (1957–2015)
Glass fibre	Mi/Ma	7
Geogrid	Ma	2
Cryotropic gel	Mi	1
Steel	Ma	1
Slag	Mi	1
Asbestos fibre	Mi	1
Wood pulp (pykrete)	Mi	5
Peat mass	Mi	1
Hay	Mi/Ma	1
Straw	Mi/Ma	1
Sawdust	Mi	12
Newspaper	Mi	1
Paper dust	Mi	1
Twigs	Ma	1
Wood chips	Mi	3
Newspaper (mash)	Mi/Ma	1
Algae	Mi	1
Cotton (fibre/cloth)	Mi/Ma	2
Sand (silica, coarse)	Mi	2
Gravel	Mi	1

*Mi – micro, Ma – macro.

Igloo, Fig. 11, was the first and most famous building made of ice reinforced with lichen in polar regions of north hemisphere [6]. It was made in a traditional way by cutting bricklike elements out of snow or ice and stacking them together. Igloos are catenoid-shaped to avoid tensile stresses [9]. Thickness of igloo ice walls and details of the reinforcement could not be obtained from research publications.

During World War II, the reinforcement of ice has started to be investigated for military purposes. In Russia (former Soviet Union), ice bridges and ice roads were being strengthened with logs, branches, and twigs to enable heavy military transportation [6], while in the USA project Habakkuk took place [7]. It was a top-secret project with a goal to make an aircraft carrier out of seawater ice combined with 14% wood pulp. The material was named pykrete after its inventor Geoffrey Pyke [7]. Artificial cooling was

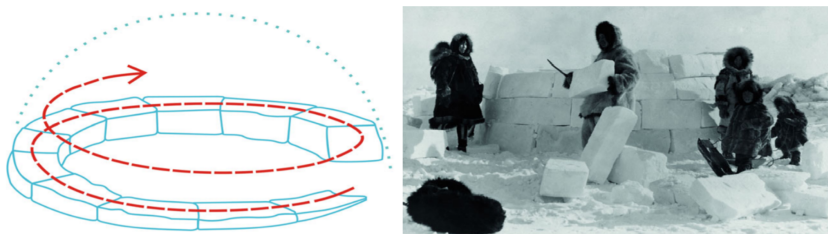


Figure 11: Construction of an igloo [9].

planned to shorten the freezing time of pykrete in the vessels. Although the project had huge support at the time, it is reported that several problems appeared and caused the work on the project to cease. First, engineers had insufficient knowledge about the physical properties of ice and therefore, were not positive whether it can perform its function safely. Also, they did not know how to build structures that can stand up to forces imposed by ice. In addition to that, as large quantities of pykrete needed to be frozen, requirements for an immense refrigeration capacity emerged. According to Gold [7], in many ways engineers have not gone forward in the understanding of ice since Habakkuk project.

In January 1961, the project Ice Way was conducted on floating sea ice on the North Star Bay, Greenland. To build an airstrip that can withstand heavy loads, three layers of parking pads were built on top of the natural ice [8]. The first pad was flooded with the sea water in 3 m thick layers, the second one had a thickness of 2 m and was reinforced with fibreglass mats at the top and the bottom and top pad was 1.5 m thick and made of ice chips, fibreglass reinforcement and saturated with sea water. Size and structure of reinforcing mats were not discussed. Successful aircraft landing, parking and take-off tests were conducted on the 4270 m long reinforced runway.

In the Glockner's paper, it was stated that reinforced ice domes represent an economical and practical solution to the problem of making temporary and semi-permanent enclosures that northern communities could use for various purposes, e.g., recreational centres, storage areas and workshops [3]. Dome structures make the best use of ice because of their much higher compressive than tensile strength. At the University of Calgary in Canada, 4 domes were created by spraying water with a compressed air-garden hose on the reusable inflatable membrane formwork. The first dome was a pilot, and the rest were made with, without or with some reinforcement. Dome number 2, Fig. 12, was fully reinforced with a network of glass fibre yarn,

a reinforcement material chosen over nylon string and wire. The exact size and shape of the reinforcing network were not provided.



Figure 12: Dome made of ice reinforced with fibreglass [3].

Difficulties encountered during the construction process were freezing of the water in the nozzle, establishing the rate and fineness of application to form a layer of ice, and sun shining onto the fabric. It was necessary to ensure continuous spraying by circling the dome at an even rate as well as allowing water enough time to freeze before applying the next layer. After completing the construction, the inflatable was pulled loose from the internal surface of the dome. To test their load-carrying capacity, domes were loaded with sandbags. The tests have shown that reinforced ice domes have larger load carrying capacity and can withstand heavy loading even during higher temperatures, Table 6. It was concluded that reinforced ice can be a useful structural material and the spraying technique was proven successful on small-scale models.

However, questions arose about the requirements for appropriate spraying equipment and the rate of application of spray as well as the placing of the reinforcement network to a large-scale model. Glockner advised using insulation if exposure to the sun is unavoidable and insulating the interior of the structure to increase its lifespan. It was suggested that additional research work needs to be done in the thermodynamic aspect of reinforced ice structures, such as heat loss, ice conductivity and the effect of air boundary layers. In addition to that, further investigation of the creep deformation and behaviour was suggested.

Research work related to ice reinforcement has stagnated for a few decades until the early two-thousands when cryogel based on ice and PVA

Table 6: Construction and testing information of the domes [3].

Dome No.	Reinforce- ment	Hours of spraying, approx.	Volume of water approx. (l)	Average erection air temp. (°C)	Load (kN)	Load duration (h)	Air temp. at failure (°C)	Average ice thickness (mm)
1	None	–	–	–	–	–	–	–
2	Full network	3	54	–21.9	1.4	72	–	–
		1	23	–19.7	2.4	190	–5.0	12
		Total:	77					
3	None	1	18	–14.2	1.7	0.2	–12.0	15
		3	59	–14.1	–	–	–	–
		Total:	77					
4	Door region only	0.5	9	–13.2	2.4	29	+6.0	8
		2	40	–16.2	–	–	–	–
		Total:	49					

was used to seal a leakage at the base of a dame at the Russian Irelyakh hydro system [16]. Cryogels are polymer gels generated due to freezing and thawing cycles of an aqueous polymer solutions. Cryogels based on a PVA, with a cross-linking agent and electrolytes as additives, are widely used and have exceptional mechanical, thermophysical and diffusional properties. It has been emphasized that PVA cryogels are easily available, simple to produce, non-toxic and biocompatible. In 2003, 51 tons of cryogel-forming solution were injected into 5 holes at the base of a dam which formed a 3 m thick barrier that covered an area of approx. 430 m². The material was found reliable, hence the technology continued to be used in the following years. In the paper mass fraction of PVA in cryogel solution was not provided. Polyvinyl alcohol powder and fibre in combination with saltwater ice was proposed and tested for cold-region constructions [29]. Results showed that PVA reinforcement improved the compressive strength of saltwater ice from 10.1 to 29.6 MPa [29]. The experiments in the field of ice road crossing rivers are of high interest for Alaska, Canada, northern Russia, and Scandinavian countries. The tests including geonets and their applications as a reinforcement of ice covers were undertaken by a group of researchers, led by Sirotyuk and Yakimenko. They tested freezing geonets from above, Fig. 13, but also from below the ice cover. As the results of the test conducted from 2014–2015 have shown, reinforcement by the geonets from above improves the bearing capacity of the ice cover up to 30%. Loading tests on the ice cover reinforced from below pointed out up to 70% higher

bearing capacity [15]. Reinforcement both from above and from below gave an excellent stabilizing effect. It has also been stated that the geonets and the geogrids can be easily removed and stored for future using what makes them environmentally acceptable solutions.

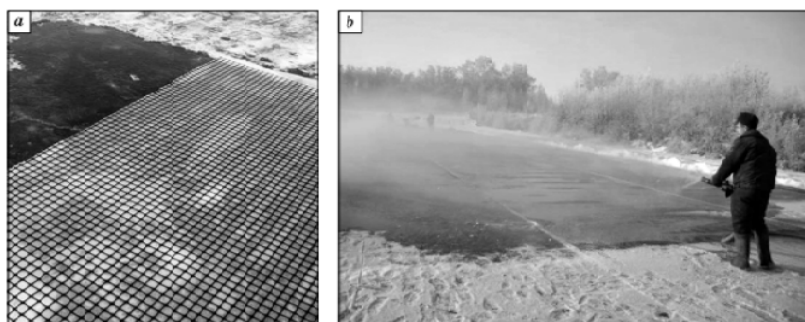


Figure 13: Reinforcement of an ice crossing from above [15].

In the winter of 2013, 30 m span Pykrete dome, Fig. 14, was built in Juuka, Finland by scientists and students from Eindhoven University of Technology [9]. The construction method was based on the research on ice shells conducted by Kokawa [27]. In the process of dome construction, instead of ice, a team led by Pronk used pykrete – a mixture of water and 10% fine sawdust. Information about the particle size of sawdust was not given. An inflatable polyethylene mould along with rope covers was fixed to the anchor points and inflated, after which a slush made from water and snow was applied to the foundation. It is not clear what spraying equipment was



Figure 14: Making of a pykrete dome [9].

used, what was the application rate and was there just one or more layers. The 150–400 mm thick dome was tested with sandbags that weighed 1850 kg and there was no deformation to measure. Afterward, pykrete samples were cut out and compared to pure ice. It was concluded that the spraying method creates ice of high quality and that the pykrete samples were stronger than the ice samples by 21%. However, pykrete samples were found nonhomogeneous with fibre reinforced ice making up only an average of 42% of the content. It was concluded that the usage of pykrete allows for even thinner shell thickness – which would lower the structure’s dead load – and that the construction of an ice shell with a 100 m span is realizable.

The research continued in 2015 with the construction of the reinforced ice replica of Gaudi’s Sagrada Familia [10], Fig. 15, and an attempt to make a replica of da Vinci’s bridge, Fig. 16 [30], also in Juuka, Finland.



Figure 15: Construction of the Sagrada Familia in reinforced ice [10].



Figure 16: Render of the da Vinci’s bridge in ice [30].

Creating of Sagrada Familia was an international project as, apart from the Eindhoven University of Technology, teams of students from Ghent University in Belgium also participated. The structure was built in the same manner as the pykrete dome, Fig. 17.

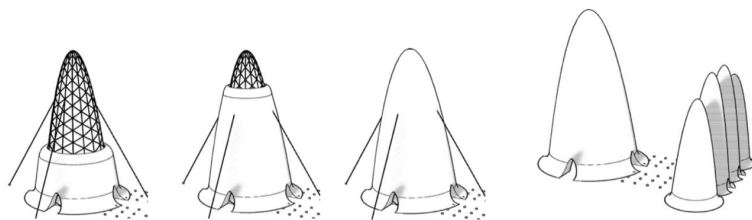


Figure 17: Schematic representation of applying pykrete around the inflated formworks [10].

Authors have stated that during the process several problems have occurred. To begin with, ice reinforced with sawdust was not homogeneous due to gravity and snow that kept falling during the construction time, so large safety factors needed to be adopted. Several delays were encountered as the outside temperature was around -5°C which is much higher than the ideal -20°C for instant freezing of pykrete. Strong wind has caused displacements of the structure and damaged the main tower which in the end was not finished completely. Finally, installations froze and there was a lack of electricity. It remained unclear how thick was the structure, as well as how much sawdust was added and what was the particle size.

Project Da Vinci's Bridge in Ice was inspired by Leonardo da Vinci's sketches of the bridge that was supposed to be built on the Bosphorus River. A mixture of water and 2% cellulose was used and sprayed on the PVC inflatable in the same building process already used in the construction of the Pykrete dome and Sagrada Familia. However, due to unexpected changes in the weather conditions, i.e., above 0°C temperatures and rain, structural capacity was jeopardized what caused an implosion of the inflatable mould and the bridge was never built [30].

Candela pavilion, Fig. 18, was another similar project inspired by Felix Candela's famous reinforced concrete hypar shells and built by staff and students from the Ghent University a part of 'Juuka in ice' manifestation [30]. A mixture of 2% cellulose and water was used to make a 0.05 m thick pavilion with a span of about 15 m. Cellulose was chosen over sawdust as it is white which is more aesthetically pleasing. Also, it is easier to make a homogenous suspension when mixed with water [11].



Figure 18: The Candela pavilion [11].

Size of the cellulose particles was not provided. It is stated that mass percentage was not determined by the strength criteria, but the mixture needed to be fluid for it to be sprayed far enough. Besides from pavilion's complex geometry, a major challenge was a very low thickness to span ratio and unfavourable weather conditions, i.e., unusually high temperatures, wind, and snow. It has been concluded that the project yielded valuable data for future reinforced ice structures.

In winter 2017–2018 two ice shell structures were created: Flamenco Ice Tower, Fig. 19, and THRICE, Fig. 20, [12]. Both were made as a part of the Harbin Ice Festival.



Figure 19: The Flamenco Ice Tower [9].

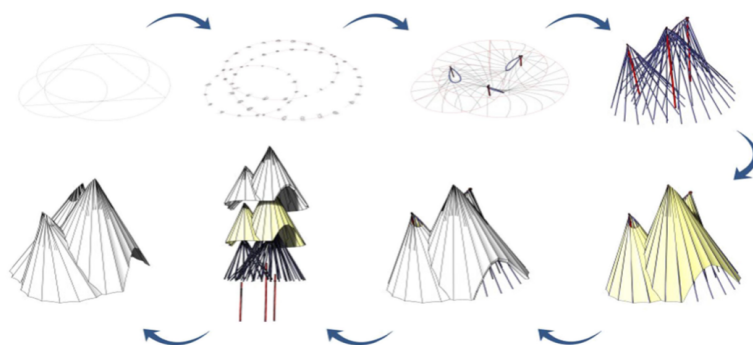


Figure 20: Assembly procedure of THRICE [12].

Flamenco Ice Tower was a joint project of students and professors from the Eindhoven University of Technology, Summa College, Harbin Institute of Technology, School of Architecture and School of Civil Engineering. It was inspired by the flamenco dress, the traditional Chinese tower, and the Harbin flower. A 30.5 m high tower with 6 surrounding shells holds the world record for the largest thin shell ice structure. The structure was made in pykrete – a mixture of 2% paper fibre (cellulose) with unknown particle size. The spraying technique was used in the same way as with the previously mentioned structures. Prior to the construction, calculations of the inflatable and of the shell structure were made, as well as finite element model in Ansys environment engineering software.

An ice pavilion THRICE, Fig. 21a, was inspired by the work of architect Heinz Isler and built by a team from the College of Architecture and Environmental Design, Kent State University in Harbin. THRICE consisted of three intersecting asymmetrical cones with an average thickness of 0.06 m and heights of 10 m, 8.5 m, and 7 m that covered an area of approx. 100 m². Aided by a computer model in Rhino, the structure was realized by spraying a mixture of water and cellulose on the membrane mould fixated with ropes, Fig. 20. Mass percentage and size of cellulose particles were not reported. It was observed that the deformations were larger than predicted which indicated a need to fully understand the connection between materials and forms used for creating the structure (ropes, oculi, and formwork) and the structure's material, thickness, and geometry.

It was emphasised that ice composite structures are still in the experimental phase with a lot of new possibilities that are yet to be discovered. However, several limitations were recognized such as the albedo effect, sub-

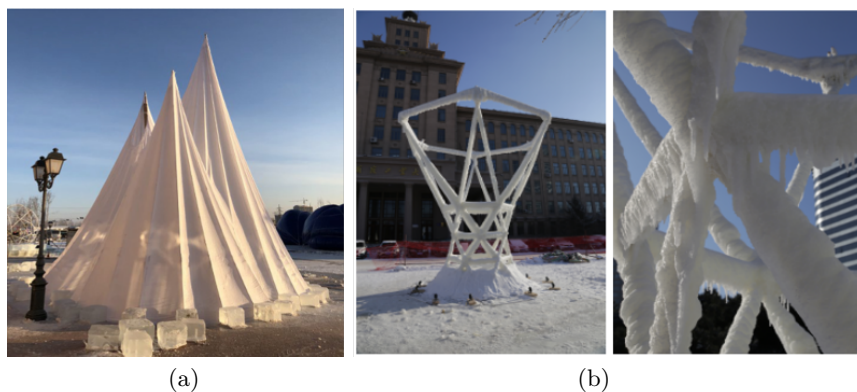


Figure 21: (a) THRICE – an ice pavilion [12]. (b) The world's first sprayed net hyperboloid ice structure [31].

limation, creep behaviour and strong temperature dependency of the structure. In conclusion, it was stated that there is a need for a building code of ice composites as there is still no technical standard for ice shells nor for reinforced ice. The world's first sprayed net hyperboloid ice structure, Fig. 21b, was built during winter of 2018 by a group of student architects and engineers of the Design Research Centre, School of Architecture and Harbin Institute of Technology. A water mixture, with 0.6% cellulose and no particle size recorded, was used to form the reinforced structure. The novelty that was introduced was the spraying of rope nets and using the rope formwork. Because of the reinforced ice properties, a formwork that enables the transformation from the completely tensile structure in construction to the completely compressive structure when released was used [31]. Previously mentioned ice structures required sophisticated formwork while hyperboloid ice structure construction was low-cost, swift, and sustainable. The observed deficiency was the waste of the cellulose-water mix while spraying [31].

The ice composite shell structure, named Koi-fish after famous ornamental fish species, realized with complexly shaped inflatable formwork was made in Harbin Ice – Snow World festival in China. The Koi-fish shell structure, Fig. 22, was built with ice reinforced with 2% white pulp-fibre material [32]. Because of the material imperfections detected, reinforced ice specimens at heights of two and four metres were collected. Density test, fibre mixing ratio test, as well as compressive and tensile strength tests, have been carried out. It has been concluded that the ice composite

density performs a normal distribution. Also, the material delamination effect on the bearing capacity, which occurs because of an unequal composite mixing while spraying, was investigated. It was shown that the material delamination has a serious material strength lowering effect [32]. Also, it was concluded the monitoring thickness was higher than the designed one and the temperature and material thickness directly affect the bearing capacity of the Koi-fish ice shell. The main surface scanning was used to compare and examine the drawbacks between the actual surface and the model. It is emphasized the spraying technique must be improved to create a satisfying quality of the reinforcement.

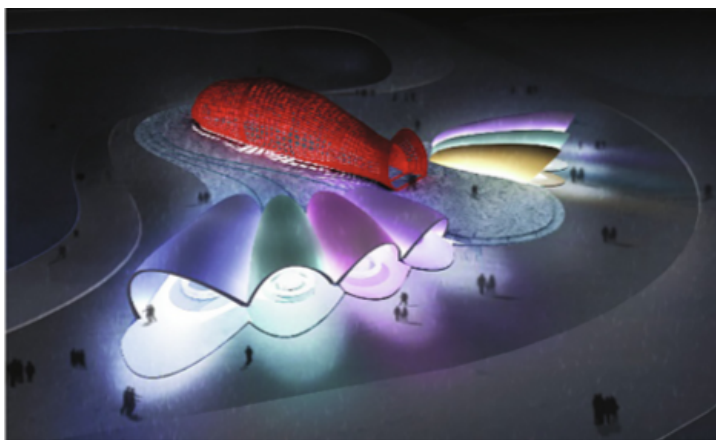


Figure 22: The Koi-fish ice shell [32].

The construction process and the design details of the ice shell restaurant, Fig. 23, were elaborated in [14]. Ice restaurant occupied 554 m^2 and could receive up to 40 people at once. Two types of inflatable mould, the airbag mould, and the air rib mould, were compared and the superiority and peculiarity of the air ribbed inflatable mould construction process, used for this structure, was discussed. The reinforcement material was 2% paper fibre because of its improved material properties compared to pure ice. Particle size was not mentioned. The structural behaviour under 10 different load conditions was analysed. As the fundamental variable for a finite analysis for the average test strength reinforced ice at -15°C was used. It was concluded that the results of the maximum tensile and the maximum compressive stress of the structure were under safety requirements. Buckling tests were not discussed.



Figure 23: Ice restaurant at the 21st Harbin Ice and Snow World [14].

Summary of reviewed papers dealing with ice structures was given in Table 7 where used reinforcement materials are synthetised, while in Table 8 construction methods and parameters are presented. It can be noted that for most ice structures construction parameters were not completely defined and nor was the size of reinforcement material.

All presented structures have been made from frozen plain or seawater, both of which are easily available in cold areas. However, if tap water is used, the cost of it should be considered as well as the cost of artificial cooling if needed. Various types of used reinforcement materials proved to be economical and environmentally friendly. Lichen has no economic value so building an igloo is cost-free. Furthermore, as lichen is a sustainable natural material, there is no waste when using it. Logs, branches, and twigs are also sustainable biodegradable materials, and their usage can be considered economical. Similar non-toxic, low-cost biodegradable materials are cellulose and pulp fibres which have been widely used in recent years. Sawdust is already a waste and therefore a low-cost material. However, it is not always available in large quantities. On the contrary, fibreglass, and PVA are much pricier than mentioned natural materials. PVA is a non-toxic and biodegradable material while fibreglass can be toxic and is not biodegradable. Given the economic and environmental aspect, most of the structures were found to be economical and environmentally acceptable.

Table 7: Reinforcement materials used for ice structures.

Reference	Time	Structure	Reinforcement			Aspect	
			material	mass fraction	particle or net size	environmental	economic
[6, 9]	ancient times	igloo	lichen	n/a	n/a	no	no cost
[6]	1941–1942	ice bridge	logs, branches, twigs	n/a	n/a	no	economical
[7]	1942–1943	aircraft carrier	wood pulp- sawdust	14%	n/a	no	economical
[6, 9]	1943	ice road	logs, branches, twigs	n/a	n/a	no	economical
[8]	1961	ice airstrip	fibreglass	n/a	n/a	yes	moderate cost
[3]	1976	ice dome	fibreglass yarn	n/a	0.87 mm	yes	moderate cost
[16]	2003–2005	watertight elements in dams	polyvinyl alcohol	n/a	-	no	expensive
[15]	2011–2015	ice roads crossing rivers	geonets from fibreglass	n.a.	4 m × 50 m, 4 m – 30 m, 2.4 m × 50 m	yes	moderate cost
[9]	2013–2014	Pykrete dome	fine sawdust	10%	n/a	no	economical
[10]	2015	Sagrada Familia in ice	fine sawdust	n/a	n/a	no	economical
[11, 27]	2015	Candela pavilion	cellulose	2%	n/a	no	economical
[27]	2015	Da Vinci's bridge	cellulose	2%	n/a	no	economical
[12]	2017–2018	Flamenco Ice Tower	cellulose	2%	n/a	no	economical
[18]	2018	hyperboloid-net ice structure	cellulose	0.6%	n/a	no	economical
[28]	2017–2019	THRICE – ice pavilion	cellulose	n/a	n/a	no	economical
[29]	2019	Koi-fish ice shell	white pulp fibre	1%	n/a	no	economical
[14]	2019	Ice restaurant	paper fibre	2%	n/a	no	economical

Table 8: Construction parameters engaged in building ice structures.

Reference	Time	Structure	Place	Construction parameters		
				construction method	wall thickness	cooling method
[6, 9]	ancient times	igloo	northern regions of Canada, USA and Russia (Eskimos, Chukchi)	brick stacking	n/a	not used
[6]	1941–1942	ice bridge	Ice railway bridge over Dnieper, Ukraine	freezing in layers	n/a	not used
[7]	1942–1943	aircraft carrier	Project Habakkuk, Canada, Great Britain	freezing in layers	n/a	artificial cooling planned
[6, 9]	1943	ice road	Ladoga Lake Life Road USSR	freezing in layers	n/a	not used
[8]	1961	ice airstrip	Arctic region, USA	freezing in layers	approx. 5.5 m	not used
[3]	1976	ice dome	Calgary, Canada	spraying water on an inflatable with reinforcement at below 0°C	n/a	not used
[16]	2003–2005	watertight elements in dams	Irel'yakh hydro system, Siberia, Russia	51 t of cryogel forming solution injected into dam holes and frozen	3 m	not used
[15]	2011–2015	ice roads crossing rivers	Arkhangelsk region, Russia	geosynthetic material froze into the ice	n/a	not used
[9]	2013–2014	Pykrete dome	Juuka, Finland	spraying suspension of water and reinforcement on an inflatable at below 0°C	0.04 m (base), 0.15 m (top)	not used
[10]	2015	Sagrada Familia in ice	Juuka, Finland	spraying suspension of water and reinforcement on an inflatable at below 0°C	n/a	not used

Table 8 [cont.]

Reference	Time	Structure	Place	Construction parameters		
				construction method	wall thickness	cooling method
[11, 27]	2015	Candela pavilion	Ghent, Belgium	spraying suspension of water and reinforcement on an inflatable at below 0°C	avg. 0.05 m	not used
[27]	2015	Da Vinci's bridge	Juuka, Finland	spraying suspension of water and reinforcement on an inflatable at below 0°C temperatures	n/a	not used
[12]	2017–2018	Flamenco Ice Tower	Harbin, China	spraying suspension of water and reinforcement on an inflatable at below 0°C	0.07 m at the top, 0.04 cm at the bottom, 1 m foundation	not used
[28]	2018	hyperboloid-net ice structure	Harbin, China	spraying mixture on the net formwork at below 0°C	n/a	not used
[19]	2017–2019	THRICE – ice pavilion	Harbin, China	spraying suspension of water and reinforcement on an inflatable at below 0°C	avg. 0.06 m	not used
[29]	2019	Koi-fish ice shell	Harbin, China	layer spraying cellulose-water mix on an inflatable formwork at below 0°C	0.05–0.15 m at the top, 0.05–0.25 m at the bottom	not used
[14]	2019	Ice restaurant	Harbin, China	spraying ice composite material on an air ribbed inflatable mold at below 0°C	0.2 m at the bottom, 0.1 m at the top	not used

4 Conclusions and future directions in field

This paper focuses on the examination of existing research studies related to reinforced ice and reinforced ice structures. Ice structures covered so far in research findings were presented with an emphasis on construction and reinforcement parameters. It was found that ice is very suitable for usage in various fields of engineering applications, but there is still insufficient knowledge of its behaviour when used as a building material. Its properties vary and are not entirely suitable for building purposes. However, thermophysical properties of ice can be significantly improved by reinforcement. Presented data shows that, with introduction of sawdust, thermal conductivity and diffusivity of pure ice can be decreased by 21% and 23%, respectively. Different kinds of reinforced ice may have up to 4–6 times higher compressive, tensile, and flexural strength than plain ice as well as lower creep rates and an improvement of brittle behaviour. For instance, ice reinforced with wood pulp (pykrete) was found to have up to 2 times higher tensile strength than concrete. Possibilities of reinforcement are numerous and there is a wide range of choices with respect to application, availability, and cost-effectiveness. Cellulose derivatives have demonstrated the best physical properties with being environmentally friendly and economically viable. However, in the analysed studies several issues were observed. In most of the studies construction parameters – construction method and wall thickness – were not defined accurately and nor was the size of reinforcement particles or nets. There is a necessity to define a procedure of preparation of ice composites for practical purposes. It is crucial to know the effects that reinforcement type, size, quantity (mass or volume fraction percentage), positioning, and distribution have on the final product. Furthermore, the freezing process and ways that ensure reinforcement material stays in the desired position during the process should be defined. Overall, it can be concluded that there is a necessity for more comprehensive, clear, and accurate data regarding reinforced ice construction methods and processes, as well as regarding the preparation of ice composites in general.

Acknowledgments

This research has been supported by the European Regional Development Fund, project Centre of Competence (CEKOM) under the grant KK.01.2.2.03.0022.

References

- [1] Huang L., Krigsvoll G., Johansen F., Liu Y., Zhang X.: *Carbon emission of global construction sector*. *Renew. Sust. Energ. Rev.* **81**(2017), P2, 1906–1916. doi: [10.1016/j.rser.2017.06.001](https://doi.org/10.1016/j.rser.2017.06.001)
- [2] Grinevich D.V., Nuzhnyi G.A., Buznik V.M., Yakovlev N.O., Goncharova G.Yu., Razomasov N.D.: *Destruction of reinforced ice composition materials upon bending mechanical loading*. *Inorg. Mater. Appl. Res.* **11**(2020), 941–946.
- [3] Glockner P.G.: *Reinforced ice and ice domes: opportunities for the North*. *Int. J. Space Struct.* **3**(1988), 2, 84–102. doi: [10.1177/026635118800300203](https://doi.org/10.1177/026635118800300203)
- [4] Liu Z., Yu T., Yan N., Gu L.: *The influence of thermophysical properties of frozen soil on the temperature of the cast-in-place concrete pile in a negative temperature environment*. *Arch. Thermodyn.* **44**(2023), 2, 21–48. doi: [10.24425/ather.2023.146557](https://doi.org/10.24425/ather.2023.146557)
- [5] Makkonen L.: *Ice and Construction, State of the Art Report prepared by RILEM Technical Committee TC-118, Ice and Construction*. Chapman & Hall, Cambridge 2005.
- [6] Vasiliev N.K., Pronk A.D.C., Shatalina I.N., Janssen F.H.M.E., Houben R.W.G.: *A review on the development of reinforced ice for use as a building material in cold regions*. *Cold Reg. Sci. Technol.* **115**(2015), 56–63. doi: [10.1016/j.coldregions.2015.03.006](https://doi.org/10.1016/j.coldregions.2015.03.006)
- [7] Gold L.W.: *Building ships from ice, Habbakuk and after*. *Interdiscip. Sci. Rev.* **29**(2004), 4, 373–384. doi: [10.1179/03080180422501878](https://doi.org/10.1179/03080180422501878)
- [8] DeGoes L., Neal J.T.: *Selected military geology programs in the Arctic, 1950–1970*. *Rev. Eng. Geol.* **XIII**(1998), 205–210.
- [9] Pronk A.: *All the possibilities researched for ice, Flexible Forming for Fluid Architecture* (1st Edn.). Springer Cham, 2021. doi: [10.1007/978-3-030-71551-9](https://doi.org/10.1007/978-3-030-71551-9)
- [10] Belis J., Pronk A., Martens K., Van Lancker B., Dispersyn J.: *Experimental construction of a temporary church in reinforced ice*. *Adv. Struct. Eng.* (2015), Abstracts, 34–34.
- [11] Belis J., Ronsse B., Martens K., Van Lancker B., Cruz P.J.S., Deruyter G.: *Reinforced ice structures: In the footsteps of Candela, Structures and Architecture* (1st Edn). CRC, London 2016.
- [12] Pronk A., Mistur M., Li Q., Liu X., Blok R., Liu R., Wu Y., Luo P., Dong Y.: *The 2017–18 design and construction of ice composite structures in Harbin*. *Structure.* **18**(2019), 117–127. doi: [10.1016/j.istruc.2019.01.020](https://doi.org/10.1016/j.istruc.2019.01.020)
- [13] Wu Y., Liu X., Chen B., Li Q., Luo P., Pronk A.: *Design, construction and monitoring of an ice composite shell structure*. *Autom. Constr.* **106**(2019), 102862. doi: [10.1016/j.autcon.2019.102862](https://doi.org/10.1016/j.autcon.2019.102862)
- [14] Luo P., Yang S., Nie Y., Wu Y., Chen J., Pronk A., Zhang R.: *Collaborative design between architecture and structure of large complex ice shell based on air-ribbed inflatable mold: A case of ice restaurant*. *Int. J. Space Struct.* **36**(2021), 1, 37–47. doi: [10.1177/09560599211000961](https://doi.org/10.1177/09560599211000961)
- [15] Sirotyuk V.V., Yakimenko O.V., Levashov G.M., Zakharenko A.A.: *Reinforcement of ice cover with geosynthetic materials*. *Kriosfera Zemli* **XX**(2016), 3, 79–86.

- [16] Altunina L.K., Kuvshinov V.A., Dolgikh S.N.: *Cryogels – a promising material for underground works in permafrost, Advances in the Geological Storage of Carbon Dioxide*. Nato Sci. S. IV: Ear. En. **65**(2006), 103–110. doi: [10.1007/1-4020-4471-2_10](https://doi.org/10.1007/1-4020-4471-2_10)
- [17] Scopus.com, <https://www.scopus.com> (accessed 25March 2023).
- [18] Schulson E.M., Duval P.: *Creep and fraction of ice*. Cambridge University Press, Cambridge 2009. doi: [10.1017/CBO9780511581397](https://doi.org/10.1017/CBO9780511581397)
- [19] Akyurt M., Habeebullah B., Zaki G.: *Freezing phenomena in ice-water systems*. Energy Convers. Manag. **43**(2002), 1773–1789. doi: [10.1016/S0196-8904\(01\)00129-7](https://doi.org/10.1016/S0196-8904(01)00129-7)
- [20] Arenson L.U., Colgan W., Marshall H.P.: *Physical, thermal, and mechanical properties of snow, ice and permafrost, Snow and Ice-Related Hazards, Risks and Disasters* (1st Edn.). Academic Press, 2014. doi: [10.1016/B978-0-12-394849-6.00002-0](https://doi.org/10.1016/B978-0-12-394849-6.00002-0)
- [21] Fukusako S.: *Thermophysical properties of ice, snow, and sea ice*. Int. J. Thermophys. **11**(1990), 2, 353–372. doi: [10.1007/BF01133567](https://doi.org/10.1007/BF01133567)
- [22] Yen Y.: *Review of thermal properties of snow, ice, and sea ice*. CRREL Techn. Rep., 1981.
- [23] GB 51202-2016: *Technical standard for ice and snow landscape buildings*. China Architecture & Building Press, 2016.
- [24] Bošnjak J., Bodrožić Čoko N., Jurčević M., Primorac I., Nizetić S.: *Investigation of thermal properties of pykrete*. IOP Conf. (EES) **1196**(2023), 1. doi: [10.1088/1755-1315/1196/1/012055](https://doi.org/10.1088/1755-1315/1196/1/012055)
- [25] Syromyatnikova A.S., Bol'shakov A.M., Kychkin A.K., Alekseeva A.V.: *Reinforcement of composites based on fresh ice with natural fillers*. Inorg. Mater. Appl. Res. **11**(2020), 4, 955–957. doi: [10.1134/S2075113320040371](https://doi.org/10.1134/S2075113320040371)
- [26] Buznik V.M., Goncharova G. Yu., Grinevich D.V., Nuzhny G.A., Razomasov N.D., Turalin D.O.: *Strengthening of ice with basalt materials*. Cold Reg. Sci. Technol. **196**(2022), 103490. doi: [10.1016/j.coldregions.2022.103490](https://doi.org/10.1016/j.coldregions.2022.103490)
- [27] Kokawa T.: *Ice shell construction in Hokkaido of Japan during 1980–2012*. Int. J. Space Struct. **36**(2021), 1, 26–36. doi: [10.1177/0956059920981867](https://doi.org/10.1177/0956059920981867)
- [28] Association of Finnish Civil Engineers: *RIL 218-2002: Snow constructions-general rules for design and construction*. <https://www.ril.fi/kirjakauppa/ohjeet-ja-normit/ril-218-2002-snow-constructions-general-rules-for-design-and-construction-p-43.html> (accessed 30 Oct. 2022).
- [29] Xie J., Yan M.-L., Yan J.-B.: *Experimental study on PVA reinforced salt-water ice under uniaxial-compression at arctic low temperatures*. Cold Reg. Sci. Technol. **206**(2023), 103751. doi: [10.1016/j.coldregions.2022.103751](https://doi.org/10.1016/j.coldregions.2022.103751)
- [30] Pronk A., Vasiliev N., Belis J.: *Historical development of structural ice, Structures and Architecture* (1st Edn.). CRC, London 2016.
- [31] Millar C., Orr J., Li Q., Yeung A., Chan A., Sheasby M., Gimenez Fernandez M., Baxter Chinery M., Qu M., Wai S.: *The world's first sprayed net hyperboloid ice structure*. In: Proc. IASS Annual Symp. 2019 – Structural Membranes, 2019.
- [32] Wu Y., Liu X., Luo P., Zhang R.: *Structural analysis and construction quality assessment of free-form ice composite shell*. Structures. **27**(2020), 868–878. doi: [10.1016/j.istruc.2020.06.032](https://doi.org/10.1016/j.istruc.2020.06.032)

Modular heat storage in waste heat recovery installations

PIOTR GÓRSZCZAK^a
MARCIN RYWOTYCKI^{a*}
MARCIN HOJNY^a
GRZEGORZ FILO^b

^a AGH University of Krakow, Mickiewicza 30, 30-059 Kraków, Poland

^b Cracow University of Technology, Jana Pawła II 37, 31-864 Kraków, Poland

Abstract The paper presents the methodology of designing a system for accumulating waste heat from industrial processes. The research aimed to analyse the fluid's movement in the heat accumulator to unify the temperature field in the volume of water constituting the heat buffer. Using the computer program Ansys Fluent, a series of computational fluid dynamics simulations of the process of charging the heat storage with water at 60°C, 70°C, and 80°C was carried out. The selected temperatures correspond to the temperature range of unmanaged waste heat. In the presented solution, heat storage is loaded with water from the cooling systems of industrial equipment to store excess heat and use it at a later time. The results of numerical calculations were used to analyse the velocity and temperature fields in the selected structure of the modular heat storage. A novelty in the presented solution is the use of smaller modular heat storage units that allow any configuration of the heat storage system. This solution makes it possible to create heat storage with the required heat capacity.

Keywords: Heat storage; Heat recovery; Waste heat, CFD

Nomenclature

$C_{1\epsilon}, C_{2\epsilon}, C_\mu$	–	turbulence model constants
c	–	specific heat, $\text{J kg}^{-1}\text{K}^{-1}$
G_k	–	generating kinetic energy of turbulence

*Corresponding Author. Email: rywotyc@agh.edu.pl

k	–	kinetic energy of turbulence
p	–	pressure, Pa
S	–	modulus of the average strain rate tensor
S_{ij}	–	strain rate tensor
T	–	temperature, K
t	–	time, s
u_i, u_j, u_l	–	velocity components, m s^{-1}
x_i, x_j, x_l	–	Cartesian coordinates, m

Greek symbols

δ_{ij}	–	Kronecker delta
ϵ	–	dissipation coefficient
λ	–	heat conductivity, $\text{W m}^{-1}\text{K}^{-1}$
μ	–	dynamic viscosity coefficient, $\text{kg m}^{-1}\text{s}^{-1}$
μ_t	–	turbulent viscosity, m^2s^{-1}
ρ	–	density, kg m^{-3}
σ_k	–	turbulent Prandtl number for k
σ_ϵ	–	turbulent Prandtl number for ϵ

1 Introduction

Thermal energy is a by-product of every energy generation and industrial process. The growing crisis and rising environmental problems force the development of heat recovery systems to mitigate the current situation [1]. Waste heat recovery is one of the most promising ways to improve the energy efficiency of many technological processes and energy devices [2]. All kinds of construction industries are among the most energy-intensive areas. This sector accounts for almost a third of the world's total energy consumption. Domestic hot water, space heating and cooling currently account for about 50% of energy consumption in the construction sector [3]. Thanks to waste heat recovery systems, it will be possible to reduce CO₂ emissions, and fossil fuel consumption [4]. Nowadays, all countries around the World are in a period of energy transformation. Distributed energy, complementary to fossil and renewable energy, is currently a research hotspot. However, the variability and discontinuity of renewable energy require the use of energy storage facilities that will provide energy in the event of insufficient production from renewable energy sources (RES) [5]. Numerous industrial processes generate a significant amount of low-temperature waste heat, a potential source for building heating systems and industries such as drying, pasteurization, water heating and distillation in the paper, food, tobacco, wood, etc., chemical and machinery sectors. A low-temperature heat

source could be sufficient to heat buildings; however, high-temperature water, steam or air is required in the abovementioned industrial branches. This temperature can be achieved by using electric heating or traditional fossil fuel boilers. This is associated with low energy efficiency and high emission of pollutants into the atmosphere. To improve energy efficiency, traditional boilers can be replaced by heat pumps, a more efficient method of high-temperature heating. When generating energy in a heat pump, no production of pollutants could get into the atmosphere [6]. However, waste heat production does not always correlate with actual heat demand. This makes it necessary to accumulate this heat and use it at a later time. Therefore, one of the most urgent issues in the power industry is collecting and storing the generated thermal energy using heat accumulators. Such devices can be used as thermal power reserves during night hours or system failures [7]. In addition, thermal energy can be converted into electrical energy for production in the thermomechanical cycle when there is a demand for it [8]. The modular heat storage is usually a few hundred litres, well-insulated accumulator tank that allows heat to be stored in the form of, for example, hot water. The heat source can be water from industrial equipment's cooling systems. Due to the risk of evaporation, heat storage with water is mainly used at temperatures below 90°C [9,10]. The dynamic and static modes can be distinguished during the water tank operation. The dynamic mode of operation refers to the process of loading and unloading the water tank. The static operating mode refers to the thermal behaviour of the heat storage when water is accumulated [11]. If necessary, the accumulated heat can be transferred at a given time and in a certain amount to various receivers in the building, such as radiators, floor heating or domestic hot water (DHW) storage heaters [12]. Unused heat should be managed for its subsequent use in low-temperature processes and heating buildings. A diagram of such an installation is shown in Fig. 1.

In such an example installation, the heating fluid operates in a closed circuit. The heated fluid flows from the waste heat source to a 4-way valve with a thermometer and, depending on the temperature, is either transferred directly to the heat consumer or heats the water in the tank thermal energy storage (TTES) for later use. An expansion vessel is used in the system and in the TTES itself to collect the excess fluid created by temperature expansion. Sensors are used throughout the system to measure the temperature of the medium.

In the literature, the static mode of operation is also called the cooling process because, due to heat loss to the environment, a natural water cool-

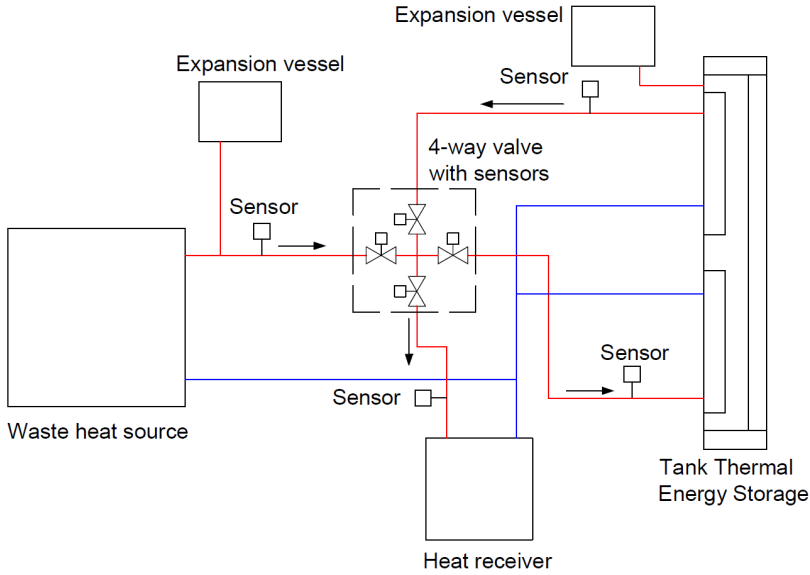


Figure 1: Scheme of waste heat storage installation.

ing process occurs [11,13]. Heat exchange between the fluid in the tank and the environment results in the creation of boundary layers of temperature and water velocity along the side wall of the tank. As a consequence of this phenomenon, thermal stratification is formed in the reservoir. This stratification significantly affects the capacity of the accumulated thermal energy and even the efficiency of the entire system [11,14]. Heat storage, also called accumulation, is present in heat accumulators, i.e., thermal energy storage (TES). Depending on the temperature of the storage medium, heat accumulation can be divided into low-temperature, whose temperature does not exceed 120°C , medium-temperature, ranging from 120°C to 500°C [15] and high-temperature, whose temperature exceeds 500°C . In thermal energy storage, heat can be accumulated using specific heat, phase-change material (PCM), and heat of chemical transformations [16,17]. Due to their construction, heat accumulators can be divided into two main groups. The first one includes underground thermal energy storage (UTES), i.e., underground heat reservoirs that use soil, water or gravel as a storage medium. The second form of storage is a water reservoir, i.e., tank thermal energy storage (TTES) [16]. In general, the energy storage density of overt heat storage materials is relatively low (in the range of approximately 10 to 50 kWh m^{-3} [9,18]), requiring more materials and larger tanks [9,19].

Heat storage with very large capacities are used in power plants [20]. This arrangement feeding the district heating system. Such solutions are applicable to areas with access to the district heating system [21].

A novelty in the presented solution is the use of smaller modular heat storage units that permit any configuration of the heat storage system and the use of thicker insulation than in standard tanks, which results in lower heat losses to the environment. The proposed solution makes it possible to create heat storage with the required heat capacity. Particularly, this work provides an analysis of heat storage accumulating heat in an overt form up to 80°C. A series of computational fluid dynamics (CFD) simulations of the TTES charging process with water at 60°C, 70°C, and 80°C were carried out. The research demonstrates the influence of the temperature and the tank's structure on the movement of the water velocity field in the tank and heat loss as a result of heat conduction through its walls. In the literature, one can find various uses of thermal energy storage with phase change substance, which accumulate waste heat and heat from solar energy [22, 23]. Phase change materials have a high heat capacity but only in a narrow temperature range, while water works better in a broader scope. Phase change material (PCM) is also much more expensive than commonly available water. Due to the low interest in the area of modular TTES loaded with water from waste heat recovery installations and the matter of extending the ranges of applied temperatures, the presented publication fills this gap.

2 Methodology: computational fluid dynamics method

Effective modelling of the charging process of modular heat storage requires the use of mathematical models that allow the determination of the temperature field and the velocity field resulting from water heating in the tank. The heated water temperature field results from two heat transport mechanisms, convection and conduction. The conduction equation with a convection term, also known as the Fourier-Kirchhoff equation, can describe their mutual overlap. The general form of this equation is [24, 25]

$$\frac{\partial T}{\partial t} + u_i \frac{\partial T}{\partial x_i} + u_j \frac{\partial T}{\partial x_j} + u_l \frac{\partial T}{\partial x_l} = \frac{\lambda}{c\rho} \left(\frac{\partial^2 T}{\partial x_i^2} + \frac{\partial^2 T}{\partial x_j^2} + \frac{\partial^2 T}{\partial x_l^2} \right). \quad (1)$$

The Navier-Stokes equation coupled with continuity equation, describes the heated water velocity field. The general form of this equation, describing the movement of a viscous fluid, is as follows [26]:

$$\frac{\partial}{\partial t}(\rho u_i) + \frac{\partial}{\partial x_j}(\rho u_i u_j) = \rho g_i - \frac{\partial p}{\partial x_i} + \frac{\partial}{\partial x_j} \left[\mu \left(\frac{\partial u_i}{\partial x_j} + \frac{\partial u_j}{\partial x_i} - \frac{2}{3} \delta_{ij} \frac{\partial u_l}{\partial x_l} \right) \right], \quad (2)$$

$$\frac{\partial \rho}{\partial t} + \frac{\partial}{\partial x_i}(\rho u_i) = 0. \quad (3)$$

Turbulent flow is a three-dimensional, non-constant, random motion observed in fluids at moderate to high Reynolds numbers above 3600 [26]. Since technical flows are usually based on low-viscosity fluids, almost all are turbulent. Many technically essential quantities, such as the mixing of momentum, energy, and substance kinds, heat transfer, pressure losses and efficiency, depend on turbulence. Turbulent flows are unsteady, and their accurate simulation requires high computing power. For this reason, averaging methods must be applied to the Navier-Stokes equations to filter out all, or at least, parts of the turbulence spectrum. The most widely used solution is trying to solve the time-averaged equations of motion for fluid flow – the Reynolds-averaged Navier-Stokes (RANS) equations. This process eliminates all turbulent structures from the flow, and a smooth change of the averaged velocity and pressure fields can be obtained. However, the averaging process introduces additional unknowns into the transport equations that need to be related to the averages somehow, which is why the so-called turbulence modelling occurs at this stage [27, 28]. The quality of the simulation may depend on the turbulence model selected. It is essential to choose a suitable model and provide the appropriate numerical mesh for the selected model. An alternative to RANS constitutes the scale-resolving simulation (SRS) model. In SRS methods, at least part of the turbulence spectrum is resolved in at least part of the flow domain. The best-known method is large eddy simulation (LES); however, many new hybrids (models between RANS and LES) are emerging. Since all SRS methods require timed simulations where the time step is relatively small, it is crucial to understand that these methods are computationally much more demanding than RANS simulations. The RANS models include the Spalart-Allmaras model, k - ϵ , k - ω , and Reynold's stress. The k - ϵ model belongs to the family of time-averaged Navier-Stokes (RANS) turbulence models in which all turbulence effects are modelled. It is a model based on two equations [29]. This

means that in addition to conservation equations, it also solves two transport equations, such as convection and diffusion of turbulent energy [30]. The standard k - ϵ model is a semi-empirical model based on default transport equations for turbulence kinetic energy, k , and its dissipation coefficient, ϵ . Both variables contribute to the turbulent viscosity, μ_t . It is designed to model the apparent increase in viscosity associated with the existence of additional fluctuations. In this case, the transport equations may be written as follows:

$$\frac{\partial u_i}{\partial t} + u_j \frac{\partial u_i}{\partial x_j} = \rho g_i - \frac{1}{\rho} \frac{\partial p}{\partial x_i} - \frac{1}{\rho} \frac{\partial}{\partial x_j} \left[(\mu + \mu_t) \left(\frac{\partial u_i}{\partial x_j} + \frac{\partial u_j}{\partial x_i} \right) \right], \quad (4)$$

$$\frac{\partial u_j}{\partial x_j} = 0, \quad (5)$$

$$\frac{\partial(\rho k)}{\partial t} + \frac{\partial(\rho k u_j)}{\partial x_j} = \frac{\partial}{\partial x_j} \left[\left(\mu + \frac{\mu_t}{\sigma_k} \right) \frac{\partial k}{\partial x_j} \right] + G_k - \rho \epsilon, \quad (6)$$

$$\frac{\partial(\rho \epsilon)}{\partial t} + \frac{\partial(\rho \epsilon u_j)}{\partial x_j} = \frac{\partial}{\partial x_j} \left[\left(\mu + \frac{\mu_t}{\sigma_\epsilon} \right) \frac{\partial \epsilon}{\partial x_j} \right] + C_{1\epsilon} G_k \frac{\epsilon}{k} - C_{2\epsilon} \rho \frac{\epsilon^2}{k}. \quad (7)$$

The transport equations for k and ϵ include additional quantities such as:

$$\mu_t = \rho C_\mu \frac{k^2}{\epsilon}, \quad G_k = \mu_t S^2, \quad S = \sqrt{2S_{ij}S_{ij}}, \quad S_{ij} = \frac{1}{2} \left(\frac{\partial u_i}{\partial x_j} + \frac{\partial u_j}{\partial x_i} \right).$$

The model also requires several constants. In the carried out research, by the general Ansys/Fluent recommendations [31], they amounted to:

$$C_\mu = 0.09, \quad C_{1\epsilon} = 1.44, \quad C_{2\epsilon} = 1.92, \quad \sigma_k = 1.0, \quad \sigma_\epsilon = 1.3.$$

Equations (4) and (5) are valid only for incompressible flows. The tested working medium is water, which is treated as an incompressible fluid. For this reason, the over mentioned equations are appropriate. The formulated equations are solvable for averaged values over a suitable time period. It is assumed that the averaged values may still vary over time to some extent [28]. In the derivation of the k - ϵ model, it was assumed that the flow is turbulent since the standard k - ϵ model is valid for fully turbulent flows [27]. Finally, based on the Ansys Fluent documentation [27,31], among many different mathematical models, the k - ϵ turbulence model was used mainly due to optimal calculation time and high stability.

3 Case study: numerical model

Calculations of the heat capacity of a single tank were carried out for different charging temperatures. It was assumed to build compact heat storage with internal dimensions of $2.0\text{ m} \times 0.5\text{ m} \times 0.5\text{ m}$, which was filled with water. The actual volume of stored medium is therefore 0.472 m^3 . This is the volume calculated with Ansys DesignModeler on the basis of the geometry after subtracting the heating and heat-receiving plates, which is filled with water. The initial temperature of the water in the tank was assumed to be 12°C , and the final temperatures amounted to 60°C , 70°C , and 80°C , respectively. The accumulator heat capacity was determined based on the energy balance. The specific heat of the water and the temperature difference were used to calculate the heat capacity. The calculated heat capacity at different charging temperatures converted to kWh is presented in Table 1.

Table 1: Summary of thermal capacity for different charging temperatures.

Charging temperature ($^\circ\text{C}$)	Heat capacity (kWh)
60	26.27
70	31.78
80	37.32

The tank geometry (Fig. 2) was created in DesignModeler, which is part of the Ansys package 2022 R2 [32]. The buffer consists of a steel sheet tank which thickness is 0.005 m , polystyrene insulation which thickness is 0.1 m ,

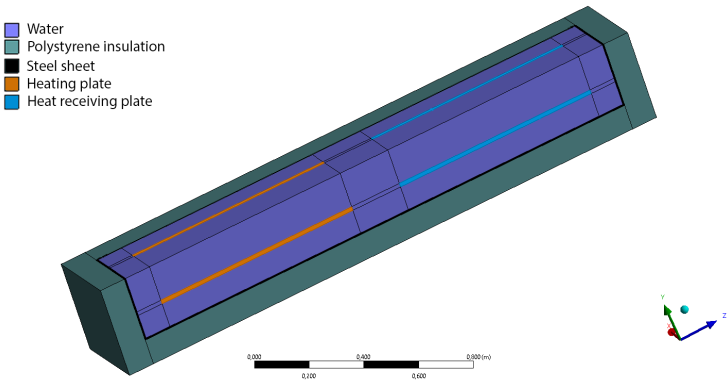


Figure 2: Tank geometry created in DesignModeler.

a copper heating plate, and a heat receiving plate which length is 0.8 m, while the width is 0.015 m. To speed up numerical calculations, symmetry was used when creating the geometry, which reduced the number of mesh elements. The external dimensions of the tank, after taking into account symmetry, are 2.21 m in height and 0.355 m in width.

Two types of model meshing methods were proposed: automatic and MultiZone. The automatic method is the default mesh generation method in Ansys Meshing. This method attempts to sweep the mesh for solid (3D) models and generate quadrilateral elements for surface solid (2D) models. Sweep mesh generates a mesh on one surface (the source surface) of the body and literally ‘sweeps’ along the body to another surface (the target surface). The mesh pattern is identical along the entire length of the body. The MultiZone mesh method automatically decomposes geometry into mapped regions (structured/stretched) and free regions (unstructured). Where possible, it automatically generates a clean cubic mesh, then fills the harder-to-grasp areas with an unstructured mesh [27,32].

Two methods, automatic and MultiZone, were used when creating the mesh on the tank model. The automatically created mesh used in the calculation is shown in Fig. 3 and has 1 523 617 elements. This method is characterized by the fact that the program selects the optimal geometry structure itself. The minimum orthogonal quality of this mesh is 0.1, and the maximum quality is 0.99. The average mesh quality is 0.77. The average skewness of the elements is 0.23. The size of mesh elements is 0.04 m. Local refinement was used in the areas where water meets solid surfaces.

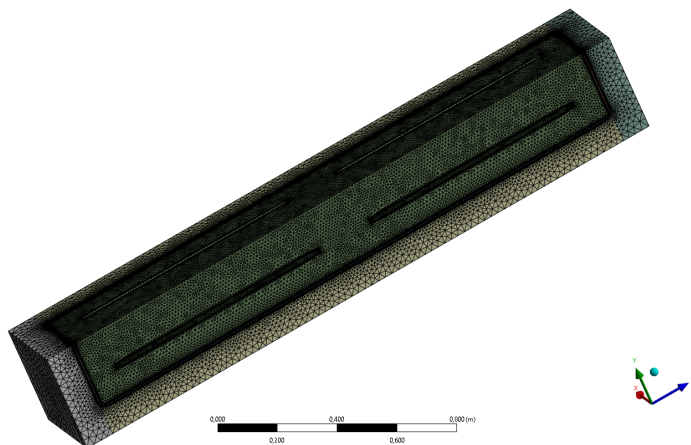


Figure 3: Tank mesh created in Ansys Meshing using automatic algorithm.

For comparison, the mesh created with the help of the MultiZone method is shown in Fig. 4 and has 665 724 elements. The minimum mesh quality is 0.58, and the maximum mesh quality is 1.00, with an average value of 0.99. The average skewness of the elements is 0.03, and the size of mesh elements is 0.008 m. The MultiZone method was used to create a mesh of the fluid body in order to obtain a hexagonal shape. Local mesh refinement was applied in the areas where water meets surfaces.

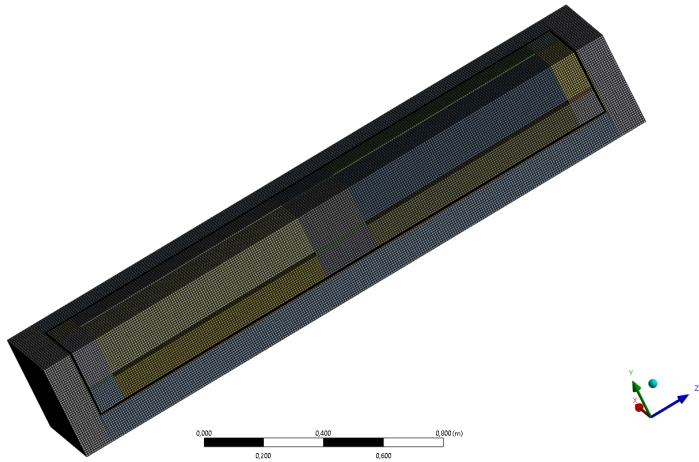


Figure 4: Tank mesh created in Ansys Meshing with the MultiZone method.

The most commonly used indicators characterizing a given mesh are skewness and orthogonal quality. Ansys recommends the minimum orthogonal quality to be higher than 0.1 and the maximum skewness less than 0.95. These values are acceptable, but the higher the minimum orthogonal quality and the lower the maximum skewness, the more reliable results can be obtained from subsequent CFD simulations [33]. Comparing the above two meshes (Figs. 3 and 4) and recommendations, it can be seen that thanks to the use of the MultiZone method, the quality is excellent. In the case of the automatic method, it is also acceptable, but its parameters are noticeably worse. In Ansys Fluent, appropriate physical properties were assigned to individual materials presented in Table 2. An initial boundary condition was assigned to each wall of the tank. For external walls (insulation) temperature of 15°C and a heat transfer coefficient of $15 \text{ Wm}^{-2}\text{K}^{-1}$ were set. System coupling was assigned to the internal walls (sheet metal) and to the heat-receiving plate. The hotplate was ascribed an initial temperature of

60°C, 70°C, and 80°C. All surfaces were assigned a wall boundary condition. The Standard k - ϵ model was used as the viscosity model in the calculations to simulate the average flow characteristics under turbulent flow conditions. Pressure-velocity coupling was used to derive an additional pressure condition. The pressure-based solver allows the flow problem to be solved separately or in combination. The calculations use the simple method solution, which means that the algorithm uses the relationship between velocity and pressure corrections to enforce mass conservation and obtain a pressure field. This is the default setting for transient simulations [27]. The computation time was 10 800 s of real process time. While loading the tank with hot water, a constant temperature was set on the surface of the bottom plate responsible for heating the system. The top plate was assigned an initial temperature of the water.

Table 2: Physical properties of materials used in calculations [31].

Material type	Specific heat ($\text{Jkg}^{-1}\text{K}^{-1}$)	Density (kgm^{-3})	Heat conductivity ($\text{Wm}^{-1}\text{K}^{-1}$)	Dynamic viscosity ($\text{kgm}^{-1}\text{s}^{-1}$)
EPS	1210	29.933	0.033	–
Copper	381	8978	387.6	–
Steel	502.48	8030	16.27	–
Water	4182	$-0.4589T + 1129.6$	0.6	0.001

To determine the impact of the mesh quality on the accuracy of the results of numerical calculations, the results obtained using two types of meshes were compared. Figures 5–7 show the distributions of the water velocity field for the automatically-generated mesh and a mesh created using the MultiZone method. The comparisons are presented in particular time periods, at charging temperatures up to 60°C.

Analysis of Figs. 5–7 shows that the usage of automatic method leads to the accumulation of higher velocities in the upper part of the tank. The maximum velocities are observed near the plate that does not transfer heat to the system. This movement does not come from the lower heating plate, unlike the MultiZone method. In the case of the MultiZone simulation, the water velocity distribution range is smaller but uniform throughout the volume of the tank. This is related to better mesh quality; therefore, the MultiZone model is selected for further calculations.

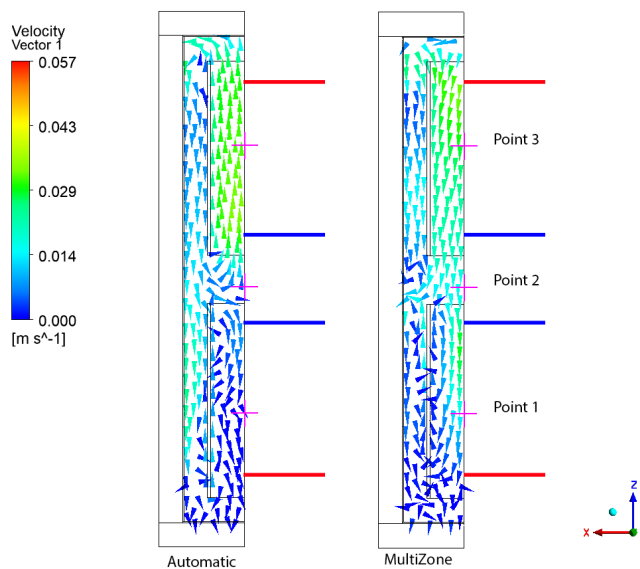


Figure 5: Distribution of water velocity in the tank after the first hour of calculations.

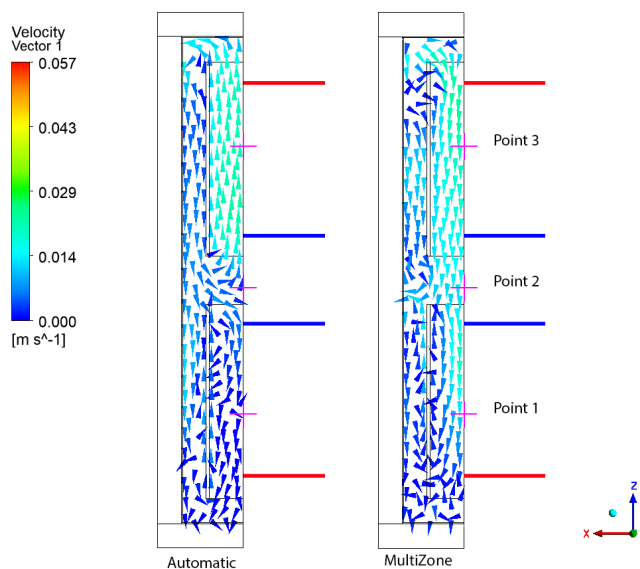


Figure 6: Distribution of water velocity in the tank after the second hour of calculations.

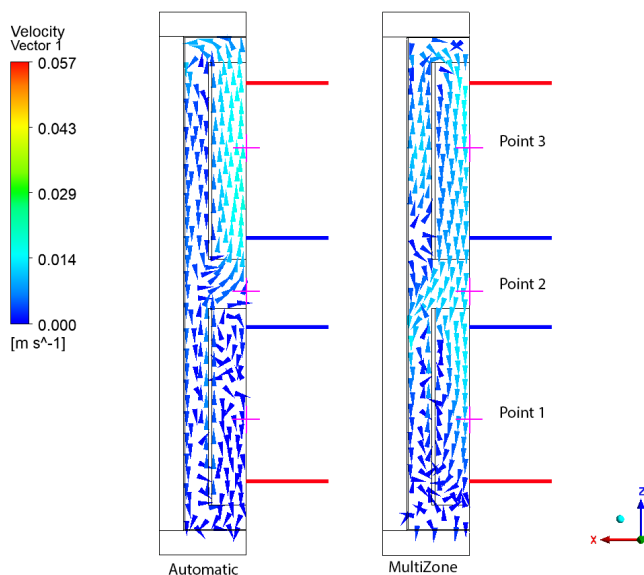


Figure 7: Distribution of water velocity in the tank after the third hour of calculations.

4 Computational fluid dynamics simulations and analysis of the results

Figures 8, 12, and 16 show the temperature distribution in the graphical form over the first, second and third hours when heating water in a tank with different required temperatures. Three points were distinguished in each figure mentioned above. Graphs of temperature distribution over time were prepared for each marked point, as shown in Figs. 9, 13, and 17. In addition, Figs. 10, 14, and 18 deliver the water velocity field in the tank as a result of temperature changes. Similarly, points were marked in the figures, and diagrams of the water velocity field distribution in time were made for them, which are presented in Figs. 11, 15, and 19. The Reynolds number was determined for the sections corresponding to points 1, 2, and 3 at the time moments, which are shown in Figs. 10, 14, and 18. The value is in the range of 3745–12 679, which corresponds to a fully turbulent flow ($Re > 3600$) [26].

In Figs. 8 and 9 at 60°C, one can see that the temperature increases with the charging time. Similarly, Figs. 12, 13 as well as Figs. 16 and 17

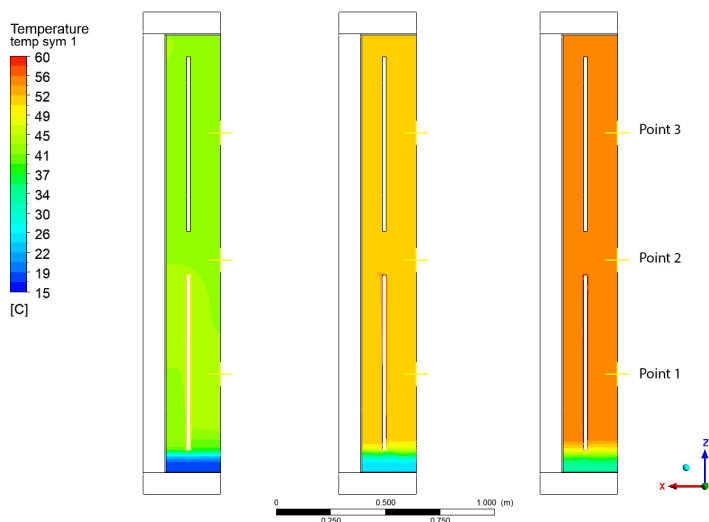


Figure 8: Temperature distribution in the tank for the maximum value of 60°C .

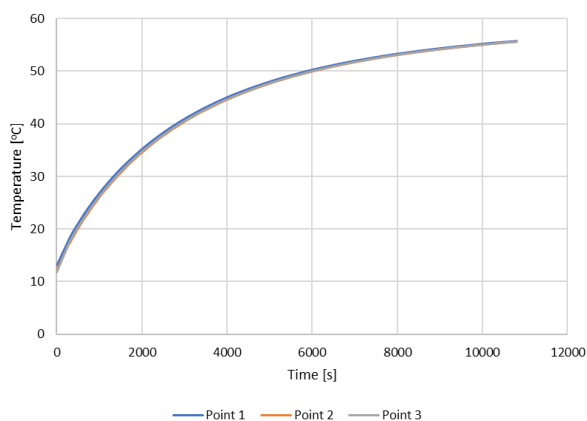


Figure 9: Graph of temperature distribution over time for a maximum value of 60°C .

refer to the temperature of 70°C and 80°C , respectively. A higher charging temperature leads to more heat stored in the warehouse and a longer discharge time. In the drawings showing the distribution of the temperature field, it can be observed that in each charging variant, there is a layer of cooler water at the bottom of the tank. This is due to the fact that the heating plate does not adhere to the bottom wall of the heat storage, so there is no global fluid movement there.

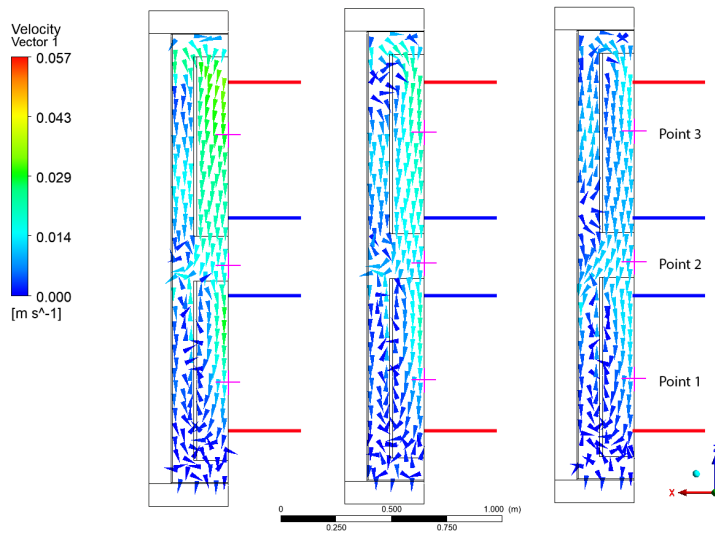


Figure 10: Water velocity distribution in the tank for the maximum temperature of 60°C .

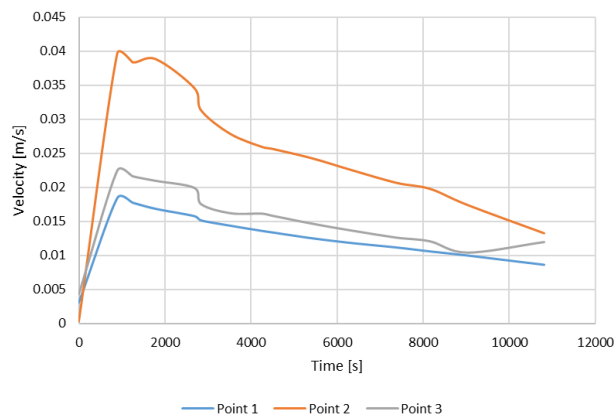


Figure 11: Graph of water velocity distribution over time for a maximum temperature of 60°C .

Figures 10, 14, and 18 show the distribution of water velocity in the tank. It can be observed that the velocity field in the upper area of the tank is significantly larger than the velocity field in the lower part. Generally, the values of the water velocity field in the entire tank are small and are caused only by the dissimilarity in water temperature resulting in its different density. Hence, it can be seen that in the tank's lower part, the fluid's

movement is negligible, which is why the temperature rises much more slowly.

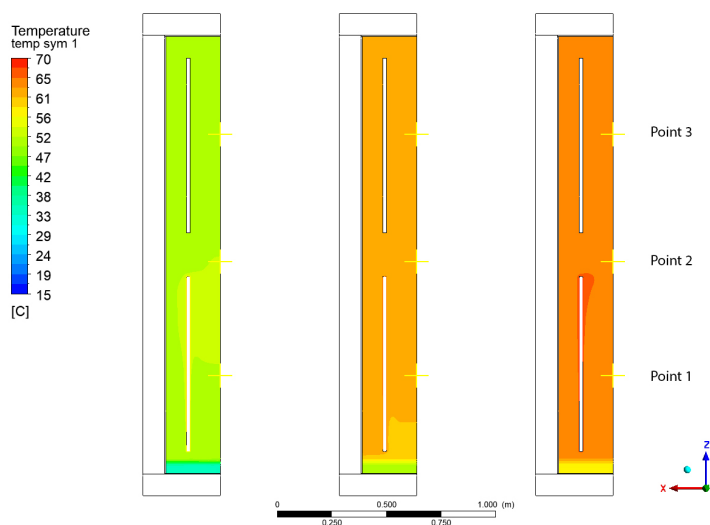


Figure 12: Temperature distribution in the tank for the maximum value of 70°C .

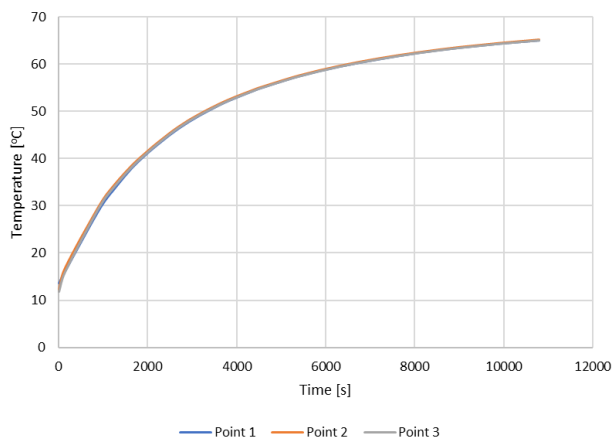


Figure 13: Graph of temperature distribution over time for a maximum value of 70°C .

Figures 11, 15, and 19 show graphs of water velocity distribution in the reservoir. In the charts, you can see an increase in speed in the initial seconds of loading. A high gradient between the initial water temperature

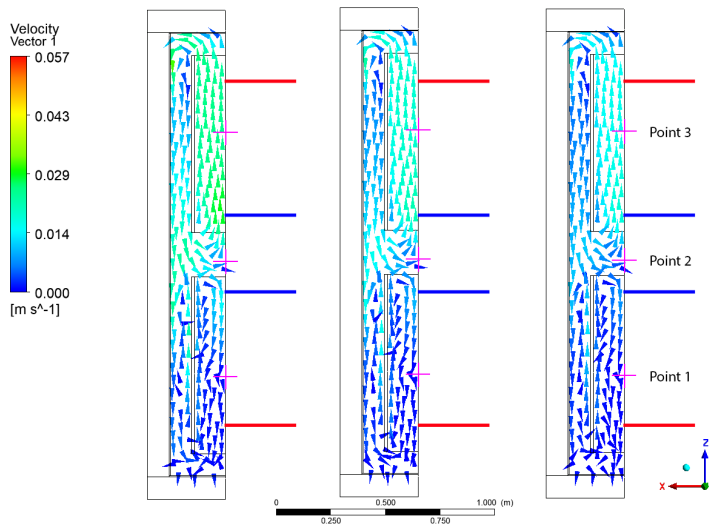


Figure 14: Water velocity distribution in the tank for the maximum temperature of 70°C.

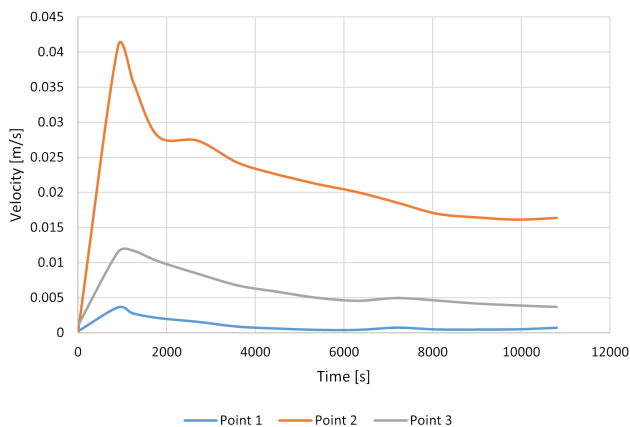


Figure 15: Water velocity distribution over time for a maximum temperature of 70°C in points 1, 2, and 3.

and the temperature of the heater causes this phenomenon. Over time, the speed starts to decrease as the temperature difference drops. In addition, the highest rate is present in the centre of the tank (point 2) since this point is close to the upper part of the heating plate. The lowest water velocity field is near the bottom of the tank (point 1) due to the faster temperature equalization.

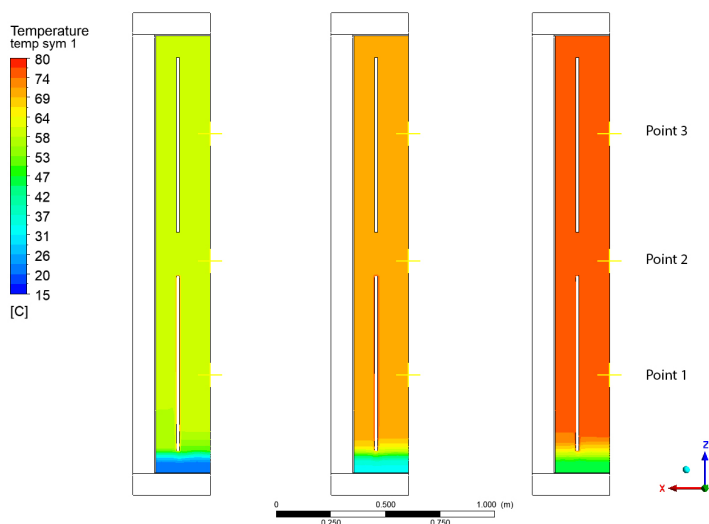


Figure 16: Temperature distribution in the tank for the maximum value of 80°C .

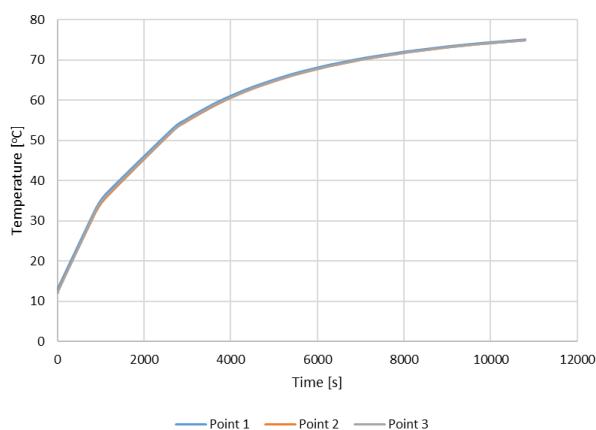


Figure 17: Graph of temperature distribution over time for a maximum value of 80°C .

From Figs. 11, 15, and 19, one can see the noticeable change in the velocity of the three points over time. The same cannot be observed for Figs. 9, 13, and 17. Temperature variation over time is still present; however, the values at each point are not significantly different. This is due to the movement of the fluid, which results in equalizing the temperature throughout the entire volume of the tank.

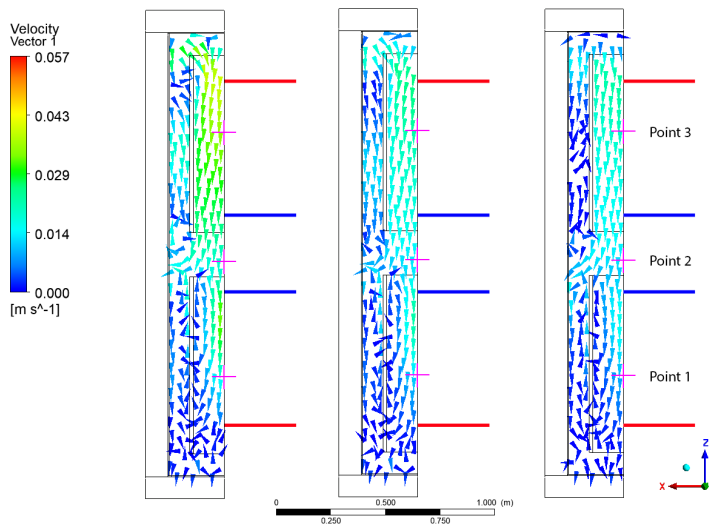


Figure 18: Water velocity distribution in the tank for the maximum temperature of 80°C.

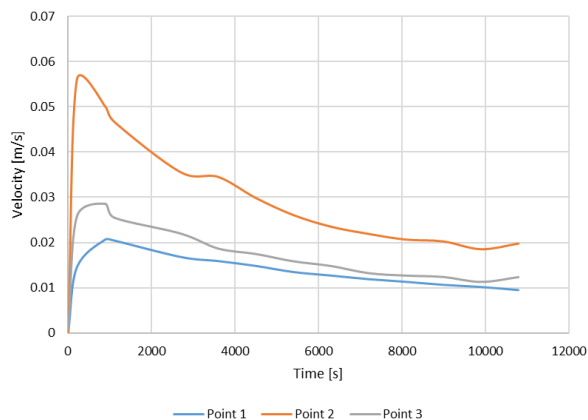


Figure 19: Water velocity distribution over time for a maximum temperature of 80°C in points 1, 2, and 3.

5 Total heat loss to the environment

In the calculations, expanded polystyrene (EPS) was used as the default insulation of the tank. It is a commonly used insulation material with a thermal conductivity $0.033 \text{ W m}^{-1} \text{ K}^{-1}$. Thanks to the applied layer of expanded polystyrene with a thickness of 0.1 m, it was possible to reduce heat losses

to the environment significantly. Table 3 shows the daily heat losses and the heat capacity of the tank at different charging temperatures and their percentage ratio. It can be read from the table that an increase in the charging temperature by 20°C causes the total heat loss to the environment increases from 1.58 to 2.33 kWh per day. However, a higher charging temperature provides more heat available to use and a longer discharge time.

Table 3: Summary of daily losses and thermal capacity of the tank.

Temperature ($^{\circ}\text{C}$)	Daily losses (kWh)	Thermal capacity (kWh)	Percentage ratio
60	1.58	26.27	6.01
70	2.02	31.78	6.36
80	2.33	37.32	6.24

Based on Table 3, it can be concluded that the ratio of daily heat losses to the heat capacity of the tank is highly comparable depending on the charging temperature. The use of better insulation would result in a reduction of heat loss to the environment. The usage of more tanks with better insulation could meet the heat demand on unfavourable days, where direct waste heat recovery would not meet the needs.

6 Conclusions

- The conducted research analysed the thermal parameters of the designed compact heat storage. The study aimed to examine the movement of the fluid in such a heat accumulator to unify the temperature field in the volume of water constituting the heat buffer. Using CFD simulations, water movement in the tank was studied.
- During the tests, the heat capacity of a tank was determined, and the heat losses to the environment at different charging temperatures were estimated. Three temperatures were selected, and the heat storage was loaded into each for an equal period of time.
- In conclusion, as it arises from the results of the calculations presented in the work heating the water in the tank to 60°C is the most energy efficient, because heat losses to the environment, in this case, are the lowest.

- Due to the fact that waste heat from industrial equipment has different temperatures, such a tank will also be charged with different temperatures. Therefore, using water as an accumulation medium instead of a variable-phase substance is less expensive.
- Due to the compactness of the designed system, it can be used in various configurations depending on the environment in which it works.

Acknowledgments

This work was supported by statutory activities of the Faculty of Metals Engineering and Industrial Computer Science of AGH University of Science and Technology, work no. 16.16.110.663 task 4.

Received 14 June 2023

References

- [1] Saini M.C., Jakhar D.O.: *CFD simulation and experimental validation of PCM thermal energy storage system for micro trigeneration system application*. Int. J. Refrig. **149**(2023), 119–134. doi: [10.1016/j.ijrefrig.2022.12.004](https://doi.org/10.1016/j.ijrefrig.2022.12.004)
- [2] Fernández-Yáñez P., Romero V., Armas O., Cerretti G.: *Thermal management of thermoelectric generators for waste energy recovery*. Appl. Therm. Eng. **196**(2021), 117291. doi: [10.1016/j.applthermaleng.2021.117291](https://doi.org/10.1016/j.applthermaleng.2021.117291)
- [3] Chu S., Sethuvenkatraman S., Goldsworthy M., Yuan G.: *Techno-economic assessment of solar assisted precinct level heating systems with seasonal heat storage for Australian cities*. Renew. Energ. **201**(2022), 841–853. doi: [10.1016/j.renene.2022.11.011](https://doi.org/10.1016/j.renene.2022.11.011)
- [4] Tohidi F., Ghazanfari Holagh S., Chitsaz, A.: *Thermoelectric generators: A comprehensive review of characteristics and applications*. Appl. Therm. Eng. **201**(2021), 117793. doi: [10.1016/j.applthermaleng.2021.117793](https://doi.org/10.1016/j.applthermaleng.2021.117793)
- [5] Wang C., Wang S., Cheng X., Zhang Y., Wang, Z.: *Research progress and performance improvement of phase change heat accumulators*. J. Energ. Stor. **56**(2022), 105884. doi: [10.1016/j.est.2022.105884](https://doi.org/10.1016/j.est.2022.105884)
- [6] Dai B., Liu C., Liu S., Wang D., Wang Q., Zou T., Zhou X.: *Life cycle techno-enviro-economic assessment of dual-temperature evaporation transcritical CO₂ high-temperature heat pump systems for industrial waste heat recovery*. Appl. Therm. Eng. **219**(2023), 119570. doi: [10.1016/j.applthermaleng.2022.119570](https://doi.org/10.1016/j.applthermaleng.2022.119570)
- [7] Dmitry S., Liubov S.: *Numerical modelling of heat accumulator performance at storage of solar energy*. Int. J. Thermofluids **17**(2023), 100268. doi: [10.1016/j.ijft.2022.100268](https://doi.org/10.1016/j.ijft.2022.100268)

- [8] Ouyang T., Qin P., Tan X., Wang J., Fan J.: *A novel peak shaving framework for coal-fired power plant in isolated microgrids: Combined flexible energy storage and waste heat recovery*. J. Clean. Prod. **374**(2022), 133936. doi: [10.1016/j.jclepro.2022.133936](https://doi.org/10.1016/j.jclepro.2022.133936)
- [9] Fan M., Wang J., Kong X., Suo H., Zheng W., Li H.: *Experimental evaluation of the cascaded energy storage radiator for constructing indoor thermal environment in winter*. Appl. Energ. **332**(2023), 120503. doi: [10.1016/j.apenergy.2022.120503](https://doi.org/10.1016/j.apenergy.2022.120503)
- [10] Haillot D., Lalau Y., Franquet E., Rigal S., Jay F., Bédécarrats J.P.: *A latent heat storage system for low-temperature applications: From materials selection to prototype performances*. Appl. Sci. **11**(2021), 10350. doi: [10.3390/app112110350](https://doi.org/10.3390/app112110350)
- [11] Bouhal T., ed. Dîn Fertahi S., Agrouaz Y., El Rhafiki T., Zeraouli Y., Jamil A.: *Towards an energy efficiency optimization of solar horizontal storage tanks and circulation pipes integrating evacuated tube collectors through CFD parametric studies*. Sustain. Energy Technol. Assess. **26**(2018), 93–104. doi: [10.1016/j.seta.2017.10.004](https://doi.org/10.1016/j.seta.2017.10.004)
- [12] *Heat accumulator – a way to reduce home heating costs* (in Polish). <https://muratordom.pl/instalacje/ogrzewanie-paliwami-stalymi/akumulator-ciepla-sposob-na-obnizenie-kosztow-ogrzewania-domu-aa-EdFw-ydbp-5P5q.html> (accessed 3 Feb. 2023).
- [13] Agrouaz Y., Bouhal T., Allouhi A., Kousksou T., Jamil A., Zeraouli Y.: *Energy and parametric analysis of solar absorption cooling systems in various Moroccan climates*. Case Stud. Therm. Eng. **9**(2017), 28–39. doi: [10.1016/j.csite.2016.11.002](https://doi.org/10.1016/j.csite.2016.11.002)
- [14] Rosen M.A., Tang R., Dincer I.: *Effect of stratification on energy and exergy capacities in thermal storage systems*. Int. J. Energy Res. **28**(2004), 177–193. doi: [10.1002/er.960](https://doi.org/10.1002/er.960)
- [15] Zhang C., Chai D., Pan X., Xie J., Chen J.: *Performance Analysis of Two Systems Combining Heat Pump and Water Vapor Compression for Waste Heat Recovery*. Appl. Sci. **12**(2022), 12853. doi: [10.3390/app122412853](https://doi.org/10.3390/app122412853)
- [16] *Heat Storage – Types of Storage* (in Polish). <https://www.cire.pl/artykuly/materialy-problemowe/119630-magazynowanie-ciepla-rodzaje-magazynow> (accessed 3 Feb. 2023).
- [17] Portarapillo M., Danzi E., Sanchirico R., Marmo L., Di Benedetto A.: *Energy recovery from vinery waste: Dust explosion issues*. Appl. Sci. **11**(2021). doi: [10.3390/app112311188](https://doi.org/10.3390/app112311188)
- [18] Ugur B.: *Thermal Energy Storage in Adsorbent Beds*. PhD thesis, Univ. of Ottawa, 2013.
- [19] Shigeishi R.A., Langford C.H., Hollebone B.R.: *Solar energy storage using chemical potential changes associated with drying of zeolites*. Sol. Energy **23**(1979), 489–495. doi: [10.1016/0038-092X\(79\)90072-0](https://doi.org/10.1016/0038-092X(79)90072-0)
- [20] Badyda K., Bujalski W., Niewiński G., Warchoń M.: *Selected issues related to heat storage tank modelling and optimisation aimed at forecasting its operation*. Arch. Thermodyn. **32**(2011), 3, 3–31. doi: [10.2478/v10173-011-0010-8](https://doi.org/10.2478/v10173-011-0010-8)
- [21] Ziębik A., Gładysz P.: *Optimal coefficient of the share of cogeneration in the district heating system cooperating with thermal storage*. Arch. Thermodyn. **32**(2011), 3, 71–87. doi: [10.2478/v10173-011-0014-4](https://doi.org/10.2478/v10173-011-0014-4)

- [22] Zhu C., Zhang J., Wang Y., Deng Z., Shi P., Wu J., Wu Z.: *Study on thermal performance of single-tank thermal energy storage system with thermocline in solar thermal utilization*. Appl. Sci. **12**(2022), 3908. doi: [10.3390/app12083908](https://doi.org/10.3390/app12083908)
- [23] Szajding A., Kuta M., Cebo-Rudnicka A., Rywotycki M.: *Analysis of work of a thermal energy storage with a phase change material (PCM) charged with electric heaters from a photovoltaic installation*. Int. Commun. **140**(2023), 106547. doi: [10.1016/j.icheatmasstransfer.2022.106547](https://doi.org/10.1016/j.icheatmasstransfer.2022.106547)
- [24] Kącki E.: *Partial Differential Equations in Physics and Engineering*. WNT, Warsaw 1992 (in Polish).
- [25] Malczewski J.: *Models of Mass, Momentum and Energy Transport Processes*. PWN, Warsaw 1992 (in Polish).
- [26] Prywer J., Zarzycki R., Orzechowski Z.: *Fluid Mechanics in Environmental Engineering*. WNT, Warsaw 2001 (in Polish).
- [27] *ANSYS Manual*. ANSYS Inc. Canonsburg 2022.
- [28] Regulski W.: *Computer modeling of turbulent flows*. https://www.meil.pw.edu.pl/za/content/download/18385/99605/file/Lab_67.pdf (accessed 3 Feb. 2023)
- [29] *K-Epsilon*. <https://www.simscale.com/docs/simulation-setup/global-settings/k-epsilon/> (accessed 3 Feb. 2023).
- [30] Paszko M., Łygas K.: *Modern methods of modeling turbulent flows in the environment of a moving city bus*. <http://yadda.icm.edu.pl/baztech/element/bwmeta1.element.baztech-86cf1eb6-09ab-40e4-b9a9-9f5fb64c9e0f> (accessed 3 Feb. 2023).
- [31] *ANSYS Fluent Manual*. ANSYS Inc. Canonsburg 2022.
- [32] *ANSYS Mesh Methods Explained*. <https://featips.com/2022/12/27/ansys-mesh-methods-explained/> (accessed 3 Feb. 2023).
- [33] *How to Verify Mesh Quality in ANSYS Workbench*. <https://featips.com/2021/05/07/how-to-verify-mesh-quality-in-ansys-workbench/> (accessed 3 Feb. 2023).

Effect of artificial coarseness on the performance of rectangular solar air heater duct: a comparative study

MANOJ KUMAR DUBEY*
OM PRAKASH

National Institute of Technology Patna, Patna, Bihar 800005, India

Abstract Solar air heater is regarded as the most common and popular solar thermal system and has a wide range of applications, from residential to industrial. Solar air heater is not viable because of the low convective heat transfer coefficient at the absorber plate which contributes to decreasing the thermal efficiency. Artificial coarseness on the plain surface is the most effective method to enhance heat transfer with a moderate rate of friction factor of flowing air in the design of solar air heater duct. The different parameters and different artificial coarseness are responsible to alter the flow structure and heat transfer rate. Over the years different artificial roughness and how its geometry affects the performance of solar air heater have been thoroughly studied. Various investigators report the correlations between heat transfer and friction factors. In the present study, a comparison of several artificial coarseness geometries and methods with a view to enhancing the performance of solar air heater has been made. A brief outline has also been presented for future research.

Keywords: Solar energy; Artificial coarseness; Heat transfer coefficient; Thermo-hydraulic performance; Friction factor

Nomenclature

D	–	hydraulic diameter, mm
d	–	dimple diameter, mm
d/W	–	relative width of the gap

*Corresponding Author. Email: manojd.phd18.me@nitp.ac.in

d/D	–	relative diameter of rib print
e	–	rib height, mm
Re^+	–	roughness Reynolds number
e/D	–	relative roughness height
F'	–	flat collector efficiency factor
F_R	–	heat removal factor
f_r	–	friction factor for roughened surface
f_s	–	friction factor of flat duct
G^0	–	mass flux, $\text{kg}/(\text{s m}^2)$
G_d	–	distance of the gap, mm
$G(Re^+)$	–	heat transfer function
$G_d/L_v, d/x$	–	relative position of the gap
g	–	groove position or gap, mm
g/e	–	relative gap position
g^I/e	–	relative additional gap in each symmetrical rib
g/P	–	relative groove position
H	–	duct height, mm
I	–	global solar irradiation, W/m^2
L	–	length of long way test section, mm
L_f	–	final length of duct, mm
L_v	–	length of V-rib, mm
L/e	–	relative long way length
l/s	–	relative length of metal grid rib
m^0	–	mass flow rate, kg/s
Nu	–	Nusselt number of roughened duct
Nu_s	–	Nusselt number of smooth duct
q_u	–	heat flux, W/m^2
P'	–	staggered rib position, mm
P_b/e_d	–	relative dimpled pitch
p/P	–	relative staggered rib pitch
P^I/p	–	relative staggered rib roughness
P/e	–	relative roughness pitch
ΔP	–	pressure drop, Pa
Re	–	Reynolds number
$R(Re^+)$	–	momentum transfer roughness function
$r/g, r/e$	–	relative staggered rib size
S	–	length of short way discrete rib, mm
S/e	–	relative short way length
St	–	Stanton number
s'/s	–	dimensionless gap position
s'	–	gap position, mm
T_{fi}	–	entry temperature, K
T_{fo}	–	exit temperature, K
T_a	–	ambient temperature, K
U_L	–	overall heat loss coefficient, $\text{W}/(\text{m}^2\text{K})$
V	–	velocity, m/s
W	–	duct width, mm
w	–	width of a single V-rib, mm
W/H	–	aspect ratio

W/w	–	relative roughness width
W_c/W_d	–	relative dimpled obstacles
w/e	–	staggered length of the rib to the height of the rib

Greek symbols

α	–	angle of inclination in flow direction, degree
Φ	–	chamfer angle, degree
ρ	–	density, kg/m ³
η	–	thermal efficiency
τ	–	transmittance

Acronyms

HVAC	–	heating, ventilation and air conditioning
SAH	–	solar air heater
THP	–	thermo-hydraulic performance

1 Introduction

Since the beginning of human civilization, energy has been one of the most vital factors for sustainability of the mankind. Today, energy remains an essential element of global economic growth and industrialization. With the rapidly diminishing fossil fuel reserves, which have been the primary source of energy so far, it has become imperative to find new energy sources. Solar energy has emerged as a viable source of alternative energy, which is clean, ensures a pollution-free environment, and which is available year-round. In other words, besides mitigating the energy crisis, it can also reduce CO₂ emissions. Another benefit is that solar energy is easy to change into other types of energy, such as thermal, mechanical, chemical, and electrical energy. A solar air heater (SAH) is an apparatus that absorbs solar energy and then transfers the heat energy to the air passing through. As SAH has been established as one of the most cost-effective techniques for converting solar energy, it is being widely used in various industries for room heating, room cooling, room drying, and other industrial purposes [1].

Absorber plates are an essential component of solar air heaters (SAHs). However, the formation of a viscous sublayer over the absorber plate tends to reduce the heat transfer coefficient and increase thermal resistance. The research established that artificial coarseness in the absorber plate could be an effective method to break laminar sublayers and increase the heat transfer coefficient [2]. However, it causes a significant pressure drop, enhancing the requirement for electricity. Many researchers have utilized artificial

coarseness geometry of various configurations and dimensions to enhance heat transfer and improve SAH efficiency. The present study provides an overview of different geometries, such as V-shape, W-shape, arc-shape, etc., and examines how different orientations of artificial roughness affect the performance of SAH. The aim of this paper is to determine which artificial coarseness surface works the best with different shapes and structures.

Generally, traditional SAH has low thermal performance because of a smooth surface that offers low convective heat transfer to flowing air, leading to major losses in surrounding. The SAH performance can be increased in two ways: by reducing the top surface heat loss of SAH or by enhancing the heat transfer at the absorber plate. Various methods are available to enhance the heat transfer but the most common method is to increase the heat transfer rate by using artificial coarseness instead of a smooth surface. Artificial roughness develops turbulence on a heated surface and breaks the laminar sublayer but it causes an increase in the pressure drop which is undesirable for the design of SAH. In this paper, the previous research of artificial coarseness used in SAH is summarized.

2 Theory of artificial roughness

Conventional SAHs are inefficient due to inadequate provision for heat transfer between the absorber plates and the air passage. As a result, the thermal resistance between the absorbing plates and the air is higher in the SAHs. Consequently, it increases the temperature, thereby increasing the heat loss to the surrounding area. The presence of a laminar sublayer interrupts heat exchange between the absorber plate and air passage [3]. By introducing artificial coarseness, the laminar sublayer can be broken so as to improve heat exchange by producing local turbulence. However, it can also increase the friction losses leading to an increase in the power consumption for fluid flow. Several studies revealed that Nusselt number (Nu) and friction factor (f) are also affected by factors, such as rib arrangement, wire form, rib height, and rib pitch.

3 Principle of solar air heater

In a nutshell, a traditional solar air heater absorbs solar radiation and converts it into thermal energy. As illustrated in Fig. 1, the SAH has a glass cover, a rear insulated cover, and a blower. To prevent heat transfer from

the top of the absorber plate to the surroundings, a glass cover is used, which simultaneously allows incoming solar light to pass through the absorber plate. In addition, it serves as insulation at the backside, thereby reducing the energy loss. The heated air is transported *via* a duct to the three insulated sides and a collector at the top side of the heater. SAH is utilized for various residential and industrial applications in moderate-temperature. Applications include industrial heating, ventilation and air conditioning (HVAC) systems, agricultural crop drying, and space heating. A conventional SAH loses the maximum amount of energy to the surrounding environment because energy cannot be transferred efficiently between the absorber plate and the air duct. Due to the formation of a laminar sublayer near the boundary exchanging thermal energy, its thermal performance is poor. As a result, it is essential to choose an appropriate method of heat transfer that will enhance the performance of SAH.

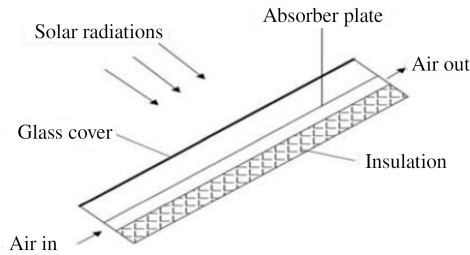


Figure 1: Schematic diagram of a solar air heater.

4 Characteristics of fluid flow and heat transfer through artificially roughened ducts in solar air heater

In the study, Nikuradse [4] used a technique called sandblasting to make the air flow more smoothly and control its temperature. He tested different levels of roughness and speed to see what works best. The ‘roughness Reynolds number’ (Re^+) is a special number that helps us understand how well a rough surface is performing in transferring heat. It is a way to figure out the best conditions for heat transfer on a rough surface.

The roughness Reynolds number is provided as

$$Re^+ = \sqrt{\frac{2}{f_r}} \left(\frac{e}{D} \right) Re, \quad (1)$$

where f_r is the roughened surface friction factor representing the pressure loss of a fluid, e/D is the relative height, which is defined as the ratio of rib height (e) to the hydraulic diameter (D) of the duct.

As explained below, three flow regions were developed for the flow roughness:

I Hydraulic flow regime ($0 < \text{Re}^+ < 5$)

For smooth pipes, the friction factor (f_s) remains constant for all values of relative height (e/D).

In the hydraulic smooth flow regime, the flow resistance in terms of friction factor is not a function of roughness height and flow behaves as laminar in such roughened pipe.

Roughness function $R(\text{Re}^+)$ is defined as dimensional flow velocity at the control volume edge enclosing roughness elements. It represents momentum losses caused by roughness. The following correlation was proposed:

$$R(\text{Re}^+) = \sqrt{\frac{2}{f_s}} + 2.5 \ln \left(\frac{2e}{D} \right) + 3.75. \quad (2)$$

II Transitional flow regime ($5 < \text{Re}^+ < 70$)

The effect of rib altitude can be observed in this transitional area. The roughness Reynolds number (Re^+) and the e/D ratio, which is defined as the ratio of rib height (e) to the hydraulic diameter of the duct, have an impact on the roughness behavior.

III Fully developed flow regime ($\text{Re}^+ > 70$)

The roughness function (R) remains constant in the rough area. Reynolds number is unaffected by roughness. Dipprey and Sabersky [5] investigated the flow across an irregular plane of densely filled-up sand grains in a conduit by using air as the moving fluid. Heat transfer correlation for the fully developed flow region is presented as follows:

$$G(\text{Re}^+) = \left(\frac{f_s}{2\text{St}} - 1 \right) \sqrt{\frac{f_s}{2}} + R(\text{Re}^+). \quad (3)$$

Here, St is the Stanton number which is defined as the ratio of heat transfer of a fluid to the thermal capacity of a fluid, and D is the hydraulic diameter of the duct which is generally defined for a non-circular duct. The roughness function is defined as for fully developed flow region (Eq. (3)).

Heat transfer function $G(\text{Re}^+)$ represents dimensionless temperature difference over the same control volume. It signifies the heat transfer capacity of a rough surface.

In addition to the analytical model, some researchers studied the heat transfer and friction flow characteristics using numerical methods. Poitras *et al.* [6] investigated the flow structure by using a numerical simulation of transverse ribs. Inter-rib spacing and Reynolds number effects were examined. The length of the recirculation zone was significantly influenced by inter-rib space.

5 Measurement of solar air heater performance

Heat transfer is enhanced by artificial roughness at the expense of friction, resulting in turbulent flow within the SAH duct. A highly efficient and economically feasible collector may be designed by enhancing the Nusselt number with the least amount of pressure drop. In this connection, several designs for solar air collectors have been presented that have different configurations of roughness geometry.

5.1 Hydraulic performance

Pressure drop in the SAH duct is used to assess hydraulic performance, which is again linked to the surplus heat, produced by the fan. Frank and Mark [7] defined the friction factor (f) as a dimensionless version of the pressure drop. The hydraulic performance of SAH is determined by the Darcy-Weisbach equation:

$$f = \frac{2(\Delta P)_d D}{4\rho L V^2}, \quad (4)$$

where $(\Delta P)_d$ is the pressure drop in the duct ρ is the density of a fluid, L is the length of the duct and V is the mean fluid velocity.

5.2 Thermal performance

This term refers to the heat transfer from the collector to the circulating air. Thermal performance is determined in terms of the energy gained by the air, solar energy gained by the collector, and the energy lost to the surroundings. Hottel and Woertz [8] presented the following energy equation:

$$q_u = I\tau\alpha - U_L(T_p - T_a), \quad (5)$$

where T_p and T_a are the plate temperature and ambient temperature, respectively, and U_L is the overall heat loss coefficient which is expressed by the following summation:

$$U_L = U_e + U_t + U_b, \quad (6)$$

where U_t is the heat transfer coefficient on the top side, U_b is the heat transfer coefficient on the bottom side, and U_e is the heat loss coefficient on the side surface.

The actual excess heat, transmitted to the air from the SAH duct is calculated using the Hottel–Whillier–Bliss [8] equation

$$q_u = F_R [I\tau\alpha - L_f (T_i - T_a)], \quad (7)$$

where L_f is the final length of the duct.

5.2.1 Heat removal factor

When the fluid inlet temperature remains as per the collector temperature, the heat removal factor is defined as the ratio of the actual heat transfer to the maximum possible heat transfer by means of the collector plate

$$F_R = \frac{m^0 C_p}{A_p U_L} \left[\exp \left(\frac{A_p U_L F_p}{m^0 C_p} \right) - 1 \right], \quad (8)$$

where C_p is the specific heat of a fluid, m^0 is the mass flow rate of a fluid, F_p is the collector efficiency factor, and A_p is the surface area of the absorber plate.

The thermal efficiency of a solar collector (η) is defined as

$$\eta = \frac{q_u}{I}. \quad (9)$$

Thermal efficiency can also be expressed by means of Hottel–Whillier–Bliss equation [8]

$$\eta = F_R \left[\frac{I\pi\alpha - U_L (T_o - T_a)}{I} \right]. \quad (10)$$

Bondi presented the following collector efficiency equation when the air inlet temperature and the surrounding temperature are equal [9]:

$$\eta = F_o \left[\tau\alpha - U_L \frac{T_{fo} - T_{fi}}{I} \right], \quad (11)$$

where T_{fo} and T_{fi} is the fluid outlet and inlet temperature, respectively.

Here F_o is the heat removal factor based on the temperature of the exit air which takes the form

$$F_o = \frac{GC_p}{U} \left[\exp \left(\frac{F'U_L}{GC_p} \right) - 1 \right], \quad (12)$$

where G is the function of heat transfer (Eq. (13)), U is the overall heat transfer coefficient and the plate collector efficiency factor F' is the ratio of the actual and the ideal heat absorption in a SAH when the fluid temperature and the collector temperature are equal.

5.3 Thermo-hydraulic performance

The objective of this comparison is to determine the performance of the roughened SAH ducts with smooth SAH ducts. Lewis proves that roughened duct provides better thermo-hydraulic performance (THP) which is defined as the ratio of actual heat transfer to the maximum possible heat transfer under the same pumping power, in accordance with the formula [10]

$$\text{THP} = \frac{\frac{\text{Nu}}{\text{Nu}_s}}{\left(\frac{f_r}{f_s} \right)^{\frac{1}{3}}}, \quad (13)$$

where Nu and Nu_s are the Nusselt numbers of rough and smooth ducts, respectively, and f_r and f_s are the friction factors of rough and smooth surfaces, respectively. Thermo-hydraulic performance thus indicates the effectiveness of SAH because it includes the pumping power losses due to pressure drop inside the duct.

6 Influence of roughness design on the flow pattern

Artificial roughness geometry can take up various forms and orientations. Rib pitch, rib height, inclination, cross-section of rib, and flow parameters, including Reynolds number, are among the major geometrical variables, which are used to indicate the artificial roughness geometry. The impact of these variables on the THP of the SAH ducts has been examined.

6.1 Influence of relative rib pitch

Prasad and Saini [11] explained the influence of the ratio of the pitch to the rib height (P/e) on the flow variation. If the P/e ratio is between 8 to

10, then the reattachment point becomes higher and the heat transfer can be the maximum. Conversely, if the P/e ratio is less than 8, then the flow deviates. If this ratio is beyond 10, it decreases the reattachment point and reduces the heat transfer rate.

6.2 Influence of relative rib height

Prasad and Saini [12] also explained how the height of rib roughness influences flow variation. In this context, the authors explained its effect on the SAH duct. While the rib height can cause the separation of flow and reattachment, the area close to the reattachment ensures the most efficient heat transfer. Reattachment occurs when the e/D is only moderate, as seen in Fig. 2.

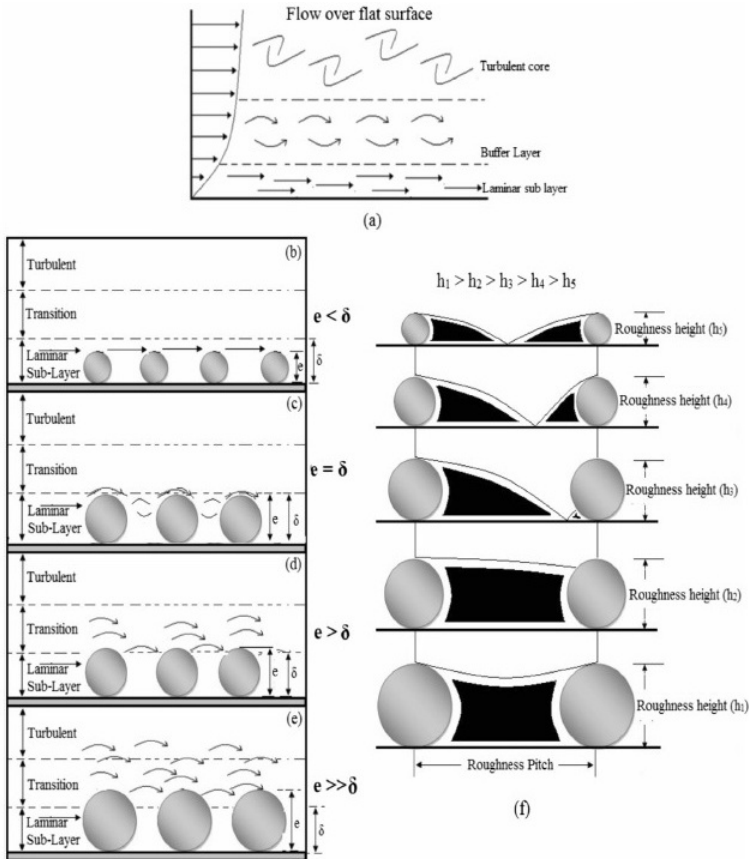


Figure 2: Influence of relative rib height (δ denotes the laminar sublayer height) [12].

6.3 Influence of rib inclination

The angle at which the rib element is aligned in relation to the flow direction is an essential factor behind the counter-revolving secondary flow throughout the span, determining variable heat discharge rates. When fluid comes out from the leading edge and goes to the trailing edge, it is trapped and its temperature goes up. It has been observed that no turbulence, created by transverse ribs, reduces the heat transfer rate because of the rise in fluid temperature at the wall. When the angle in the rib geometry alters, turbulence is created, thereby enhancing the heat transfer rate. Therefore, it is always beneficial for the rib geometry to have a degree of inclination. The heat transfer is maximum at the leading edge and it reduces when it goes to the trailing edge, as shown in Fig. 3.

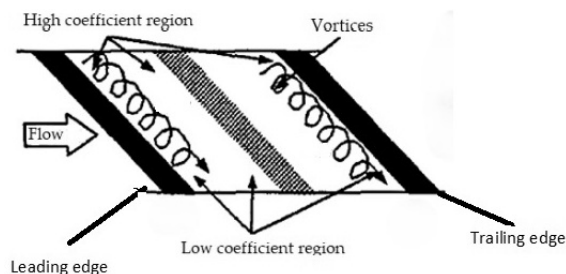


Figure 3: Flow pattern due to angled rib [13].

6.4 Influence of duct aspect ratio

The ratio of the width to height of the duct (W/H) is known as the aspect ratio, which considerably impacts the thermal performance of the SAH. With a moderate increase in the heat discharge, a high duct aspect ratio enhances turbulence inside the duct and raises the friction factor. On the other hand, with a minimum height-to-width ratio, SAH exhibits better heat convective performance. The flow is faster in the duct because the cross-sectional area is shorter. Hence, it increases the heat transfer rate of the flowing fluid. A number of researches have been undertaken to find out the parameters for the optimal width and height of a duct to achieve the optimum heat transfer.

6.5 Influence of relative gap position

A secondary heat flow is released by creating a space in continuous ribs. Afterwards, the main heat flow along with the secondary flow passes through the gap and the flow. As a result, the thermal barrier layer weakens, resulting in a greater heat transfer coefficient. On the one hand, a small gap cannot offer enough area for adequate heat flow. On the other hand, if there is a large gap, the flow is retarded [14]. Hence, the gap should have the optimal width for attaining the best heat transfer coefficient.

6.6 Influence of relative roughness width

The relative roughness width (W/w) pertains to the total width of the absorber plate (W). For understanding the concept, one can consider attaching a rib to the absorber plate in a V-shape, with two of its edges at the leading sections and a third one at the trailing section. One would observe that in comparison to the trailing edge, the heat transfer rate is higher at the leading edges. It is due to the turbulent nature of the fluid at the leading edges that the heat transfer rate is higher there. When the flow moves into the trailing edge, it becomes almost stagnant, reducing the heat transfer rate [15]. It has been established that when W/w rises from 1 to 6, the rate of heat transfer improves. The peak is at 6 after which it declines.

7 Artificial roughness patterns in the solar air heater

During the present study, various rib arrangements that influence friction and heat transfer properties were examined. The following sections focus on the effects of different patterns of roughened surfaces as observed in SAH ducts.

7.1 Transverse rib

7.1.1 Continuous transverse rib

The solar air heater, designed by Prasad and Saini [16], made use of wires with small diameters for ensuring roughness. As part of their experiments, the authors increased the P/e ratio from 10 to 20 while changing the e/D

ratio from 0.02 to 0.033. Following their experiment, Prasad and Saini found the maximum increase in Nu and f by 2.38 and 4.25 times, respectively, at the P/e of 10.

Verma and Prasad [17] examined the Nu and f in circular wire ribs with fixed geometrical parameters. Their experiments revealed the e/D ratio varying from 0.01 to 0.03, the P/e ratio varying from 10 to 40, Re^+ varying between 8 and 42, and Re ranging between 5000 and 20000. Furthermore, the maximum THP of 71% was recorded at a roughness Reynolds number of 24.

The impact of transverse wire, attached to the absorber plate, as well as the effect of heat transfer and friction on the transition flow regime, were examined by Gupta *et al.* [18]. The Reynolds number is, in fact, a function of the Stanton number. The St rises when Re increases and it reaches its maximum value when Re reaches 12 000.

7.2 Transverse broken ribs

Sahu and Bhagoria [19] investigated Nu and f for broken transverse ribs with fixed geometrical parameters. Their study involved four parameters, including the P/e ratio varying from 10 to 30, e/D ratio of 1.5, aspect ratio (W/H) of 8, and Re ranging from 3000 to 12 000. Their experiments established that the optimum range of the Nusselt number could be attained when the pitch was at $P = 20$ mm. The maximum enhancement of the heat transfer coefficient by 1.25 to 1.4 times as compared to the smooth plate was obtained. Figure 4 depicts the transverse broken rib geometry.

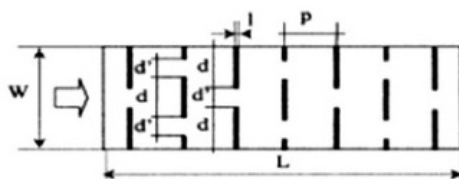


Figure 4: Transverse broken small diameter wire [19].

7.3 Inclined ribs

7.3.1 Continuously inclined ribs

According to Gupta *et al.* [18], inclined ribs are superior to transverse ribs. During experimentation, the authors changed the W/H ratio from 6.8 to

11.5, the e/D value varied from 0.018 to 0.052, the P/e ratio was fixed at 10 and the Re changed from 3000 to 18 000. Following their experimentation, Gupta and his team found the thermal efficiency in the roughened plates to improve by a range of 1.16–1.25 times compared to the smooth plates.

7.3.2 Inclined broken ribs

The impact of a gap in the continuously inclined ribs was examined by Aharwal *et al.* [14]. The different parameters of the continuous inclined ribs included the P/e ratio at 10, the e/D ratio of 0.377, the W/H ratio of 5.84, the angle of attack (α) at 60 deg, and the Re varied from 3000 to 18 000. During experimentations, the gap width of the ribs was also changed from 0.5 to 2 and the relative gap position was altered from 0.16 to 0.67. Accordingly, the maximum enhancements in the Nu and f in ducts with the continuous inclined ribs were recorded at 2.59 and 2.87 that for a flat plate, respectively. Figure 5 depicts the continuous inclined geometry of the ribs. Aharwal *et al.* [20] changed the dimensions and calculated Nu and f . In their study, different parameters were varied, such as the P/e ratio altered from 4 to 10, the e/D ratio changed from 0.018 to 0.0377, and the angle of inclination in flow direction (α) altered from 30 to 90 deg. Aharwal and his team attained the highest Nu and f increased by 2.83 and 3.6 times, respectively, as compared to flat ducts. Thermo-hydraulic performance was reported to be maximum for relative gap width of 1.0 and a relative gap position of 0.25.

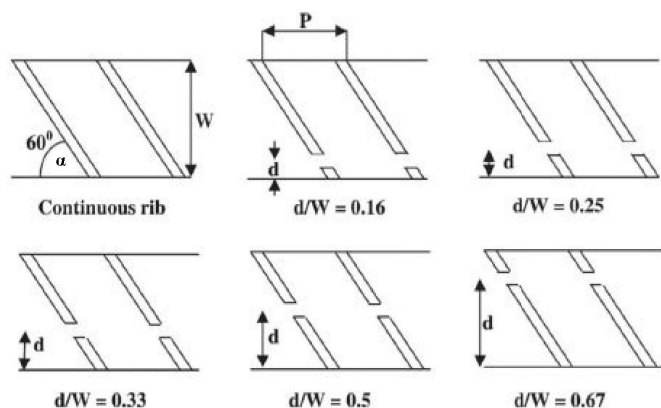


Figure 5: Inclined broken ribs [20].

7.4 V-shape rib

7.4.1 V-shape continuous rib

Momin *et al.* [21] investigated the impact of the V-shaped ribs connected to the absorber plate. During the experiments, the authors varied α from 30 to 90 deg and the e/D ratio from 0.02 to 0.034. Both the Nu and f were enhanced to the maximum at the 60-degree α as compared to a flat duct. In the course of their probe, the authors discovered that the V-shaped ribs performed better than the inclined ribs. The performance of Nu in V-shape rib was 1.14 times the one for the inclined ribs, having equal rib height, pitch, and other operating conditions.

Roughness geometry in V-shaped rib was investigated by Isanto *et al.* [22]. According to their published article, they set the e/D ratio at 0.033, α at 30 to 80 degrees, and P/e at 10. Following their experiments, the f and Nu were recorded to increase 2.45 and 2.34 times, respectively, when compared to the flat plate.

7.4.2 Discrete V-rib

Karwa *et al.* [23] used V- discrete and V- discontinuous ribs in their experiment. The parameters, set by them, were the P/e ratio at 10.63, relative roughness length (B/S , Fig. 6) which is defined as the ratio of the half-length of the V-rib element to the short-way length of the mesh and varied from 3 to 6, and angles of attack set at 45 to 60 deg. The Re value also varied from 2850 to 15 500. The authors observed that discrete ribs outperformed discontinuous ribs and the angle of attack at 60-degree ribs performed better compared to 45-degree ribs. Figure 6 depicts the V-shape's rough geometry.

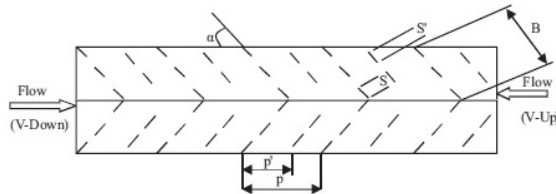


Figure 6: V-shape rib different geometry [23].

Muluwork *et al.* [24] compared the V-down rib, V-up rib, transverse discrete rib, and V-down discrete rib. Studies revealed that the value of St for V-up

and transverse discrete ribs is less than for V-down discrete ribs. Within the range of the parameters studied, the St was found to have a maximum value between 1.32 and 2.47. Karwa [25] examined the V-down continuous, V-up continuous, inclined transverse, V-down discrete, and V-up discrete ribs. He found that the V-down ribs facilitated the maximum heat transfer when pumping powers were equal in both artificially roughened and smooth ducts.

Singh *et al.* [26] investigated the discrete rib with a V-shaped geometry. In their study, the Re values varied from 3000 to 15 000, the relative gap position (g/e) from 0.5 to 2.0, the e/D ratio from 0.015 to 0.043, α varied from 30 to 75 deg and the P/e ratio ranged between 4 and 12. They found that maximum Nu and f increased by 3.04 and 3.11 times, respectively, as compared to smooth plates. Figure 7 depicts the V-down discrete roughness geometry.

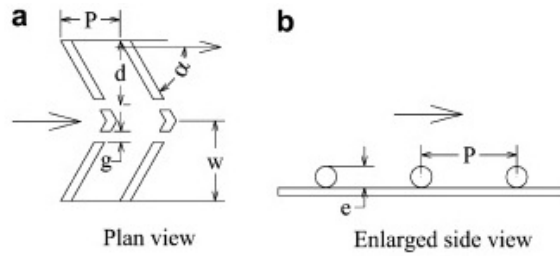


Figure 7: V-down discrete rib [26].

7.5 Ribs with multiple V-shape

7.5.1 Continuous multi V-rib

According to Hans *et al.* [27], the roughness of a variety of V-ribbed ducts is characterized by Reynolds numbers, the e/D and P/e ratios, the angle of inclination, and the W/w value changes from 1 to 10. They observed heat transfer to be the maximum when W/w is equal to 6. The authors pointed out that if the W/w value is less or greater than 6, the extent of heat transfer decreases. Figure 8 depicts the roughness geometry. Maximum enhancement in Nusselt number and friction factor was six- and five-fold, respectively, in comparison to the smooth duct for the range of parameters investigated.

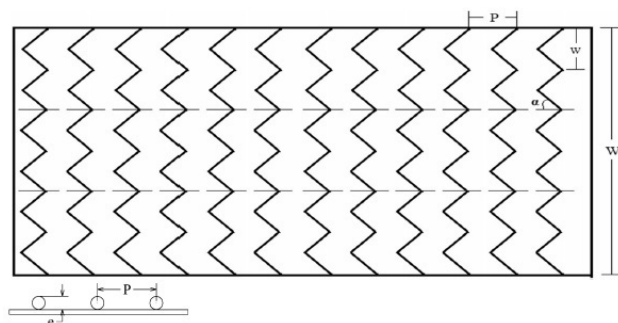


Figure 8: Continuous multi V-rib [27].

7.5.2 Multi V-shaped ribs with a gap

Kumar *et al.* [28] examined the acceleration of heat flow and generation of local turbulence by creating a gap between the V-shaped ribs. Accordingly, the e/D ratio was recorded at 0.043, angles of inclination at 30 to 75 deg, relative roughness pitch at 10, relative gap distance ratios at 0.20 to 0.80, relative gap widths at 0.55 to 1.5, relative width ratio at 6, and Re varied from 2000 to 20 000. The thermo-hydraulic performance (THP) was also found to be significantly boosted compared to a smooth plate. They reported maximum enhancement in Nu and f as 6.32 and 6.12 times that of smooth duct, respectively.

7.6 Arc-shaped ribs

Roughness geometry in an arc-shaped rib was investigated by Saini and Saini [29]. Accordingly, the e/D ratio ranged from 0.0213 to 0.0422, angles of inclination varied from 30 to 75 deg, the P/e value was 10 and Re varied from 2000 to 17 000. The roughness geometry of the arc-shaped ribs improved the Nu to a maximum value of 3.80 and f increased 1.75 times compared to the smooth plate. Figure 9 depicts the arc roughness geometry.

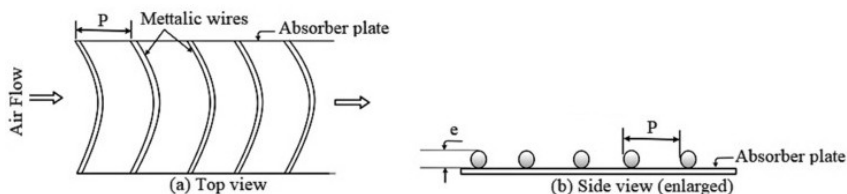


Figure 9: Rib roughness in arc shape [29].

7.7 Multi-arc ribs

Continuous arc multi-rib

Singh *et al.* [30,31] probed the concept of multi-arc roughness. The Reynolds numbers were kept between 2200 and 22 000, the e/D ratio ranged between 0.018 and 0.045, the P/e value varied from 4 and 16, whereas the width ratio was between 1 and 7. They reported maximum enhancement in the Nu and f as 3.71. and 5.07 times that of smooth duct, respectively.

7.7.1 Multiple arc ribs with a gap

Pandey *et al.* [32] studied the concept of multi- arc-shaped roughness geometry with a gap. During the experimentation, e/D varied from 0.016 to 0.044, P/e varied from 4 to 16, the gap width ratio changed from 1 to 7, α varied from 30 to 75 deg, the relative gap varied from 0.5 to 2 and the dimensionless position of the gap ranged from 0.25 to 0.85. The heat transfer on this rough surface is much better than on a smooth one. In fact, it's 5.85 times more effective in moving heat. So, the rough surface is a lot better at transferring heat. Figure 10 depicts the arc roughness geometry.

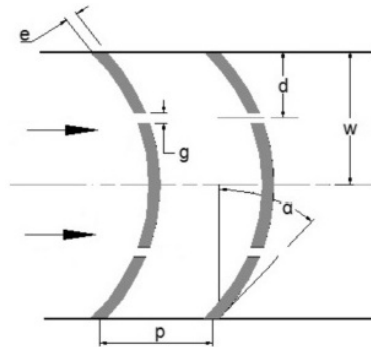


Figure 10: Multiple arc-shaped ribs with gap [32].

7.8 W-shape ribs

The roughened W-shaped SAH duct used by Lanjewar *et al.* [33,34] is shown in Fig. 11. The authors carried out experiments by varying Re from 2000 to 14 000, e/D from 0.018 to 0.03375, angle of inclination from 30 to 75 deg while keeping P/e fixed at 10. They reported maximum enhancement in

Nu as 2.36 times and in friction factor as 2.01 times in comparison to the smooth plate for a 60-degree angle of inclination.

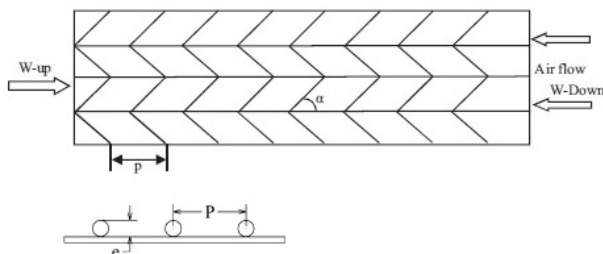


Figure 11: Continuous W-shape rib roughness [33].

7.8.1 Discrete W-shaped rib

Roughness geometry in discrete W-shaped was investigated by Kumar *et al.* [35]. During experimentation, the authors changed e/D from 0.0168 to 0.0338, P/e was fixed at 10, the angle of attack was between 30 to 75 deg, while the Reynolds number varied from 2000 to 15 000. The rise of 2.16 and 2.75 times in Nu and f were observed, respectively, as compared to a flat plate at an angle of inclination of 60 deg.

7.9 Arc-shaped dimple rib

Yadav *et al.* [36] experimented with the arc-shaped dimple coarseness as shown in Fig. 12. During test series, the authors changed different parameters, including e/D , P/e , Reynolds number, and angle of inclination. Yadav and his team found that the thermal efficiency in the roughened plates improves as compared to smooth plates. The friction factor and Nusselt number were increased by 2.93 and 2.89 times with respect to the smooth duct for an angle of attack of 60 deg, a relative pitch of 10, and a relative rib height of 0.03.

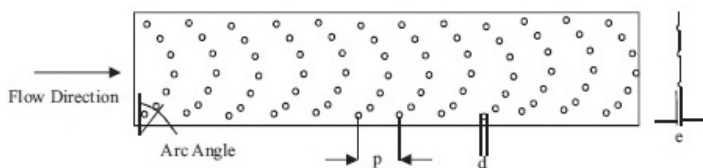


Figure 12: Dimple arc-shaped roughness [36].

Sethi *et al.* [37, 38] examined angular dimple-shaped ribs with different relative pitches and heights. They investigated the geometries with the P/e set from 10 to 20, e/D from 0.021 to 0.036, and arc angles from 45 to 75 deg. The maximum Nu was calculated based on the P/e at 10, e/D at 0.036, and arc angles at 60 deg. They observed an improvement in the thermo-hydraulic performance (THP) of 1.10 to 1.887 times in comparison to the smooth plates.

7.10 Transverse dimple roughness

Saini *et al.* [39] were the first to experiment with artificial roughness created by means of dimpled ribs instead of transverse ribs. During experimentation, the authors changed various parameters like e/D and P/e ratios, and Reynolds numbers. Saini and his team also determined the maximum Nu and f value for P/e at 10. They reported the maximum value of the Nusselt number for a relative roughness height of 0.0379 and a relative roughness pitch of 10.

7.11 Staggered dimple roughness

Bhushan *et al.* [40] experimented with the staggered dimpled roughness instead of the transverse-shaped dimpled roughness. In their study, the duct aspect ratio was 10 while the relative print diameter ranged from 0.147 to 0.367, the relative long-way length (L/e) 25 was set at 37.50 and the relative short-way length (S/e) ranged from 18.75 to 37.5. The maximum enhancement of the Nusselt number and friction factor was increased by 3.8 and 2.2 times, respectively, as compared to the smooth plates. Figure 13 depicts the staggered dimple roughness geometry.

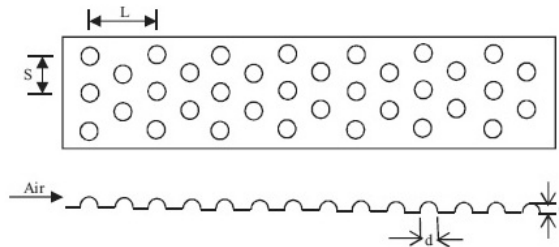


Figure 13: Staggered dimple rib roughness [40].

7.12 Wedge-shaped ribs

According to Bhagoria *et al.* [41] the SAH heat flow and flow characteristics can be improved by roughening the absorber plates and by incorporating transverse ribs, as shown in Fig. 14. In their experiment, the rib wedge angle (Φ) ranged from 8 to 15 deg, e/D from 0.015 to 0.033 and the Reynolds number from 3000 to 18 000. When the difference between the rough and flat plates is compared, the Nu and f were increased by 2.4 and 5.3 times, respectively, in comparison to the flat plates following this experiment.

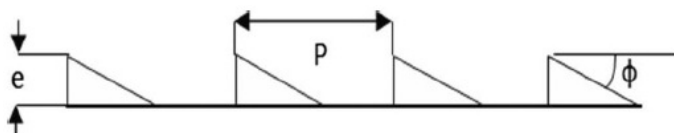


Figure 14: Wedge rib roughness [41].

7.13 Chamfered ribs

The artificial chamfered rib roughness, as shown in Fig. 15, was analyzed by Karwa *et al.* [42]. In their experiment, the relative roughness pitch varied between 4.5 and 8.5, the roughness height within 0.0141–0.0328, the duct aspect ratio ranged from 4.8 to 12, the rib chamfer angles from 15 to 18 deg, and the Reynolds numbers varied between 3000 and 20 000. They observed an improved THP in plates having chamfered-shaped ribs as compared to the smooth plate. The maximum enhancement factor in friction factor and Nusselt number were found to be 3.74 and 3.24, respectively.

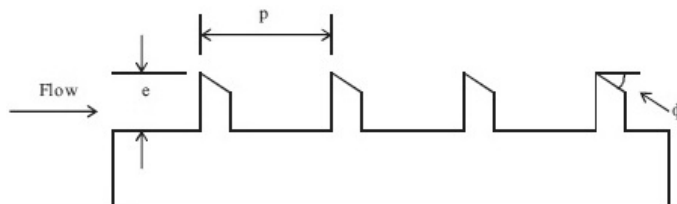


Figure 15: Chamfered ribs [42].

7.14 Combination of ribs

Varun *et al.* [43] investigated the effects of combined inclined and transverse ribs. The researchers modified some parameters, such as P/e , e/D , and

Reynolds number, and tried with a fixed ratio of the duct aspect ratio. The geometry having a relative roughness pitch of 8 had the maximum thermal efficiency. Layek *et al.* [44] investigated the effects of chamfer grooved ribs. They experimented with the e/D ratio ranging from 0.022 to 0.04, P/e from 0.3 to 0.6, relative groove position (g/P) from 0.3 to 0.6, as well as the chamfered angles of 50 to 30 degrees. They found the maximum thermal performance by keeping the relative groove position at 0.4.

Ravi and Saini [45] studied the multi-V-shaped gap with staggered ribs by using different operating parameters, as shown in Fig. 16. They varied the staggered rib pitch (p/P) from 0.2 to 0.8, the staggered rib ratio (r/e , where r is the staggered rib length) between 1 and 4 and kept the W/w ratio at 8. The authors achieved the maximum augmentation of heat transfer at p/P of 0.6, r/e of 3.5, and W/w equaling 8. In another work, Ravi and Saini [46] investigated the double-pass (DP) SAH, having a multi V-shaped gap with staggered ribs. The analysis included parameters such as p/P varied from 0.2 to 0.8, r/e ratio between 1 and 4, and W/w values from 5 to 8. At the corresponding values of p/P amounting to 0.6, r/e ratio of 3.5, and W/w of 7, they found the maximum thermo-hydraulic performance (THP) parameter as compared to the smooth plates.

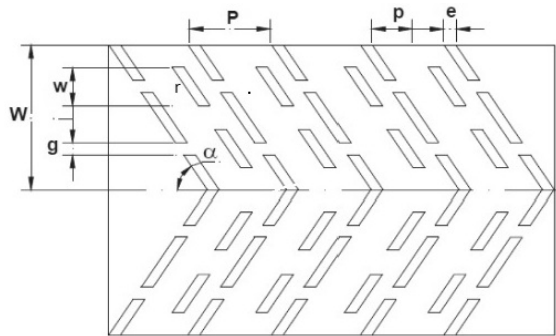


Figure 16: Multi-V-shaped discrete and staggered rib [45, 46].

The performance of the V-shaped discrete and staggered rib was analyzed by Patel and Lanjewar [47], as shown in Fig 17. The maximum value of Nu and f were found to be 2.27 and 4.28 times that of a flat plate, respectively.

Patel and Lanjewar [48] experimented with symmetrical V-shaped gaps and staggered ribs in the duct to evaluate their influence on SAH. They found that the number of gaps in the ribs affects the performance of SAH. At the number of gaps of 3, the authors attained the maximum rise of

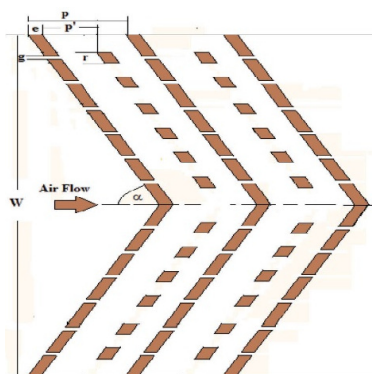


Figure 17: Multiple V-shaped discrete combined with staggered ribs [47].

2.05 and 3.39 times, respectively, in the Nu and f as compared to a flat plate. They also found the maximum THP value of 1.59 as compared to the smooth plate when the number of gaps was 3. Figure 18 depicts the symmetrical V-shaped gap and staggered rib roughness geometry.

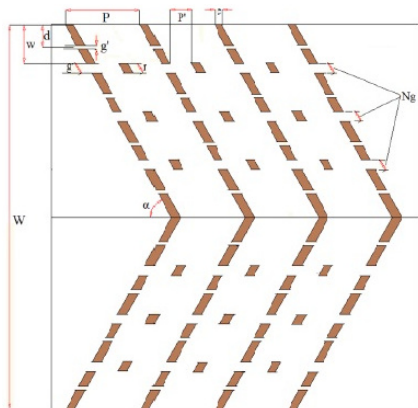


Figure 18: Symmetrical V-shaped gap and staggered rib roughness [48].

In their study, Patel and Lanjewar [49] also observed that the relative roughness pitch P/e varied while other parameters, including e/D , relative gap position (g/e) , dimensionless gap width (d/W) , p'/P , r/e and the number of gaps, remained constant. They found the maximum value of Nu at P/e of 10.

A novel V-rib symmetrical gap and staggered rib element in a SAH were examined by Jain and Lanjewar [50]. They found how artificial roughness

affects the SAH performance, as shown in Fig. 19. They found the maximum value of the THP parameter at $P/e = 12$.

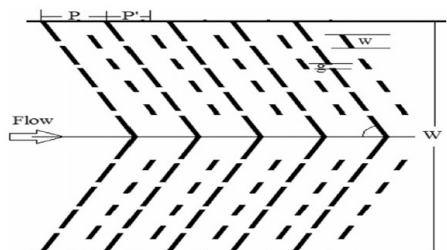


Figure 19: V-rib symmetrical gap with staggered element rib [52].

Patil *et al.* [51–53] investigated a SAH plate with V-rib gaps combined with staggered elements, as shown in Fig. 20. The relative gap positions were changed from 0.2 to 0.8 while all other parameters, including e/D , P/e , relative staggered rib size, and the staggered rib location, remained unchanged. They noted an enhancement in the hydraulic performance varying from 1.48 to 2.10 times and a rise in the Nusselt number from 1.89 to 2.85 times that of the smooth plate.

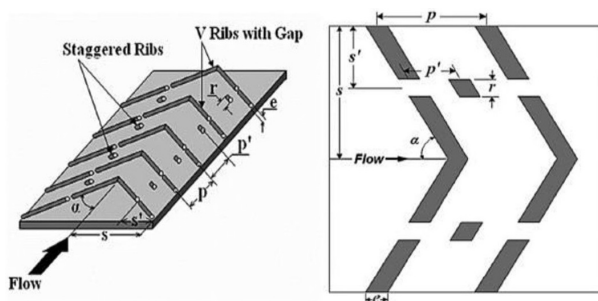


Figure 20: Combination of V-rib gaps with staggered element rib [51–53].

Similarly, Deo *et al.* [54] experimented with V-rib gaps combined with the staggered element. Several parameters were altered, including the relative roughness diameter (e/D) of 0.065, the relative pitch of ribs (P/e) from 4 to 14, the angle of attack from 40 to 80 deg, the number of gaps per limb fixed at 2, relative staggered rib size (r/e) of 4.5 and relative gap width (w/e) of 1. They found the maximum thermal performance as compared to the flat plate.

7.15 Wire mesh

7.15.1 Expanded metal mesh

Saini *et al.* [55] focused on the expanded metal mesh roughness geometry, as shown in Fig. 21. First, they combined relative long way length (L/e) and relative short way length (s/e). They also studied the effects of friction and heat transfer. Their experiments revealed heat transfer coefficients and friction factors rising 4 and 5 times, respectively, as compared to the flat plate.

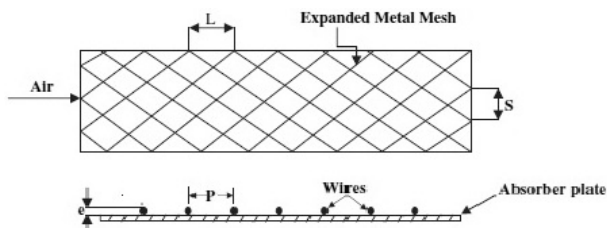


Figure 21: Expanded metal mesh [55].

7.15.2 Discrete metal mesh

Karmare and Tikekar [56] investigated discrete metal mesh, as illustrated in Fig. 22. The authors studied a number of parameters, such as e/D , P/e , Reynolds number and metal grid dimensions. They discovered that plates with roughness values of $e/D = 0.044$, $l/s = 1.72$, and $P/e = 17.5$ performed best.

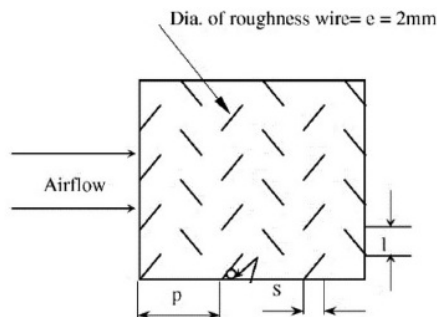


Figure 22: Metal grid rib roughness [56].

7.16 Other roughness

7.16.1 W-rib roughness geometry

Thakur and Thakur [57] investigated W-shaped rib geometry. They experimented with a unique roughness geometry. During the investigation, they altered several parameters, such as the relative staggered length (w/e), relative staggered pitch (p/P), e/D , α , P/e , Re and number of gaps. With the experiment, Thakur and his team could enhance the Nu and f by 3.3 and 4.1 times as compared to smooth ducts, respectively.

Kumar *et al.* [58] examined the effect of an S-shaped configuration on the arc ribs. The parameters used by the team included the e/D was 0.022, W/w varying from 1-4 to 0.054, the P/e varying from 4 to 16, and the angle of attack (α) fixed at 60 deg. Kumar and his team could enhance the Nusselt number 2.71 times and friction factor 4.64 times, as compared to smooth ducts.

7.16.2 Combination of the arc with gap shape and staggered piece

Gill *et al.* [59] investigated a SAH with a broken arc paired with staggered rib roughness geometry. The authors conducted experiments to investigate the impact of different coarseness parameters on Nu and f , including P/e , r/g , e/D , W/w , and relative staggered rib position (P'/P). Figure 23 depicts the roughness geometry. The maximum obtained enhancement of Nusselt number and friction factor was 2.04 and 4.18 times that of a flat plate, respectively.

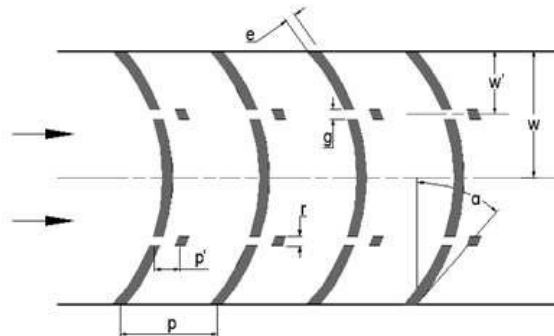


Figure 23: Combination of broken arc rib with staggered rib [59].

7.16.3 A symmetrical arc with multiple gaps:

Jain *et al.* [60–62] investigated arc shape geometry using various gaps in a single arc. The parameters, used in their study, were the Reynolds number between 3000 and 18 000, relative roughness pitch (P/e) at 12, arc angle (α) at 60 deg, g/e varying from 2 to 5, and e/D of 0.047. With the experiment, Jain and his team could enhance the Nusselt number 2.77 times and the friction factor 3.66 times, as compared to flat ducts.

8 Thermo-hydraulic effectiveness of artificial roughened surfaces

To sum up, a significant rise in the friction factor was observed with the incorporation of artificial coarseness in order to improve heat transfer. Hence, roughness geometry proved to be essential for heat transfer to a greater degree while minimizing friction losses. While choosing the methods for enhancement of heat transfer, one has to account for the huge requirement of pumping energy as turbulence in the flow results in a significant pressure drop. A high rate of heat transfer at the minimum pumping energy is essential for developing an effective and compact SAH.

During the present study, the Nusselt number and the friction factor values for the roughened and smooth absorber surfaces were compared using the parameters for thermo-hydraulic performance (THP). Figure 24 represents the friction factor *versus* the Reynolds number and shows that an increase in the Reynolds number results in a friction factor decrease. According to Fig. 24, the optimal outcome for the friction factor along the whole range of the Reynolds number is not a single geometry. The maximum value of friction factor is obtained in the case of continuous multi V-rib geometry.

They were also compared with their respective Reynolds numbers, as shown in Fig. 25. The THP characteristics with a wide array of values, ranging from 0.49 to 3.70, are presented in Fig. 25. The THP parameter is the lowest when the inclined angle and transverse ribs are combined. However, multiple V-ribs with a gap ensure the highest rate of heat transfer. At low Reynolds numbers, multi-arc ribs with gaps are not very effective. However, their performance improves dramatically as the Reynolds number increases.

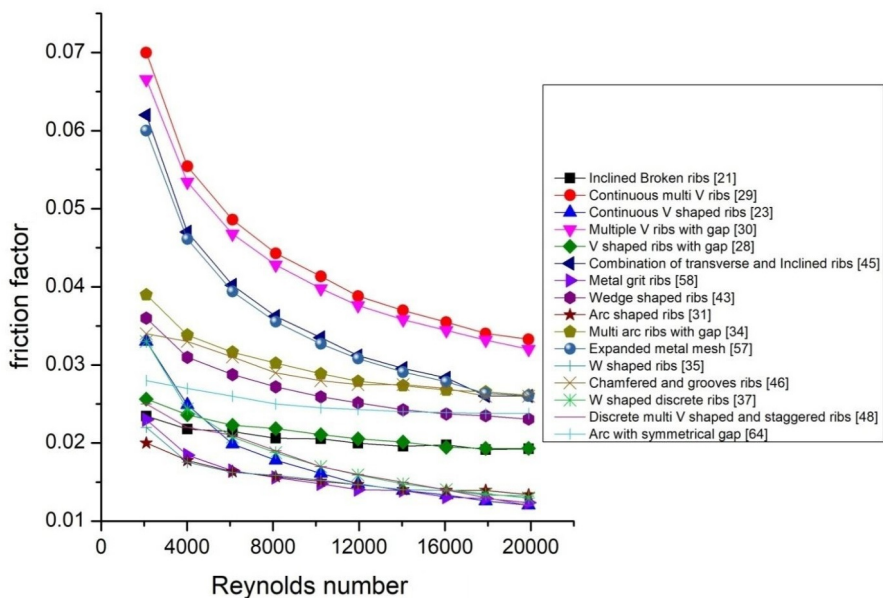


Figure 24: Friction factor with respect to Reynolds number, based on data from different research works.

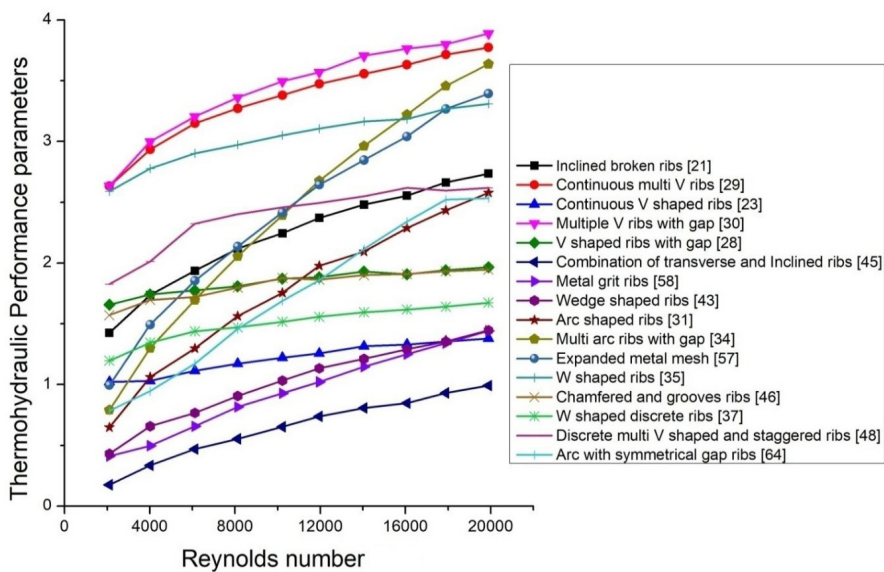


Figure 25: Comparison of thermo-hydraulic performance parameters for various roughened surfaces determined based on data reported by different researchers.

9 Conclusions

The present study has attempted a thorough examination of several artificial roughness configurations in solar air heaters as suggested by a number of researchers. The impact of different shapes of coarseness and flow characteristics on heat transfer and friction factors has also been discussed. The following conclusions may be taken from the data that has been analyzed.

1. Artificial coarseness in the form of small ribs on the undersurface of the absorber plate is an excellent alternative for improving heat transfer in solar air heaters. However, at the same time, artificial roughness is responsible for the increased friction factor which enhances the demand for pumping power.
2. The characteristics of various parameters such as relative roughness pitch, relative roughness height, angle of attack, and rib arrangement, i.e. inclined, transverse, single V-shape, multiple V-shape, arc-shape, and multi arc-shape ribs were investigated.
3. For almost the entire experimental setup, the maximum values of the Nusselt number and friction factor were obtained for the relative roughness pitch (P/e) of 8 to 10, the relative roughness height (e/D) of 0.03, and an angle of attack (α) of 60 deg.
4. Compared to continuous ribs, insertion of V-gaps in continuous ribs, continuous arc ribs, and continuous W-ribs enhance the friction factor and heat transfer rate.
5. The maximum increase in heat transfer was recorded for multiple V-rib geometry with a gap, followed by multiple V-shaped rib geometry and multiple arc-shaped rib geometry with a gap. Due to providing a gap in continuous V-ribs, multi V-ribs, arc ribs, and multi arc-ribs, the Nusselt numbers were increased by 1.32, 1.12, 1.33, and 1.15 times, respectively.
6. Continuous multiple V-rib geometry showed a significant increase in the friction factor, followed by multiple V-rib geometry with a gap.
7. S-shaped ribs, metal rib grids, and ribs with grooves proved to be inadequate. Each of these types needed machining in order to create grooves.

8. Comparison of the-hydraulic performance parameter with respect to the Reynolds number has been performed. Maximum of thermo-hydraulic performance were found for W-ribs, multiple V-ribs with a gap, and multiple arc-rib with a gap in different Reynolds number.

This review article will assist researchers in understanding the importance of the roughness aspect that significantly increases the the Nusselt number and friction factor, thereby improving the operation of solar air heaters. Accordingly, one could work on the development of designs for alternative configurations of rectangular solar air heater ducts by using these roughness factors.

Received 22 October 2022

References

- [1] Tiwari G.N.: *Solar Energy: Fundamentals, Design, Modelling and Applications*. Alpha Sci., 2002.
- [2] Gawande V.B., Dhoble A.S., Zodpe D.B., Chamoli S.: *A review of CFD methodology used in literature for predicting thermo-hydraulic performance of a roughened solar air heater*. *Renew. Sustain. Energy Rev.* **54**(2016), 550–605.
- [3] Bhatti M.S., Shah R.: *Turbulent and transition flow convective heat transfer in ducts*. In: *Handbook of Single-Phase Convective Heat Transfer* (S. Kakaç, R.K. Shah, W. Aung, Eds.). Wiley, New York 1987.
- [4] Nikuradse J.: *Laws of Flow in Rough Pipes*. NACA TM 1292, Washington 1950.
- [5] Dipprey D.F., Sabersky R.H.: *Heat and momentum transfer in smooth and rough tubes at various Prandtl numbers*. *Int. J. Heat Mass Transf.* **6**(1963), 5, 329–353.
- [6] Poitras G.J., Brizzi L.E., Gagnon Y.: *Structure of channel flows with surface mounted ribs*. *J. Therm. Sci.* **13**(2004), 3, 213–219.
- [7] Kreith F., Bohn M.S.: *Principles of Heat Transfer*. Thomson Learning, 2001.
- [8] Hottel H.C., Bernard B.W.: *The performance of flat-plate solar heat collectors*. In: *Renewable Energy* (Bent Sorensen, Ed.). Taylor & Francis, Routledge 2018, 324–355.
- [9] Biondi P., Cicala L., Farina G.: *Performance analysis of solar air heaters of conventional design*. *Sol. Energy* **41**(1988), 1, 101–107.
- [10] Lewis M.J.: *Optimising the thermohydraulic performance of rough surfaces*. *Int. J. Heat Mass Transf.* **18**(1975), 11, 1243–1248.
- [11] Prasad B.N., Saini J.S.: *Optimal thermohydraulic performance of artificially roughened solar air heaters*. *Sol. Energy* **47**(1991), 2, 91–96.
- [12] Prasad, B.N., Saini J.S.: *Effect of artificial roughness on heat transfer and friction factor in a solar air heater*. *Sol. Energy* **41**(1988), 6, 555–560.

- [13] Taslim M.E., Li T., Kercher D.M.: *Experimental heat transfer and friction in channels roughened with angled, V-shaped, and discrete ribs on two opposite walls*. J. Turbomach. **118**(1996), 1, 94-GT-163, V004T09A018.
- [14] Aharwal K.R., Gandhi B. K., Saini J.S.: *Experimental investigation on heat-transfer enhancement due to a gap in an inclined continuous rib arrangement in a rectangular duct of solar air heater*. Renew. Energy **33**(2008), 4, 585–596.
- [15] Kumar A., Kim M.-H.: *CFD analysis on the thermal hydraulic performance of an SAH duct with multi V-shape roughened ribs*. Energies **9**(2016), 6, 415.
- [16] Prasad B.N., Saini J.S.: *Effect of artificial roughness on heat transfer and friction factor in a solar air heater*. Sol. Energy **41**(1988), 6, 555–560.
- [17] Verma S.K., Prasad B.N.: *Investigation for the optimal thermohydraulic performance of artificially roughened solar air heaters*. Renew. Energy **20**(2000), 1, 19–36.
- [18] Gupta D., Solanki S.C., Saini J.S.: *Heat and fluid flow in rectangular solar air heater ducts having transverse rib roughness on absorber plates*. Sol. Energy **51**(1993), 1, 31–37.
- [19] Sahu M.M., Bhagoria J.L.: *Augmentation of heat transfer coefficient by using 90 broken transverse ribs on absorber plate of solar air heater*. Renew. Energy **30**(2005), 13, 2057–2073.
- [20] Aharwal K.R., Gandhi B.K., Saini J.S.: *Heat transfer and friction characteristics of solar air heater ducts having integral inclined discrete ribs on absorber plate*. Int. J. Heat Mass Transf. **52**(2009), 25-26, 5970–5977.
- [21] Momin A.-M.E., Saini J.S., Solanki S.C.: *Heat transfer and friction in solar air heater duct with V-shaped rib roughness on absorber plate*. Int. J. Heat Mass Transf. **45**(2002), 16, 3383–3396.
- [22] Istanto T., Danardono D., Yaningsih I., Wijayanta A.T.: *Experimental study of heat transfer enhancement in solar air heater with different angle of attack of V-down continuous ribs*. AIP Conf. Proc., **1737**(2016), 1, 060002.
- [23] Karwa R., Bairwa R.D., Jain B.P., Karwa N.: *Experimental study of the effects of rib angle and discretization on heat transfer and friction in an asymmetrically heated rectangular duct*. J. Enhanc. Heat Transf. **12**(2005), 4, 343–355.
- [24] Muluwork K.B., Saini J.S., Solanki S.C.: *Studies on discrete rib roughened solar air heaters*. In: Proc. National Solar Energy Convention-98, Roorkee SESI **75**(1998), 84.
- [25] Karwa R.: *Experimental studies of augmented heat transfer and friction in asymmetrically heated rectangular ducts with ribs on the heated wall in transverse, inclined, V-continuous and V-discrete pattern*. Int. Commun. Heat Mass Transf. **30**(2003), 2, 241–250.
- [26] Singh S., Chander S., Saini J.S.: *Heat transfer and friction factor correlations of solar air heater ducts artificially roughened with discrete V-down ribs*. Energy **36**(2011), 8, 5053–5064.
- [27] Hans V.S., Saini R.P., Saini J.S.: *Heat transfer and friction factor correlations for a solar air heater duct roughened artificially with multiple v-ribs*. Sol. Energy **84**(2010), 6, 898–911.

- [28] Kumar A., Saini R.P., Saini J.S.: *Experimental investigation on heat transfer and fluid flow characteristics of air flow in a rectangular duct with Multi V-shaped rib with gap roughness on the heated plate*. Sol. Energy **86**(2012), 6, 1733–1749.
- [29] Saini S.K., Saini R.P.: *Development of correlations for Nusselt number and friction factor for solar air heater with roughened duct having arc-shaped wire as artificial roughness*. Sol. Energy **82**(2008), 12, 1118–1130.
- [30] Singh A.P.: *Effect of artificial roughness on heat transfer and friction characteristics having multiple arc shaped roughness element on the absorber plate*. Sol. Energy **105**(2014), 479–493.
- [31] Singh A.P.: *Heat transfer and friction factor correlations for multiple arc shape roughness elements on the absorber plate used in solar air heaters*. Exp. Therm. Fluid Sci. **54**(2014), 117–126.
- [32] Pandey N.K., Bajpai V.K.: *Experimental investigation of heat transfer augmentation using multiple arcs with gap on absorber plate of solar air heater*. Sol. Energy **134**(2016), 314–326.
- [33] Lanjewar A., Bhagoria J.L., Sarviya R.M.: *Heat transfer and friction in solar air heater duct with W-shaped rib roughness on absorber plate*. Energy **36**(2011), 7, 4531–4541.
- [34] Lanjewar A., Bhagoria J.L., Sarviya R.M.: *Experimental study of augmented heat transfer and friction in solar air heater with different orientations of W-rib roughness*. Exp. Therm. Fluid Sci. **35**(2011), 6, 986–995.
- [35] Kumar A., Bhagoria J.L., Sarviya R.M.: *Heat transfer and friction correlations for artificially roughened solar air heater duct with discrete W-shaped ribs*. Energy Convers. Manage. **50**(2009), 8, 2106–2117.
- [36] Yadav S., Kaushal M.: *Nusselt number and friction factor correlations for solar air heater duct having protrusions as roughness elements on absorber plate*. Exp. Therm. Fluid Sci. **44**(2013), 34–41.
- [37] Sethi M., Thakur N.S., Varun: *Heat transfer and friction characteristics of dimple-shaped roughness element arranged in angular fashion (arc) on the absorber plate of solar air heater*. J. Renew. Sustain. Energy **4**(2012), 2, 023112.
- [38] Sethi M., Thakur N.S.: *Correlations for solar air heater duct with dimpled shape roughness elements on absorber plate*. Sol. Energy **86**(2012), 9, 2852–2861.
- [39] Saini R.P., Verma J.: *Heat transfer and friction factor correlations for a duct having dimple-shape artificial roughness for solar air heaters*. Energy **33**(2008), 8, 1277–1287.
- [40] Bhushan B., Singh R.: *Nusselt number and friction factor correlations for solar air heater duct having artificially roughened absorber plate*. Sol. Energy **85**(2011), 5, 1109–1118.
- [41] Bhagoria J. L., Saini J.S., Solanki S.C.: *Heat transfer coefficient and friction factor correlations for rectangular solar air heater duct having transverse wedge shaped rib roughness on the absorber plate*. Renew. Energy **25**(2002), 3, 341–369.
- [42] Karwa R., Solanki S.C., Saini, J.S.: *Heat transfer coefficient and friction factor correlations for the transitional flow regime in rib-roughened rectangular ducts*. Int. J. Heat Mass Transf. **42**(1999), 9, 1597–1615.

- [43] Varun, Saini R.P., Singal S.K.: *Investigation of thermal performance of solar air heater having roughness elements as a combination of inclined and transverse ribs on the absorber plate*. Renew. Energy **33**(2008), 6, 1398–1405.
- [44] Layek A., Saini J.S., Solanki S.C.: *Heat transfer and friction characteristics for artificially roughened ducts with compound turbulators*. Int. J. Heat Mass Transf. **50**(2007), 23–24, 4845–4854.
- [45] Ravi R.K., Saini R.P.: *Effect of roughness elements on thermal and thermohydraulic performance of double pass solar air heater duct having discrete multi V-shaped and staggered rib roughness on both sides of the absorber plate*. Exp. Heat Transf. **31**(2018), 1, 47–67.
- [46] Ravi R.K., Saini R.P.: *Nusselt number and friction factor correlations for forced convective type counter flow solar air heater having discrete multi V shaped and staggered rib roughness on both sides of the absorber plate*. Appl. Therm. Eng. **129**(2018), 735–746.
- [47] Patel S.S., Lanjewar A.: *Experimental analysis for augmentation of heat transfer in multiple discrete V-patterns combined with staggered ribs solar air heater*. Renew. Energy Focus **25**(2018), 31–39.
- [48] Patel S.S., Lanjewar A.: *Performance study of solar air heater duct with gap in V-rib with symmetrical gap and staggered ribs*. Heat Mass Transf. **55**(2019), 9, 2517–2532.
- [49] Patel S.S., Lanjewar A.: *Experimental and numerical investigation of solar air heater with novel V-rib geometry*. J. Energy Storage **21**(2019), 750–764.
- [50] Jain P.K., Lanjewar A.: *Overview of V-rib geometries in solar air heater and performance evaluation of a new V-rib geometry*. Renew. Energy **133**(2019), 77–90.
- [51] Patil A.K., Saini J.S., Kumar K.: *Effect of gap position in broken V-rib roughness combined with staggered rib on thermohydraulic performance of solar air heater*. Green **1**(2011), 5–6, 329–338.
- [52] Patil A.K., Saini J.S., Kumar K.: *Heat transfer and friction characteristics of solar air heater duct roughened by broken V-shape ribs combined with staggered rib piece*. J. Renew. Sustain. Energy **4**(2012), 1, 013115.
- [53] Patil A.K., Saini J.S., Kumar K.: *A comprehensive review on roughness geometries and investigation techniques used in artificially roughened solar air heaters*. Int. J. Renew. Energy Res. **2**(2012), 1, 1–15.
- [54] Deo N.S., Chander S., Saini J.S.: *Performance analysis of solar air heater duct roughened with multigap V-down ribs combined with staggered ribs*. Renew. Energy **91**(2016), 484–500.
- [55] Saini R.P., Saini J.S.: *Heat transfer and friction factor correlations for artificially roughened ducts with expanded metal mesh as roughness element*. Int. J. Heat Mass Transf. **40**(1997), 4, 973–986.
- [56] Karmare S.V., Tikekar A.N.: *Heat transfer and friction factor correlation for artificially roughened duct with metal grit ribs*. Int. J. Heat Mass Transf. **50**(2007), 21–22: 4342–4351.
- [57] Thakur S., Thakur N.S.: *Impact of multi-staggered rib parameters of the ‘W’ shaped roughness on the performance of a solar air heater channel*. Energ. Source Part A (2020), 1–20.

- [58] Kumar K., Prajapati D.R., Sushant S.: *Heat transfer and friction factor correlations development for solar air heater duct artificially roughened with 'S' shape ribs*. Exp. Therm. Fluid Sci. **82**(2017), 249–261.
- [59] Gill R.S., Hans V.S., Singh S.: *Investigations on thermo-hydraulic performance of broken arc rib in a rectangular duct of solar air heater*. Int. Commun. Heat Mass Transf. **88**(2017), 20–27.
- [60] Jain S.K., Agrawal G.D., Misra R.: *Heat transfer augmentation using multiple gaps in arc-shaped ribs roughened solar air heater: An experimental study*. Energ. Source Part A **43**(2021), 24, 3345–3356.
- [61] Jain S.K., Agrawal G.D., Misra R.: *Experimental investigation of thermohydraulic performance of the solar air heater having arc-shaped ribs with multiple gaps*. J. Therm. Sci. Eng. Appl. **12**(2020), 1, 011014.
- [62] Jain S.K., Misra R., Agrawal G.D.: *Effect of gap width on thermal performance of solar air heater having arc-shaped ribs with symmetrical gaps: An experimental investigation*. Environ. Dev. Sustain. **22**(2020), 7, 6563–6583.

Notes for Contributors

ARCHIVES OF THERMODYNAMICS publishes original papers which have not previously appeared in other journals. The journal does not have article processing charges (APCs) nor article submission charges. The language of the papers is English. The paper should not exceed the length of 25 pages. All pages should be numbered. The plan and form of the papers should be as follows:

1. The heading should specify the title (as short as possible), author, his/her complete affiliation, town, zip code, country and e-mail. Please indicate the corresponding author. The heading should be followed by *Abstract* of maximum 15 typewritten lines and *Keywords*.

2. More important symbols used in the paper can be listed in *Nomenclature*, placed below *Abstract* and arranged in a column, e.g.:

u – velocity, m/s

v – specific volume, m³/kg

etc.

The list should begin with Latin symbols in alphabetical order followed by Greek symbols also in alphabetical order and with a separate heading. Subscripts and superscripts should follow Greek symbols and should be identified with separate headings. Physical quantities should be expressed in SI units (*Système International d'Unités*).

3. All abbreviations should be spelled out first time they are introduced in the text.
4. The equations should be each in a separate line. Standard mathematical notation should be used. All symbols used in equations must be clearly defined. The numbers of equations should run consecutively, irrespective of the division of the paper into sections. The numbers should be given in round brackets on the right-hand side of the page.
5. Particular attention should be paid to the differentiation between capital and small letters. If there is a risk of confusion, the symbols should be explained (for example *small c*) in the margins. Indices of more than one level (such as B_{fa}) should be avoided wherever possible.
6. Computer-generated figures should be produced using **bold lines and characters**. No remarks should be written directly on the figures, except numerals or letter symbols only. Figures should be as small as possible while displaying clearly all the information requires, and with all lettering readable. The relevant explanations can be given in the caption.
7. The figures, including photographs, diagrams, etc., should be numbered with Arabic numerals in the same order in which they appear in the text. Each figure should have its own caption explaining the content without reference to the text.
8. Computer files on an enclosed disc or sent by e-mail to the Editorial Office are welcome. The manuscript should be written as a MS Word file – *.doc, *.docx or L^AT_EX file – *.tex. For revised manuscripts after peer review process, figures should be submitted as separate graphic files in either vector formats (PostScript (PS),

Encapsulated PostScript (EPS), preferable, CorelDraw (CDR), etc.) or bitmap formats (Tagged Image File Format (TIFF), Joint Photographic Experts Group (JPEG), etc.), with the resolution not lower than 300 dpi, preferably 600 dpi. These resolutions refer to images sized at dimensions comparable to those of figures in the print journal. Therefore, electronic figures should be sized to fit on single printed page and can have maximum 120 mm x 170 mm. Figures created in MS Word, Excel, or PowerPoint will not be accepted. The quality of images downloaded from websites and the Internet are also not acceptable, because of their low resolution (usually only 72 dpi), inadequate for print reproduction.

9. The references for the paper should be numbered in the order in which they are called in the text. Calling the references is by giving the appropriate numbers in square brackets. The references should be listed with the following information provided: the author's surname and the initials of his/her names, the complete title of the work (in English translation) and, in addition:
 - (a) for books: the publishing house and the place and year of publication, for example:
[1] Holman J.P.: *Heat Transfer*. McGraw-Hill, New York 1968.
 - (b) for journals: the name of the journal, volume (Arabic numerals in bold), year of publication (in round brackets), number and, if appropriate, numbers of relevant pages, for example:
[2] Rizzo F.I., Shippy D.I.: *A method of solution for certain problems of transient heat conduction*. AIAA J. **8**(1970), No.11, 2004-2009.

For works originally published in a language other than English, the language should be indicated in parentheses at the end of the reference.

Authors are responsible for ensuring that the information in each reference is complete and accurate.

10. As the papers are published in English, the authors who are not native speakers of English are obliged to have the paper thoroughly reviewed language-wise before submitting for publication.

Manuscript submission Manuscripts to be considered for publication should be electronically submitted to the Editorial Office via the online submission and reviewing system, the Editorial System, at <http://www.editorialsystem.com/aot>. Submission to the journal proceeds totally on line and you will be guided stepwise throughout the process of the creation and uploading of your files. The body of the text, tables and figures, along with captions for figures and tables should be submitted separately. The system automatically converts source files to a single PDF file article, for subsequent approval by the corresponding Author, which is then used in the peer-review process. All correspondence, including notification confirming the submission of the manuscripts to the Editorial Office, notification of the Editors's decision and requests for revision, takes place by e-mails. Authors should designate the corresponding author, whose responsibility is to represent the Authors in contacts with the Editorial Office. Authors are requested not to submit the manuscripts by post or e-mail.

The illustrations may be submitted in color, however they will be printed in black and white in the journal, so the grayscale contributions are preferable. Therefore, the figure

caption and the entire text of the paper should not make any reference to color in the illustration. Moreover the illustration should effectively convey author's intended meaning when it is printed as a halftone. The illustrations will be reproduced in color in the online publication.

Further information All manuscripts will undergo some editorial modification. The paper proofs (as PDF file) will be sent by e-mail to the corresponding author for acceptance, and should be returned within two weeks of receipt. Within the proofs corrections of minor and typographical errors in: author names, affiliations, articles titles, abstracts and keywords, formulas, symbols, grammatical error, details in figures, etc., are only allowed, as well as necessary small additions. The changes within the text will be accepted in case of serious errors, for example with regard to scientific accuracy, or if authors reputation and that of the journal would be affected. Submitted material will not be returned to the author, unless specifically requested.

A PDF file of published paper will be supplied free of charge to the Corresponding Author.

Submission of the manuscript expresses at the same time the authors consent to its publishing in both printed and electronic versions.

Transfer of Copyright Agreement Submission of the manuscript means that the authors automatically agree to assign the copyright to the Publisher. Once a paper has been accepted for publication, as a condition of publication, the authors are asked to send by email a scanned copy of the signed original of the Transfer of Copyright Agreement, signed by the Corresponding Author on behalf of all authors to the Managing Editor of the Journal. The copyright form can be downloaded from the journal's website at <http://www.imp.gda.pl/archives-of-thermodynamics/> under Notes for Contributors.

The Editorial Committee

